STRUCTURE AND EVOLUTION OF PLANETARY NEBULAE

by

Gary John Robinson BSc., ARCS, FRAS

September 1981

A thesis submitted for the degree of Doctor of Philosophy of the University of London and for the Diploma of the Imperial College.

Astronomy Group,
Blackett Laboratory,
Imperial College,
London SW7 2BZ.

Abstract

The physical characteristics of Planetary Nebulae are reviewed, followed by a survey and discussion of the published nebular and central star classification schemes.

New [OIII] line profiles of 35 nebulae are presented, obtained with a high resolution Fabry-Perot interferometer, and are compared with a compilation of published optical data on line splittings. New electronographic data in the [OIII] and HI lines, obtained with a " Spectracon " image tube , are also presented. These are used to interpret the line profiles with the aid of a simple model to yield mean expansion velocities and linear radii for these nebulae. Published Fabry-Perot line profile data on other Planetaries is also interpreted with the model. Possible correlations between expansion velocity, linear radius, morphological type and central star spectral type of a total of 81 objects are examined. Two relatively distinct sequences of nebulae appear : a " High-velocity " sequence (which seems to encompass the two sequences of Smith, 1973) characterised by mainly type III / IV morphology and OVI sequence or continuum spectral type central stars ; and a " Low-velocity " sequence characterised by O type central stars. Despite the considerable scatter the data are fitted reasonably well by two roughly linear sequences of low (0.2 M_o) and high (0.5 M_o) stellar radiation pressure-driven model nebulae of Ferch and Salpeter (1975).

A detailed investigation of NGC 7027 is undertaken, in which new and published data are used to model this nebula with a hollow prolate spheroid shell of varying density. The radio appearance, recombination line and free-free spectra predicted by this model closely match the available data. The radio data are used to derive an accurate astrophysical distance to NGC 7027 of 1.33 Kpc.

Acknowledgements

I would like to express my thanks to Dr. Ken Reay for his continuous supervision and interest in this work. I am also extremely grateful for the assistance of many past and present members of the Astronomy Group at Imperial College.

From October 1976 to October 1979 I was in grateful receipt of a post-graduate grant from the Science Research Council, U.K.

I would like to dedicate this work to my wife Sharon which, without her constant encouragement, would not have been completed so soon.

Contents

II OBSERVATIONS

Chapter 1

1.1 Definition and Characteristics

The term " Planetary Nebula " is generally thought to have originated from the description of a certain class of nebulae as " Greenish discs, similar to the planets Uranus and Neptune " by William Herschel in 1785. In fact, Darquier in 1781 had already discovered in the constellation of Lyra the so-called " Ring Nebula ", which he described as " Looking like a faded planet ". The earliest recorded, but not identified, Planetary Nebula is NGC 6853 - the " Dumbell Nebula " - to which Messier assigned the number 27 in his famous comet-seekers' catalogue of " Objects to Ignore " , published in 1764. This work also contains three other Planetaries.

Planetary Nebulae are HII regions which spectroscopically exhibit many of the characteristics of the larger diffuse HII regions. However, they differ from the diffuse HII regions in many important aspects :-

(i) they are much smaller, being typically a few tenths of parsecs in diameter.

(ii) a very hot centrally situated exciting star, sometimes a member of a binary system, is associated with them.

(iii) they usually have some degree of symmetry, either axial or bi-axial.

(iv) they appear to be expanding in an ordered manner at typical speeds of 30 Km s^{-1}, which is several times greater than the local speed of sound.

(v) their galactic positions and kinematic distribution are typical of disk population stars, whereas diffuse HII regions are associated with several young hot O or early B type spiral-arm stars.

(vi) their nebular masses are about 0.1 $M_\odot$, compared with 10^3 $M_\odot$ for diffuse HII regions.

It is widely believed that Planetaries are the ejected outer envelopes of the stars which are to be found at their centres. Diffuse HII regions on the other hand, are thought to be the birth-places of stars, and so are not so necessarily intimately linked to the stars making them shine.

Since a substantial proportion of all stars pass through the Planetary Nebula stage it is important to realise that Planetaries play a major rôle in the chemical processing and evolution of the Galaxy (Tinsley 1978).

1.2 Ionization Structure

Broad-band colour photographs of Planetary Nebulae provide one of the most striking methods of demonstrating the phenomenum known as the " stratification of radiation ". This is due to the variation in degree of ionization through a nebula. For example [OIII] is observed to be located nearer the central exciting star than [OII] , which in turn is closer than [OI]. The dominant visible emission from O^{++} ions falls in the green, that of O^{+} in the blue, whilst that of O^{o} lies in the red. Therefore, the coloured zones that make up the image of a nebula indicate the relative locations of the ionization states of a particular element.

The physical mechanism for the ionization structure of nebulae was first investigated by Stromgren (1939), and is briefly outlined here :

Consider a uniformly dense sphere of hydrogen surrounding a hot star. Radiation from the star will ionize neutral atoms if its frequency is equal to or greater than the Lyman limit, and in doing so will be absorbed. At progressively greater distances from the star less Lyman continuum radiation is available for photo-ionization until (if a sufficient amount of hydrogen is present) a distance is reached where equal number densities of ionized and neutral atoms exist due to the balancing of the photo-ionizing and recombination rates. The thickness of the HI/HII transition boundary is approximately equal to the mean free-path of a Lyman-alpha photon. For a typical Planetary this is about one percent of the nebular diameter, and so the boundary is very sharp. When the amount of matter present is insufficient to absorb all of the Lyman continuum radiation from the star an outer region of neutral hydrogen may not exist - in this case the nebula is said to be " density bounded ". The opposite case is referred to as being " radiation bounded ".

A straightforward relation exists between the number of Lyman continuum photons Q emitted by the star per second and the number density n_H of a purely hydrogen nebula :-

$$Q = \frac{4}{3}\pi . R_s^3 . n_H^2 . \alpha_B$$

where α_B is the hydrogen recombination coefficient to excited levels and R_s - the " Stromgren radius " - is the radius within which virtually all of the hydrogen is ionized.

The presence of other elements, in particular helium and oxygen, results in competition for the stellar photons by the different elements. However, due to the nature of photo-ionization cross-sections, the elements only absorb strongly in certain regions of the spectrum. For example, hydrogen absorbs most strongly at λ912Å (the Lyman limit), whereas the peak occurs for HeI at λ504Å . Therefore photons with wavelengths between λ504Å and λ912Å are capable of ionizing hydrogen only, while below λ504Å photons are capable of ionizing helium as well. The Stromgren radii for hydrogen and helium depend upon the stellar spectrum and the helium abundance.

Figure 1.1 , which is adapted from Osterbrock (1974), shows the ionization structure of a model Planetary Nebula composed of H, He and O with a black-body central star of 10^5 K. He^{++} is only present in nebulae with stellar temperatures in excess of 10^5 K because of the high (54.4 eV) ionization potential of He^+. The close similarity of the He^{++} and O^{+++} zones is a result of their approximately equal ionization potentials, 54.4 and 54.9 eV respectively.

An additional ionization mechanism is one arising from charge-exchange reactions. These occur at interfaces between O^o and O^+ regions for example. The reaction in this case is :-

$$O^o(^3P) + H^+ \rightleftharpoons O^+(^4S) + H^o(^2S)$$

The cross-section for this process is large because of the attractive polarization force between the neutral oxygen atom and the proton and also the ionization potentials of O^o and H^o are similar. Charge-exchange reactions are only important in Planetary Nebulae at the outer edges of their O^+ zones, but do not alter the HI/HII balance significantly owing to the low oxygen abundances.

Figure 1.1

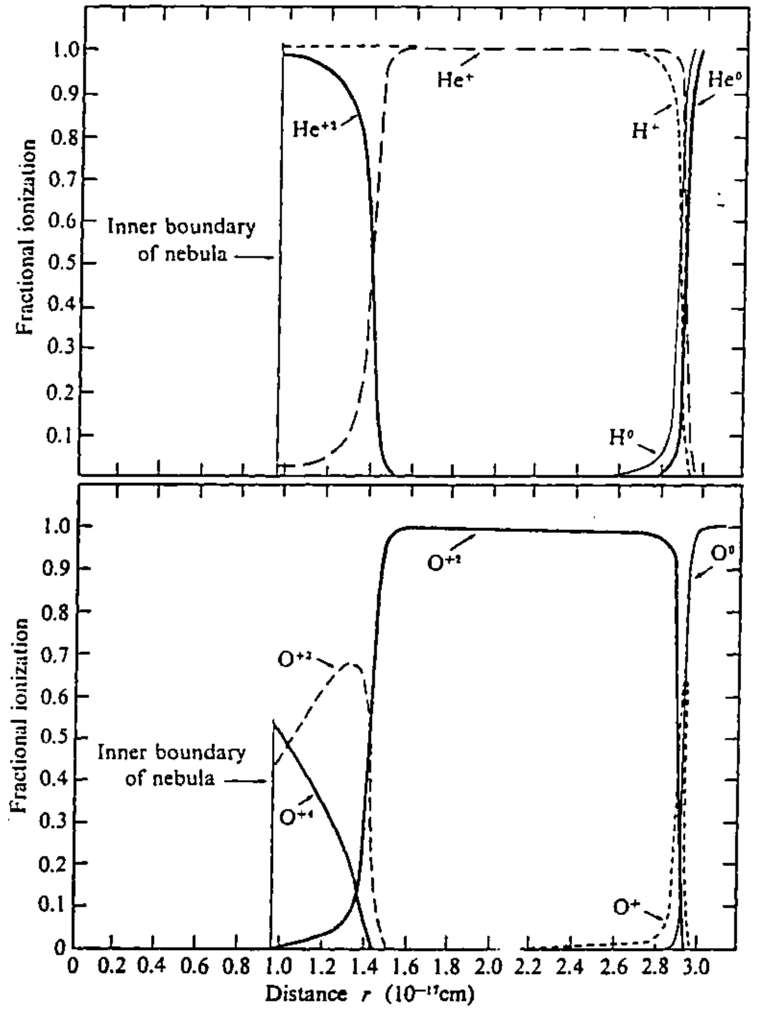

Ionization structure of a model nebula surrounding a 10^5 K star

1.3 Nebular Radiation

1.3.1 Recombination Line Emission

When a proton and an electron recombine the electron will cascade down the energy levels radiating a variety of photons. If the recombination is directly to the ground state then a Lyman continuum photon will result which may photo-ionize another neutral hydrogen atom. Transitions from bound states to the ground state generate the Lyman series. This is capable of exciting other atoms if they are in the ground state which, if they emit Lyman photons, provides a mechanism for scattering Lyman radiation. Eventually however, photons of non-Lyman series will be produced which will escape from the nebula because the majority of the neutral atoms exist in the ground state. The net effect of a recombination is the creation of a Lyman α photon and at least one other non-Lyman series photon. If a Lyman α photon is created it cannot be degraded into two or more line photons. Instead it either escapes from the nebula by making sufficient scatterings, is red-shifted away from absorption lines by velocity gradients within the nebula, is degraded by the two-photon process, or is absorbed by dust.

Nebulae that are optically thin to Lyman lines are referred to as case A nebulae, whilst the converse is referred to as case B. The relative strengths of the lines for the hydrogen series have been calculated for both cases in the following limits :

(i) low electron density (Pengelly 1964)
(ii) collisional transitions between degenerate states are faster than radiative transitions (Seaton 1959)

Line strengths vary by up to a factor of two between these extremes and so Pengelly and Seaton (1964) have calculated line strengths for the intermediate case.

For the Balmer series, for example, the set of line ratios is referred to as the " Balmer decrement ", in which the intensity of Hβ is defined to be 100. The Balmer decrement is a function of electron temperature and so may be used to estimate the amount of interstellar extinction if the electron temperature can be found by other methods.

1.3.2 Forbidden Line Emission

The origin of the green N_1 and N_2 lines at λ5007Å and λ4959Å and certain other lines in HII regions was unknown for many years and was attributed to a hitherto unknown element christened " Nebulium " - in a similar fashion to the mystery of the origin of lines later found to be due to helium. Bowen (1928) showed that inelastic collisions between electrons and ions sometimes result in an ion being left in a low-lying meta-stable state. At the low electron densities characteristic of HII regions (10^4 cm^{-3}) potentially de-exciting collisions are so infrequent that the excited ion has a non-negligible probability of decaying via an electric quadrupole or magnetic dipole transition - both of which are normally " forbidden " under laboratory conditions. Lifetimes of these meta-stable states are typically of the order of a few seconds, whereas those of allowed transitions are a factor 10^8 smaller.

Figure 1.2 shows sections of the Grotrian energy level diagrams for O^{++}, O^+ and S^+ ions. Some of the transitions for the more important lines are indicated.

When account is taken of collisional de-excitation by free electrons the ratio of nebular to auroral lines of, for example O^{++}, is found to be a sensitive function of electron temperature, but less dependent upon electron density (Osterbrock 1974) :-

$$\frac{I(\lambda4959 + \lambda5007)}{I(\lambda4363)} = \frac{8.32 \exp(3.29\ 10^4/T_e)}{1.0 + 4.5\ 10^{-4}.N_e/T_e^{\frac{1}{2}}} \tag{1.1}$$

On the other hand, doublet ratios tend to be less dependent upon electron temperature than electron density because they arise from the same upper level. A commonly used doublet is that arising from O^+ :-

$$\frac{I(\lambda3727)}{I(\lambda3729)} = \frac{1.5 + 4.41\ 10^{-4}.N_e(10^4/T_e)^{\frac{1}{2}}}{1.0 + 1.26\ 10^{-3}.N_e(10^4/T_e)^{\frac{1}{2}}} \tag{1.2}$$

Since doublet lines tend to be fairly close in terms of wavelength their intensity ratios are relatively independent of interstellar reddening.

The great strength of many of the forbidden lines results from

Figure 1.2

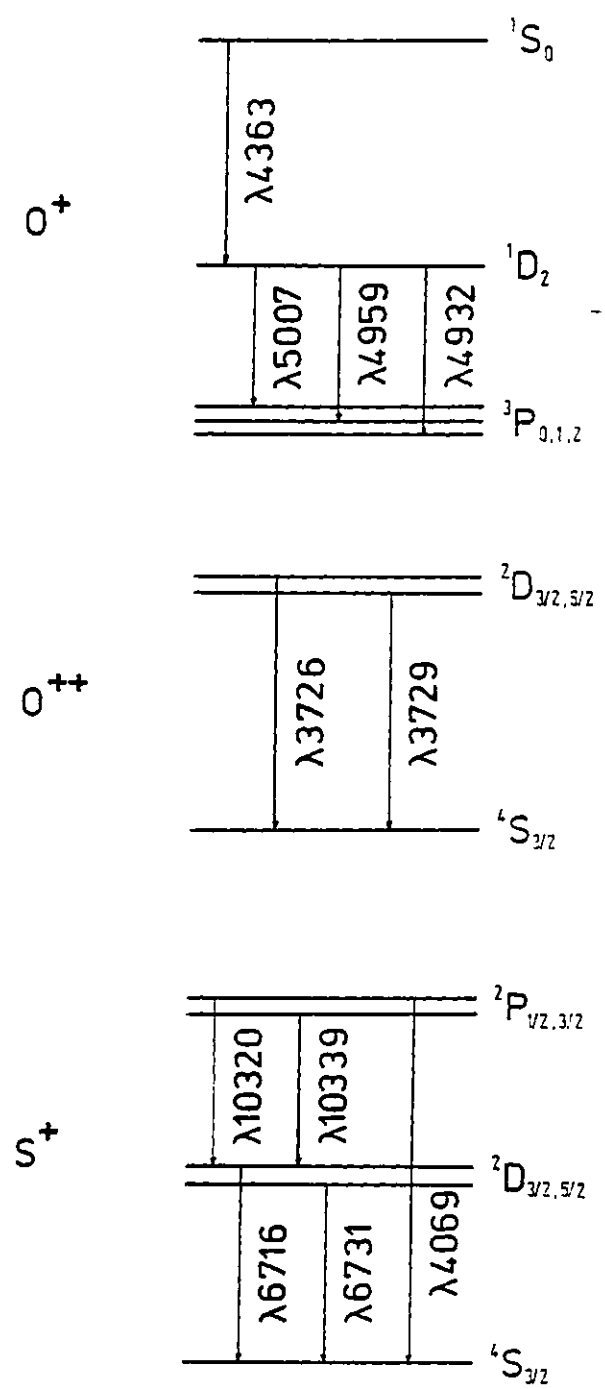

Grotrian diagrams for O^{++}, O^+ and S^+ ions the lack of free electrons with sufficient kinetic energy to excite ions to higher energy levels from where they can emit permitted lines. For this reason forbidden lines are one of the major cooling mechanisms in gaseous nebulae. An extra cause of the strength of the Nebulium lines in high excitation nebulae arises from a fluorescent resonance effect (Bowen 1928). In this mechanism HeII Lyman-alpha radiation at λ303.78Å resonantly excites O^{++} ions from the $2p^2\ ^3P_2$ state to the $3d^3\ ^OP_2$ state, the energy difference being equivalent to radiation of wavelength λ303.80Å.

Some Infra-red forbidden lines have been detected fairly recently, notable examples being : [NeIII] λ12.8μm, [SIV] λ10.5μm and [ArIII] λ9.0μm (Rank et al 1970, Holtz et al 1971, Gillett et al 1972 and Geballe and Rank 1973). Due to the exponential nature of the Boltzmann factor $\exp(^{h\nu}/_{k_BT_e})$ the intensities of these lines are insensitive to electron temperature, since $h\nu << k_BT_e$.

1.3.3 Molecular Line Emission

The spectra of molecules are in general very complex. However they originate from a combination of three basic mechanisms : electronic, vibration and rotation. The relative strengths of these are in the approximate ratio $10^4 : 10^2 : 1$. Electronic transitions tend to lie in the Ultra-violet or visible region of the spectrum because of the relatively large energy differences involved. A model commonly used in the explanation of the structure of molecular spectra is one in which the radial component of the inter-atomic potential is approximated by the quadratic potential well of a Quantum Harmonic Oscillator. The energy levels of such a model would normally be equally spaced and degenerate with respect to the quantised rotational angular momentum. But, as the molecule in general is rotating there is a dependence of vibration frequency upon angular momentum due to the centrifugal forces involved. Transitions between such energy levels result in a spectrum which has a banded structure. In homo-nuclear molecules such as H_2 there is no intrinsic dipole moment and so the electric quadrupole transitions tend to be fairly weak.

Molecular line emission from Planetaries has only fairly recently been detected. For example, Mufson et al (1975) have observed ^{12}CO from NGC 7027, IC 418 and NGC 6543, whilst Treffers et al (1976) have detected H_2 from NGC 7027. Even more recently Beckwith et al (1980) have scanned NGC 7027 along North-South and East-West traverses through its' centre at the 1 — 0 S(1) $\lambda 2.122\mu m$ line of H_2. They explain their results in terms of a shock excited HI shell located at the outer edge of the nebula.

1.3.4 Free-Bound Continuous Emission

The intensity step in the observed continuum of nebulae at $\lambda 3650\text{Å}$ is due to the radiation from electrons combining with protons which fall directly into the n = 2 state. The intensity ratio of the spectrum on either side of the step is called the " Balmer jump " and is a function of electron temperature and density. Similar steps occur at the thresholds of other atomic energy levels, and the intensity variation for most of these goes as the -2.5 power of the frequency on the high frequency side of each threshold.

1.3.5 Free-Free Continuous Emission

Free electrons passing near ions in a nebula undergo accelerations and hence radiate a continuous spectrum known as " free-free " or " thermal Bremsstrahlung " radiation. At densities ($\sim 10^4$ cm^{-3}) and temperatures ($\sim 10^4$ K) typical of gaseous nebulae the peak of this emission lies in the radio region at 1 to 10 GHz, where the optical depth is unity. Below the peak frequency the spectrum is of a black-body ν^2 form, whereas above the peak frequency it is essentially constant, apart from a weak $\nu^{-0.1}$ dependence upon the free-free Gaunt factor. Scheuer (1960) gives a detailed review of the theory of free-free radiation. A more comprehensive treatment of the theory appears in chapter six, where it is used in the analysis of the radio structure and spectrum of NGC 7027.

1.3.6 2-Photon Continuous Emission

2^2S to 1^2S transitions in hydrogen are normally forbidden by the angular momentum selection rule. However, Spitzer and Greenstein (1951) and independently Ya Kipper (1950) have proposed a mechanism whereby a hydrogen atom finding itself in this situation can make a downward transition via a short-lived " virtual " intermediate level. In doing so two photons are created, the wavelengths of which may take any value subject to the conservation of energy :-

$$\Delta E(2^2S - 1^2S) = h\nu_1 + h\nu_2$$

The spectrum of this process rises from zero at zero frequency and is symmetric about the maximum which occurs when the two photons have the same frequency.

The transition rate for this mechanism is 8.2 s^{-1} and is only important at electron densities below about 10^3 cm^{-3}. This is because at densities above this value collisions with protons are more likely to transfer the excited atom into the 2P state, from where an allowed downward transition can occur.

1.3.7 Infra-Red Excess Continuous Emission

The Infra-red flux from Planetaries is often observed to be far greater than that which would be expected from free-free radiation. For instance, in NGC 7027 the Infra-red flux is about 100 times greater than the extrapolated radio spectrum would predict (see chapter six).

The excess is thought to arise from thermal radiation by dust grains which are well mixed with the hot gas in the nebular shell and are heated by direct Ultra-violet radiation from the central star and scattered Lyman α line photons. Dust therefore provides an additional mechanism for the destruction of Lyman α radiation.

The observed proportionality of the wide-band $\lambda 400 \mu m$ flux with 2cm radio continuum flux for several HII regions suggests that the whole of the Infra-red excess originates from the absorption of diffuse Lymanα photons, because these are both proportional to the number of recombinations (Osterbrock 1974). However, model calculations indicate that the majority of the excess arises from the absorption of stellar radiation directly (Ferch and Salpeter 1975).

The shape of the Infra-red excess spectrum is typical of a Black-body at a temperature of a few hundred degrees Kelvin but which is modified by a λ^{-1} efficiency factor.

1.4 Nebular Expansions and Distances

1.4.1 Expansion Velocities

At one time it was thought that the twisted and bowed forms of the emission lines from Planetaries arose from their rotation (Campbell and Moore 1918). The objection to this interpretation was that although it could account for the tilt of the lines it could not explain their splitting. In fact, the angular momentum of a nebula according to the rotation hypothesis would require the progenitor star to revolve at relativistic speeds ! Eventually it was realized that Planetaries are expanding radially, and measurements were made of the magnitude of the line splittings for many nebulae in the light of several ions. The most important of these investigations was that of Wilson (1950) who found that line splittings were typically 40 Km s^{-1} in terms of Doppler shifts when averaged over the HI, [OIII] and [NII] lines. He also noticed that the splitting in an individual nebula tended to increase with decreasing ionization potential, as did the image size. From this he deduced that the more highly ionized species exist near the central star and that the velocity of expansion of a nebula increases with increasing distance from the central star.

Weedman (1968), using similar techniques to those of Wilson, has found that the relation between the velocity and radius at any point in a nebula is a linear one such that the velocity extrapolates to zero at a position between the star and the inner edge of the nebula. This latter point implies that a nebula undergoes significant acceleration after its' ejection from the parent star.

1.4.2 Angular Expansions

Various attempts have been made to measure the rates of change of angular dimensions of nearby Planetaries using photographs taken many years apart on long focal length telescopes. For example, Liller and Liller (1968) report on preliminary results obtained on three relatively close nebulae : NGC 2392, NGC 6818 and NGC 7662. They employed a 40 year long baseline interval. The difficulties encountered with this sort of work are :-

(i) A lack of sufficiently sharp features.

(ii) The angular expansions are at most very small, typically 0.5" per century, which necessitates the use of long baselines.

(iii) The use of long baseline intervals may result in the 1st and 2nd epoch plates having different spectral properties and, less importantly, slightly different plate scales arising from emulsion shrinkage.

(iv) The nebular ionization structure may change between the exposures and lead to an incorrect interpretation of the measurements as a real expansion.

Expansion rates measured by the Lillers are : $+0.72\pm0.06$ "/cy for NGC 2392 and $+0.26\pm0.09$ "/cy for NGC 7662, whilst the data for NGC 6818 are too ambiguous to infer meaningful results.

1.4.3 Distances

One of the most crucial parameters in the description of a Planetary Nebula is its' Helio-centric distance. An astronomically determined distance may be calculated for a nebula if its' expansion velocity and angular expansion rate are known. However, to do this one must assume a model for the nebula since one does not have a priori knowledge of the true three-dimensional structure. In the case of NGC 2392, for example, it has been suggested that this nebula is a prolate shell which is viewed along its' major axis (Weedman 1968). Now Liller and Liller assume spherical symmetry in their analysis, and if one adopts Weedmans' linear velocity-radius relationship, then their derived distance is an underestimate. This might explain why the distances to NGC 2392 found using other methods are generally larger.

Other astronomical methods which have been applied in the estimation of nebular distances include :-

(i) Trigonometric parallaxes - measured values tend to be very small, typically of the order of or less than the errors of observation (Van Maanen 1934).

(ii) Statistical parallaxes - Cudworth (1974) has measured the proper motions of many Planetaries and calculated their distances. This method may be suspect because of the non-circular Galactic orbits of the Planetary sub-system.

(iii) Statistical sizes and magnitudes - several attempts have been made to find an empirical relationship between, for example, the absolute magnitude and linear radius of a nebula (Camm 1938). Such methods invariably result in a high degree of error.

(iv) Association with other objects - at least one Planetary is known to be physically bound to a globular cluster (K 348 in M15). Planetaries in the Magellanic Clouds have been used to calibrate other distance scales (Seaton 1966).

(v) Binary systems - the spectroscopic parallax of the cooler companion may yield a distance. This method is useful in the case where the hotter star is not visible (Shao and Liller 1968).

Astronomical techniques for finding distances are :-

(i) Shklovskiis' (1956) method - the basic equation used in this process, which is also the starting point for many similar schemes, relates the mass M, luminosity L and volume V of a nebula : $M \propto \sqrt{LV}$. From this one can derive an expression for the nebular radius : $R \propto M^{2/5} S^{-1/5}$, where S is the nebular surface brightness. Shklovskii assumes that M is a constant for all nebula and at all stages in the evolution of a nebula, except when a nebula becomes optically thick - in which case the distance is an upper limit. A more refined version (Seaton 1966), employed extensively by Cahn and Kaler (1971) for both optically thin and thick nebulae, used Planetaries in the Magellanic Clouds for the distance scale calibration. Liller (1978) notes that $\langle M \rangle$ generally lies between 0.14 and 0.47 M_o which means that the possible scales may vary by a factor of 1.62.

(ii) Sobolevs' (1958) method - if the electron density in a nebula can be found by a distance-independent method, eg. forbidden line ratios, then the observed flux at say H which is a function of density and distance gives the distance, after correction for interstellar reddening.

(iii) Balmer decrement - This technique uses the theoretical Balmer decrement of a nebula and a Galactic interstellar absorption model.

(iv) HeIII method (Gurzadyan 1969) - some Planetaries are optically thick beyond their He^{++} zones and so their He^{++} Stromgren radii may be calculated if the radius and temperature of their central stars are known.

Acker (1978), using a large number of individually determined distances, has re-calibrated thirteen separate distances catalogues which use many of the techniques outlined above. Her list should serve as the most reliable and consistent source of distances for optically thin and thick Planetaries.

1.5 Central Stars

1.5.1 Hertzsprung-Russell Diagram

The position of the central stars of Planetary Nebulae in the Hertzsprung-Russell diagram is shown in figure 1.3. O'Dell (1963) and Harman and Seaton (1964) have shown that the central stars evolve in the direction indicated, using the observation that the nebular radii increase in the same sense. The lifetime of a typical nebula is given by the maximum observed radius divided by an average expansion velocity and is about 35,000 years. This means that the central stars must undergo very rapid evolution in comparison with other stages in their lives, during which time their radii decrease from 1 R_o to 10^{-2} R_o, whilst their temperatures rise from 5000 K to around 20,000 K or more.

Central stars tend to have photo-visual magnitudes $m_{pv} \sim 0.0$ and fall into the disk population . Their mean distance from the galactic plane indicates that their masses range from 1.0 to 1.3 M_o.

Estimates of the effective temperature of a central star may be made by a variety of techniques :-

(i) Ultra-violet colour - this employs the directly observed continuous spectrum, especially at UV wavelengths. For O - type stars the spectrum approximates quite well to that of a black-body (Pottasch et al 1977).

(ii) Zanstra (1931) - this method uses the measured flux in a nebular line (such as those from HI, HeI or HeII depending upon the excitation level of the nebula) to calculate the HI Lyman continuum flux from the star. If the nebula is optically thin to this radiation then the HeII Lyman continuum is used instead (Harman and Seaton 1964). The ratio of either of these stellar UV fluxes to the stellar flux observed at an optical wavelength yields a long baseline black-body temperature. More refined calculations employ model stellar atmospheres.

(iii) Stoy (1933) - this method is essentially similar to that of Zanstra, except that it has the advantage that only nebular line ratios are used. It has been generally used only upon

Figure 1.3

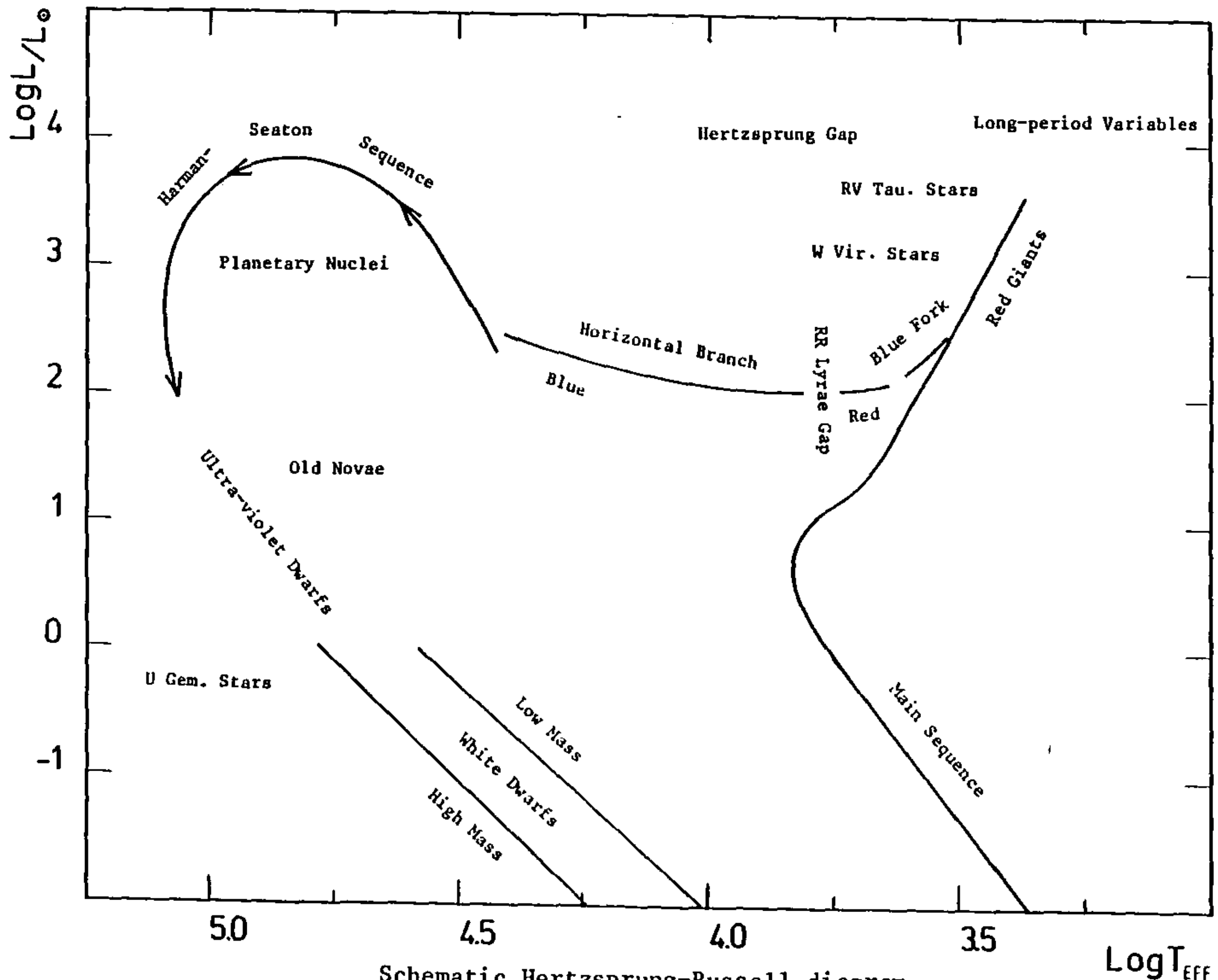

Schematic Hertzsprung-Russell diagram

low-excitation nebulae. Physically, the method is to find what temperature the central star should have in order that the heating and cooling rates of the nebula are equal at the measured electron temperature and He/H ratio. Kaler (1976) has shown that there is a strong correlation between the stellar temperature found by this method and the N_1 to Hβ flux ratio. This is because the majority of the nebular cooling is due to forbidden line emission, of which the N_1 line ([OIII]λ5007Å) is the strongest.

(iv) Certain features in the spectrum of a central star, eg. the OVI emission lines, can be used to estimate the effective temperature (Heap 1975).

Agreement amongst these methods appears to revolve around the presence or absence of HeII emission in the nebula. When it is not observed the HI and HeI Zanstra temperatures tend to agree with the UV colour temperature. However, when it is present the temperatures derived using HeII lines are found to differ substantially from those found using other methods, especially the HI and HeI Zanstra temperatures. Temperatures derived from the Stoy and UV colour methods are generally found to agree. No satisfactory explanation has so far been put forward to account for the HeII discrepancy (Lutz 1978) although Harman and Seaton (1964) have argued that it may arise from the incomplete absorption of HI Lyman continuum photons by the nebula, in which case the HeII temperature would seem to be the most representative of the radiation field of the star.

1.5.2 Progenitors

The proximity of the central stars of small, and therefore young, Planetaries to the end of the horizontal giant branch in the Hertzsprung-Russell diagram has led many people to propose that Red Giants are the fore-bearers of Planetary Nebulae (Shklovsky 1956, Abel and Goldreich 1966). This picture is attractive because it is easier to account for the low dispersion of nebular expansion velocities in terms of the small escape velocities of Red Giants (typically 30 Km s^{-1}) than with the higher escape velocities of a few hundred Km s^{-1} of the remnant central stars.

A theory which seeks to explain the formation of a Planetary Nebula has to account for the rapid transition of the progenitor to the observed central star, which is generally hydrogen deficient. Since the nebulae tend to have typical disk population abundances this might suggest that the formation process involves the separation of the unprocessed outer layers of a star from the helium rich core. Several possible mechanisms have been put forward over the years, which differ in their primary ejection methods :-

(i) Unstable thermal relaxations (Rose 1966, Smith and Rose 1972).
(ii) Ionization equilibrium instabilities (Lucy 1967).
(iii) Radiation pressure (Finzi and Woolf 1971, Faulkner 1970).

Although these three mechanisms are not mutually exclusive the first one seems the most likely, especially as it can account for multiple shells.

1.5.3 Evolution of the Central Stars and Nebulae

Weedmans' observation (1968) that the outer parts of a nebula expand faster than would be predicted by a proportional velocity-radius relationship indicates acceleration of the nebula following its' ejection from the progenitor. Indeed, the model nebulae of Mathews (1966) rely on an outward acceleration to account for the presence of a central cavity. Whether this acceleration is provided by radiation or corpuscular pressure (or both) is uncertain, but the very wide OVI emission lines seen in some central stars indicates very active stellar winds (Smith and Aller 1969).

Most stars are observed to rotate and so one might expect that if the outer envelope of a large star such as a Red Giant or a Mira variable were to be thrown off it would assume an oblate form. However, Wilson (1958) and Weedman (1968) believe that many moderately evolved nebulae are intrinsically prolate in shape. How therefore are we to explain this transition? Most explanations appear to make use of differential radiation or gas pressure. For example, Kirkpatrick (1976) has shown that an initially slightly oblate shell can develop into a significantly prolate shell purely under the influence of pressure within it.

The very fact that the central star is spinning may also help to account for the formation of a prolate shell :-

Making the assumption that the progenitor is a star of large radius then it will have an escape velocity V_{esc} of approximately 30 Km s^{-1} It is relatively straightforward to show using a simple ballistic approach that the ratio of the terminal velocities of the ejected shell in the equatorial and polar regions is given by :-

$$\frac{V(eq)}{V(pl)} = 1 + \frac{V_{esc}^2 . e}{V_o^2}$$

where V_o is the initial velocity imparted to the envelope by the ejection mechanism, and $e \sim \omega^2 R_*^3/GM_*$ is the eccentricity of the rotating star at the moment of ejection. V(eq) and V(pl) are observed to be of the order

30 Km s^{-1} and so V_o will be typically $\sqrt{2}$ times greater. Since $e \sim 0.05$ for Red Giants this means that a simple ballistic picture would predict very modest oblate, not prolate, shells. However, when account is taken of the conclusion of Weedman (1968) that significant acceleration of the nebula occurs after ejection then we have to modify our analysis by including the effects of stellar radiation pressure and internal Lyman α radiation pressure. The latter has the dynamical effect described by Kirkpatrick of changing the oblate shell into a prolate one. The role of stellar rotation in modulating the radiation field has in the past been virtually ignored. However, it must play an important part in the shaping and general ionization structure of a nebula by the amplification of Kirkpatricks' mechanism since the flux from the polar regions of a star will be greater than that from the equatorial regions for these reasons :-

(i) a rotating star subtends a larger solid angle when viewed from above its' poles by a factor $1 + e$.

(ii) the effective stellar temperature is higher at the poles owing to the higher surface gravity. Von Zeipels' theorem (1924) states that the local gravity is proportional to the fourth power of the local temperature.

(iii) less material will be ejected from the polar regions due to the higher gravitational forces.

The Ultra-violet flux from the polar regions will therefore be greater than that from the equatorial regions by a factor $1 + 2e$. Although $e \sim 0.05$ for a Red Giant this factor will increase as the star contracts and spins up. The net result will be more extensive ionization of the regions above the stars' poles compared with elsewhere. Also, one might expect the velocity at these points to be greater.

Eventually the nebula will move too far away from the star to be accelerated further and any subsequent changes in form will be due to differential velocity fields and the weakening radiation flux from the star. After about 35,000 years the stellar radiation is too dilute to ionize the tenuous nebula and finally all that is seen is the hot remnant star.

1.5.4 Later Evolutionary Stages of the Central Stars

Harman and Seatons' (1964) evolutionary track of the older central stars points towards the White Dwarf region of the Hertzsprung-Russell diagram (figure 1.3). This suggests that a fraction of White Dwarfs are old Planetary Nebulae nuclei which are cooling down, since their masses (typically less than 1 $M_\odot$) are insufficient to initiate the Carbon burning cycle.

Further evidence that the central stars evolve into White Dwarfs is afforded by Weidemann (1968) who has shown that the birth-rate of White Dwarfs in the solar neighbourhood is 1.6 to 5.0 10^{-3} $Kpc^{-3}yr^{-1}$ whilst the formation rate of Planetary Nebulae according to the estimates of Cahn and Kaler (1976) is approximately 3.2 $Kpc^{-3}yr^{-1}$.

Chapter 2

2.1 Discoveries and Catalogues

Up until about 1860 all recorded Planetary Nebulae had been discovered visually, using telescopes. The Planetaries in the catalogues of Charles Messier (1771-84) and Sir William Herschel (1786-1802) tend therefore to be medium sized and of fairly high surface brightness.

In the 1860's Huggins (1864) observed the nebulae with a visual spectroscope and found that Planetaries, and HII regions in general, had line spectra. This meant that they could easily be distinguished from star clusters and external galaxies which have predominantly continuous spectra, and led to the discovery of Planetaries of smaller angular dimensions. At about the same time, Dreyer (1888) was compiling the " New General Catalogue of Nebulae and Star Clusters " (the NGC catalogue), and so virtually all of the Planetaries listed in this work are extended objects. In contrast, the two later supplements- the Index catalogues (published in 1894 and 1908)- contain many of the spectroscopically discovered smaller nebulae.

The next major advance was made with the combination of the photographic plate and objective prism, with which Minkowski (1946,47,48) discovered about 200 Planetaries. Henize (1961,64) extended this survey to include the Southern Hemisphere and discovered a further 150 nebulae.

The complementary technique to objective prism observations is direct photography. By careful scrutiny of the Palomar Sky Survey plates and prints several workers, in particular Abell (1955), have found many more large, low surface brightness objects.

All Planetary Nebulae discovered up to 1965 appear in the "Catalogue of Galactic Planetary Nebulae ", compiled by Perek and Kohoutek (1967). Post P-K catalogue discoveries, and a list of misclassified objects, appear in the proceedings of the 76th IAU Symposium (Kohoutek 1978).

Long exposures of known objects have led to the discovery of very faint outer shells around many Planetaries, and in a few cases two outer shells have been observed (Kaler 1974, Millikan 1974).

The following sections outline the various classification schemes proposed for Planetaries and discuss the ability of the different empirical and theoretical models in explaining their appearance.

2.2 Classification Schemes

One of the major occupations of astronomers is to place the objects they observe in pigeon-holes, according to a consistent scheme. The reason for this is usually to reduce the number of variables or parameters which have to be explained. Planetary Nebulae are no exception to this treatment, and over the years there have appeared many nebular classification schemes. Figure 2.1 is a schematic flow-chart which shows the various parameters, and their inter-connections, with which Planetary Nebulae and their central stars can be described or defined.

The simplest, and at first sight, least useful scheme is one in which all Planetary Nebulae are lumped together into one class. However, even this exercise encounters problems, since some small nebulae originally thought to be Planetaries are now classed as compact HII regions (Kohoutek 1978).

By going to the opposite extreme one can place each Planetary in its' own class. This is equally of no real practical use as one is in general attempting to explain :-

(i) the evolution of a " typical " or " average " nebula.
(ii) The differences between nebulae in terms of chemical composition, age, excitation level, mass, galactic location etc.....

All of the practical schemes put forward so far fall between these two extremes and as a rule split into morphological/spectral and spectral descriptions of the nebulae and central stars, respectively. A " good " classification scheme may be defined as one in which each and e every object falls into only one class and can be placed there objectively, ie. by independent observers. It should also take into account both the morphology and spectrum of the nebula , and preferably the spectrum of its' central star.

The morphological description of a nebula depends strongly upon the wavelength region it is photographed in because of the stratification effect. For instance, NGC 7293 looks quite different in the light of [NII] compared to its' appearance at Hα (Capriotti 1978). The observed form of a

Figure 2.1

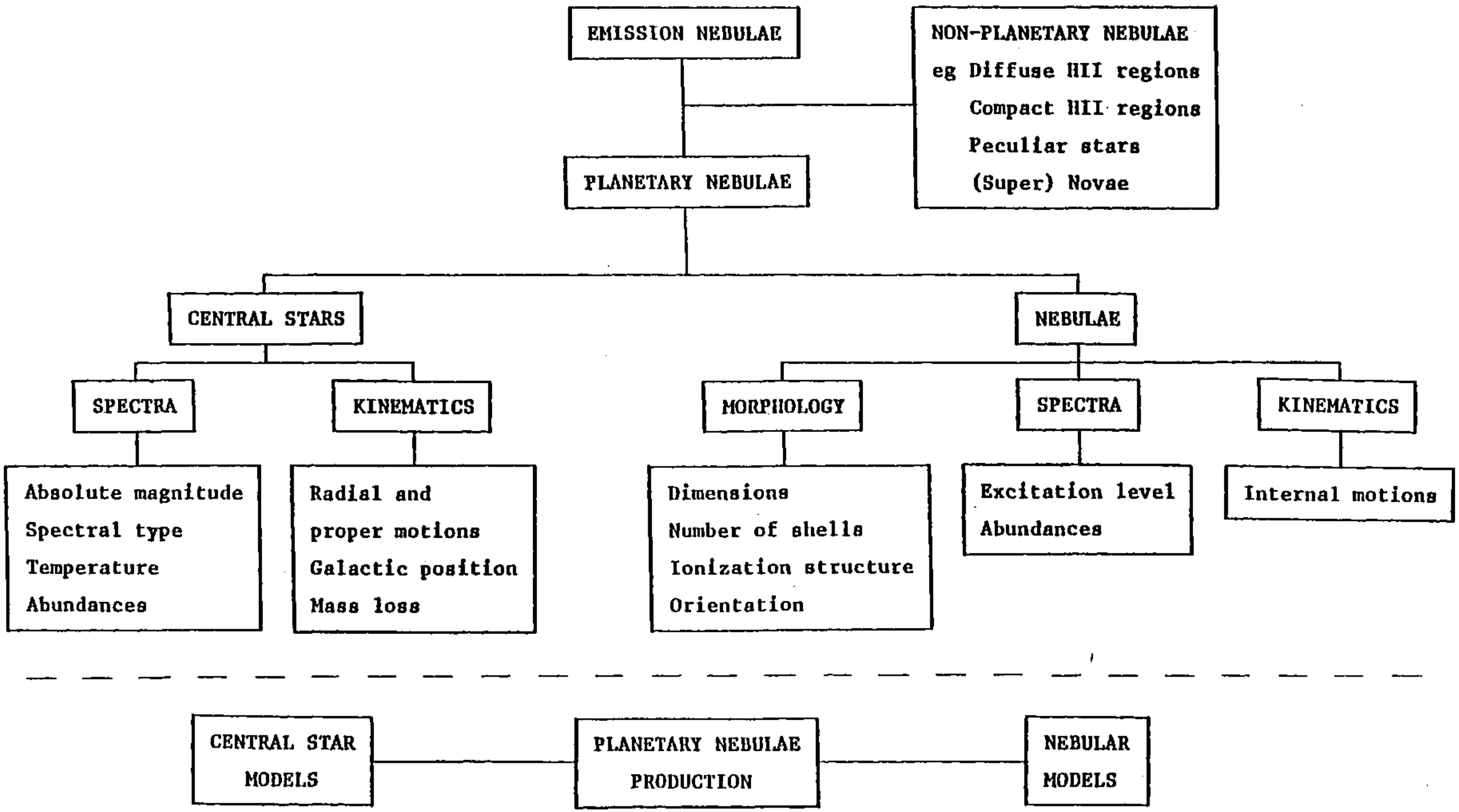

Schematic flow-chart showing the various characteristics of Planetary Nebulae.

nebula is also a function of the depth of exposure, owing to non-linear photographic effects, and its' orientation with respect to the line of sight. A consistent scheme should account for the latter effect in that the overall class of an object should be independent of viewing angle. However, a sub-class could be used to describe this feature.

Spectral classifications conveniently split into descriptions of the nebula and central star (see figure 2.1). Classification of the nebular spectrum is more difficult than that of the central star because here again one runs into problems with the stratified nature of the nebula. This is a result of the fact that most nebular spectra are obtained with slit spectrographs or small aperture spectrophotometers which accept only selected portions of the nebula. Consequently, it is sometimes difficult to place a nebular spectrum in a definite class.

The following sections discuss in greater detail how Planetary Nebulae and their central stars are classified.

2.2.1 Central Star Spectra

The classic stellar classification schemes such as the Harvard system have been applied to the central stars of Planetary Nebulae. Over the years there has evolved a sub-set of eight classes into which most potentially classifiable centrals stars fall. In order of number present in each class (shown in brackets) these are (Lutz 1978) :-

(i) Continuous (21) - no emission or absorption lines are seen even at the highest available spectral resolution.

(ii) Ofp - Of (9+1) - exhibit spectral features similar to Population 1 Of stars. Only one Of central star is known (in NGC 2392). CIII is present in Ofp stars.

(iii) OVI (10) - very high excitation stars, similar to Ofp type stars but have strong OVI emission lines at $\lambda\lambda 3811$-34Å.

(iv) O (9) - absorption lines characteristic of normal O stars.

(v) Peculiar (8) - apparent central stars have spectral types between A and K and are too cool to account for the level of excitation of their associated nebulae.

(vi) WR (7) - mainly of type WC, or between WC and WN. One possible WN type central star is known.

(vii) WR+O - WR+Of (6) - exhibit spectral characteristics of both WR and O or WR and Of type stars.

(viii) O-subdwarves (6) - these show broad absorption lines, typical of a hot, high surface gravity star.

Seven other central stars do show emission lines but do not appear to fall into these categories.

The reason that so few central stars have been satisfactorily classified is because central stars are often only of tenth magnitude and are generally fainter than their surrounding nebulae. This means that it is difficult to separate stellar emission lines from those of the nebula. Differences in resolving power may also explain why an individual object has been assigned several different spectral types by independent observers (see the catalogue of Perek and Kohoutek (1968) for examples).

A significant number of central stars have been discovered to have changed in spectral type. A notable example is FG Sge, the central star of He 1-5. This star has been observed to have steadily increased in brightness from 1955 to 1967 (Herbig and Boyarchuk 1968) with a corresponding change in spectral type of B4 to A5.

2.2.2 Nebular Spectra

One of the first schemes in which the spectra of Planetaries were classified was that proposed for gaseous nebulae by Cannon (1916), which appeared in the Henry Draper catalogue. The defining criterion she chose was the strength of the HeII λ4686Å line, and because this line is dominant in the spectra of O type stars she placed the spectra of the gaseous nebulae near to spectral class O. This scheme was eventually found to be inadequate (Wright 1918) and consequently Payne (1928) separated the gaseous nebulae and O type stars and arranged the former into ten divisions. This scheme also employed as the principal criterion the strength of the HeII λ4686Å line, which was strongest in the P1 nebulae and disappeared at the high end of the scale (P10), where the spectra resembled those of the reflection nebulae.

Page (1942), in a photographic study of the continuous emission from Planetary Nebulae, devised a nebular excitation scale of one to eight. For excitation classes one to four inclusive he used as his criterion the strength of HeII λ4686Å relative to Hβ, whereas for the remaining classes he used the strength of [OII] λ3727Å relative to [OIII] λ4959Å. Where spectra showed characteristics of both high and low nebular excitation, he appended " pec " (for peculiar) to the excitation number.

An extended version of Pages' scheme was suggested by Aller (1956) in which six criteria are used to arrange the spectra of nebulae within ten excitation classes (Table 2.1). Class 1 is used to denote spectra devoid of [OIII] emission lines. This particular scheme is the one most commonly used today.

Table 2.1

CRITERION	Cn 3-1	IC 418	IC 2149	IC 4634	NGC 7026	J 900	NGC 6309	IC 2165	Hu 1-2
$N_1+N_2/H\beta$	.21	1.9	5.5	10.6	12.4	16.7	14.1	18.1	10.4
3727/4959	32	3.1	.2	.03	.04	.03	.03	.02	.04
4686/Hβ	-	-	-	-	.13	.47	.77	.6	.9
[NeV]/Hβ	-	-	-	-	-	.28	.5	.8	2.4
[NeV]/3869	-	-	-	-	-	.38	.5	.95	3.8
EXCITATION CLASS	2	3	4	5	6	7	8	9	10

Allers' (1956) nebular excitation level classification scheme.

2.2.3 Nebular Morphology

The overwhelming variety of shapes which Planetary Nebulae possess might appear to make their morphological classification in terms of a relatively small number of classes an almost impossible task. Consequently, the early schemes tended to be totally descriptive and often used half a dozen or so separate classes. Table 2.2 lists the published major morphological classification schemes and summarises their particular definitions. Figure 2.3 performs a similar task in diagrammatic form for a few of these schemes.

The uniqueness of many of the classes in for example the schemes of Curtis (1918) or Gurzadyan (1969) is poor, as can be seen by noting that from the eleven principal classes of Gurzadyan it is possible to find forty four different nebular types, albeit the majority of these being redundant. Curtis himself pointed out that in his scheme it is possible for one object to fall into two classes. Stoy (1933) also criticises Curtis' scheme by saying that an object may fall into as many as five classes, and that too much attention is paid to extraneous detail. Stoys' own scheme is the only one in table 2.2 in which an attempt is made to include a spectral description of the nebulae. However, because it is such a heterogeneous system it has never come into widespread use.

Greig (1971,72) has described a system, based on the symmetry of the nebulae, which divides Planetaries into two major classes (B and C) and two smaller classes (A and E). " B " nebulae have two bright peaks and tend to be low excitation objects whereas " C " nebulae have a single bright peak and are generally higher excitation objects. Greig suggests that the " B" and " C " nebulae are two physically distinct classes of Planetary Nebulae , based on their different galactic spatial and kinematical distributions. More precisely, he identifies " B " nebulae with intermediate population I stars and " C " nebulae with intermediate population II or old disk stars. It is perhaps pertinent to note that Kaler (1970) has found a correlation between elemental abundances and galactic location of Planetary Nebulae, indicating that there are two types of nebulae.

Table 2.2

Morphological classification schemes.

Curtis (1918)

Class	Description	Example
A	Helical	NGC 6543
B	Annular	NGC 1535
C	Ring on disc	NGC 1501
D	As C, with truncated ends	NGC 40
E	Bipolar	NGC 6818
F	Centric distribution	IC 3568
H	Stellar	IC 4997

Stoy (1933)

Class	Description	Example
α	Irregular	NGC 7027
β	Ring on disc	NGC 7662
γ	Disc	NGC 6572
δ	Stellar	NGC 6790
θ	Low surface brightness	
ε	" Hydrogen " nebula	

Vorontsov-Velyaminov (1948)

Class	Description
I	Stellar
II	Disc : a) Centric distribution
	b) Uniform
	c) Traces of ring (Supplement from Perek and Kohoutek 1967)
III	Irregular disc : a) Quite irregular
	b) Traces of ring
IV	Ring
V	Irregular
VI	Anomalous

Table 2.2

Evans and Thackeray (1950)

Class	Description	
a	Simple disc	Circularly symmetric
b	Simple ring	
c	Simple disc	Bi-axial symmetry about two orthogonal axes
d	Doubly indented disc	
e	Simple ring	
f	Doubly indented ring	
g,h,j	Complex bi-axial	
k	Helical	
l,m	Symmetric about centre	

Westerlund and Henize (1967)

Class	Description
1	Elliptical: Uniform
2	: Increase towards centre
3	: Bright centre
4	: Irregular
5	Ring
6	Bipolar
7	Interlocking rings
8	Peculiar
9	Doubtful

Hromov and Kohoutek (1968)

Main structure :

Class	Description	Example
1	Round or ring	NGC 6337
2	Elliptical	NGC 6720
3	Bipolar	NGC 650-1

Peripheral structure :

Class	Description
a	Closed filaments
b	Open filaments
c	Faint ring

Table 2.2

Gurzadyan (1969)

Class	Description	Example
I	Planet-like	NGC 6803
II	Double enveloped	NGC 1534
III	Ring	NGC 2418
Ba	Bipolar : 1st type	NGC 6720
Bb	: 2nd type	NGC 3587
Bc	: 3rd type	A 19
Bd	Rectangular	IC 4406
Sp	Spiral	NGC 4361
Sz	Z-shaped	NGC 6778
S	Stellar	IC 4997
D	Diffuse	A 16

Greig (1971)

Class	Description
B	Binebulous
C	Centric distribution
A	Annular
E	Egg-shaped

Symmetry classes :

Class	Description
0	Asymmetric
1	Uni-axially symmetric
2	Bi-axially symmetric
3	Circularly symmetric
Z	Z-shaped

Figure 2.3

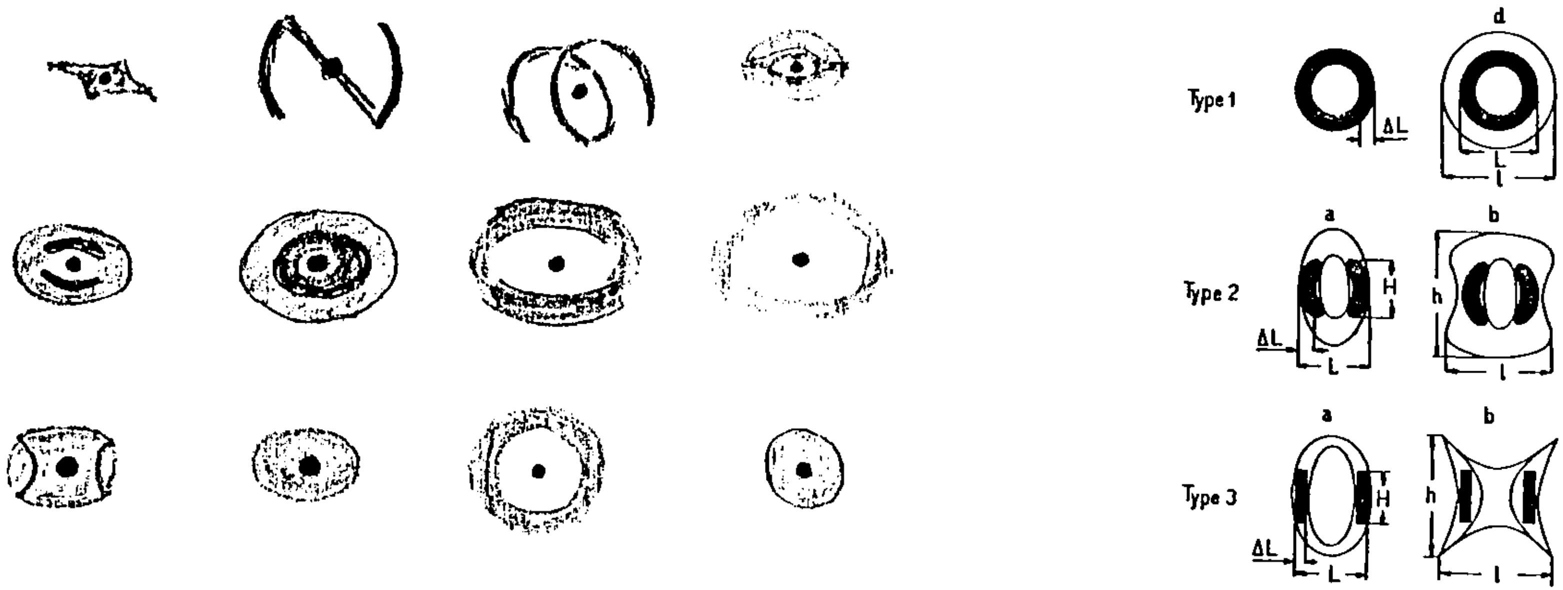

Morphological classification schemes.

a) Evans and Thackeray (1950)

b) Hromov and Kohoutek (1968)

Figure 2.3

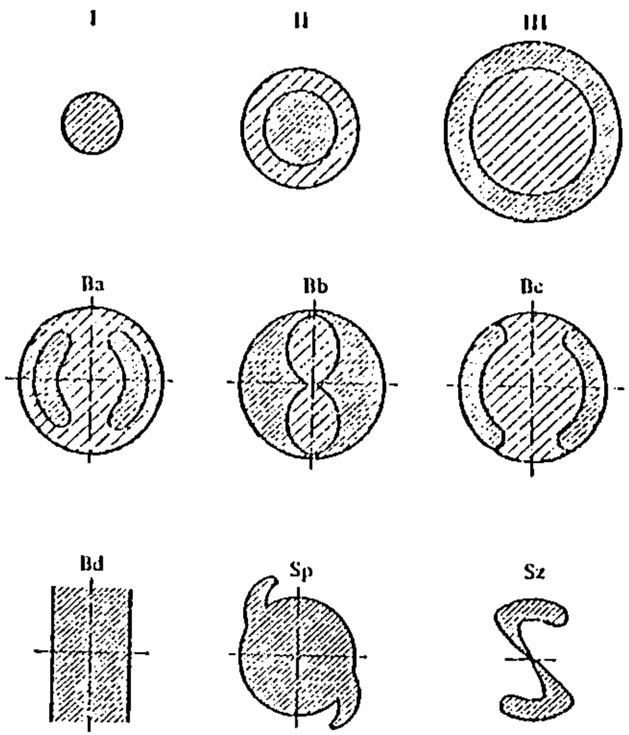

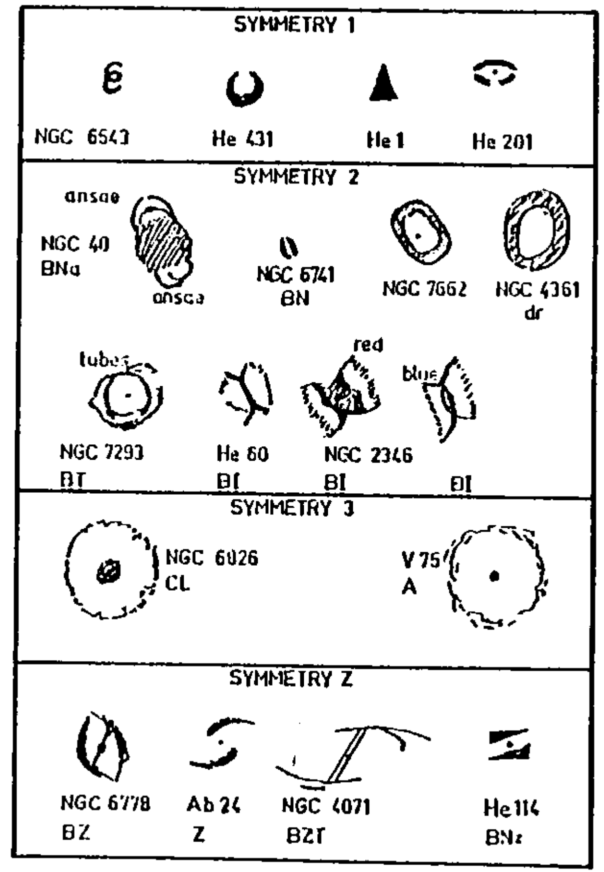

Morphological classification schemes.

c) Gurzadyan (1969)

d) Greig (1971)

2.3 Nebular Models

One of the objects of classifying Planetary Nebulae is to try to find a common unifying feature of the nebulae which may be explained by one parameter, or at least a very small number of parameters. In the past various schemes have tended to use one spatial model for each individual class, rather than one model for all classes. In this respect Hromov (1962) has stated that since Planetaries appear to form a physically related family of astronomical objects their spatial forms must be governed by the same set of dynamical forces and so they must have the same intrinsic form. Consequently, the diversity of observed shapes must be the result of the projection onto the plane of the sky of this one form.

Figure 2.2 shows some of the possible approaches that have been or can be employed in determining the intrinsic form of a Planetary. In more detail these are :-

(i) Empirical - generally uses a simple model to explain the form of the majority of Planetaries, or uses a more detailed model to account for the structure of a few nebulae.

(ii) Derived - by assuming some form of symmetry it is possible to derive the spatial distribution of radiating matter in an individual nebula.

(iii) Theoretical - these tend to divide into explanations of :-

a) The general ionization structure of a non-evolving spherically symmetric nebula.

b) The overall structure of a spherically symmetric evolving nebula.

c) The evolution of the general shape of a simple cylindrically symmetric model nebula.

Each of these approaches is discussed in turn, in more detail, in the following sections.

Figure 2.2

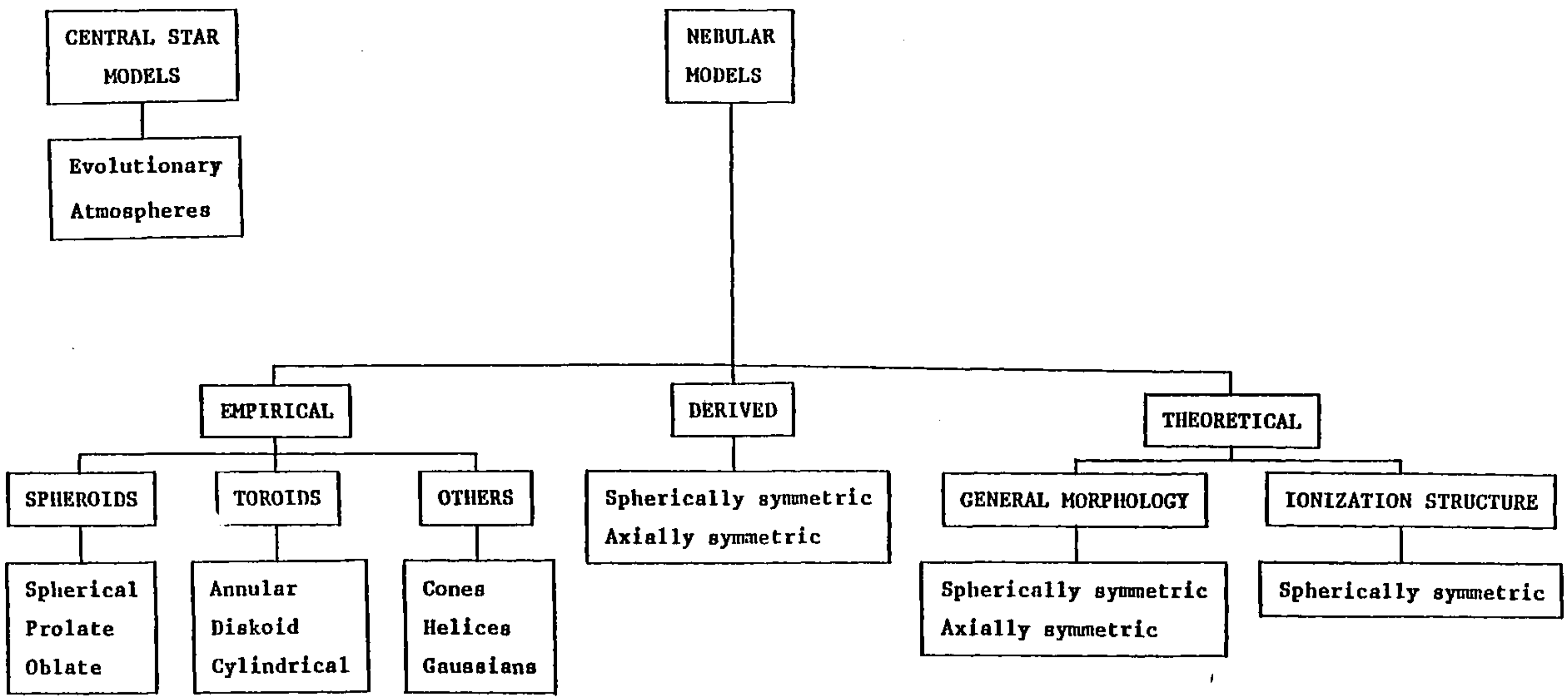

Schematic flow-chart showing the different ways of modelling Planetary Nebulae.

2.3.1 Empirical

Considerable discussion has ranged over the years as to whether Planetary Nebulae are inherently toroidal or spheroidal in form. The main argument for the toroidal interpretation is based on the observation that in many objects, for example NGC 6720, the ring to centre intensity ratio is too high to be accounted for by a closed shell configuration such as a prolate or an oblate spheroid (Minkowski and Osterbrock 1960, Curtis 1918). Conversely, the case against toroidal forms is a statistical one, whereby it is argued (Greig 1971) that if Planetary Nebulae are toroids then too many are observed face on, that is they resemble annuli, than can be explained by a random ditribution of their axes of rotational symmetry.

NGC 6720 may be used as an example to highlight the conflicting interpretations used in explaining the observed two-dimensional structures of the images of Planetary Nebulae.

Osterbrock (1950) and Minkowski and Osterbrock (1960) have interpreted NGC 6720 as an inclined toroid.

Hua and Louise (1970) have used as their model a flat ring, tilted at 45° to the line of sight. Surrounding this is a thin spherical shell to account for the faint outer envelope.

Atherton et al (1978) have carried out an extensive study of the [OIII] velocity field in NGC 6720 and find that :-

(i) The mean position of the line profiles does not alter along either the apparent major or minor axes.
(ii) The maximum line splitting occurs at the centre of the nebula and falls monotonically to zero at the edges.

Using additional electronographic data on a range of ions they conclude that NGC 6720 can be described by an oblate spheroidal shell.

Gulak (1958), using a technique outlined in a later section, has found that NGC 6720 can be interpreted as a cylindrically symmetric object with its' axis lying in the plane of the sky along the major axis. In other words, it resembles a prolate spheroid.

A recent study by Phillips and Reay (1980) of NGC 6720 and NGC 2474/75 may possibly help to resolve the controversy concerning intrinsic nebular forms. They point out that whilst the image of a nebula in the hydrogen lines can be quite adequately described by a closed shell model, it is the low centre to ring intensity ratios of the low excitation forbidden forbidden lines that indicate a toroidal nature. One possible explanation is that the low excitation ionic radiation arises in sheets of gas and so can not be described by a simple smooth distribution of radiating material.

2.3.2 Derived

The two methods of finding the distribution of emitting matter within a nebula, integro-differential solutions and matrix inversion, both rely upon the solution of Abels' Integral, an outline of which follows.

Consider figure 2.3. This shows a spherically symmetric nebula bounded by an outer surface of radius R, outside of which the volume emissivity E(r) is zero. The observed intensity I(x) at a projected radius x is simply the integral of E(r) along the line of sight, assuming that the nebula is optically thin at the given wavelength of observation. This integral equation is similar to Abels' Integral.:-

$$I(x) = 2 \int_x^R \frac{r.E(r)}{\sqrt{r^2-x^2}}.dr \qquad (2.1)$$

The general solution of this equation involves the differentiation of I(x) with respect to x :-

$$E(r) = -\frac{1}{\pi} \int_r^R \frac{1}{\sqrt{x^2-r^2}}.\frac{dI(x)}{dx}.dx \qquad (2.2)$$

Vorontsov-Velyaminov (1948) has given a discrete version of the solution of equation 2.1 :-

$$E(r) = -\frac{1}{\pi} \frac{\sqrt{R^2-x^2}}{R} \left[\frac{dI(x)}{dx}\right]_R + \frac{r}{\pi} \sum_{x=r}^{R} \sqrt{x^2-r^2} \,.\frac{d}{dx}\left(\frac{I(x)}{x}.\frac{dI(x)}{dx}\right) \qquad (2.3)$$

He used this solution in deriving the emissivity distribution in the fairly symmetric nebula NGC 6572.

In practice when either equation 2.2 or equation 2.3 is applied to real data it is found that very high signal to noise ratios are required. This is because the differentiation of the signal (I(x)) tends to amplify any noise present.

The corresponding equation for the matrix inversion technique is realised by converting equation 2.1 into a discrete equation :-

Figure 2.3

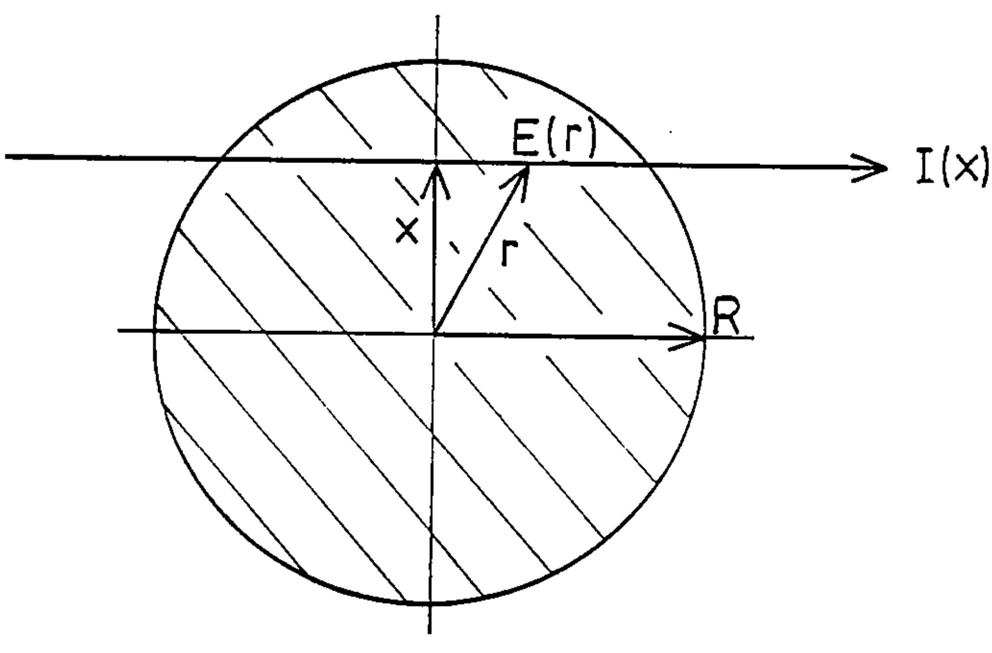

Spherically symmetric model used in the derivation of Abels' Integral Equation. Refer to text for explanation of symbols.

$$I(x_i) = 2 \sum_{j=i}^{k} \frac{r_j . E(r_j) . \Delta}{\sqrt{r_j^2 - x_i^2}}$$

k is defined as : $R = x_k$ and $\Delta = r_{j+1} - r_j = x_{i+1} - x_i$. Written as a matrix equation this is :-

$$I = T\ E \qquad (2.4)$$

I and E are now column matrices of length k and T is a square matrix composed of purely geometric factors, which are zero below the leading diagonal. Clearly the solution of equation 2.4 involves the inversion of T, and when this is carried out once it is unnecessary to repeat the procedure, unless the x_i's and r_j's are changed. This method also suffers from the problem of amplified noise since it involves the differencing of similar data values. Wilson and Aller (1951) have used this technique in a study of the spatial distribution of H, He, N^+, O^+, O^{++}, Ne^{++} and S^+ in the low excitation nebula IC 418. Although this nebulae is not symmetric it is very nearly so, and in their analysis Wilson and Aller computed a mean radial distribution for each of the ions.

By invoking cylindrical symmetry Gulak has taken the solution of Abels' Integral one step further by using it to solve for the volume emissivity distribution E(r,z) along chords at right angles to the axis of symmetry. This requires that the axis of cylindrical symmetry lies in the plane of the sky. Gulak also assumes that this axis also points along the apparent major axis of the nebula. With these assumptions he has found E(r,z) in NGC 6720, 7009 and 7662 (Gulak 1958). However, the second assumption appears to rely upon an apriori knowledge that these objects are prolate in form. Therefore, it may be interesting to repeat these analyses for the case where the axis of cylindrical symmetry lies along the minor axis.

Another method for finding a cylindrically symmetric emissivity distribution, without actually directly solving equation 2.1, is to use an iterative approach. Essentially this involves adopting an initial form for E(r,z), computing the corresponding intensity variation over the nebula and looking for the best match to the observed intensity distribution by a process of iteration. The advantage of this technique over the preceeding ones is although it takes more computer time it is less susceptible to the effects of noise. Additionally, by tilting the axis of symmetry relative to the plane of the sky it is possible to obtain a better fit to the data. Unfortunately, when the tilt becomes too great an infinite number of solutions $E(r,z)$ result. This is because the solutions for the intensity variations over the object become uncoupled from each other.

2.3.3 Theoretical

The aim of calculating the theoretical ionization structure of a model nebula is to produce a self-consistent picture which can account for the observed spectra of the nebula and central star in terms of elemental abundances and density and temperature distributions. In the past the majority of these models have been spherically symmetric. One of the main failures of such models has been the inability to produce the correct intensity levels of lines from singly ionized elements in high-excitation nebulae. This has led to the proposal of models which contain neutral globules. Unfortunately, Hummer and Seaton (1973) have shown that the shielding effect of these globules is inadequate to produce high enough intensities from the gas behind them. Certainly such globules do in fact exist, because they are visible in photographs of the nearest Planetary Nebula NGC 7293. The eventual explanation for the current failure of the models may lie in the spectrum of the central stars or in an unconsidered physical process, such as charge exchange reactions or shock effects.

Evolutionary models of spherically symmetric nebulae have been computed by Weedman (1968) and Sofia and Hunter (1968). The principal conclusions to be drawn from these investigations are :-

(i) An outwardly directed force is necessary to maintain the central holes observed in real nebulae.

(ii) Photo-ionization effects dominate over expansion cooling of the nebulae. According to Sofia and Hunter this may explain the discrepancy in electron temperature found between static ionization models and observation.

(iii) A monotonic, roughly linear, velocity - radius relation results from most of the models, which agrees with the conclusions of Wilson (1950) and Weedman (1968).

(iv) The evolution of the central star seems to have little effect upon the overall structure of the nebula, although it should be borne in mind that this applies to spherically symmetric models and may not be true in general.

Because of the extra dimension involved two-dimensional static or kinematic model nebulae have not been investigated. However, by ignoring the detailed ionization structure of a nebula several people have looked at ballistic type models. Louise (1974) has considered what would happen if the outer layers of a rotating extended star were to be suddenly ejected. His results show that such nebulae would assume oblate forms. A more detailed investigation, along similar lines, was undertaken by Phillips and Reay (1977). They also found that the overall form of the models were oblate, although some assumed toroidal shapes. Under the influence of radiation pressure directed from the central star however , the parts of the shell situated above the stellar poles can " blow out " owing to the lower material density at these points and their smaller distance from the star. On the other hand, Kirkpatrick (1976) has shown that an initially slightly oblate nebula can evolve into a significantly prolate shell solely under the influence of internal pressure. Clearly, to reconcile these two opposite models a more realistic picture must be developed which takes into account both gravitational and radiation pressure forces.A great deal of work still remains to be done in this area of nebular structure.

Chapter 3

3.1 Published Data

In their investigations of the spectra of Planetary Nebulae with a prism spectrograph Campbell and Moore (1918) noticed that many of the emission lines, especially the so-called bright " Nebullium " lines, were distorted. In the majority of cases these distortions were of a tilted and / or bowed nature. To account for this phenomenum they proposed that the nebulae were rotating shells - a three-dimensional analogue of the rings of Saturn. This theory supposed that the shells were quasi-stable configurations, except that at the polar regions it was necessary to have infalling material since there was no centrifugal force capable of supporting the shell at these points. This picture was found difficult to reconcile with observation and eventually it was realised that the nebulae were not rotating but were in fact radially expanding (Perrine 1929).

Many years elapsed before any further significant work on the kinematics of Planetaries was carried out, although the origin of the " Nebullium " lines was finally attributed to normally forbidden transitions in O^{++} (Bowen 1928). Wilson (1950) after World War II undertook a major investigation of the nebular spectra of many bright Planetaries with a Coudé grating spectrograph, and this work still forms the basis of many kinematic studies.

Grating and prism spectrographs are limited to doing useful work only upon the brighter nebulae, and so for the fainter larger objects it is essential to use an instrument which can accept large input solid angles efficiently. Such an instrument is the Fabry-Perot interferometer, which is especially well suited to the study of extended emission line sources because of its high Luminosity-Resolution product (Jacquinot 1954). The inherent problem of multiple wavelength pass-bands in this device may be overcome by the addition of a narrow pass-band interference filter , or even another interferometer. Although no major investigation of the kinematics of Planetaries using a Fabry-Perot interferometer has been done to date the work of Bohuski and Smith (1974) must be mentioned. In this study they employed a single pressure-scanned Fabry-Perot interferometer combined with an interference filter to record

[OIII] λ5007Å line profiles at several positions on a handful of well-evolved Planetaries, the purpose of which was to investigate the possible linear expansion velocity - radius relationship indicated by Smith (1969) for medium sized nebulae.

An alternative use of the Fabry-Perot interferometer is as a constant pass-band filter which is placed immediately in front of a two-dimensional detector, such as a photographic plate. The resulting picture will be composed of interference fringes superimposed upon the image of the nebula which are distorted by internal motions within the nebula. In this way line profiles at many positions across the object can be recorded simultaneously. A variation of this technique is used in the " Insect-eye " interferometer (Meaburn 1976) in which a hexagonal array of small lenses divides up the image of the nebulae into many individual ring patterns which are recorded via a Westinghouse image tube on IIIaJ photographic plate. Each ring pattern is then scanned with a micro-densitometer and averaged to produce a line profile of the part of the nebula taken in by the corresponding " Insect-eye " lens. This instrument is therefore in effect a simultaneous multi-aperture interferometer.

Table 3.1 is a compilation of all kinematics observations published to date and is listed in terms of ionic species rather than wavelengths. Results obtained with slit spectrographs tend to be averages over several lines for an individual ion, whereas data obtained with a Fabry-Perot interferometer is invariably of a single line such as the N_1 line of O^{++} , or [NII] λ6584Å.

Table 3.1

Object	[OIII]	HI	[NII]	[NeIII]	[OII]	HeII	[NeV]	[OI]	[SII]	HeI	OIII	[AIV]	HgI	NIII	[SIII]	(u)	Source
NGC 246	73	71															J1
NGC 650/1																20:	LWL
		0:	62														T3
NGC 1360		m100															Do2
	55.0																BS
NGC 1535	40.0		39.0														W2
	28	0:															J1
NGC 2392	105.3		113.9	106.0		0:											W2
NGC 2440	44.6	61.5	44.8	65.6	0:												W2
	m28	m14	m28				m30	m30									KA
NGC 2474/5		0:	70														DK
NGC 2899	>28.5																BS
NGC 3242	39.5	40.7		38.2		34.4											W1
	39.6	40.8		39.0		33.6					32.5	35.6					W2
NGC 3587																89	LWL
NGC 3699	>38.3																BS
NGC 3918													56				D
NGC 4071	>21.3																BS
NGC 4361	>46.7																BS
NGC 5189	72																A
	55	0:															J1
NGC 6210	42.8	42.1	71.1	41.6	71.1					38.3							W2
	38.8	37.8															OHW
NGC 6302	21.1																BS
		m---	m---					m---									EH
NGC 6543	m---			m---	m---												Mu
NGC 6567	36.9	35.6	71.5	29.8													W2
NGC 6572			29.5		33.7			32.0	31.0								W2
		0:	29.6														OHW
NGC 6720				60:													W2
																58.6	LWL
	50																AH
NGC 6741	41.6		42.1	41.0	44.2		0:										W2
NGC 6803	29.0		40.1	26.6													W2
NGC 6818	56.2	55.5		58.0	60.2	42.4	32.6										W2
NGC 6826	14.9	0:															OHW
NGC 6853																56	L
																55.8	LWL
		0:	62.3														BSW
			63.0														HL
			54.3														Da
		100															Do1
	m---																M
	m30		m66					m66									GMM

Published nebular line splittings and widths.

NGC 6857		w31.7													BRS
NGC 6884	45.5	45.6		42.0											W2
NGC 6886	32.8	34.4		40.6	45.3		0:								W2
NGC 6905	99	82													J1
NGC 7009	41.1	42.1		38.7	40.9	35.8				44.1	32.9	39.7			W2
	39.0	38.4			35.1										OMW
NGC 7026		81.7													W2
NGC 7027	40.9	42.4	41.6	44.7	47.2	39.6	38.2	45.5	42.7		41.4				W2
	27.0														HP
NGC 7293			■---												CCL
	26.6														BS
	m27														T1
								■---							T2
NGC 7662	52.7	51.9		51.8	58.0	46.1	38.6				50.6	46.0		47.7	W2
	53	52		52	58	46	39					39			W3
	54.0	46.0				46.0									OMW
IC 351	29.0														W2
IC 418	0:	0:	0:	0:	0:			49.9	34.7	0:					W2
	0:	0:	23	0:	21			47	34				39		W3
	0:	0:	21.2												O
IC 972	e19.0														BS
IC 2149					40.3										W2
IC 2165	40.0		39.9		0:										W2
IC 3568	15.7														BSW
IC 4406	e8.0														BS
IC 4634	29.8		28.6												W2
IC 4997	w49	w49		w49	w48				w41	w46					WO
A 21		0:	106												Lo
A 33	>60.6														BS
A 35	<7														BS
A 36	68.6														BS
BD+30 3639		52.8	51.9		59.6				43.2						W2
Cn 1-5	64	60													J2
H 1-36	w33	w52													J2
H 1-47		w41													J2
H 2-43		w71													J2
He 1-5		68.0	67.7												FH
J 320				34.6											W2
J 900	35.8		45.0	35.2	50.4										W2
K 1-3	e21.6														BS
K 1-22	49	0:													SG
K 3-2		w17													J2
M 3-31	w28	w43													J2
PC 18		w63													J2
SwSt 1	w37	w43													J2
Th 4-10		w37													J2
Vd 1-1		w40													J2
Vy 2-2	w44	w44													J2

Source Key

A : Acker (1975) AH : Atherton et al (1978) BRS : Bohuski et al (1970) BS : Bohuski and Smith (1974)
BSW : Bohuski et al (1970) CCL : Carranza et al (1968) D : Dopita (1978) DA : Danks (1971)
DK : Doroshenko and Kolotilov (1973) Do1/Do2 : Doroshenko (1971/73) EM : Elliot and Meaburn (1977)
FH : Flannery and Herbig (1973) GMM : Goudis et al (1978) HL : Hua and Louise (1970) HP : Hicks et al (1976)
J1/J2 : Johnson (1976/77) KA : Kaler and Aller (1974) L : Liller (1965) Lo : Lozinskaya (1973)
LWL : Liller et al (1966) M : Meaburn (1971) Mu : Munch (1968) O : Osterbrock (1970)
OMW : Osterbrock et al (1966) SG : Smith and Gull (1975) T1/T2/T3 : Taylor (1974/77/79)
W1/W2/W3 : Wilson (1946/50/58) We : Webster (1978) WO : Wilson and O'Dell (1962)

Symbol Key

e : e-folding width.   m : Multi-position observation.   u : Unspecified ion.   w : Full-width at half-maximum.
---: Line splitting or width not given.   0:.: Line splitting not resolved.

3.2 New Observations

The aim of this thesis is to investigate the structure and evolution of Planetary Nebulae and so a variety of different sized objects were selected to be observed according to accessibility and reasonable surface brightness. Since Bohuski and Smith (1974) had already looked at some of the more evolved nebulae the objects selected for the new program tend to have smaller linear dimensions, and this is reflected in the list of nebulae observed (Table 3.2).

In common with the majority of the studies shown in table 3.1 the [OIII] λ5007Å emission line was chosen for the observations because it is generally the brightest nebular line and has only a quarter of the thermal half-width of HI lines. Moreover, Wilsons'(1950) results show that the line splitting in a density bounded nebula are very nearly the same in the light of HI, [OIII] and [NeIII]. This, together with the fact that HI and [OIII] photographs of such objects appear the same, indicates that the distributions of H^+ and O^{++} are co-spatial. Therefore, observations of just the [OIII] λ5007Å line from density bounded objects should provide a means of mapping the velocity fields of the HII regions within these nebulae.

Spectral observations of NGC 6210, NGC 7027 and NGC 2392 using an image tube grating spectrograph were secured in May 1978 at the Cassegrain focus of the 36" Yapp Equatorial Reflector, Royal Greenwich Observatory, Herstmonceux. Figure 3.1 shows the [OIII] λ5007Å line profile of NGC 6210 obtained with an East-West slit orientation. The double peak has a separation of approximately 40 Km s^{-1} and there is a suggestion of two additional components on either side of the main double profile which are separated by about 70 Km s^{-1}. Results obtained on NGC 7027 appear in chapter six.

The principal kinematic program was carried out in August and September 1978 at the Cassegrain focus of the 60" Tenerife Flux Collector, using a Fabry-Perot interferometer. These results and an outline of how they were aquired are presented in the following sections.

Figure 3.1

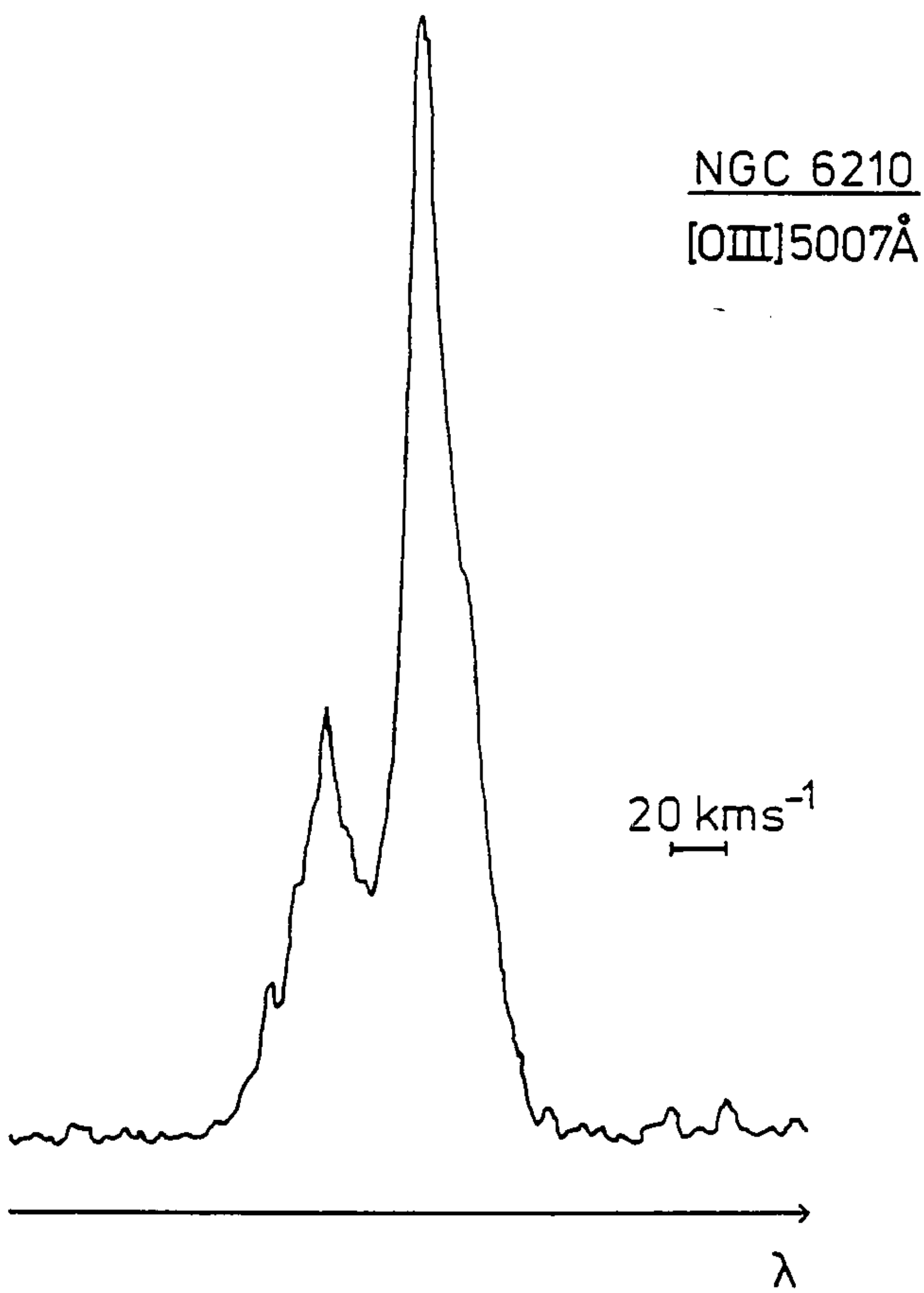

Line profile of NGC 6210, obtained with an image tube grating spectrograph.

3.3 The Instrument

The Fabry-Perot interferometer used in recording [OIII] line profiles of the program objects (Table 3.2) was developed in the Imperial College Astronomy Group by P.D. Atherton and is described in detail elsewhere (Atherton 1978). However, it is useful the discuss the salient features of the instrument :-

Figure 3.2 shows in diagrammatic form the important features which characterise the heart of the instrument - the plates. Each of the quartz optical quality plates has deposited upon it a multi-layer dielectric enhanced reflection coating. Surrounding these coatings are five 1 cm diameter gold capacitor pads, which are vacuum deposited upon quartz pillars. The two plates are held apart facing each other by three piezo-electric transducers in such a way that the effective distance between the reflecting surfaces is 650 μm, whilst the separation of the opposing capacitor pads is only 50 μm. Parallelism of the plates is maintained by sensing differences in capacitance between the capacitors situated at opposite ends of the X and Y axes. Any difference is amplified and is used to alter the voltages applied to the transducers via a servo-loop (Hicks et al 1974). The plate separation (Z) is referred to an external constant gap capacitor, and are scanned by introducing a calibrated offset voltage into the Z channel servo-loop.

The advantages of this technique over other methods, such as tilting or pressure scanning are :-

(i) very rapid scanning is possible.
(ii) The instrumental profile retains a constant, symmetric form.

Any inaccuracies in the system are usually due to drift in the reference capacitor, which arise from temperature and humidity variations.

Because HII emission line sources tend to have very weak continua and widely separated emission lines a single narrow pass-band interference filter is generally sufficient to suppress lines outside the region of interest. For the 650 μm gap the free spectral range is about 2 Å at 5000Å, which corresponds to a Doppler velocity range of 115 Km s^{-1}.

Figure 3.2

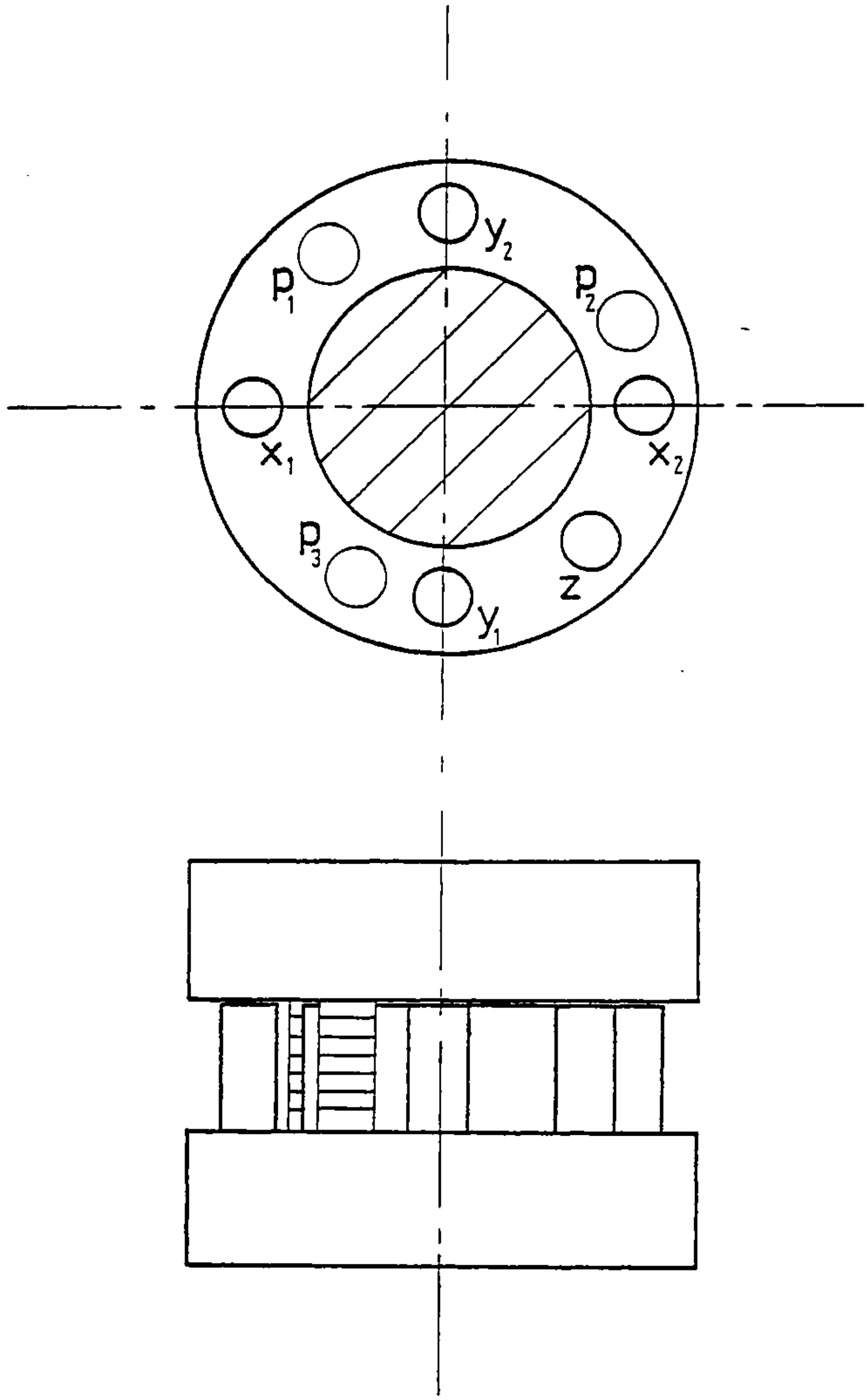

Schematic representation of Fabry-Perot plates, showing capacitor pads (x_1,x_2,y_1,y_2) and piezo-electric transducers (p_1,p_2,p_3).

The interference filter used has a full-width at half-maximum of 5Å, and the detector used was an RCA Ga As photo-multiplier tube which, when cooled to dry ice temperatures, has a dark count of about 5 s^{-1}.

3.4 Instrument Control and Data Collection

For the purposes of instrument control and data collection a Data General NOVA mini-computer was used, running under a BASIC program with Assembler subroutines to control the instrument via CAMAC (Vine 1978) The control program, written by M. Wells, enabled the instrument to scan through any range up to a maximum of about two free spectral ranges. Two scan modes were available, both having a maximum capacity of 256 spectral elements or bins which corresponds to approximately 1.3 inter-order spacings. The first mode stepped the interferometer slowly, integrating at each bin for about 300 ms. Scans could be displayed in real-time on a small Visual Display Unit (VDU) and, upon completion could be added to an accumulated array - depending on the scan quality. As an aid to this procedure, the VDU could display the completed current scan and the accumulated scan simultaneously. Sky conditions and guiding errors were found to alter significantly within the duration of a typical scan using this mode and consequently the second mode was preferred. In this mode the interferometer was rapidly scanned at about 50 ms per bin and an on-going integrated array was built up until a satisfactory signal to noise ratio was achieved, whereupon the scan was terminated at the end of the scan cycle currently in progress by means of a CAMAC pushbutton interrupt facility.

Output of the data arrays for both modes was on punched paper tape in Interdata ASCII format. A header preceded each data array, and contained such information as scan identification, number of points in the scan, start of scan position, integration time per bin and calibration information etc..

3.5 Data Reduction

Calibration of the data was carried out using the λ5183.28Å line from a hollow cathode magnesium lamp, and was generally performed before and after observations of each object. The calibration provided an accurate record, in spectral bin number, of the inter-order spacing, finesse and a reference position for the zero-shifted λ5007Å line.

Reduction of the data was undertaken on the CDC 6000 series computers at Imperial College using an interactive FORTRAN program and a TEKTRONIX graphics terminal. However, before any processing could be commenced it was necessary to translate the Data General ASCII characters on the paper tapes into CDC compatible ASCII characters. For this purpose a standard Imperial College Computer Centre library routine was used, with which data sets of approximately 50 or so scans were translated as a single batch job. The translated data was placed on disc for ease of access, and once there could be processed by the program - a listing of which appears in the appendix. The function of the reduction program was to shift,add and calibrate individual scans of each object using the information in the header which preceeded each scan. The line profiles were plotted on the terminal screen as a function of heliocentric radial velocity. The motion of the Earth around the Sun was corrected for using a simple program ran on a programmable Hewlet-Packard HP65 electronic calculator.

Various methods of smoothing the data were investigated, such as convolution with top hat, Airy and Sinc functions. Eventually it was decided that the resulting gain in signal to noise ratio was minimal, and therefore the data which is shown in figure 3.3 is essentially raw, except where the ends of the scans have been folded over. Occasionally, mains fluctuations caused spikes to appear in the data, and these have been removed where they were obvious.

The wavelength accuracy of the data is mainly limited by the stability of the instrument between calibration scans and is typically of the order of 3 Km s^{-1}.

Output of the processed line profiles was carried out using the micro-film facility of the University of London Computer Centre and copies of these micro-films have been used to produce figure 3.3.

Table 3.2 lists the measured mean line positions,full-widths at half-maxima and where appropriate the peak splitting of the program objects. The inherent ambiguity in ascribing a particular Fabry-Perot order to a Doppler-shifted line profile was resolved by recourse to previous measurements of radial velocity, given in Perek and Kohoutek (1968). For only one nebula, K 3-62, was this procedure impossible, and so the uncertainty in helio-centric radial velocity for this object is an integral multiple of the inter-order spacing (115 Km s^{-1}).

Figure 3.3(1-4)

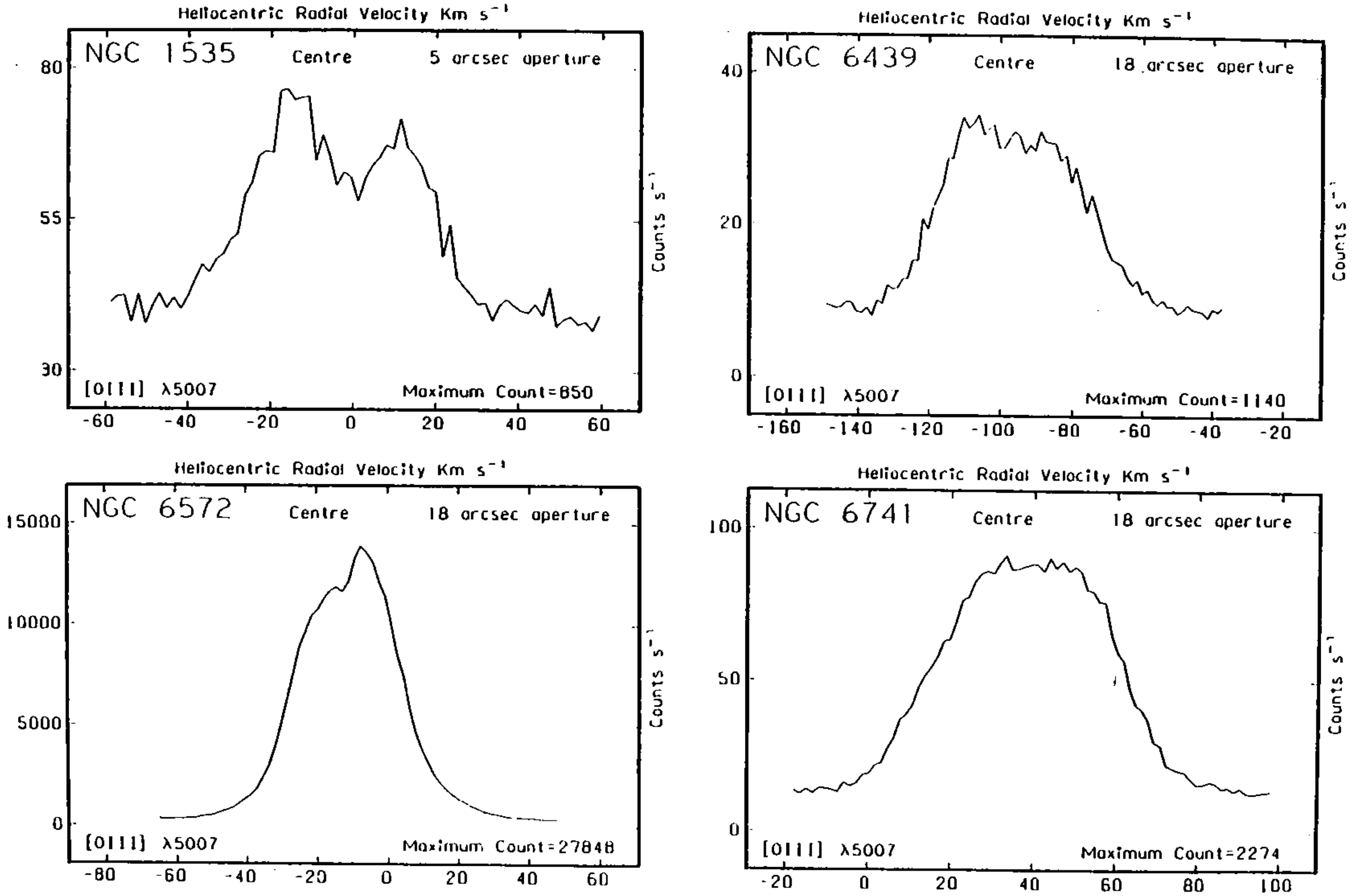

Heliocentric Radial Velocity Km s⁻¹
NGC 1535
Centre
5 arcsec aperture
[OIII] λ5007
Maximum Count=850
Counts s⁻¹
80
55
30
-60 -40 -20 0 20 40 60
Heliocentric Radial Velocity Km s⁻¹
NGC 6439
Centre
18 arcsec aperture
[OIII] λ5007
Maximum Count=1140
Counts s⁻¹
40
20
0
-160 -140 -120 -100 -80 -60 -40 -20
Heliocentric Radial Velocity Km s⁻¹
NGC 6572
Centre
18 arcsec aperture
[OIII] λ5007
Maximum Count=27848
Counts s⁻¹
15000
10000
5000
0
-80 -60 -40 -20 0 20 40 60
Heliocentric Radial Velocity Km s⁻¹
NGC 6741
Centre
18 arcsec aperture
[OIII] λ5007
Maximum Count=2274
Counts s⁻¹
100
50
0
-20 0 20 40 60 80 100

Figure 3.3(5-8)

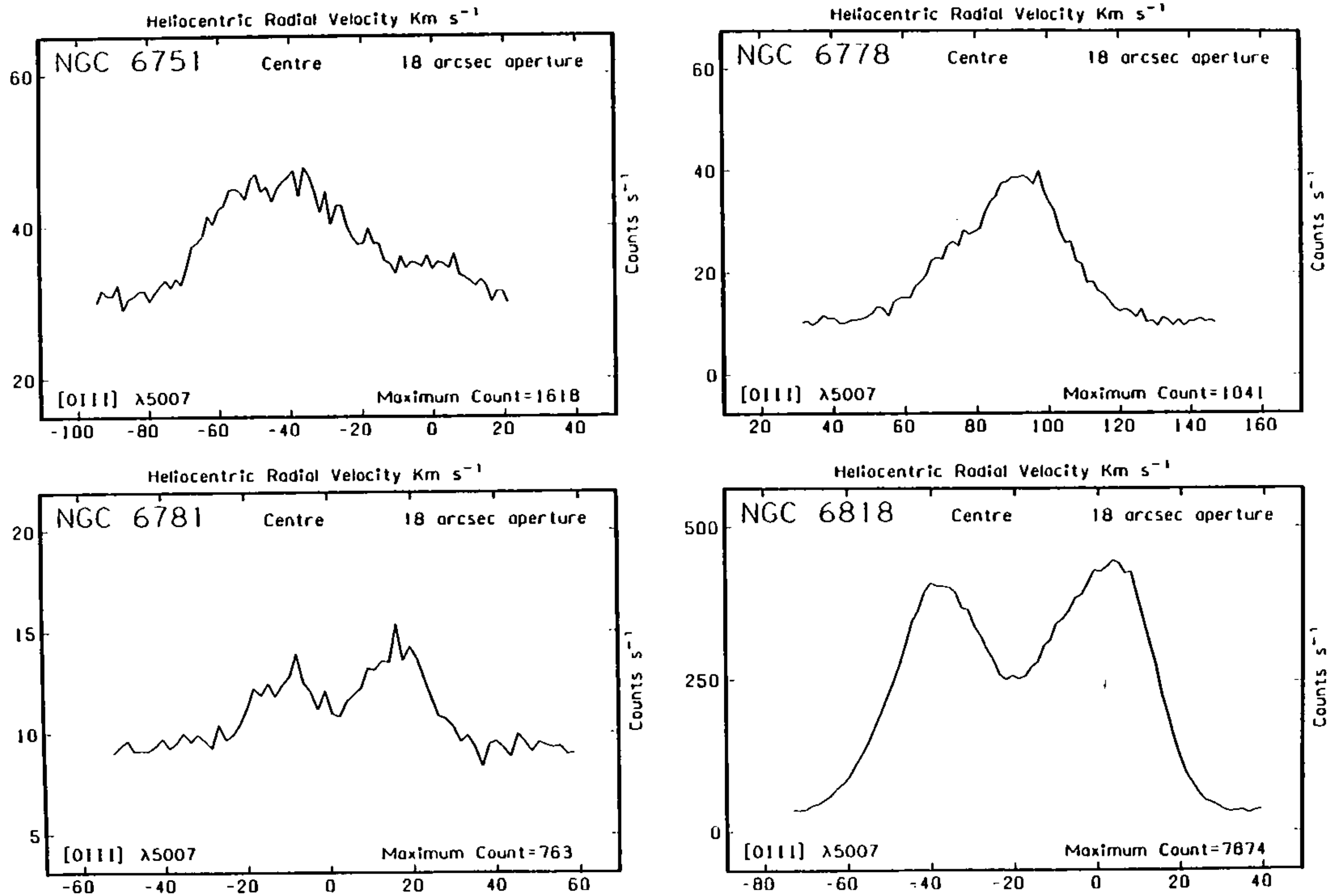
Heliocentric Radial Velocity Km s⁻¹
NGC 6751 Centre 18 arcsec aperture
[OIII] λ5007 Maximum Count=1618
60
40
20
-100 -80 -60 -40 -20 0 20 40
Counts s⁻¹
Heliocentric Radial Velocity Km s⁻¹
NGC 6778 Centre 18 arcsec aperture
[OIII] λ5007 Maximum Count=1041
60
40
20
0
20 40 60 80 100 120 140 160
Counts s⁻¹
Heliocentric Radial Velocity Km s⁻¹
NGC 6781 Centre 18 arcsec aperture
[OIII] λ5007 Maximum Count=763
20
15
10
5
-60 -40 -20 0 20 40 60
Counts s⁻¹
Heliocentric Radial Velocity Km s⁻¹
NGC 6818 Centre 18 arcsec aperture
[OIII] λ5007 Maximum Count=7874
500
250
0
-80 -60 -40 -20 0 20 40
Counts s⁻¹

Figure 3.3(9-12)

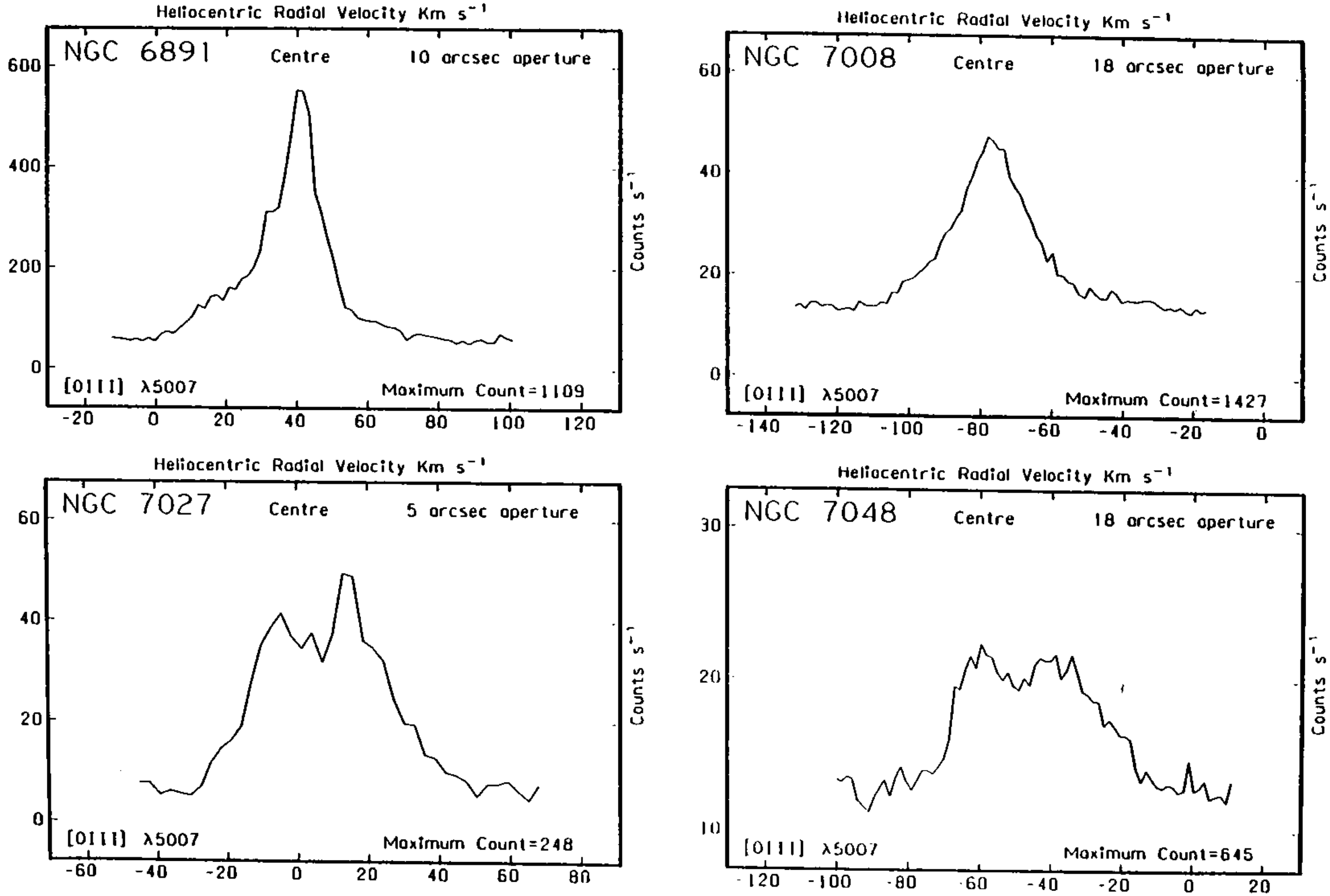

Figure 3.3(13-16)

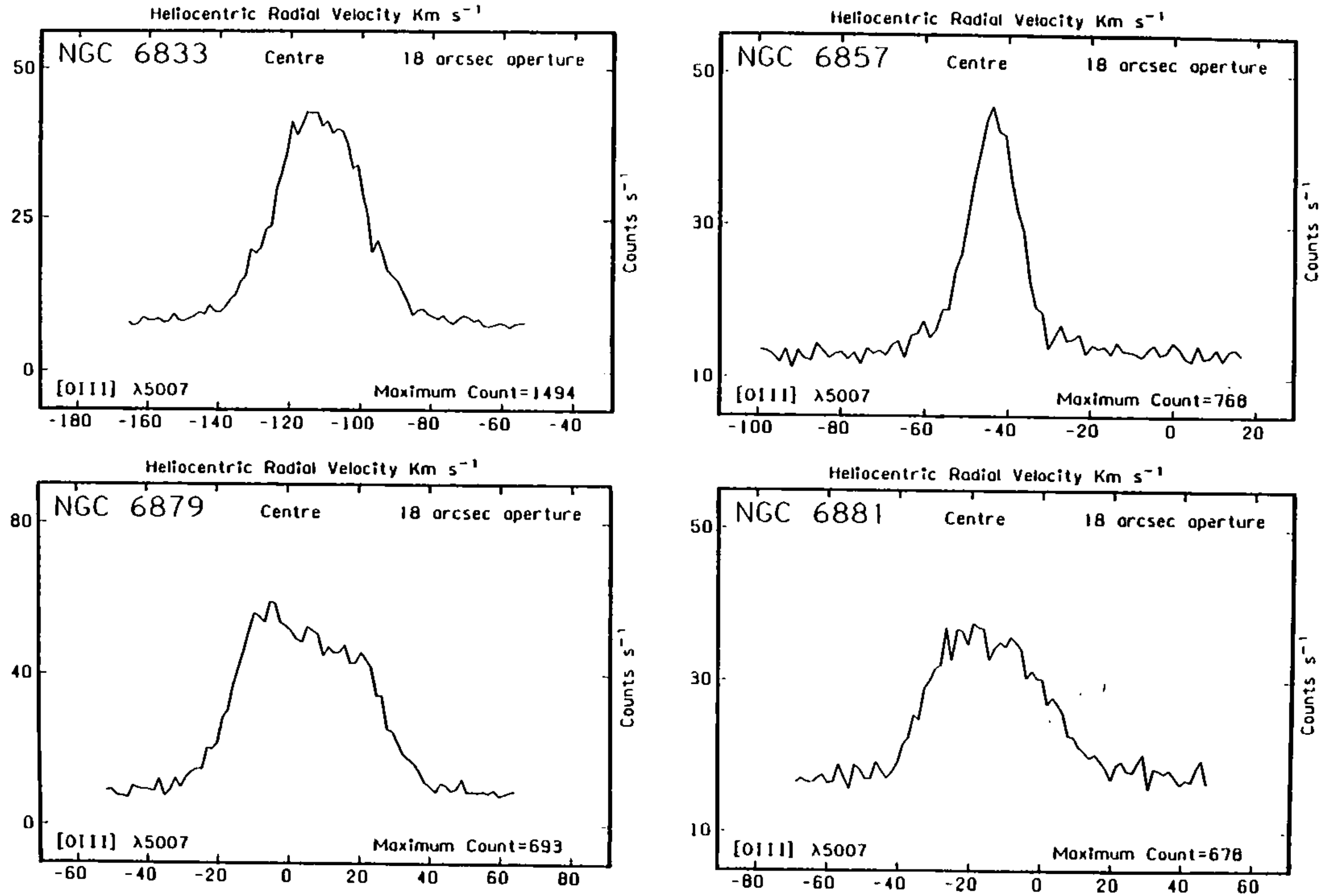

Figure 3.3(17-20)

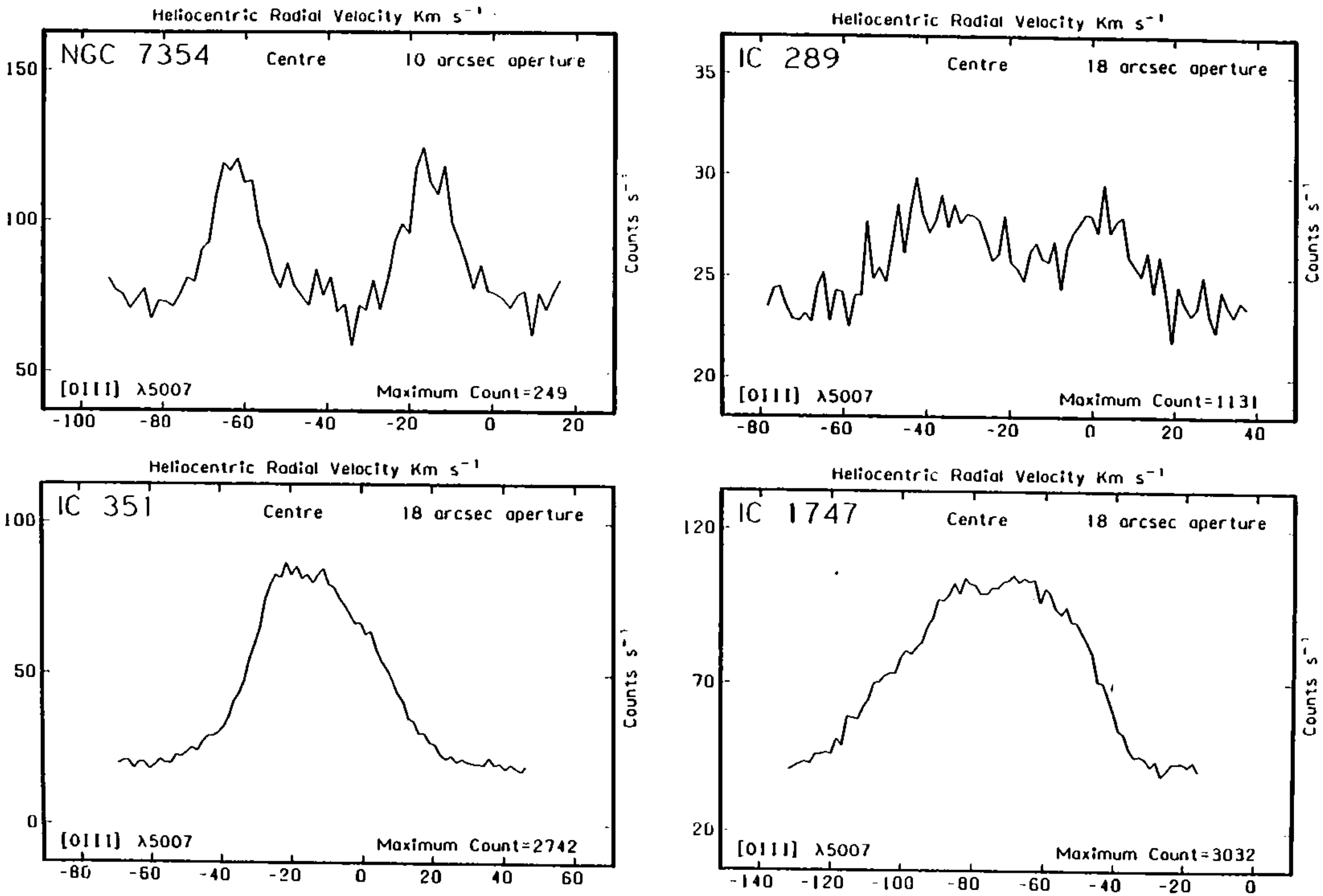

Figure 3.3(21-24)

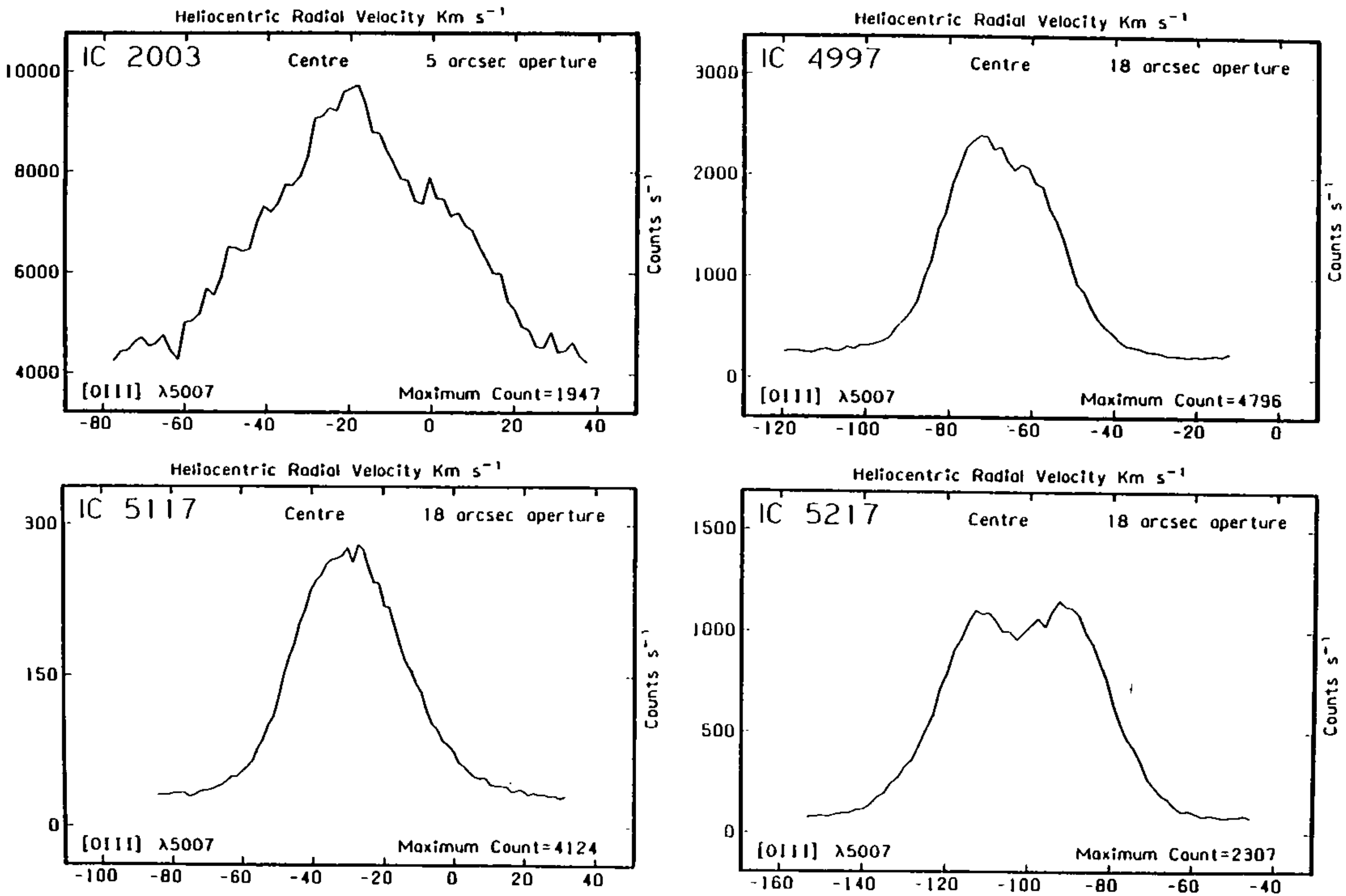

Figure 3.3(25-28)

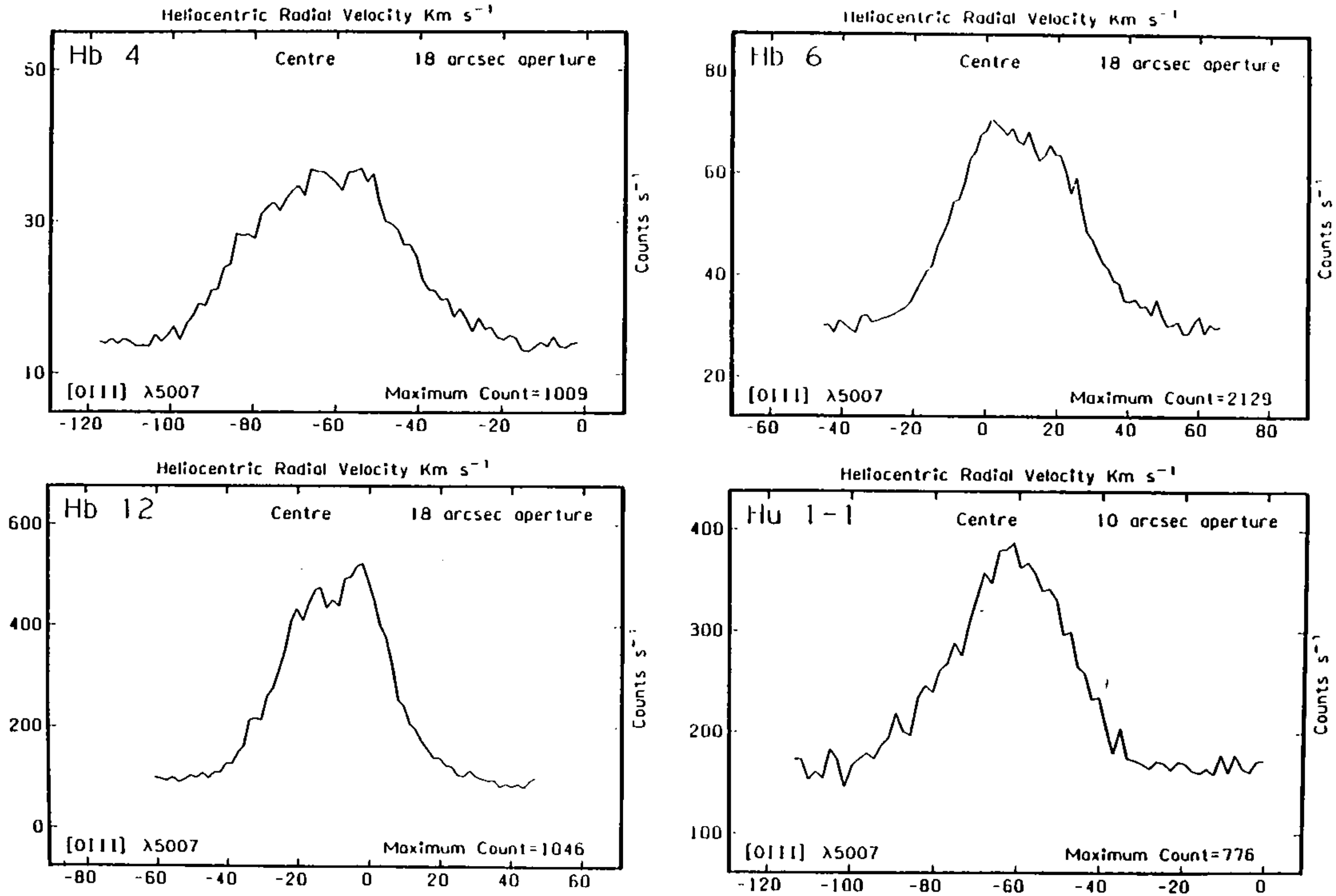

Figure 3.3(29-32)

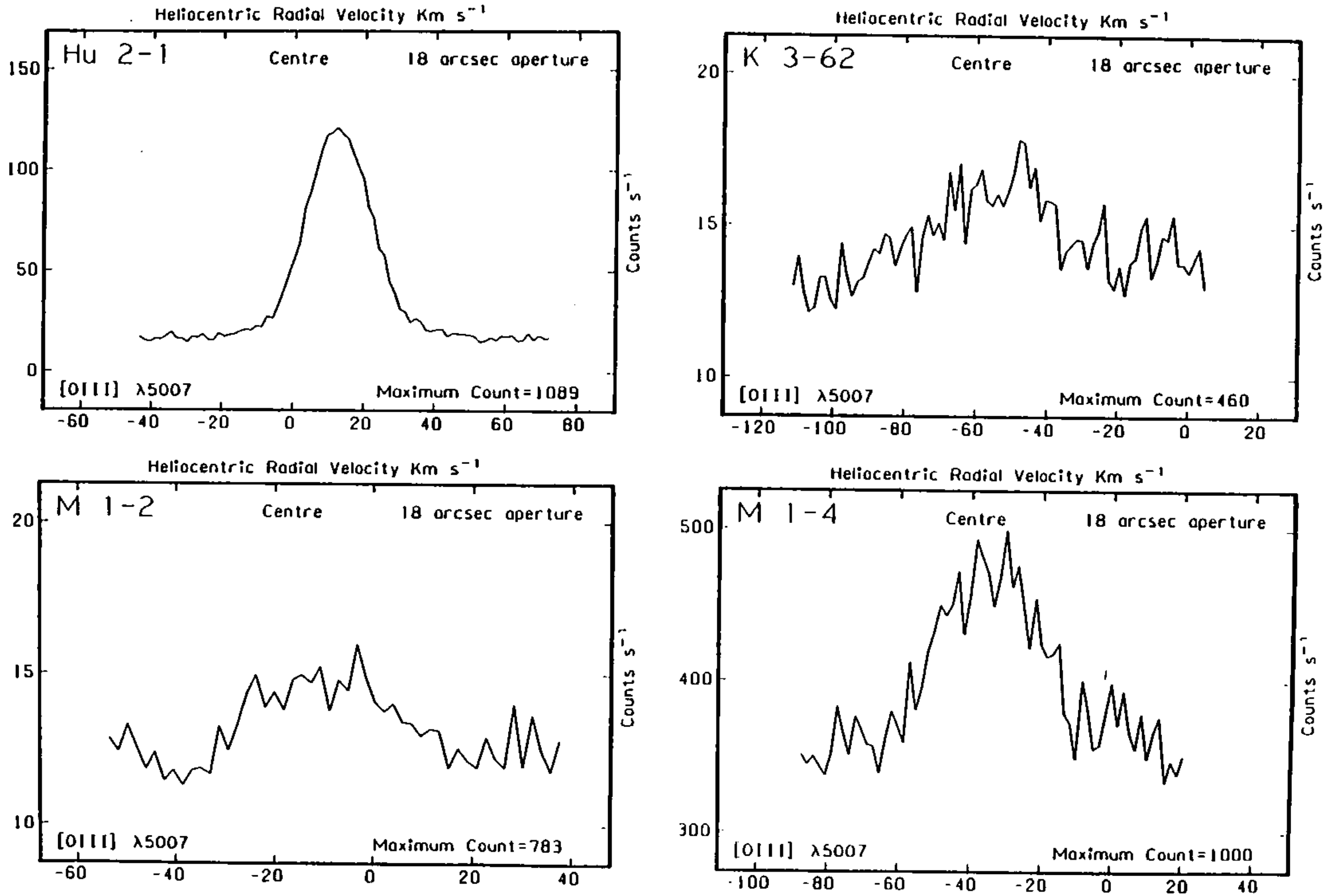

Figure 3.3(33-35)

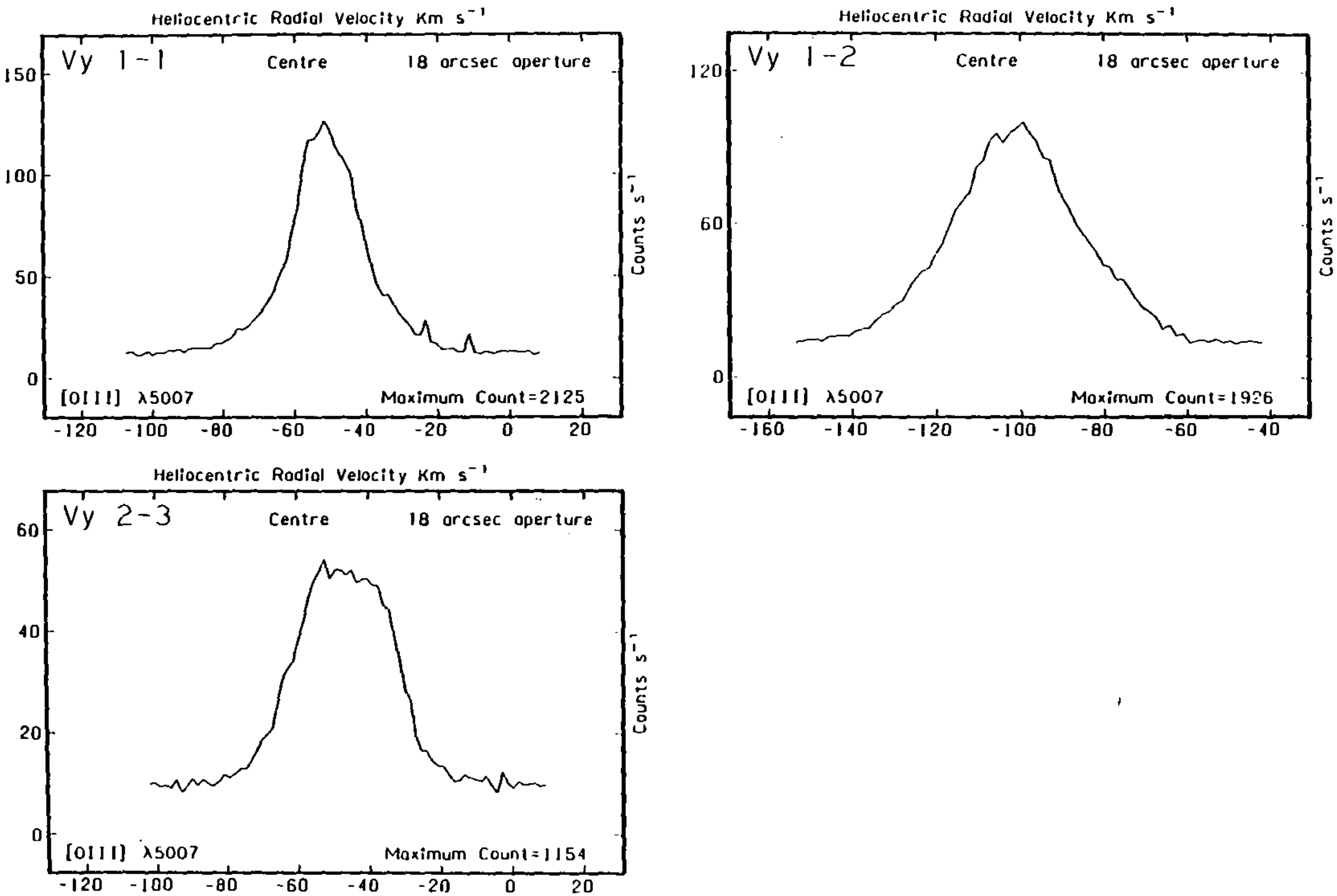

Table 3.2

Figure Number	Name	P-K Number	Entrance Aperture (arcseconds)	Mean Diameter (arcseconds)	Helio-centric Velocity (Km.s^{-1})	Full-width at Half-maximum (Km.s^{-1})	Splitting (Km.s^{-1})
3.2(1)	NGC 1535	206-40°1	5	18	-3	49	25
(2)	6439	11+5°1	18	5.5	-97	49	
(3)	6572	34+11°1	18	14.4	-11	32	
(4)	6741	33-2°1	18	6	39	47	
(5)	6751	29-5°1	18	21	-41	48	45
(6)	6778	34-6°1	18	16	89	47	
(7)	6781	41-2°1	18	108	4	44	25
(8)	6818	25-17°1	18	18.2	-16	67	42
(9)	6833	82+11°1	18	2	-112	28	
(10)	6857	70+1°2	18	34	-42	14	
(11)	6879	57-8°1	18	4.4	5	46	
(12)	6881	74+2°1	18	3.1	-15	37	
(13)	6891	54-12°1	10	14	39	16	7
(14)	7008	93+5°2	18	82	-77	23	
(15)	7027	84-3°1	5	12	7	41	18
(16)	7048	88-1°1	18	59	-46	46	20
(17)	7354	107+2°1	10	20	-39	60	47
(18)	IC 289	138+2°1	18	35	-19	63	39
(19)	351	159-15°1	18	7	-11	41	
(20)	1747	130+1°1	18	13	-73	60	
(21)	2003	161-14°1	5	6.6	-17	49	
(22)	4997	58-10°1	18	1.5	-68	31	
(23)	5117	89-5°1	18	2	-29	37	
(24)	5217	100-5°1	18	5	-101	43	
(25)	Hb 4	3+2°1	18	6	-63	46	
(26)	6	7+1°1	18	6.6	8	40	
(27)	12	111-2°1	18	10	-3	33	
(28)	Hu 1-1	119-6°1	10	5	-51	30	
(29)	2-1	51+9°1	18	6	12	21	
(30)	K 3-62	95+0°1	18	<1	-53	33	
(31)	M 1-2	133-8°1	18	<1	-10	33	
(32)	1-4	147-2°1	18	4	-33	35	
(33)	Vy 1-1	118-8°1	18	<1	-50	21	
(34)	1-2	53+24°	18	4.6	-102	33	
(35)	2-3	107-13°1	18	4.5	-48	33	

Measured parameters of the line profiles presented in Figure 3.3

3.6 The Line Profiles

Some of the more interesting line profiles are discussed below.

NGC 1535

As the entrance aperture is a significant fraction of the nebular diameter the value of the line splitting should be taken as a lower limit. Even so, there still remains a discrepancy between the value shown in table 3.2 and Wilsons' (1950) value. The shoulders either side of the main double peak may be due to the outer envelope.

NGC 6778

This object is very similar to NGC 7026 in appearance. Two components are present in the line profile. The wide wings are consistent with the extensive envelope seen in [OIII] electronographic contour maps presented in the next chapter.

NGC 6781

The observed line splitting should be a very good estimate of the true expansion velocity as the entrance aperture used subtends an angle much less than the nebular diameter.

NGC 6857

Although the optical and radio appearances indicate that this object is a Planetary Nebula (Seyfert 1947) it has been suggested that it is really a compact HII region within the extensive HI region SH2-100 (Chopinet and Lortet-Zuckermann 1976). The narrowness of the line profile and extensive Hα halo observed in electronographic contour maps agree with this conjecture.

NGC 6891

The lack of splitting of the central peak is consistent with the size of aperture used and narrow line width observed by Stoy (1939). The wings may possibly arise from the large (>60 arcsec. diameter) outer envelope.

NGC 7008

This is a peculiar looking nebula, which is generally ring-shaped with a bright region in the north. The line profile is triangular and is not split, even though the aperture is much smaller than the nebula.

NGC 7027

A more detailed study of this nebula is presented in chapter six.

NGC 7048

This is a large bipolar nebula which, although having a split line profile, has a very low expansion velocity.

The Stellar and Integrated Objects

The integrated line profiles of the stellar nebulae and those subtending less than about 5 arcsec. in diameter exhibit a remarkable range of shapes and widths. Johnson (1977), in a study of different stellar nebulae, remarked that his observations of integrated line profiles showed them to deviate little from Gaussian forms. In contrast, the results pre presented here, which have been obtained at nearly four times the resolution, show profiles which do depart significantly from Gaussians. For example, Vy 2-3 has an extremely steep sided profile whereas the profile of Vy 1-2 is very triangular.

A substantial proportion (50%) of the integrated objects shown in table 3.2 eg. NGC 6439, NGC 6741 and IC 1747 show evidence of having flat tops, which may indicate that they are hollow shells (Beals 1931).

The interpretation of these line profiles is left until chapter five, where along with other published data, they are used to investigate the kinematics and evolution of Planetary Nebulae as a whole.

Chapter 4

4.1 Photography of Planetary Nebulae

The observations presented in this chapter were obtained primarily to aid in the interpretation of the kinematic data presented in the previous chapter, for example - the estimation of shell thicknesses. The interpretation of both sets of data is left until chapter five.

An important parameter in the interpretation of Planetary Nebulae is their linear size, which is usually obtained from the knowledge of their distances and angular dimensions. Traditionally, the angular sizes of nebulae have been measured by eye from the extreme limits of their images on, for example Palomar Sky Survey plates or prints. Two effects occur in this process which determine the actual value derived. Firstly, the edges of some nebulae are not sharply defined and so the im image size will tend to increase with depth of exposure. Non-linearities in the photographic emulsion will also affect the variation of photographic density at theedge of the image. In addition, Baum (1968) has remarked that the measured dimensions of a nebula tend to increase with the advent of improved detection techniques. Secondly, the size and usually the entire appearance of a nebula will depend upon the spectral region it is observed in owing to the stratification effect. Capriotti (1978) cites NGC 7293 as an example, in which the images at Hα and [NII] λ6584Å appear quite different - even though both lines lie in the red region of the spectrum.

Aller (1956) has described the use of a slitless spectrograph to record monochromatic pictures of nebulae in the light of many spectral lines simultaneously. Such spectra perhaps provide one of the best ways of demonstrating the stratification effect, examples of which may be found in Wright (1918). When quantitative analyses of slitless spectra are attempted several problems are encountered, which are inherent to the technique :-

(i) The images of large objects often overlap, even at very high dispersion.

(ii) Doppler broadening, especially of the HI lines, smears the images in the direction parallel to the dispersion.

(iii) The image scale along the dispersion axis differs from that along the orthogonal axis.

(iv) The smeared spectrum of the central star, if present, will overlie the images of the nebula.

In spite of these drawbacks many isophotal contour maps have been produced of several nebulae, in which problem (iii) has been corrected for (Aller 1956).

The availability of commercial narrow-band interference filters capable of isolating single emission lines has solved the problems met with slitless spectrography. However, if ordinary photographic plates are employed as the recording medium then there still remains the problems of non-linearities, such as reciprocity failure. This latter effect is especially severe when one is attempting to record faint emission lines or objects of low surface brightness. In these cases it is essential to use an efficient detection technique. Such a process, which is particularly well suited to the photography of Planetary Nebulae, is electronography. The advantages of electronography are that it is extremely linear (better than 2%), has virtually no threshold and has a very large dynamic range (typically 10^3). This means that density calibrations are unnecessary, and high and low surface brightness regions may be recorded simultaneously. Digitisation of the electronograph using a microdensitometer results in a precise record of the two-dimensional distribution of intensity across a nebula. This information may be used for a variety of purposes :-

(i) To provide a simple method for presenting the data at various wavelengths in a selection of visual formats, eg. contours.
(ii) The fitting of, or comparison with, morphological models.
(iii) The derivation of emissivity distributions.
(iv) The ratioing of two exposures to determine :-
  a) Differential extinction across a nebula.
  b) Line-of-sight average density across a nebula.
  c) Line-of-sight average temperature across a nebula.
(v) The calibration of photoelectric data.
(vi) The measurement of angular expansions.

The following sections describe a project in which a catalogue of emission line contour maps of many Planetary Nebulae at various wavelengths was initiated, the purpose of which is to provide a data source for many of the analyses outlined above. Preliminary results are presented, the majority of which correspond to the nebulae selected for the kinematical investigation of the preceeding chapter.

4.2 Electronographic Observations at Kottomia

In September/October 1979 a program of observations of Planetary Nebulae using the 74" reflecting telescope located at the Kottomia Observatory, Egypt was initiated. The purpose of this was to create a catalogue of Planetary Nebulae emission line contour maps. An S20 photo-cathode Spectracon electronographic camera was the instrument employed, and the data were recorded on G5 nuclear track emulsion. Details of the Spectracon and G5 emulsion may be found in McGee et al (1972).

Prior to this investigation several individual, reasonably bright objects had been observed electronographically at various wavelengths (Walker 1972,74, Atherton et al 1978, Reay and Worswick 1978). Using ordinary photographic techniques, Feibelman has presented isophotic contour maps of over a dozen nebulae (Feibelman 1970,71a,b).

One of the objects of this investigation was to accurately define the dimensions of many of the so called " stellar " Planetary Nebulae, which subtend less than two arcseconds in diameter. Since these nebulae tend to have roughly Gaussian type intensity distributions conventional photographic measurements of thier angular sizes depend strongly upon the depth of exposure.

As the brightest lines from Planetaries are usually the N_1 and N_2 lines ([OIII] $\lambda\lambda$5007,4959Å) these were chosen as the principal lines for the project. Hα and occasionally Hβ were also recorded for the majority of the nebulae. For density bounded nebulae the [OIII] and HI images often appear similar, which implies that the three-dimensional distributions of H^+ and O^{++} are also similar. Hence, by only photographing such nebulae in the light of [OIII] one may hope to simultaneously record the intensity distribution of HI also. Since the N_1 and N_2 lines were recorded together with a nominally 50Å wide filter an occasional problem arose when the continuous emission from the central star came through more intensely than the nebular lines. For this reason a narrower (10Å) filter, centred on the λ5007Å line, was sometimes used. The Hα and Hβ filters were also 10Å wide.

Table 4.1 lists some of the objects observed which are common to this program and the kinematic investigation reported upon in the previous chapter. Table 4.1 also gives the various exposure details and measured image dimensions.

Table 4.1

Fig. No.	Name	P-K Number	Filter	Exposure (minutes)	Dimensions (") 1% level	FWHM	Position angle (°)
1a	NGC 1535	206-40 1	N1+N2	5	47 X 43	21 X 18	35
b			H alpha	10	45 X 40	20 X 17	50
2	6439	11+ 5 1	H alpha	20	15 X 14	6.7 X 5.5	60
3a	6572	34+11 1	N1+N2	1/6	20 X 18	8.7 X 8.3	60
b			N beta	2	20 X 20	8.7 X 8.2	50
4a	6751	29- 5 1	N1+N2	5	36 X 29	19 X 17	10
b			H alpha	60	43 X 41	21 X 20	110
5a	6778	34- 6 1	N1+N2	15	35 X 31	13 X 17	40
b			H beta	50	35 X 30	14 X 17	40
6a	6804	45- 4 1	N1+N2	15	55 X 55	27 X 24	60
b			H alpha	50	55 X 55	29 X 25	55
7a	6818	25-17 1	N1+N2	1	35 X 33	21 X 21	20
b			H alpha	10	33 X 31	20 X 19	15
8	6833	82+11 1	N1+N2	3	17 X 13	7.0 X 5.8	70
9	6842	65+ 0 1	N1+N2	10	65 X 63	51 X 54	55
10a	6857	70+ 1 2	N1+N2	10	53 X 44	33 X 31	
b			H alpha	60	116 X 95	32 X 39	300
11a	6879	57- 8 1	N1+N2	5	13 X 16	7.6 X 5.8	80
b			H alpha	20	16 X 14	7.1 X 5.9	30
12a	6884	82+ 7 1	N1+N2	1	17 X 16	7.8 X 7.0	35
b			H alpha	10	16 X 14	5.8 X 6.0	30
13a	6886	60- 7 2	N1+N2	5	20 X 20	8.1 X 8.1	
b			H alpha	10	15 X 13	5.9 X 5.9	120
14a	6891	54-12 1	N1+N2	1	23 X 23	9.6 X 9.6	
b			H alpha	10	24 X 21	9.4 X 9.3	110
15a	6894	69- 2 1	N1+N2	5	51 X 48	39 X 34	50
b			H alpha	60	51 X 47	41 X 36	50
16a	6905	61- 9 1	N1+N2	15	48 X 38	18 X 29	170
b			H alpha	60	55 X 41	21 X 29	170
17	7008	93+ 5 2	N1+N2	5	96 X 76		20
18a	7026	89+ 0 1	N1+N2	3	35 X 24	10 X 13	10
b			H alpha	10	34 X 23	8.5 X 12	10
19a	7048	88- 1 1	N1+N2	5	62 X 58	45 X 38	40
b			H alpha	20	67 X 57	48 X 48	55
20	IC 351	159-15 1	N1+N2	2	20 X 20	10 X 10	
21a	2003	161-14 1	N1+N2	2	20 X 20	9.1 X 9.1	
b			H beta	10	20 X 20	9.2 X 9.2	
22	4846	27- 9 1	N1+N2	5	17 X 16	7.5 X 6.1	75
24a	Vy1 1	118- 8 1	N1+N2	5	18 X 15	8.5 X 6.9	75
b			H alpha	15	17 X 13	7.5 X 6.2	75
25a	2	53+24 1	N1+N2	1	16 X 15	7.8 X 6.2	85
b			H alpha	20	13 X 10	5.7 X 5.1	85
26	Vy2 2	45- 2 1	N1+N2	5	15 X 13	6.5 X 6.2	85

Measurements of electronographic data.

4.3 Data Reduction

The plate scale at the Newtonian focus of the 74" telescope is 22.5 arcsec./mm. Therefore, for a typical seeing disc diameter of 2 arcssec. the image size of a star is approximately 10 μm. This is nicely matched to the resolution of the Spectracon/G5 combination, which at single loop focus, is about 80 line pairs/mm.

All the electronographic data were scanned with a 17 μm. square aperture on a 20 μm. square grid by a PDS microdensitometer, situated at the Royal Greenwich Observatory, Herstmonceux. A FORTH-interactive program (written by I.G. van Breda) , running on a PDP 11/34 minicomputer, was used to scan and record the data digitally on 9-track magnetic tape at 1600 bpi. The program also had a facility whereby rapid visual inspection of a completed scan could be made, using a TEKTRONIX graphics terminal.

Because the detailed data analysis was carried out on the CDC 6000 computers at Imperial College it was necessary to translate the 16 bits/word data tape into a 60 bits/word format. For this purpose an existing 7-track FORTRAN conversion program was upgraded to include a 9-track facility. A listing of this program, PDSTRAN, appears in the appendix. The process of translation enabled the addition to each scan of additional information, such as exposure duration, filter, scan parameters etc. It is in this latter format that the data is kept for archival and processing purposes, the original tape being re-used for scanning other data.

At first, existing contouring routines (written in the Imperial College Astronomy Group) were used to process and contour the data. However, since these programs ran as batch jobs the turnaround time of the analysis was found to be unacceptably long. Another drawback of these programs was the maximum array size they could deal with , typically 13200 points. This necessitated the averaging or " blocking up " of large data arrays, which led to unacceptable over-smoothing of the data. Consequently it was felt advisable in view of the great quantities of data to be reduced to write a new data reduction package capable of handling very large data arrays interactively. The program SIMCONT, a listing of which appears in the appendix, is this interactive data processing routine. The essence of SIMCONT is that it only works upon two lines of data at a time, instead of the whole data array. A subroutine for smoothing the data prior to its' contouring is provided which can remove noise " spikes " and/or block up. Linearly or logarithmically spaced contours are drawn on the screen of a TEKTRONIX graphics terminal, and at the same time information is written to disc which can be used to generate a micro-film copy of the screen contents at the University of London Computer Centre.

Copies of the contour maps produced by SIMCONT are reproduced as figure 4.1, corresponding to the nebulae listed in table 4.1. The contours are equi-spaced between the surrounding background level and the peak intensity of each object, except the lowest contour which is set at 1% above the background.

Figure 4.1(1a,b)

NGC 1535 5 MINS. 4959/5007 19/9/79

POS- 20 MIC STEP 17 MIC. 74 KOTT AS 18 G5

LINE: 1 TO: 200 COLUMN: 1 TO: 200 BLOCKING FACTOR: 2 DATA IS SMOOTHED

NGC 1535 10 MINS. 6563 19/9/79

POS- 20 MIC STEP 17 MIC. 74 KOTT AS 18 G5

LINE: 1 TO: 200 COLUMN: 1 TO: 200 BLOCKING FACTOR: 3 DATA IS SMOOTHED

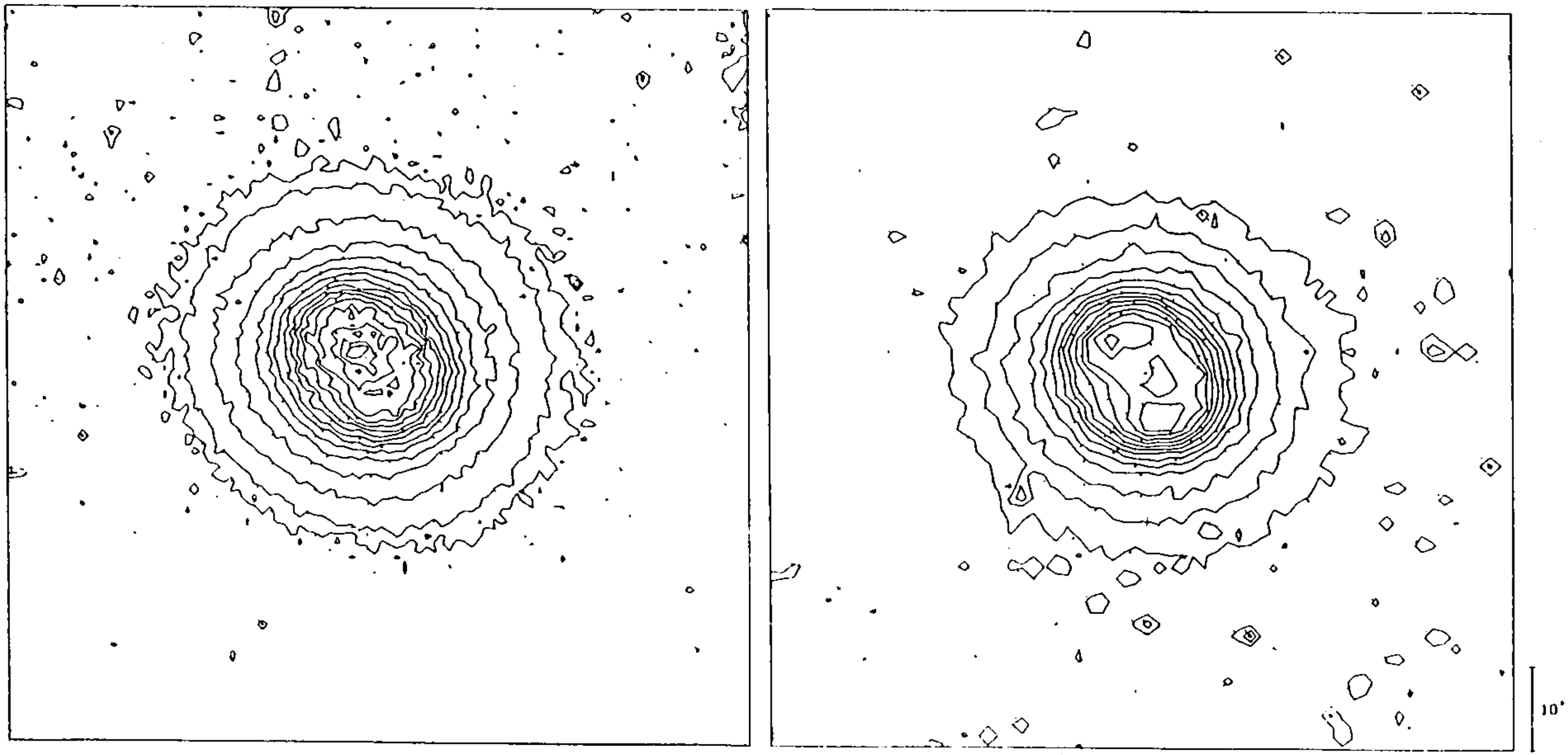

Figure 4.1(2)

NGC 6439 20 MINS. 6563 25/9/79

POS· 20 MIC STEP 17 MIC. 74 KOTT AS 18 G5

LINE: 1 TO: 50 COLUMN: 1 TO: 50 BLOCKING FACTOR: 2 DATA IS SMOOTHED

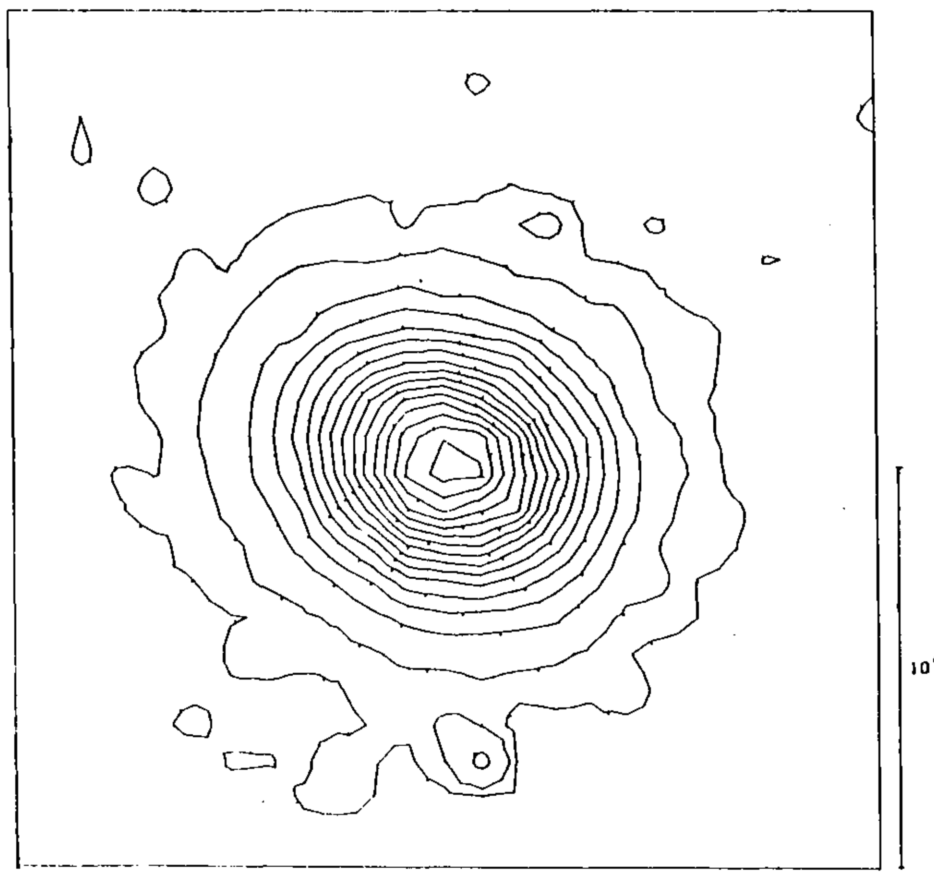

Figure 4.1(3a,b)

NGC 6572 10 SECS. 4959/5007 17/9/79
POS- 20 MIC STEP 17 MIC. 74 KOTT AS 18 G5
LINE: 1 TO: 100 COLUMN: 1 TO: 100 BLOCKING FACTOR: 2 DATA IS SMOOTHED

NGC 6572 2 MINS. 4861 17/9/79
POS- 20 MIC STEP 17 MIC. 74 KOTT AS 18 G5
LINE: 1 TO: 100 COLUMN: 1 TO: 100 BLOCKING FACTOR: 2 DATA IS SMOOTHED

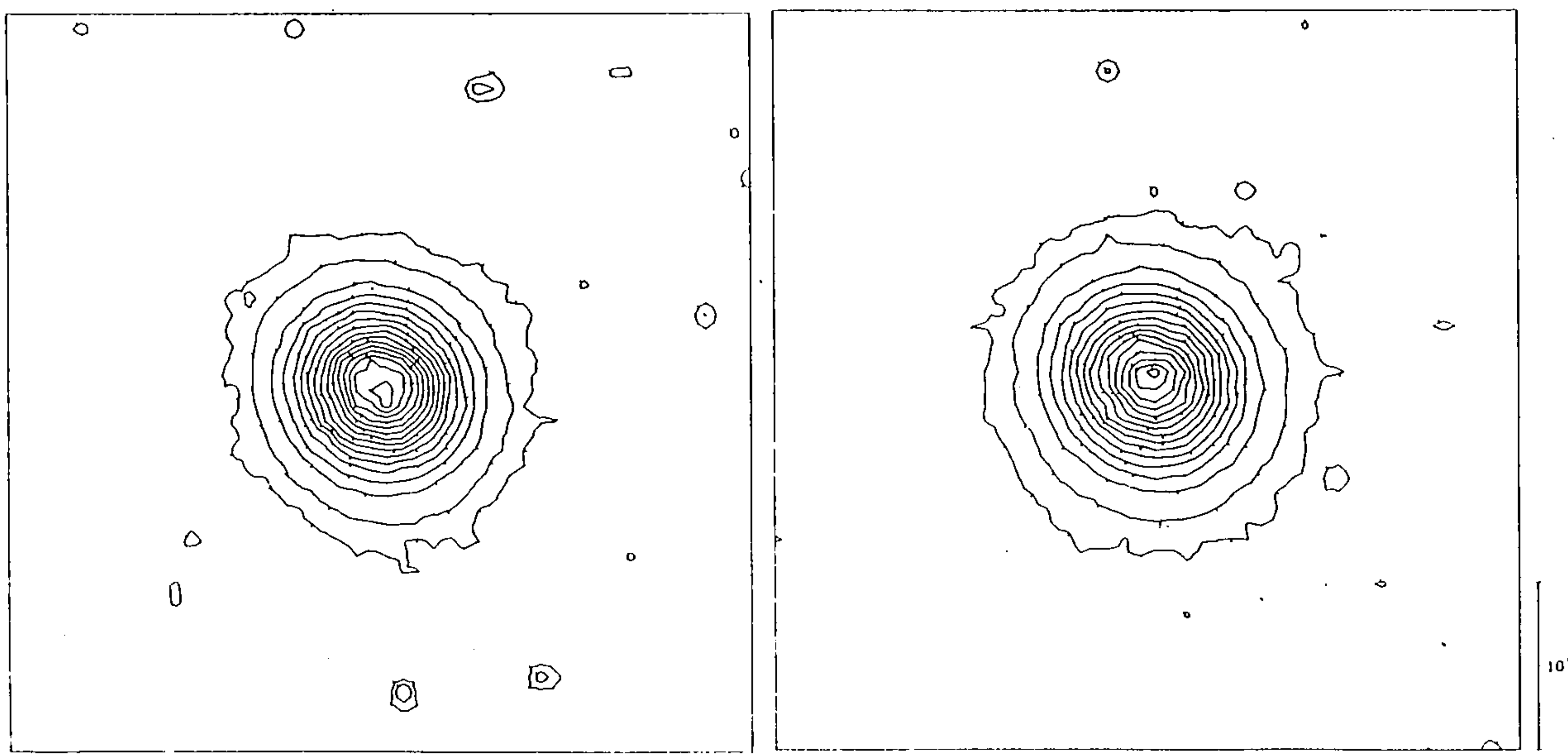

Figure 4.1(4a,b)

NGC 6751 5 MINS. 4959/5007 20/9/79

POS- 20 MIC STEP 17 MIC. 74 KOTT AS 18 GS

LINE: 1 TO: 200 COLUMN: 1 TO: 200 BLOCKING FACTOR: 3 DATA IS SMOOTHED

NGC 6751 60 MINS. 6563 20/9/79

POS- 20 MIC STEP 17 MIC. 74 KOTT AS 18 GS

LINE: 1 TO: 200 COLUMN: 1 TO: 200 BLOCKING FACTOR: 3 DATA IS SMOOTHED

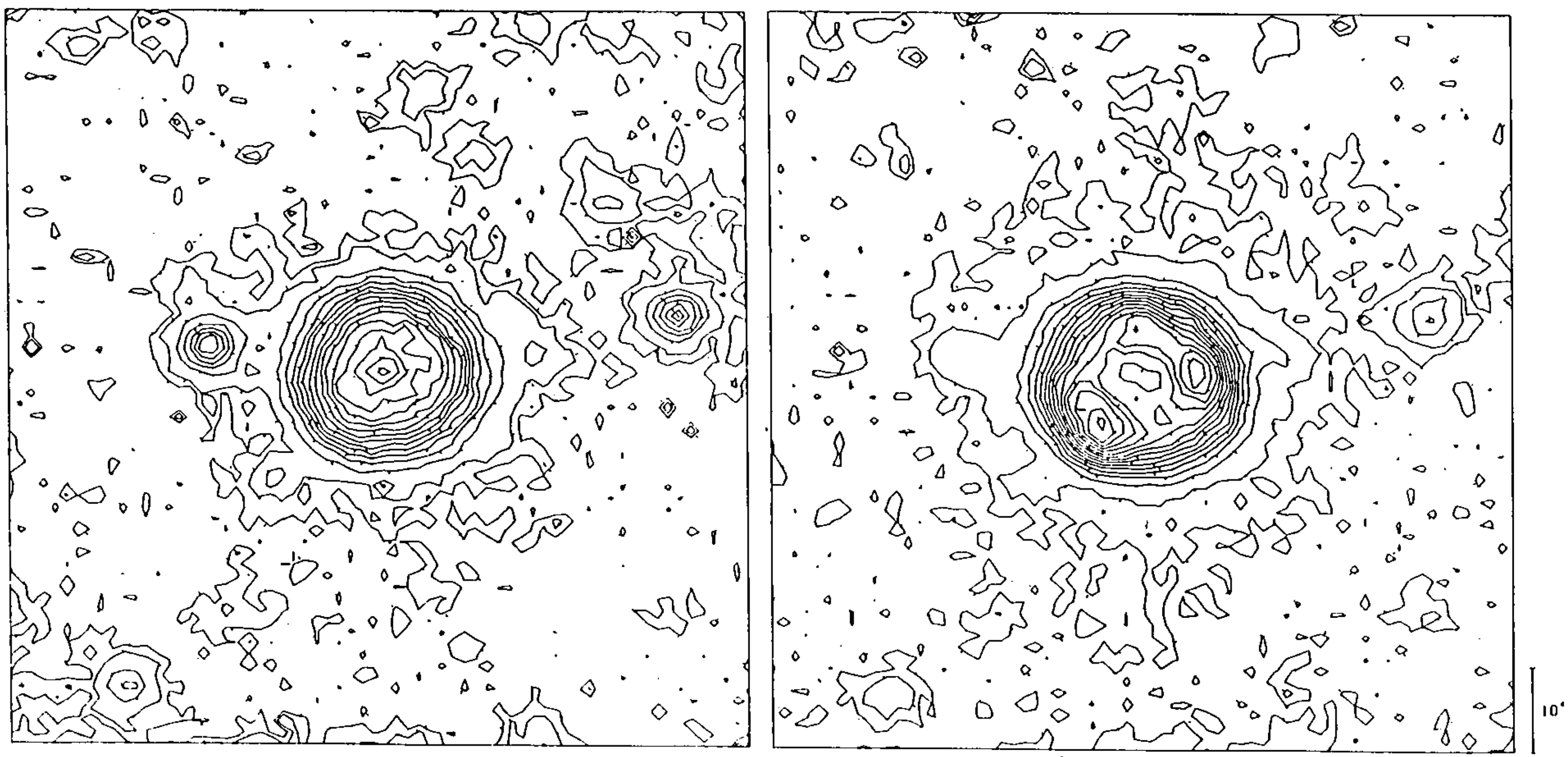

Figure 4.1(5a,b)

NGC 6778 15 MINS. 4959/5007 16/9/79

POS- 20 MIC STEP 17 MIC. 74 KOTT AS 18 GS

LINE: 1 TO: 100 COLUMN: 1 TO: 100 BLOCKING FACTOR: 3 DATA IS SMOOTHED

NGC 6778 50 MINS. 4861 16/9/79

POS- 20 MIC STEP 17 MIC. 74 KOTT AS 18 GS

LINE: 1 TO: 100 COLUMN: 1 TO: 100 BLOCKING FACTOR: 3 DATA IS SMOOTHED

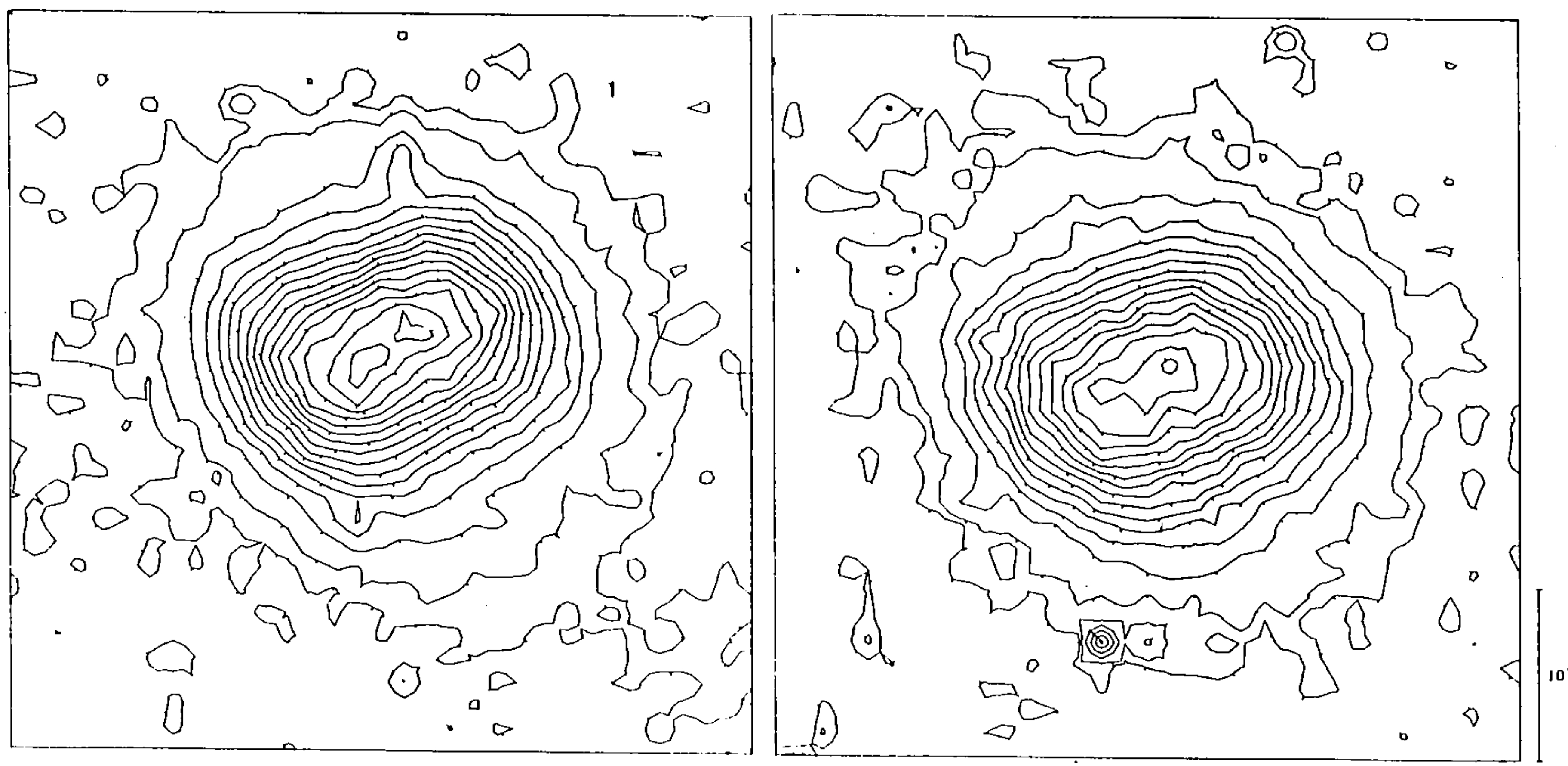

<u>Figure 4.1(6a,b)</u>

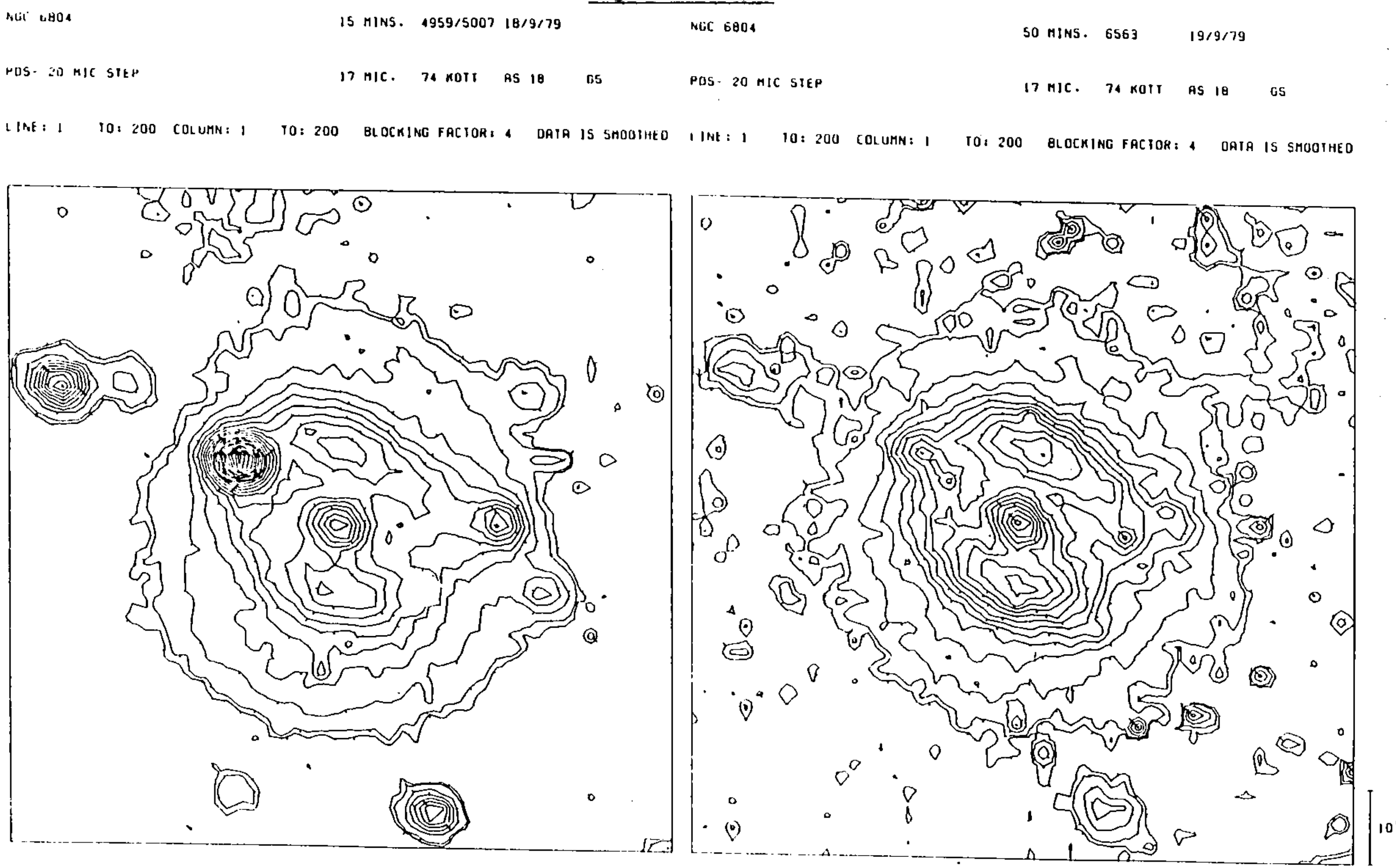

Figure 4.1(7a,b)

NGC 6818 | 1 MIN. 4959/5007 20/9/79
PDS- 20 MIC STEP | 17 MIC. 74 KOTT AS 18 GS
LINE: 1 TO: 100 COLUMN: 1 TO: 100 BLOCKING FACTOR: 2 DATA IS SMOOTHED

NGC 6818 | 10 MINS. 6563 20/9/79
PDS- 20 MIC STEP | 17 MIC. 74 KOTT AS 18 GS
LINE: 1 TO: 100 COLUMN: 1 TO: 100 BLOCKING FACTOR: 2 DATA IS SMOOTHED

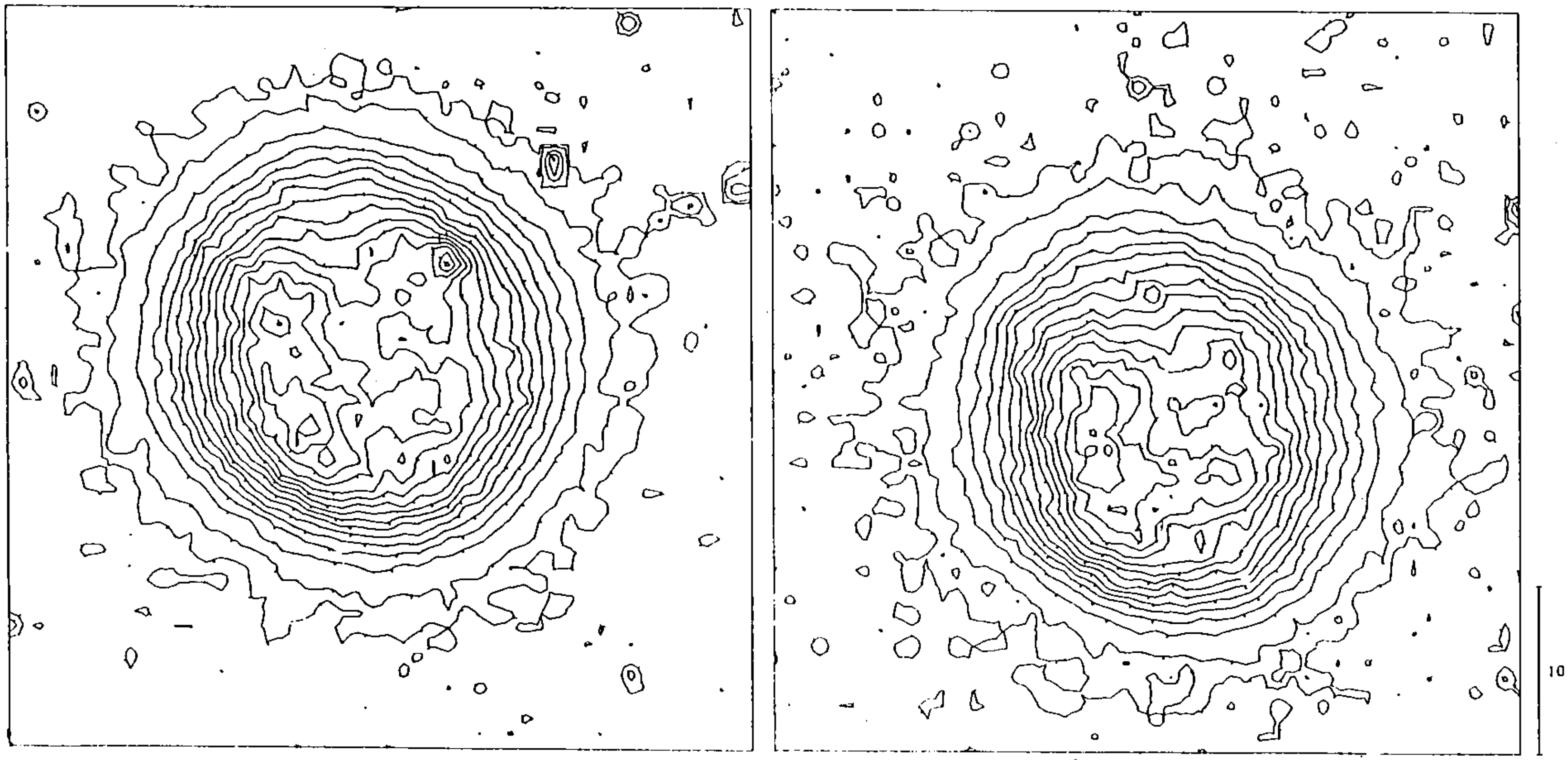

Figure 4.1(8,9)

NGC 6833   3 MINS.   4959/5007 26/9/79

POS- 20 MIC STEP   17 MIC.   74 KOTT   AS 18   GS

LINE: 1   TO: 50   COLUMN: 1   TO: 50   BLOCKING FACTOR: 2   DATA IS SMOOTHED

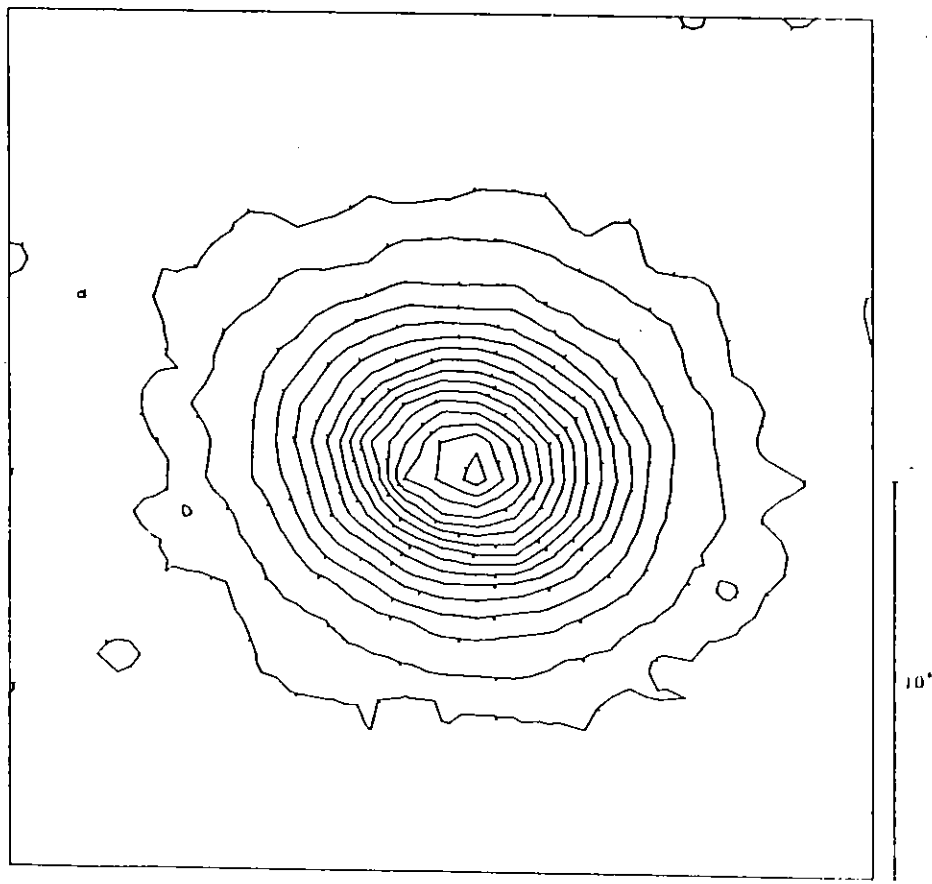

NGC 6842   15 MINS.   4959/5007 23/9/79

POS- 20 MIC STEP   17 MIC.   74 KOTT   AS 18   GS

LINE: 1   TO: 300   COLUMN: 1   TO: 300   BLOCKING FACTOR: 5   DATA IS SMOOTHED

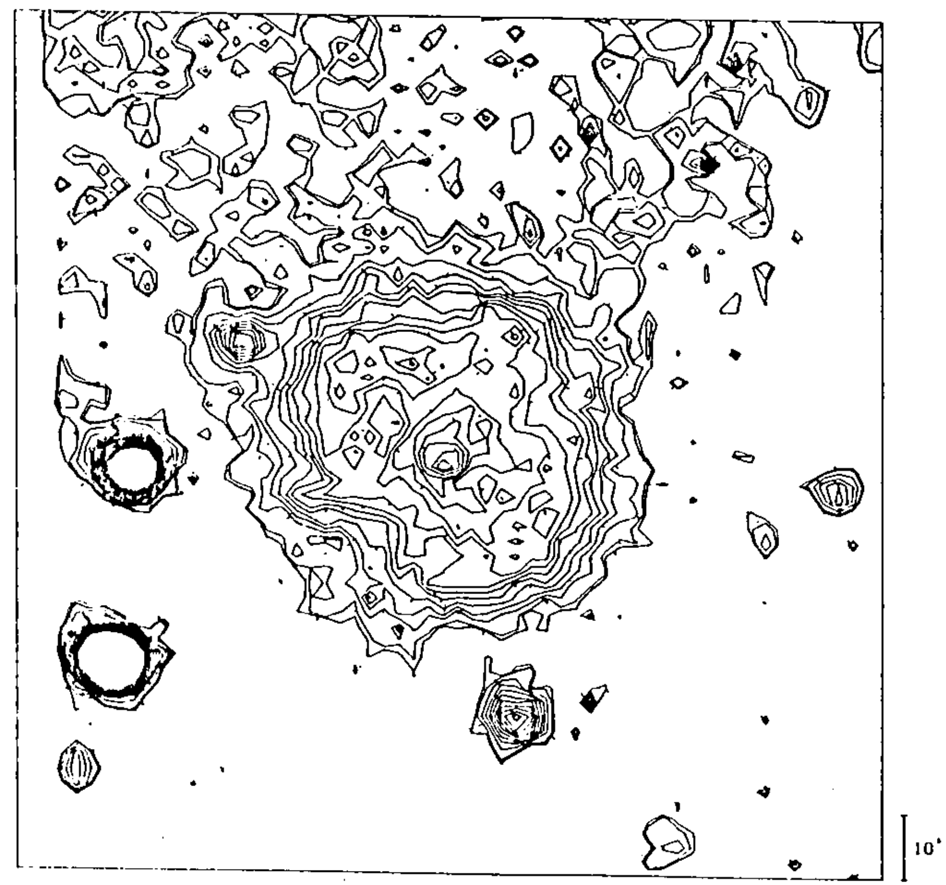

Figure 4.1(10a,b)

K 3-50/NGC 6857 10 MINS. 4959/5007 24/9/79

PDS- 20 MIC STEP 17 MIC. 74 KOTT AS 18 G5

LINE: 1 TO: 350 COLUMN: 1 TO: 300 BLOCKING FACTOR: 3

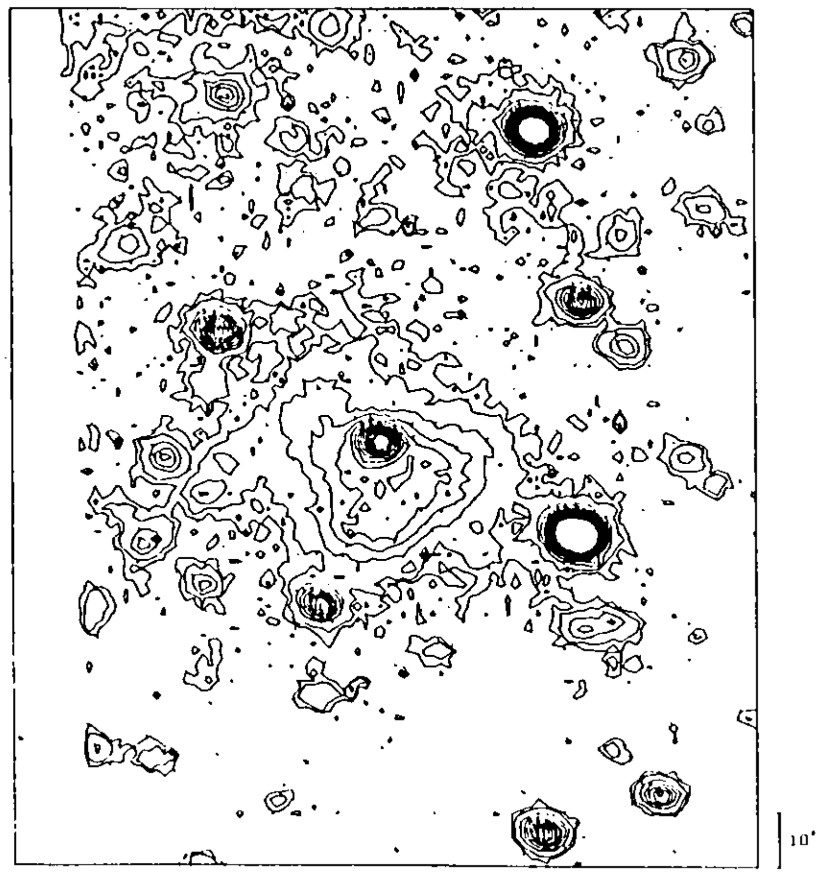

K 3-50/NGC 6857 60 MINS. 6563 24/7/79

PDS- 20 MIC STEP 17 MIC. 74 KOTT AS 18 G5

LINE: 1 TO: 350 COLUMN: 1 TO: 300 BLOCKING FACTOR: 3

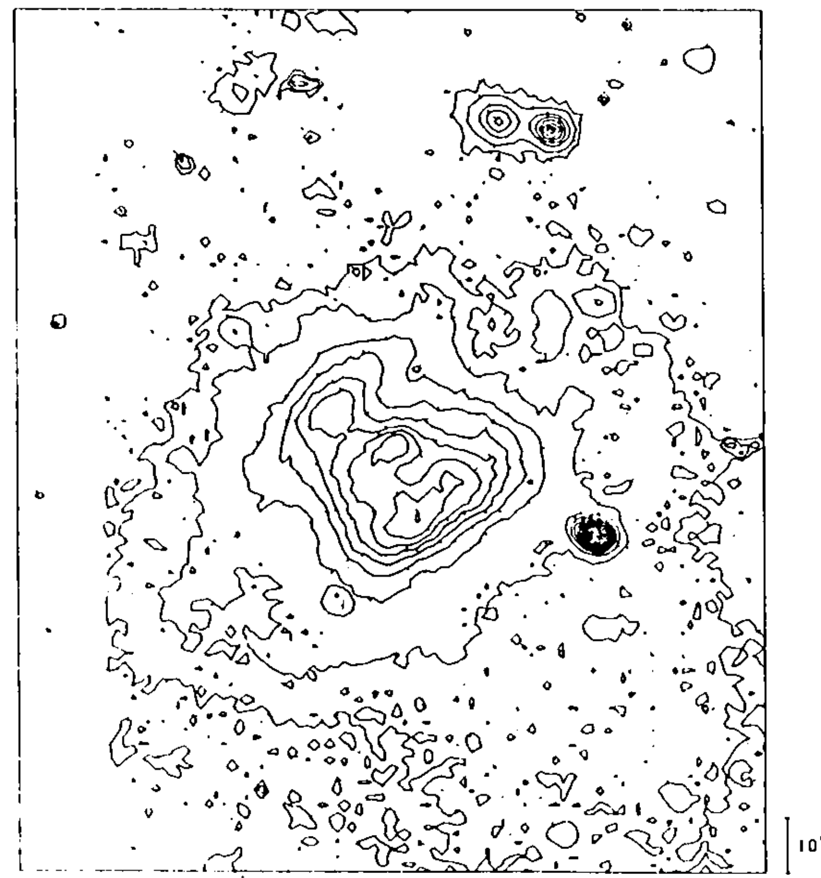

Figure 4.1(11a,b)

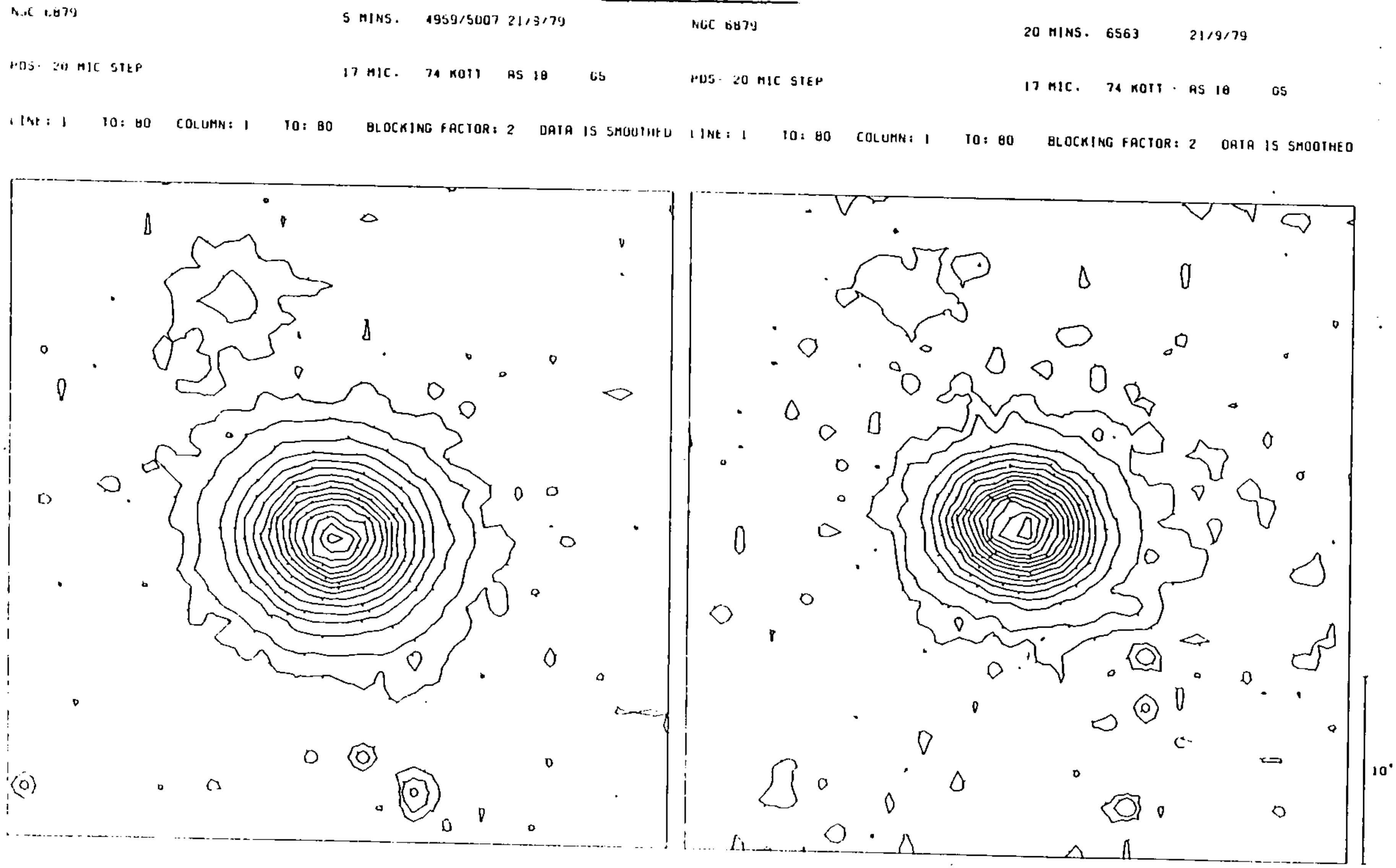

Figure 4.1(12a,b)

NGC 6884 | 1 MIN. 4959/5007 26/9/79
PDS- 20 MIC STEP | 17 MIC. 74 KOTT AS 18 G5
LINE: 1 TO: 50 COLUMN: 1 TO: 50 BLOCKING FACTOR: 2 DATA IS SMOOTHED

NGC 6884 | 10 MINS. 6563 26/9/79
PDS- 20 MIC STEP | 17 MIC. 74 KOTT AS 18 G5
LINE: 1 TO: 50 COLUMN: 1 TO: 50 BLOCKING FACTOR: 2 DATA IS SMOOTHED

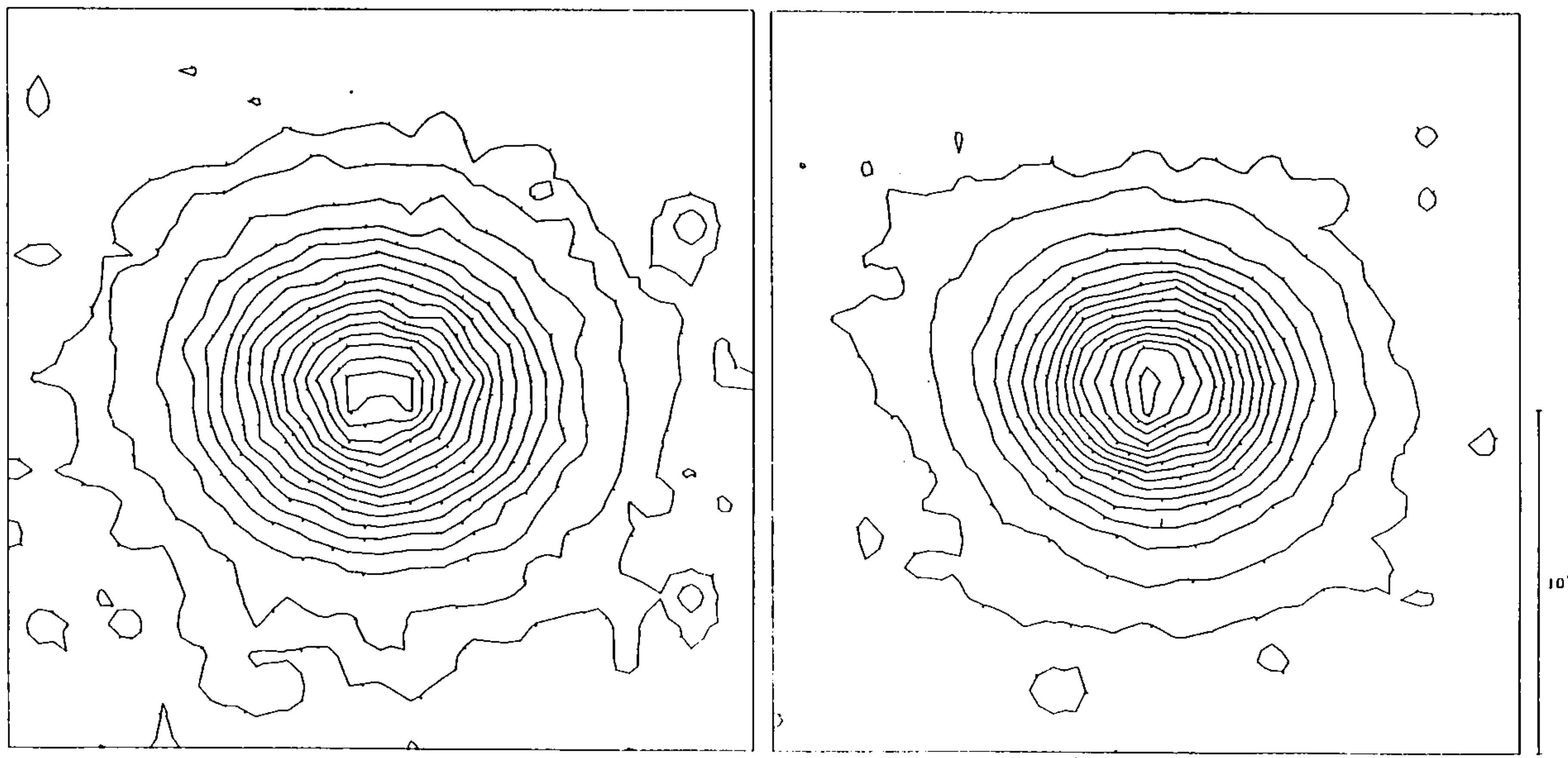

Figure 4.1(13a,b)

NGC 6886 5 MINS. 4959/5007 22/9/79

PDS- 20 MIC STEP 17 MIC. 74 KOTT AS 18 GS

LINE: 1 TO: 100 COLUMN: 1 TO: 100 BLOCKING FACTOR: 2 DATA IS SMOOTHED

NGC 6886 10 MINS. 6563 22/9/79

PDS- 20 MIC STEP 17 MIC. 74 KOTT AS 18 GS

LINE: 1 TO: 100 COLUMN: 1 TO: 100 BLOCKING FACTOR: 2 DATA IS SMOOTHED

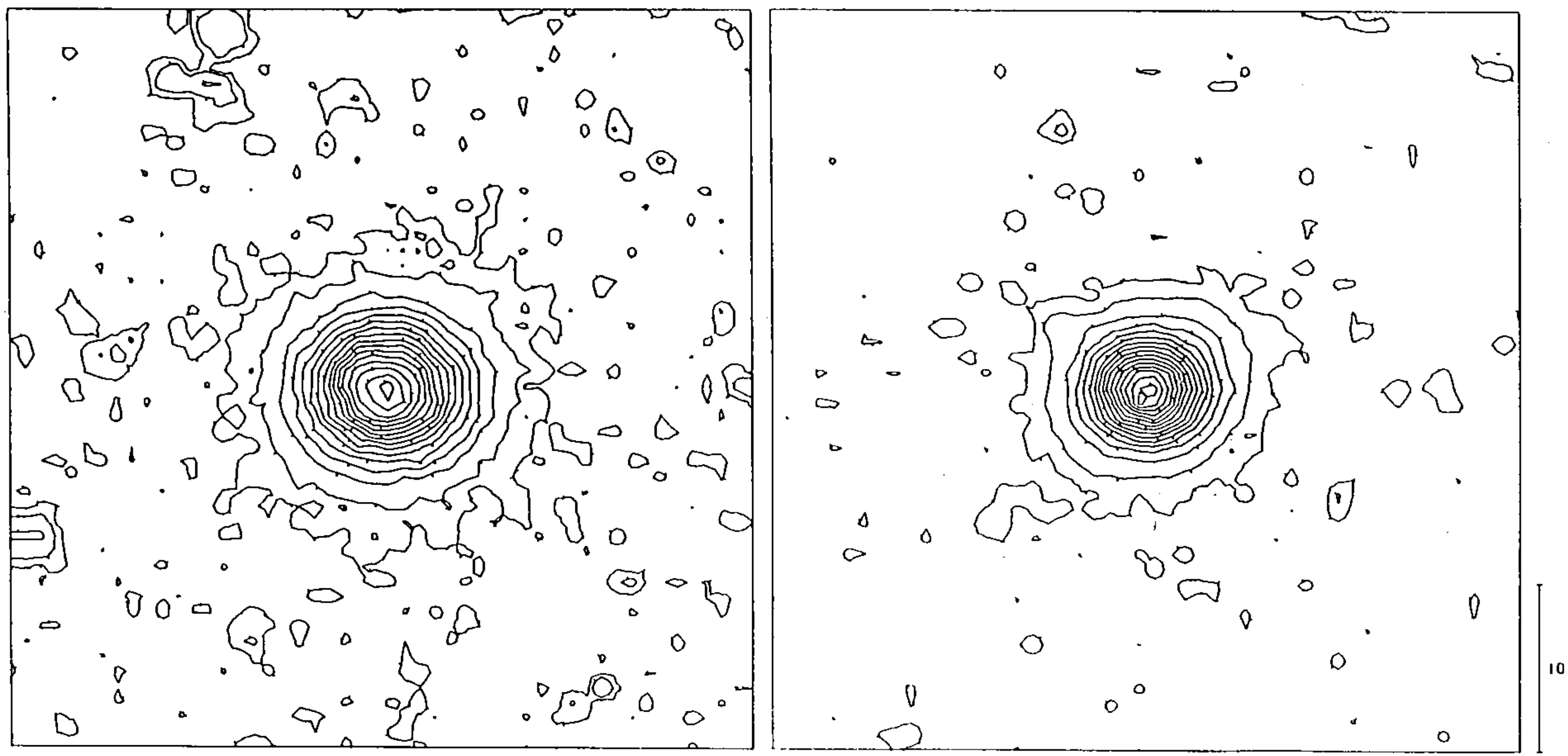

Figure 4.1(14a,b)

NGC 6891 1 MIN. 4959/5007 21/9/79

POS- 20 MIC STEP 17 MIC. 74 KOTT AS 18 GS

LINE: 1 TO: 100 COLUMN: 1 TO: 100 BLOCKING FACTOR: 2 DATA IS SMOOTHED

NGC 6891 10 MINS. 6563 21/9/79

POS- 20 MIC STEP 17 MIC. 74 KOTT AS 18 GS

LINE: 1 TO: 100 COLUMN: 1 TO: 100 BLOCKING FACTOR: 2 DATA IS SMOOTHED

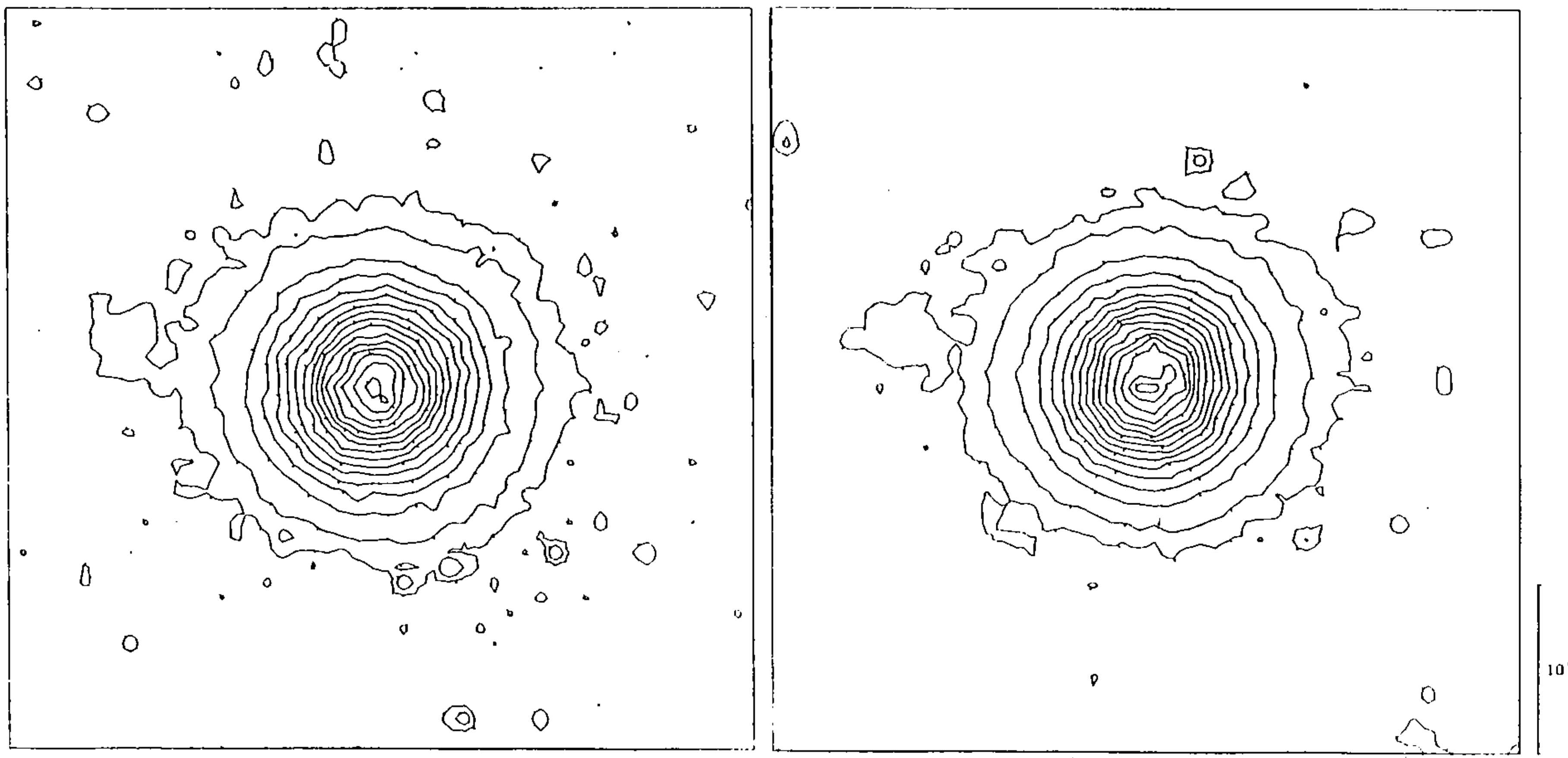

Figure 4.1(15a,b)

NGC 6894 5 MINS. 4959/5007 22/9/79

PDS- 20 MIC STEP 17 MIC. 74 KOTT AS 18 G5

LINE: 1 TO: 200 COLUMN: 1 TO: 200 BLOCKING FACTOR: 5 DATA IS SMOOTHED

NGC 6894 60 MINS. 6563 22/9/79

PDS- 20 MIC STEP 17 MIC. 74 KOTT AS 18 G5

LINE: 1 TO: 200 COLUMN: 1 TO: 200 BLOCKING FACTOR: 4 DATA IS SMOOTHED

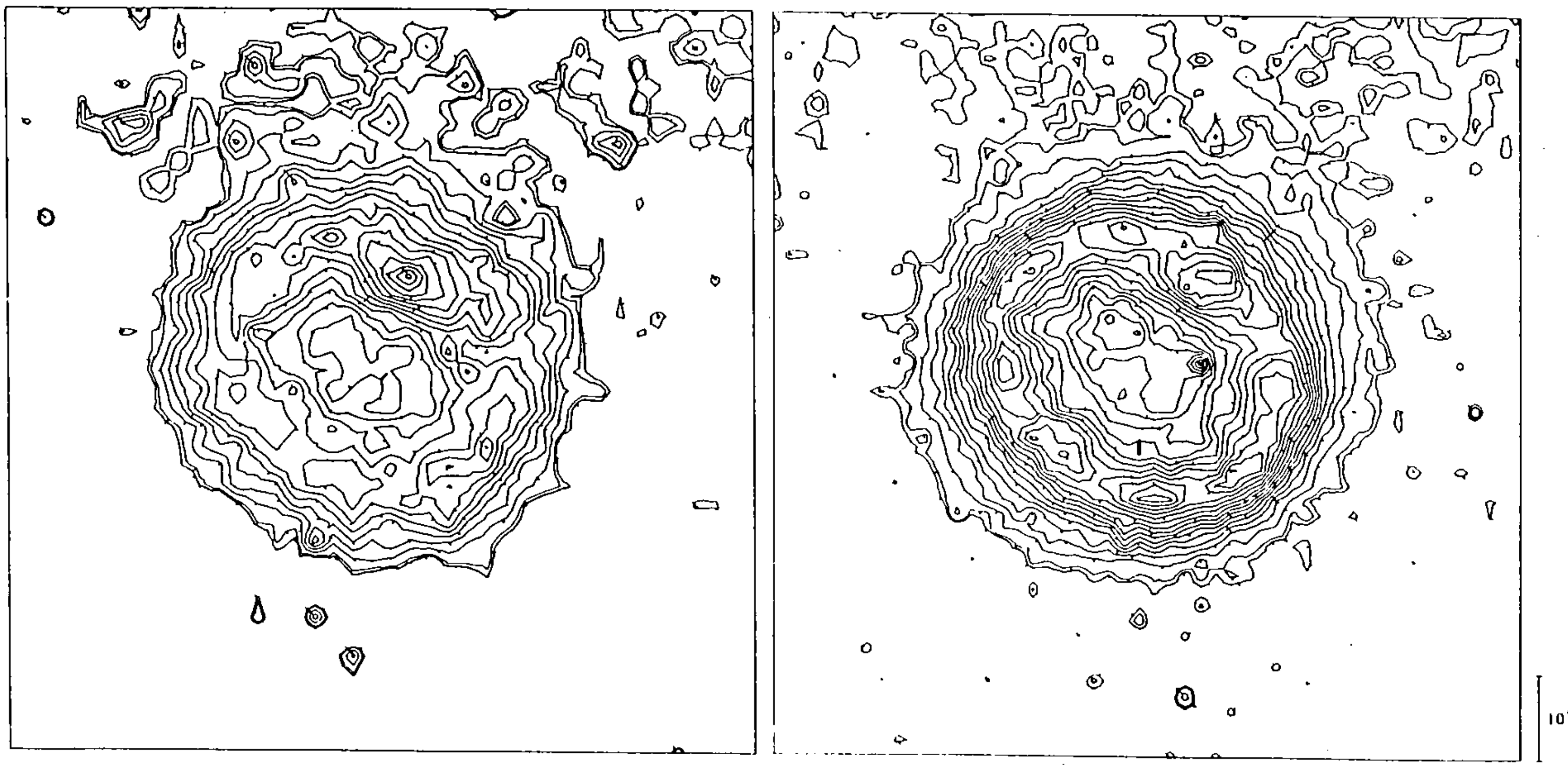

Figure 4.1(16a,b)

NGC 6905 15 MINS. 4959/5007 17/9/79 NGC 6905 60 MINS. 6563 18/9/79

POS- 20 MIC STEP 17 MIC. 74 KOTT AS 18 05 POS- 20 MIC STEP 17 MIC. KOTT 74 AS 18 05

LINE: 1 TO: 200 COLUMN: 1 TO: 200 BLOCKING FACTOR: 2 DATA IS SMOOTHED LINE: 1 TO: 200 COLUMN: 1 TO: 200 BLOCKING FACTOR: 3 DATA IS SMOOTHED

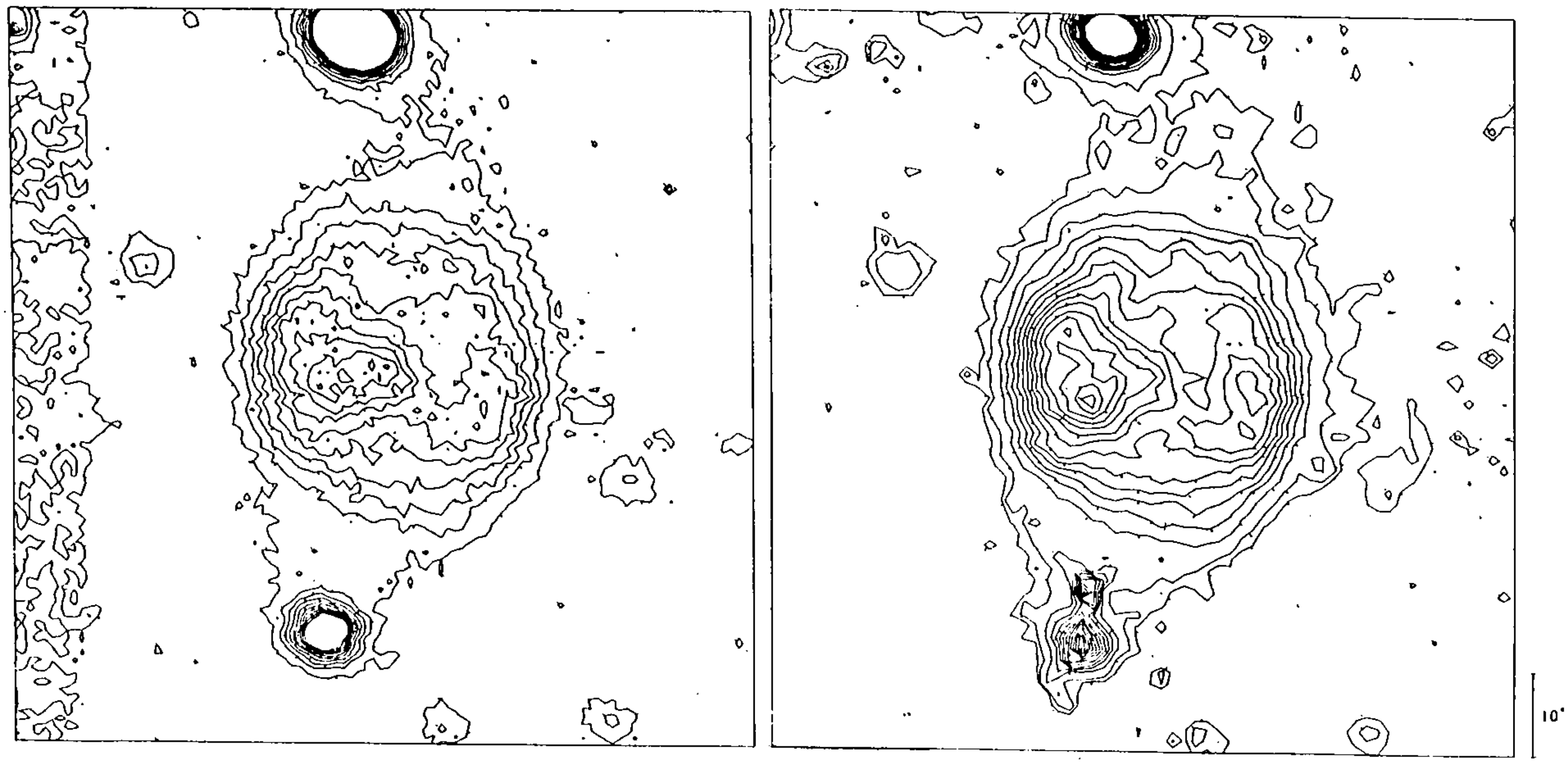

Figure 4.1(17)

NGC 7008 5 MINS. 4959/5007 27/9/79

POS- 20 MIC STEP 17 MIC. 74 KOTT AS 18 G6

LINE: 1 TO: 350 COLUMN: 1 TO: 250 BLOCKING FACTOR: 4 DATA IS SMOOTHED

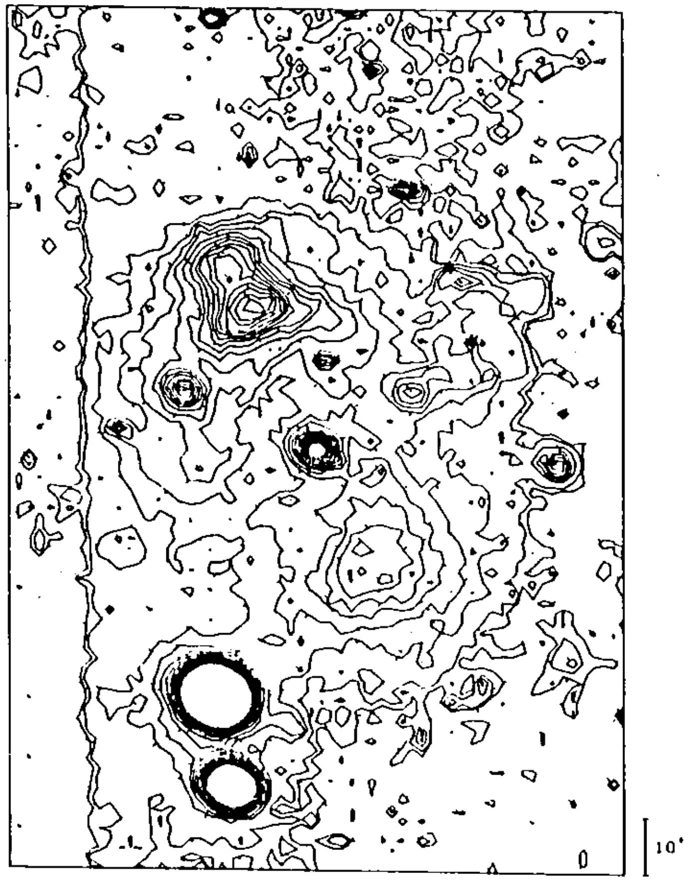

Figure 4.1(18a,b)

NGC 7026 3 MINS. 4959/5007 26/9/79

POS- 20 MIC STEP 17 MIC. 74 KOTT AS 18 GS

LINE: 1 TO: 100 COLUMN: 1 TO: 100 BLOCKING FACTOR: 2 DATA IS SMOOTHED

NGC 7026 10 MINS. 6563 26/9/79

POS- 20 MIC STEP 17 MIC. 74 KOTT AS 18 GS

LINE: 1 TO: 100 COLUMN: 1 TO: 100 BLOCKING FACTOR: 2 DATA IS SMOOTHED

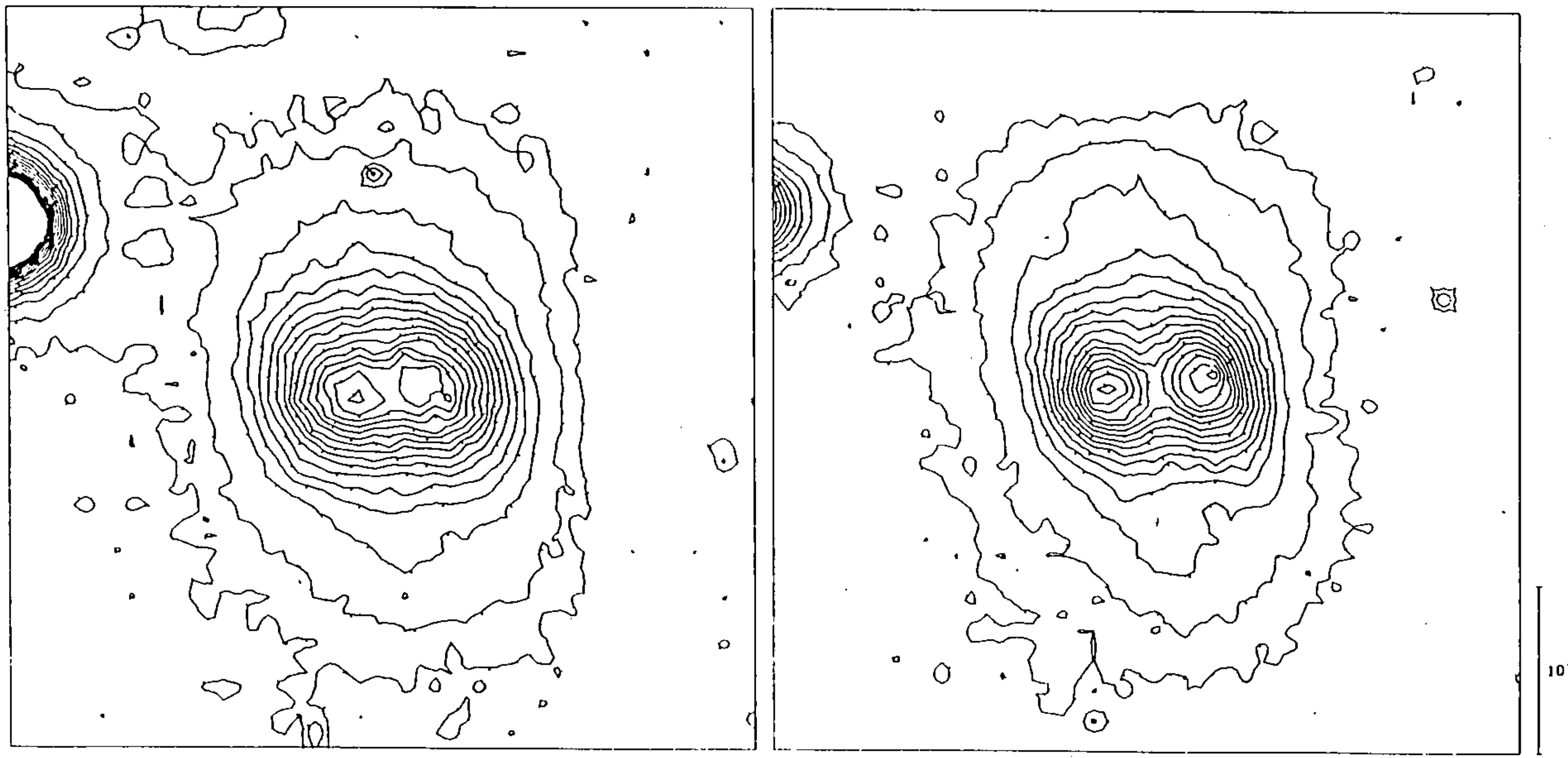

Figure 4.1(19a,b)

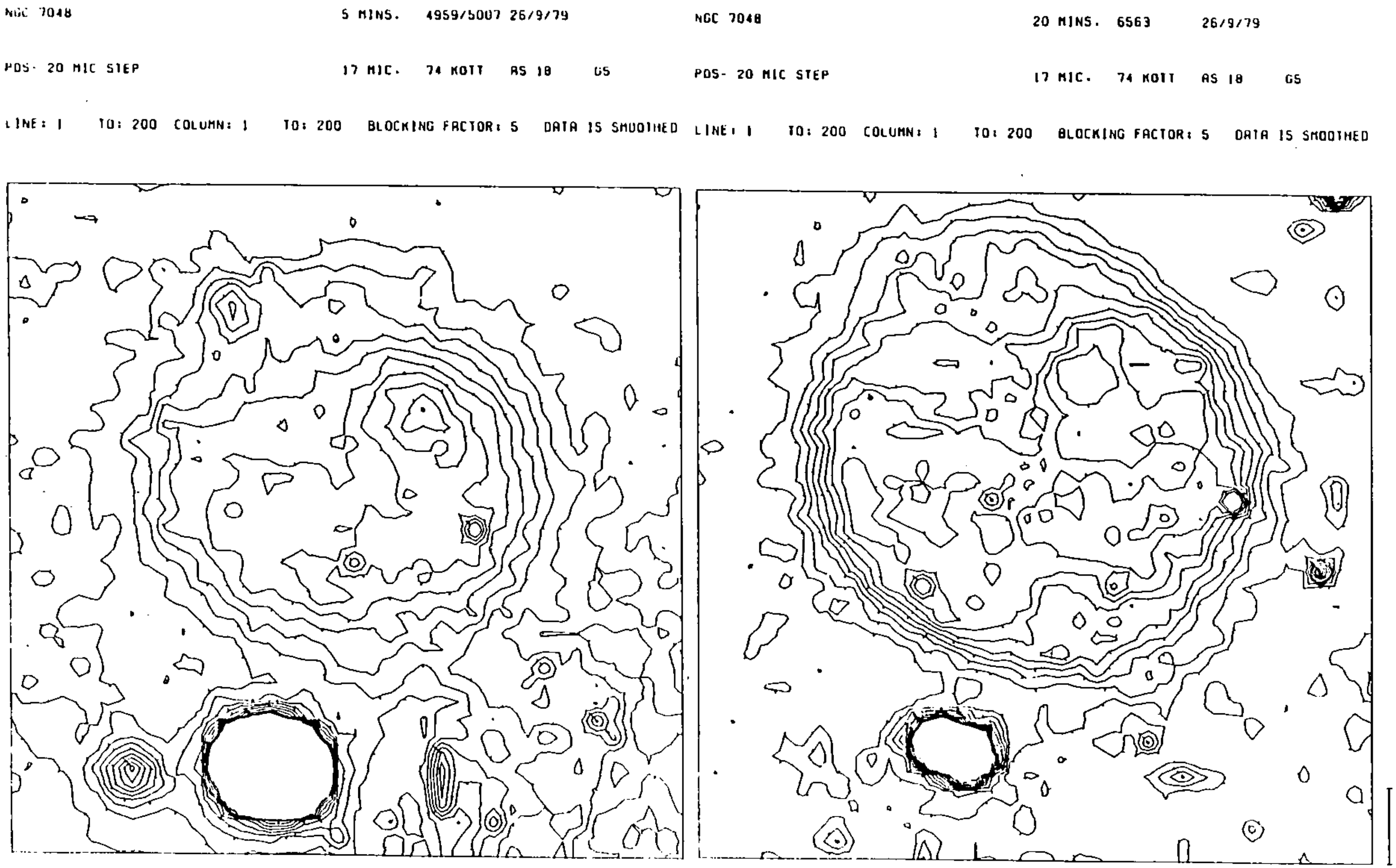

<u>Figure 4.1(20)</u>

IC 351 2 MINS. 4959/5007 19/9/79

POS- 20 MIC STEP 17 MIC. 74 KOTT AS 18 05

LINE: 1 TO: 100 COLUMN: 1 TO: 100 BLOCKING FACTOR: 2 DATA IS SMOOTHED

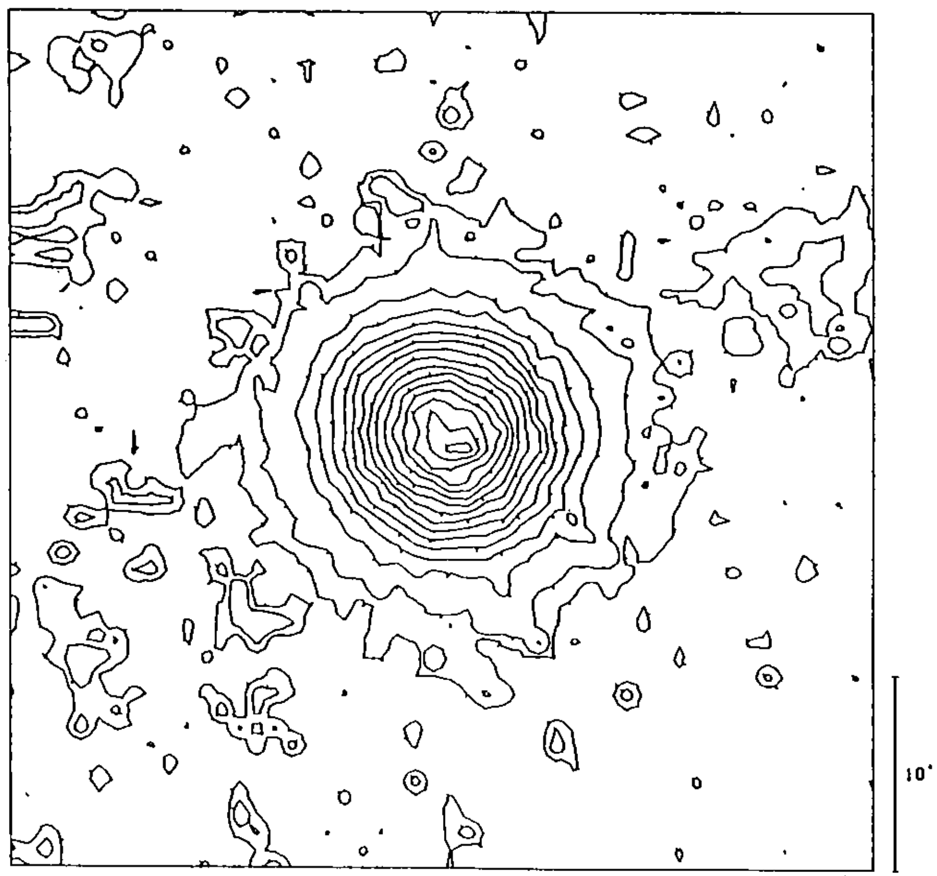

Figure 4.1(21a,b)

IC 2003 2 MINS. 4959/5007 15/9/79

POS- 20 MIC STEP 17 MIC. 74 KOTT AS 18 GS

LINE: 1 TO: 100 COLUMN: 1 TO: 100 BLOCKING FACTOR: 2 DATA IS SMOOTHED

IC 2003 10 MINS. 4861 15/9/79

POS- 20 MIC STEP 17 MIC. 74 KOTT AS 18 GS

LINE: 1 TO: 100 COLUMN: 1 TO: 100 BLOCKING FACTOR: 2 DATA IS SMOOTHED

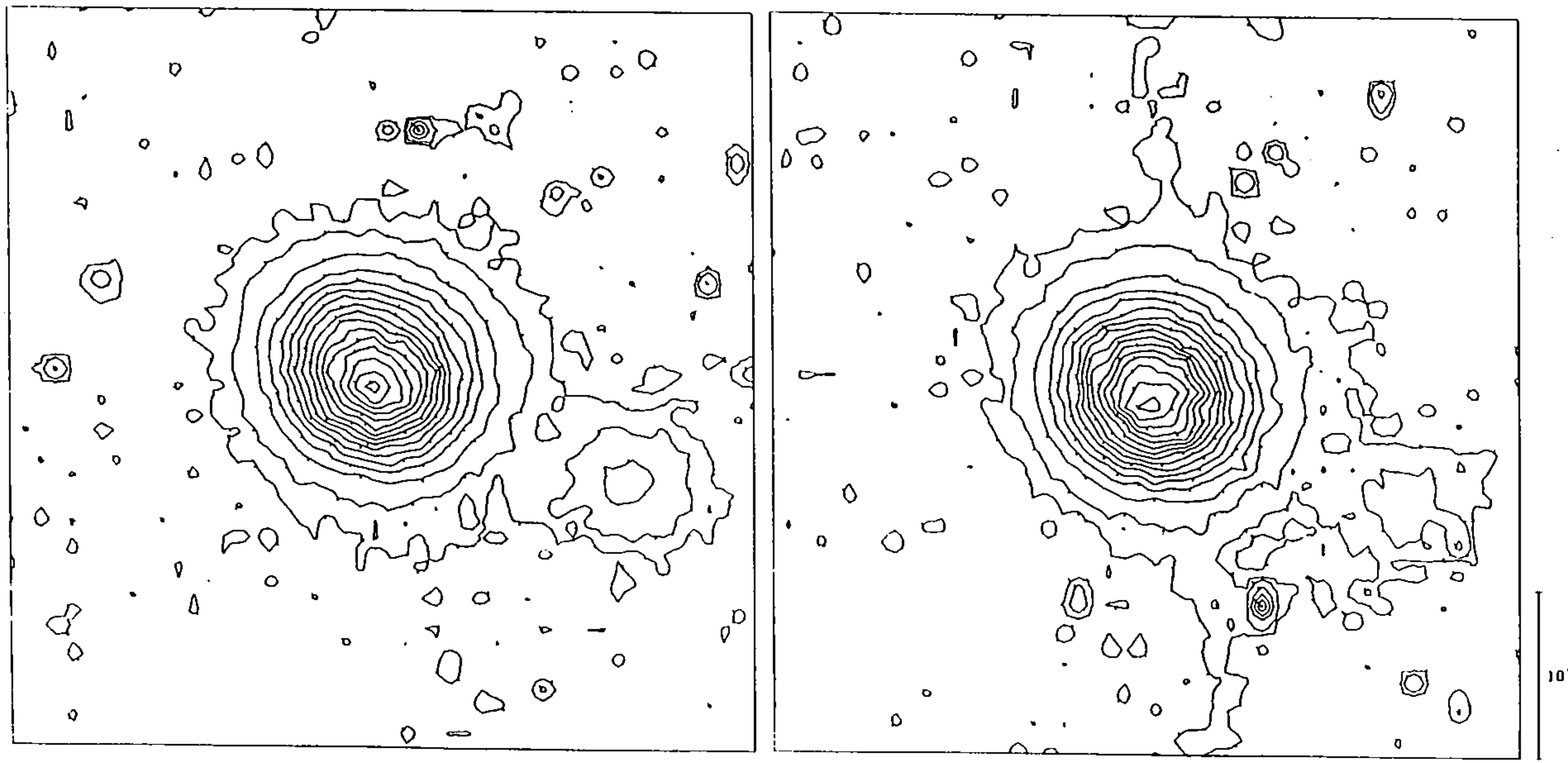

Figure 4.1(22,23)

IC 4846 5 MINS. 4959/5007 26/9/79

PDS- 20 MIC STEP 17 MIC. 74 KOTT AS 18 G5

LINE: 1 TO: 80 COLUMN: 1 TO: 80 BLOCKING FACTOR: 2 DATA IS SMOOTHED

IC 4997 1 MIN. 4959/5007 22/9/79

PDS- 20 MIC STEP 17 MIC. 74 KOTT AS 18 G5

LINE: 1 TO: 80 COLUMN: 1 TO: 80 BLOCKING FACTOR: 2 DATA IS SMOOTHED

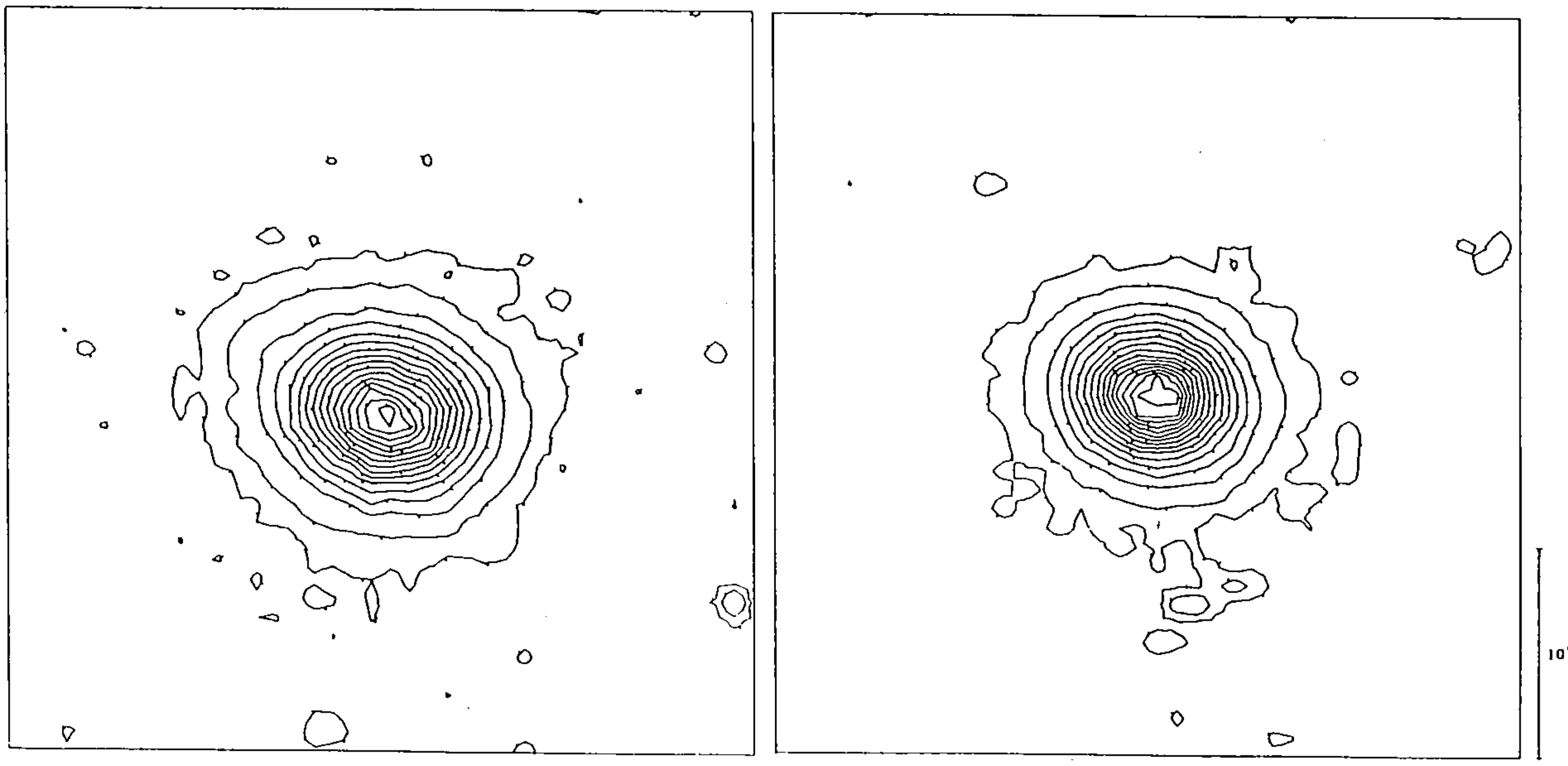

Figure 4.1(24a,b)

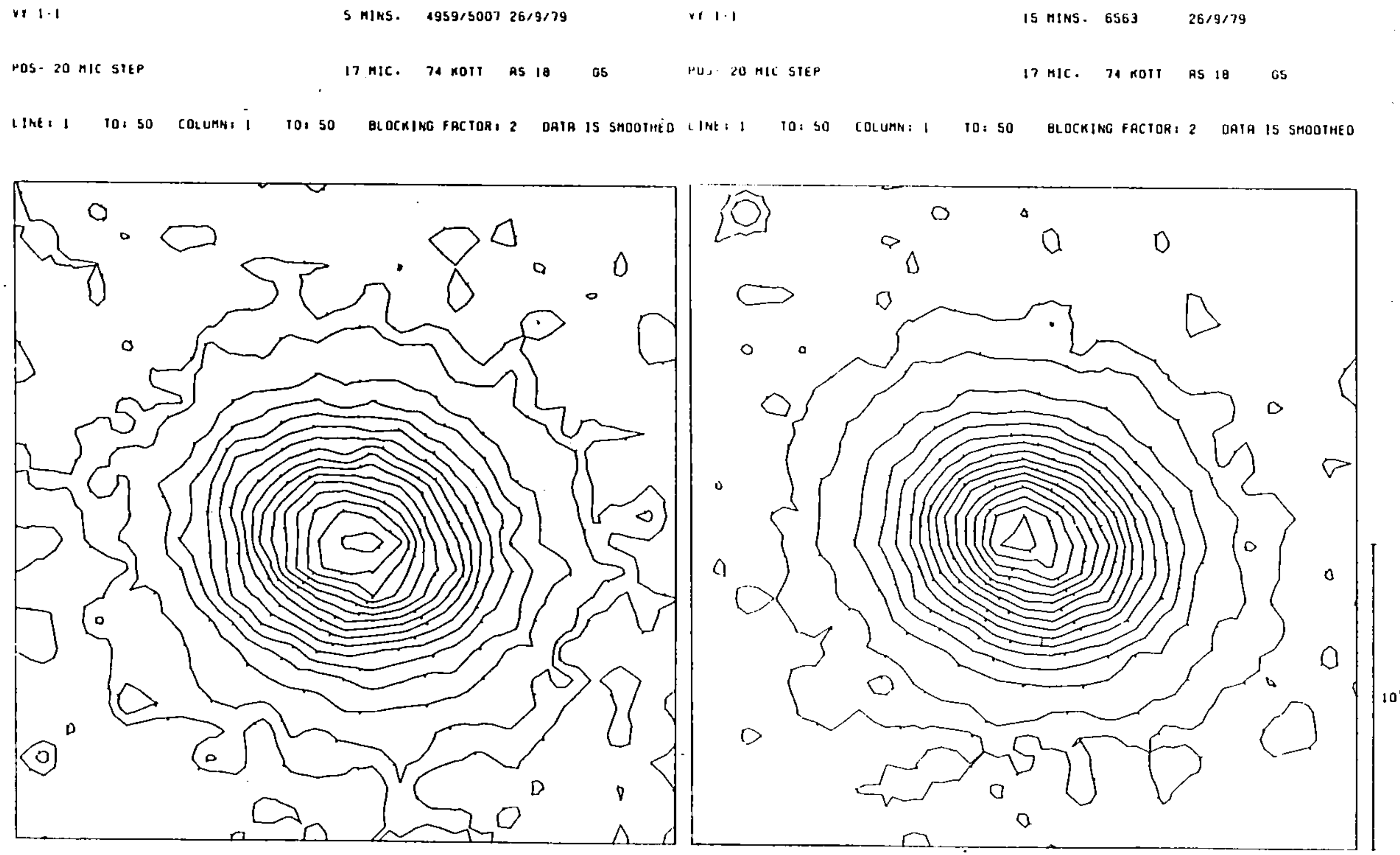

Figure 4.1(25a,b)

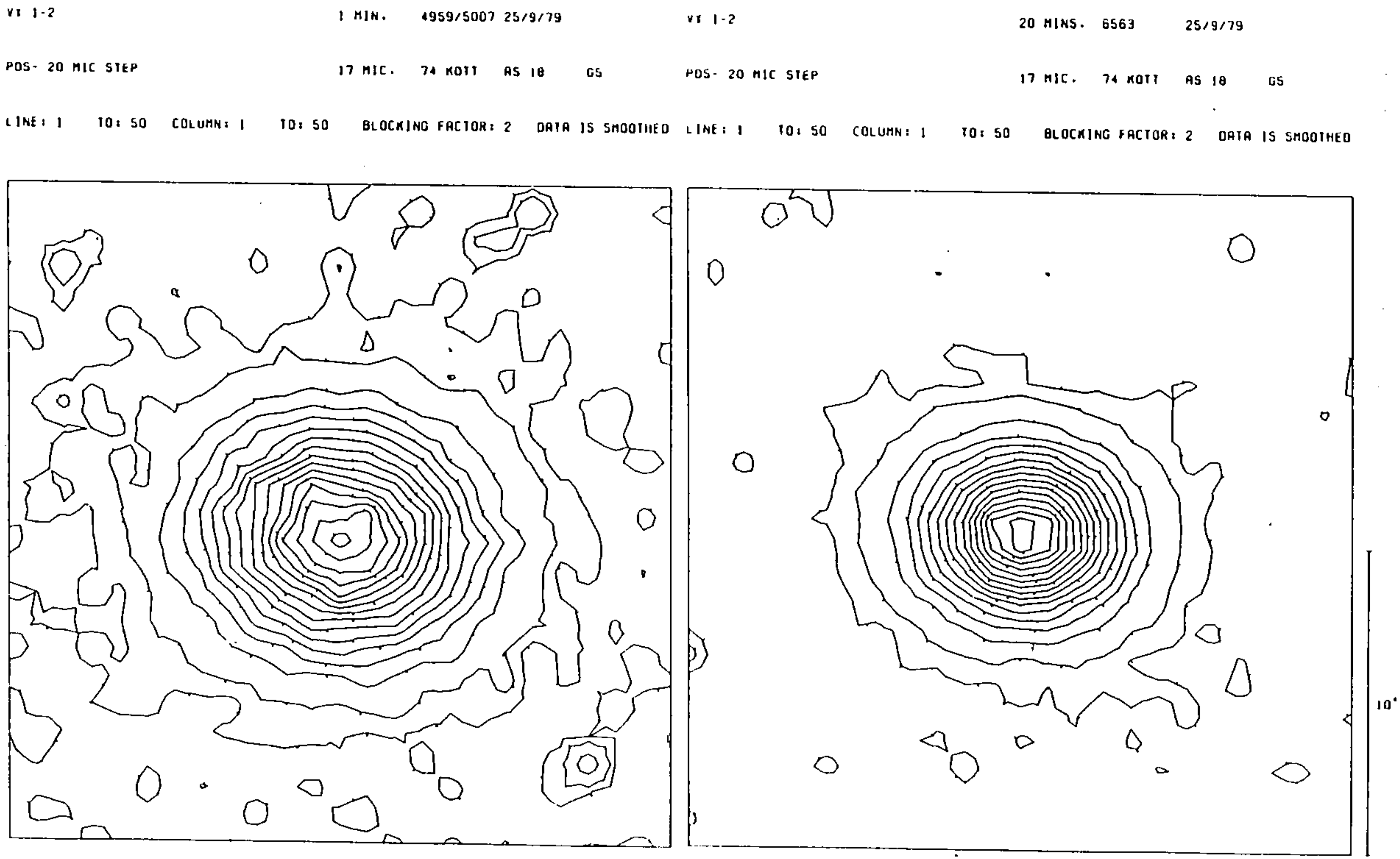

Figure 4.1(26)

VY 2-2 5 MINS. 4959/5007 25/9/79

POS- 20 MIC STEP 17 MIC. 74 KOTT AS 18 G5

LINE: 1 TO: 50 COLUMN: 1 TO: 50 BLOCKING FACTOR: 2 DATA IS SMOOTHED

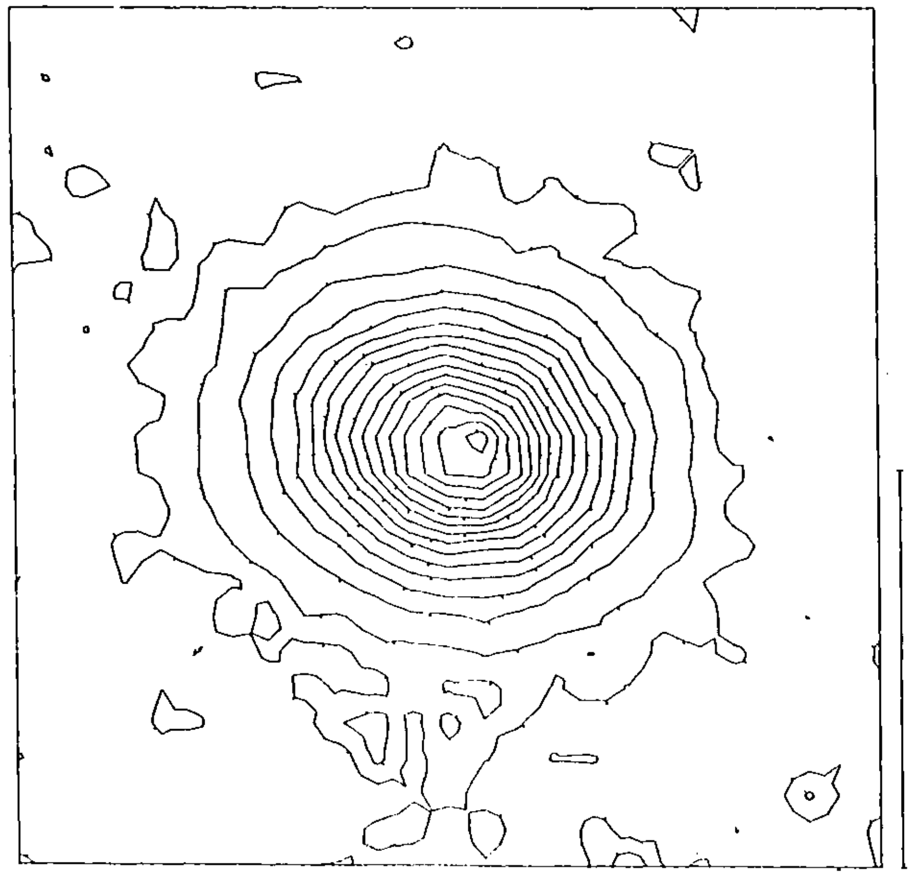

Chapter 5

5.1 Introduction

The purpose of this chapter is to use the published data listed in table 3.1 and the new results presented in chapter three to investigate the evolution and kinematical characteristics of Planetary Nebulae. This requires the comparison and matching of line profile data obtained with different instruments, in particular grating spectrographs and Fabry-Perot interferometers.

Information is present in the line profile of a nebula which can be used to investigate the velocity field within its' nebular shell (Beals 1931, Bappu and Menzel 1954). However, to look at the evolution of Planetary Nebulae as a whole one has to " smooth over " this detailed structure and generate a parameter which describes a mean velocity for an individual nebula.

Similarly, photographs and contour maps provide a wealth of detail about the complex nature of nebular forms. Again this information has to be " smoothed over " to yield a parameter which describes the linear size of a nebula. This involves a knowledge of the mean angular radius and distance of each nebula.

The following sections describe the method used in correlating data obtained with different instruments to produce the parameters introduced above,viz. the mean expansion velocities and radii. Finally, the relation between these parameters in terms of central star type, nebular morphological type and other functions is discussed.

5.2 The Interpretation of Line Profiles

A consequence of using Fabry-Perot interferometers in the observation of the line profiles from Planetary Nebulae is that the value of the observed line splitting is found to decrease as the entrance aperture increases. This effect is discussed by Bohuski and Smith (1974), who conclude that when the aperture subtends an angle greater than 25% of the mean nebular diameter the observed line splitting should be taken as a lower limit to the expansion velocity. Since a significant proportion of the new observations presented in chapter three were made with entrance apertures of the order of or greater than the nebular diameters we have attempted to estimate the true expansion velocity for each nebula using a simple model.

The model used is optically thin, has a radial emissivity variation proportional to $(\text{radius})^{-\alpha}$ and is bounded by two spherical surfaces of radii R and $R(1+\delta)$. To facilitate the analysis we have also adopted a proportional relation between the bulk velocity and radial distance at any point within the shell. This assumption is based on the conclusions of Weedman (1968).

Three cases are dealt with in the following sections :-

(i) Entrance aperture much less than the nebular diameter.
(ii) Entrance aperture greater than the nebular diameter.
(iii) Entrance aperture subtending a significant fraction of the nebular diameter.

5.2.1 Small Entrance Apertures

When the entrance aperture of diameter ϕ is less than about R/2 a particularly simple expression for the line splitting results from the model. In the limit of an infinitely small aperture, compared with the nebular diameter, the observed line splitting ΔV may be defined as the difference between the centre of gravities of the red and blue components of the line profile. For $\delta<0.25$ this expression is (to first order) :-

$$V(\phi = 0) = 2\ V_R(1 + \delta/2)$$

where V_R is the bulk velocity (in $Km.s^{-1}$) at radius R.

The next step involves looking at the effect of finite aperture diameters on ΔV. This was performed for values of α = 0, 0.5, 1, 1.5, 2, 3 and 4. These values of α result in algebraic expressions for $\Delta V(\phi)$, which when written as first order equations in the shell thickness δ assume the same format :-

$$\Delta V(\phi) = 2\ V_R(1 + \delta/2)\left(1 - \frac{(1-\delta)}{4}\left(\frac{\phi}{2R}\right)^2\right) \qquad (5.1)$$

The independence of $\Delta V(\phi)$ on the particular value of α suggests, to this degree of approximation, that it is insensitive to the exact nature of the emissivity distribution through the shell.

For a typical value for δ of 0.2 the error in measurement of line splitting due to the use of an entrance aperture subtending 25% of the mean nebular diameter is approximately 3%, which agrees with the result found by Bohuski and Smith mentioned earlier.

5.2.2 Integrating Apertures

When the entrance aperture is larger than the nebula line splitting is generally not observed, and so one has to define the mean expansion velocity otherwise. The simple analytical model was used to derive algebraic expressions for the line profiles for various values of α. As in the preceeding section these equations, when written as third order equations in δ, resulted in the same expression for the full-width at half-maximum :-

$$W_\infty = 2\ V_R(1 + \delta/2 + (1-\alpha)\delta^2/8) \qquad (5.2)$$

which is valid for δ 0.25 and $\alpha>0$.

The corresponding expression for the peak splitting using an infinitely small aperture is :-

$$W_o = 2\ V_R(1 + \delta/2 - \alpha\delta^2/12) \qquad (5.3)$$

To first order in δ or when $\alpha \sim 3$ equations 5.2 and 5.3 are the same. Hence we arrive at the interesting conclusion that the line splitting observed in an object using a small aperture is approximately the same as the full-width at half-maximum of its' integrated intrinsic profile.

The effects of instrumental and thermal broadening will, to the degree of approximation involved, only apply to the intrinsic profile. To find the intrinsic profile width we assume that it is approximately Gaussian in form, hence :-

$$W^2(\text{obs}) = W_\infty^2 + W^2(\text{Dopp}) + W^2(\text{inst}) \qquad (5.4)$$

At typical nebular temperatures of 10^4 K the thermal Doppler width W(Dopp) $\sim$ 5.4 $Km.s^{-1}$ for the [OIII] lines. The instrumental profile of a Fabry-Perot interferometer is an Airy function, which for our purposes is well represented by a Gaussian of full-width at half-maximum W(inst) = 3 $Km.s^{-1}$. Broadening is therefore only significant in the observed line profiles when their full-width at half-maxima exceed about 15 $Km.s^{-1}$.

5.2.3 Intermediate Apertures

When the entrance aperture does not encompass the nebula but does subtend greater than 25% of its diameter we have to resort to the use of computer generated line profiles, again using the simple model. Figure 5.1 is an example of a set of such computed line profiles, which were calculated for the following aperture sizes :-

a) 1.2R b) 0.75R c) 0.5R d) 0.25R and e) effectively 0.0R

The values for α and δ were 4.0 and 0.2 respectively, and the profiles were broadened with a temperature corresponding to a Doppler velocity of $\frac{1}{2}$ V_R.

An interesting point to note is that these calculated profiles show the approximate equality indicated in the last section between the totally resolved profile splitting and the integrated profile full-width at half-maximum.

Figure 5.1

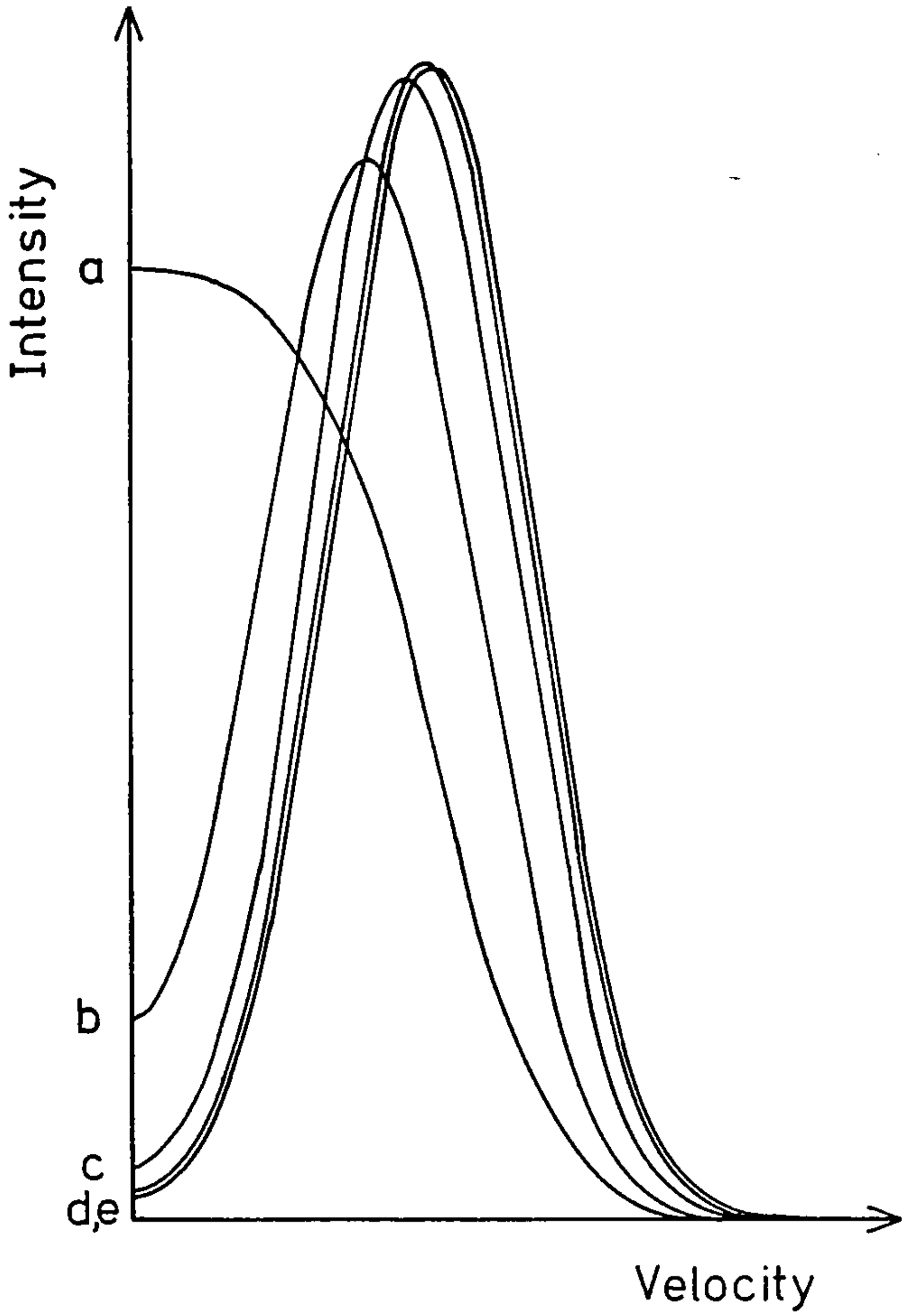

Line profiles from the simple model. See text for details.

5.3 Application of the Model to NGC 1535

The result of applying the simple model to real nebulae is illustrated in figure 5.2 which shows the [OIII] λ5007Å line splittings and full-width at half-maxima observed in NGC 1535 using the new data and published data. The 18 arcsec. aperture observation made in Tenerife is not reported here. A triangle marks the line splitting measured by Wilson (1950), where we have assumed an effective entrance aperture for his slit spectrograph of 2 arcsec. Points above 40 $Km.s^{-1}$ show the peak splittings from the new data and that of Johnson (1976), whilst the lower points show the full-widths at half-maxima from the latter two sets of data - regardless of whether line splitting is present or not.

The line in figure 5.2 corresponds to equation 5.1, in which the parameters R and are measured as 5.5 arcsec. and 0.25 respectively from the electronographic data presented in chapter four.

With the exception of the new 5 arcsec. aperture result the line splittings in figure 5.2 follow the parabolic fall-off with increasing aperture size indicated by equation 5.1. Johnson measures the full-width at half-maximum of his 60 arcsec. result as 43 $Km.s^{-1}$. With a thermal Doppler width of 5.4 $Km.s^{-1}$ and his instrumental width of 13 $Km.s^{-1}$ equation 5.4 implies that the full-width at half-maximum of the intrinsic profile is approximately 40.6 $Km.s^{-1}$. This figure is in excellent agreement with the value of 40.3 $Km.s^{-1}$ predicted by extrapolation to an infinitely small aperture of the peak splitting measurements, and supports our use of the simple model in the interpretation of line profiles.

As Planetary Nebulae do not in general admit to being representable by spherically symmetric models a rough investigation using prolate spheroidal models was also undertaken. The model adopted in this study was an infinitely thin-shelled prolate spheroid of axial ratios : e:e:p, where p > e. Again assuming a proportional velocity - radius relation one finds that the observed line splitting using an infinitely small aperture varies as :-

$$\Delta V \sim \Delta V_p (1 - \varepsilon \cos^2\theta)^{\frac{1}{2}}$$

and the mean nebular radius R varies as :-

$$R \sim e(1 - \varepsilon \sin^2\theta)^{\frac{1}{4}}$$

Figure 5.2

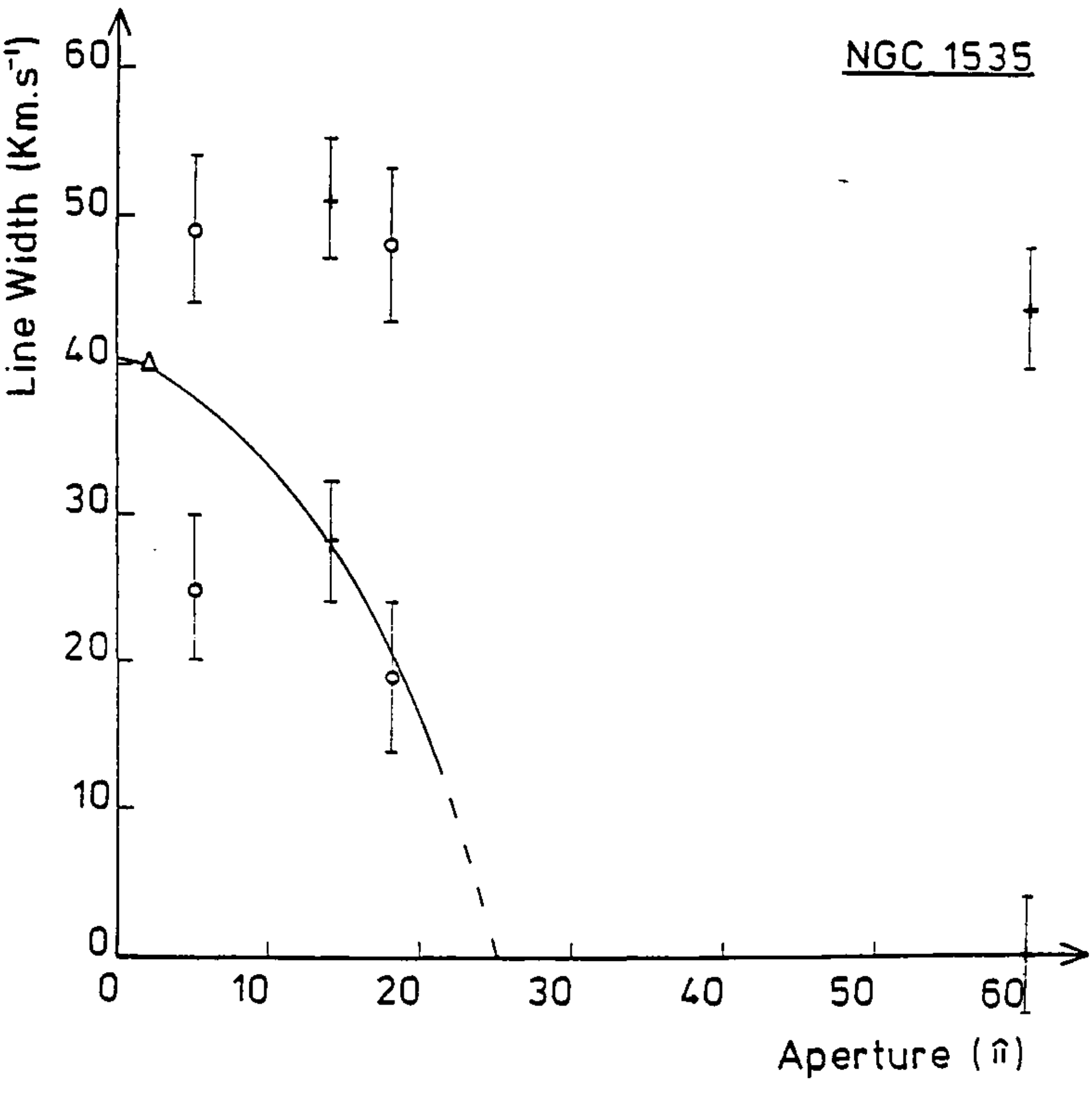

Measured line splitting and widths in NGC 1535.

Key :

Triangle – Wilson (1950)

Crosses – Johnson (1976)

Circles – New data

See text for further explanation.

In both of these expressions θ is the angle between the major axis and the sky, ΔV_p is the peak splitting which would be observed if the major axis of the prolate spheroid were to be aligned along the line of sight and ε is defined as :-

$$\varepsilon = 1 - e^2/_{p^2}$$

Owing to the complex and diverse forms of Planetary Nebulae a more detailed study of the effects of non-spherical geometry on line profiles was not carried out. Instead, only the simpler spherically symmetric model was used to deduce true expansion velocities from the Fabry-Perot data. However, the effect of non-spherical geometry will lead to a statistical spread in the values of the observed expansion velocities and mean radii, and this effect is discussed in the next section. Although one might expect that nebular orientation will change the magnitudes of W_o and W_∞ , their approximate equality as expressed by the similarity of equations 5.2 and 5.3 will still hold.

5.4 Application of the Model to Other Nebulae

The results of applying the simple model described in section 5.3 to other nebulae are presented in two tables: Table 5.1 covers the nebular observations presented in chapter three, whilst table 5.2 lists the nebulae with previously published expansion velocities (from table 3.1). Linear radii are derived from the distances of Acker (1978) and angular diameters from Perek and Kohoutek (1967). The expansion velocities in both tables are preferentially taken from slit spectrographic data as these are less susceptible to the broadening effects of large entrance apertures.

Table 5.1

Name	P-K Number	V_{exp} (Model) (Km.s^{-1})	V_{exp} (Km.s^{-1})	R_{lin} (parsecs)
NGC 1535	206-40°1	13 ± 6	20	.069
6439	11+5°1	24 ± 2	24	.073
6572	34+11°1	16 ± 2	16	.018
6741	33-2°1	23 ± 2	21	.023
6751	29-5°1	24 ± 2	43	.097
6778	34-6°1	23 ± 2	23	.089
6781	41-2°1	12 ± 2	12	.211
6818	25-17°1	25 ± 5	28	.066
6833	82+11°1	14 ± 2	14	.008
6857	70+1°2	8 ± 3	8	
6879	57-8°1	23 ± 2	23	.062
6881	74+2°1	18 ± 2	18	.035
6891	54-12°1	7 ± 2	7	.074
7008	93+5°2	11 ± 2	11	.163
7027	84-3°1	12 ± 7	20	.031
7048	88-1°1	11 ± 3	11	.186
7354	107+2°1	26 ± 3	26	.077
IC 289	138+2°1	22 ± 3	22	.102
351	159-15°1	20 ± 2	15	.066
1747	130+1°1	30 ± 2	33	.066
2003	161-14°1	24 ± 2	24	.070
4997	58-10°1	15 ± 2	15	.006
5117	89-5°1	18 ± 2	18	.011
5217	100-5°1	21 ± 2	21	.039
Hb 4	3+2°1	23 ± 2	23	.022
6	7+1°1	20 ± 2	20	.017
12	111-2°1	16 ± 2	16	.056
Hu 1-1	119-6°1	15 ± 2	15	.057
2-1	51+9°1	10 ± 2	10	.018
K 3-62	95+0°1	16 ± 2	16	
M 1-2	133-8°1	16 ± 2	16	.005
1-4	147-2°1	17 ± 2	17	.026
Vy 1-1	118-8°1	10 ± 2	10	
1-2	53+24°1	16 ± 2	16	.063
2-3	107-13°1	16 ± 2	16	.079

Predicted expansion velocities, adopted expansion velocities and linear radii of those nebulae which have new observations presented in chapter three.

Table 5.2

Name	P-K Number	V_{exp} ($Km.s^{-1}$)	R_{lin} (parsecs)	Notes
NGC 40	120+9°1	29	.081	1
246	118-74°1	38	.201	2
1360	220-53°1	28	.242	2
1501	144+6°1	39	.144	2, 3
2022	196-10°1	29	.092	1
2392	197+17°1	54	.034	
2440	234+2°1	22	.038	
2899	277-3°1	>15	.256	2, 4
3242	261+32°1	20	.039	1
3587	148+57°1	44	.213	1, 5
3699	292+1°1	29	.227	2, 4
4071	298-4°1	19	.242	2, 4
4361	294+43°1	38	.085	2, 4
5189	307-3°1	36	.288	2, 4
6210	43+37°1	21	.036	
6302	349+1°1	10		4, 6
6309	9+14°1	35	.101	1
6445	8+3°1	38	.109	1
6543	96+29°1	20	.030	7
6563	358-7°1	<11	.130	2, 4
6567	11-0°2	18	.026	
6720	63+13°1	30	.096	1
6803	46-4°1	15	.022	
6826	83+12°1	8	.063	8
6853	60-3°1	15	.222	
6884	82+7°1	23	.052	
6886	60-7°2	16	.038	
6905	61-9°1	48	.124	1
7009	37-34°1	21	.056	
7026	89+0°1	42	.069	9
7293	36-57°1	14	.216	2, 4
7662	106-17°1	26	.034	
IC 418	215-24°1	<12	.010	
972	326+42°1	16	.228	2, 4
2149	166+10°1	21	.020	1
2165	221-12°1	20	.045	
3568	123+34°1	8	.031	10
4406	319+15°1	<6	.102	2, 4
4634	0+12°1	15	.059	
A 24	217+14°1	<14	.199	2, 4
33	238+34°1	32	.376	2, 4
35	303+40°1	<4	.374	2, 4
36	318+41°1	36	.355	2, 4
BD+30°3639	64+5°1	26	.008	
He 1-5	60-7°1	34	.165	11
Hu 1-2	86-8°1	28	.048	2, 3
J 320	190-17°1	17	.062	
900	194+2°1	18	.044	
K 1-3	346+12°1	17	.201	2, 4
1-22	283+25°1	25	.085	12

[OIII] expansion velocities (taken from Wilson 1950, except where noted) of nebulae not listed in table 5.1 but which do appear in table 3.1

Key to table 5.2 :

(1) Wilson 1965, taken from Smith (1971,73)

(2) Inferred expansion velocity using model.

(3) Reay (1981)

(4) Bohuski and Smith (1974)

(5) Unspecified ion.

(6) Not a Planetary Nebula; not plotted in figures 5.3a,b.

(7) Munch (1968)

(8) Osterbrock et. al. (1966)

(9) HI and [OIII] velocities assumed identical.

(10) Bohuski et. al. (1970)

(11) Flannery and Herbig (1973)

(12) Smith and Gull (1975)

appears to encompass the two classes of nebulae suggested by Smith (1971,73) on the basis of magnitude differences between nebulae and their stars, whereas the latter sequence contains many of the larger older nebulae observed by Bohuski and Smith (1974). With this model the concept of " kinematic age " is meaningless.

No obvious correlation between morphological type and V_{exp} or R_n appears to exist on the basis of figure 5.3a, although there is a tendency for the large nebulae of both the " High velocity " and " Low velocity " sequences to be of class III or above (i.e. more ring shaped).

Theory predicts a roughly linear relationship between expansion velocity and linear radius for Planetary Nebulae (e.g. Mathews 1966, Hunter and Sofia 1971). Since the data shown in figure 5.3a would appear to indicate that two separate classes of Planetary Nebulae exist we have plotted for comparison in figure 5.3a two theoretical curves for the models 1 and 4 of Ferch and Salpeter (1975) which relate the radius of maximum shell density r_m to the bulk velocity U_m at that point for shells containing dust which are accelerated by radiation pressure from the central star. Model 1 has a shell mass of 0.15 $M_\odot$ and an initial velocity of 10 $Km.s^{-1}$, whilst model 4 has a mass of 0.5 $M_\odot$ and an initial velocity, proportional to radius, of between 5 and 12.5 $Km.s^{-1}$.

The solid lines in figure 5.3a refer to the assumption that $r_m = R_n$ and $U_m = V_{exp}$. Model 1 seems to follow the " High velocity " sequence reasonably well and the adjustment of the initial parameters could well improve the correspondence between model 4 and the " Low velocity " sequence (e.g. an increase in shell mass would flatten out the velocity-radius curve).

For the model curves reproduced in figure 5.3a as solid lines the radius R_n is taken to be equal to the radius of maximum shell density. Whilst the expansion velocity V_{exp} is probably appropriate to this position in the shell because emission measure is proportional to the density squared, the nebular radius R_n may be better represented by the maximum shell radius (Bohuski and Smith 1974). Figure 1 of Ferch and Salpeter (1975) suggests that the maximum shell radius can be two or more times greater than r_m and so the model curves are replotted in figure 5.3a with $R_n = 2 \times r_m$ as dotted lines.

Figure 5.4

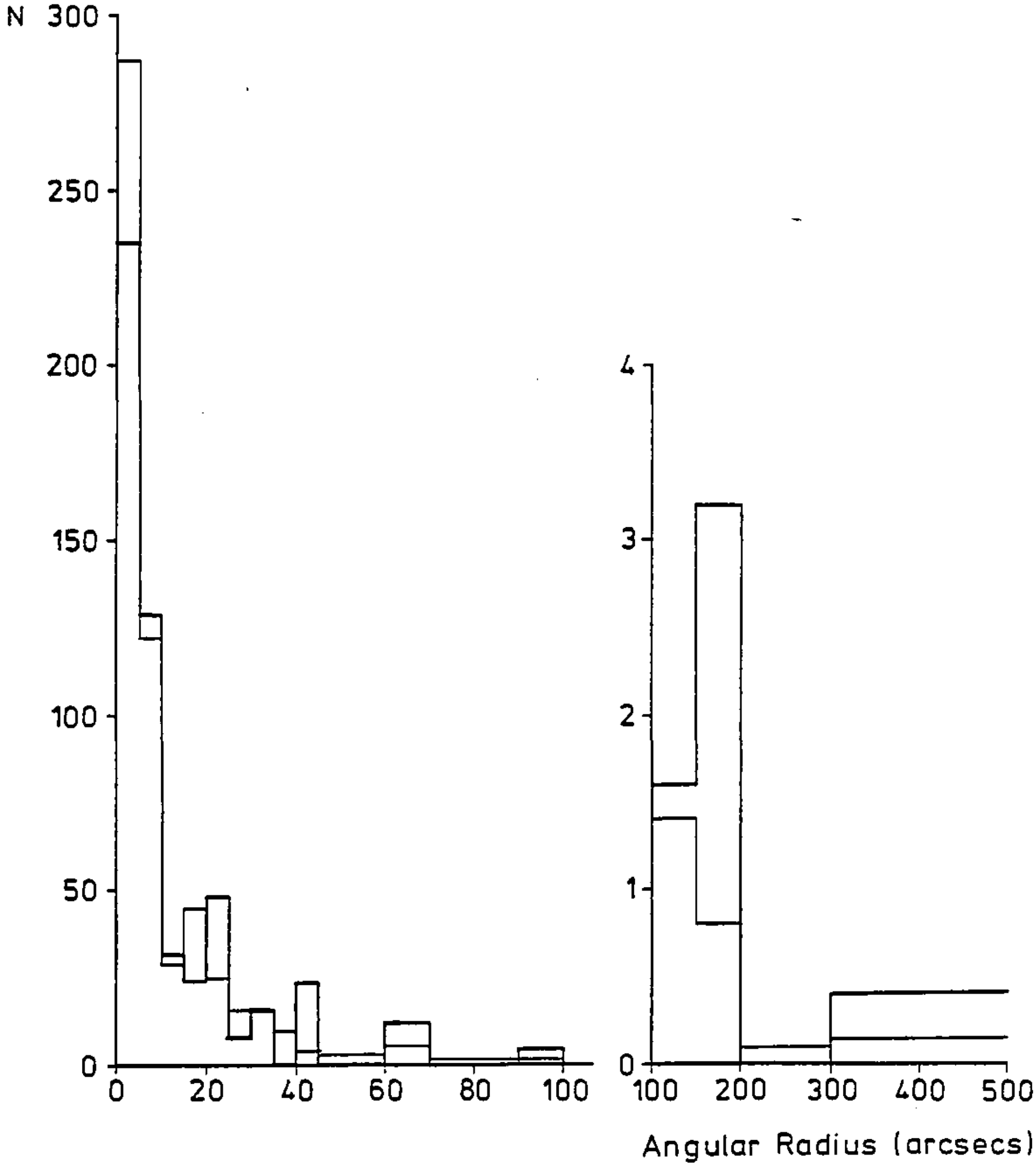

Distribution of nebular angular diameters in present study (thick line), compared with those from Perek and Kohoutek (1967).

5.5 The Expansion Velocity-Linear Radius Relation

Figure 5.3a ia a plot of [OIII] expansion velocity (V_{exp}) versus linear radius (R_n) for the nebulae listed in tables 5.1 and 5.2.

The data points are represented by the corresponding nebular morphological classes (Vorontsov Velyaminov 1948) which are taken from the catalogue of Perek and Kohoutek (1967). Unclassified nebulae are denoted "U", although the majority of these objects would appear to be of irregular form. Underlined symbols indicate the prescence of an outer envelope(s). The numbers along the top and down the right hand side refer to the kinematic nebular age in years - defined as R_n/V_{exp}.

In spite of the considerable scatter the data points appear to fall along two lines (figure 5.3a) suggesting that two distinct, approximately linear, expansion velocity-linear radius relationships may exist. At present it has been impossible to identify any selection effect which might account for the distribution of data points in figure 5.3a. In fact, the distribution of nebular angular diameters for the present sample matches quite closely with the distribution for all nebulae in the catalogue of Perek and Kohoutek (1967) (figure 5.4). Any selection effect in the present sample must therefore also be present in this catalogue.

A number of schemes of Planetary Nebulae evolution can be proposed to account for the distribution of data points in figure 5.3a:-

The simplest, and possibly least likely, is one in which Planetary Nebulae are formed with a wide range of initial expansion velocities, which are maintained at roughly the same value over a significant fraction of the nebular lifetime. Figure 5.3a would then suggest that two distinct epochs of nebular creation exist, with few being formed between kinematic times of 5000 and 9000 years ago. This is unlikely however in view of our current understanding of stellar evolution, in particular the link between Red Giants and White Dwarfs that Planetary Nebulae probably represent.

An alternative view is that data represents evolutionary tracks of two distinct classes of Planetary Nebulae: a " High velocity " sequence which essentially begins life with an envelope expansion velocity $\sim$ 10 $Km.s^{-1}$, and a " Low velocity " sequence which starts life at $\sim$ 5 $Km.s^{-1}$ and accelerates to lower velocities than the other sequence. The former sequence

Agreement between the model curves and the data in figure 5.3a is reasonably good suggesting that radiation pressure driven models are capable of accounting for the observations and that the larger nebulae of the " Low velocity " sequence are of relatively high mass. Only about 20% of the shell mass will be observable (Ferch and Salpeter 1975), consistent with most observational estimates that shell masses are $\lesssim 0.2M_{\odot}$.

5.6 Central Stars

Correlations between central star spectral type and V_{exp} and R_n may help to clarify the interpretation of figure 5.3a. Figure 5.3b is the same as figure 5.3a except that the points are plotted as central star spectral types, where these are available. It can be seen that nebulae with OVI sequence central stars (Smith and Aller 1969) and continuum type stars account for the majority of the " High velocity " sequence nebulae, whereas the " Low velocity " sequence contains only O type stars.

Closer examination of those objects for which stellar temperatures are available (Pottasch et al 1978, Pottasch 1980) reveals two effects :-

(i) A trend of increasing effective stellar temperature and decreasing stellar radius with increasing kinematic age. This observation may be accounted for by the evolution of central stars to higher temperatures and smaller radii (O'Dell 1963, Paczynski 1971) - confirming that central stars of the "Low velocity " sequence are generally older than those of the " High velocity " sequence.

(ii) A tendency for the effective stellar temperature to increase with V_{exp} and R_n along the two sequences of figures 5.3a,b. This is possibly a combination of two effects :

a) The radius of the O^{++} zone is a function of stellar temperature, depending as it does on the number of ionising photons available from the star.

b) Hotter central stars may impart higher expansion velocities to the nebular shells during and after their ejection. Nebulae with OVI sequence central stars lend support to this hypothesis since they fall in the highest expansion velocity group of figure 5.3b, are of extremely high excitation (Smith and Aller 1969) and are known to have wide emission lines indicative of strong stellar winds, which together with the concomitant high radiation fluxes, are thought to drive the expansion of the nebular shells.

Figure 5.3a

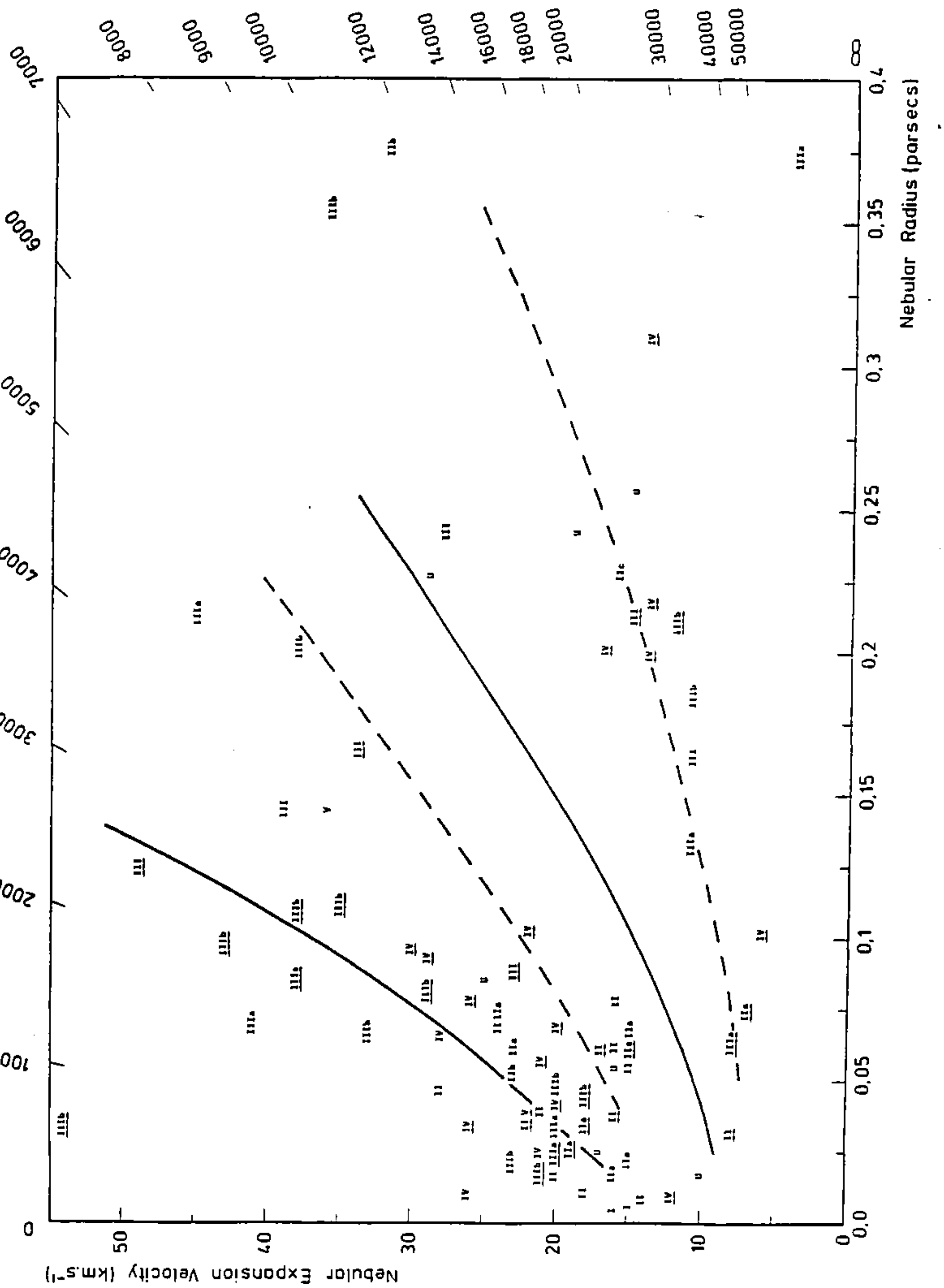

[OIII] expansion velocity versus linear radius for the nebulae listed in tables 5.1 and 5.2. Refer to text for explanation of axes and symbols. Lines indicate predictions of model nebulae.

Figure 5.3b

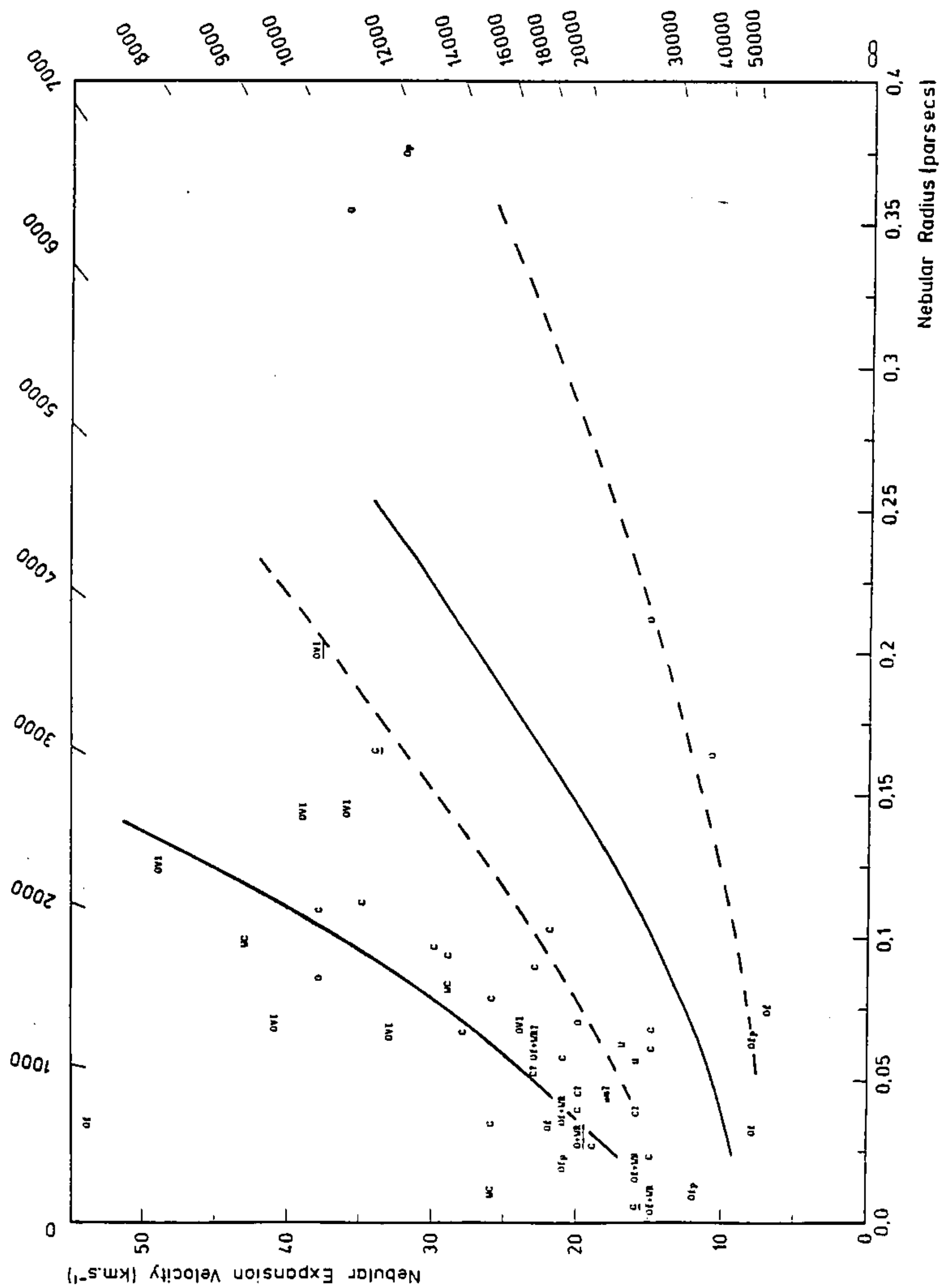

As figure 5.3a but with data plotted as central star spectral type.

5.7 Conclusions

The scatter of the data points in Figures 5.3a, b is quite considerable. In fact, a scatter of $\sim 0.3\ V_{exp}$ and $\sim 0.15\ R_n$ is to be expected from the random orientation of prolate nebular shells of axial ratio 1:1.5 (section 5.3). Further errors in R_n will result from errors in distance determination (Acker 1978) - which may well amount to a factor of two - and in the determination of angular radii.

In spite of this, however, there appear to be systematic trends in the data. Two distinct expansion velocity - linear radius relationships seem to exist. The " High-velocity " sequence contains nebulae with predominantly OVI and continuum type central stars, whilst the " Low-velocity " sequence consists of the larger, older nebulae with mainly O type central stars.

The radiation pressure driven models of Ferch and Salpeter (1975) show reasonable agreement with the data, suggesting that the " High-velocity " sequence corresponds to nebulae with total shell mass $\sim 0.15\ M_o$, and the " Low-velocity " sequence is composed of nebulae with shell masses $\sim 0.5\ M_o$. Only about 20% of this latter shell mass will be observable (Ferch and Salpeter 1975) - consistent with most observational estimates that nebular shell masses are typically of the order of $0.2\ M_o$.

There is some observational evidence that a trend of increasing stellar temperature and decreasing radius supports the view that the nebulae of the " Low-velocity " sequence are older than those of the " High-velocity " sequence, and that progression along these sequences to higher R_n values represents an age progression.

Chapter 6

6.1 Introduction

NGC 7027 has, to paraphrase many authors, " an exceedingly rich and varied optical spectrum " . It is one of the brightest and therefore most comprehensively studied Planetary Nebulae, and for this reason it was chosen as the prototype for a detailed spatio-kinematic analysis.

It is interesting to note that whilst NGC 7027 is often taken to be the archetype of the Planetaries, Allen (1975) questions its authenticity, mainly on the grounds of its irregular optical form and the lack of an observable central star. Recent high resolution radio observations however have revealed a bipolar structure characteristic of Planetary Nebulae. This chapter presents additional evidence which enforces the belief that NGC 7027 is a young bona-fide Planetary.

Sections 2 to 6 deal with optical observations of NGC 7027, and include some new results. Narrow-band filter electronography with Spectracon image tubes is used to map the variation of external extinction across the face of the nebula and locate a possible candidate for the central star. Observations with a Fabry-Perot interferometer and an image tube grating spectrograph reveal the distribution of internal obscuring matter. Data obtained with the Fabry-Perot interferometer are used to investigate velocity fields in the nebula, which is then interpreted in terms of a simple tilted prolate spheroidal model.

Sections 7 to 13 contain reviews of current radio free-free and radio recombination line theory, which is then used with radio and optical observations to propose a consistent model for the HII region of NGC 7027. A distance of 1.33 Kpc to NGC 7027 is predicted.

6.2 External Extinction

At optical wavelengths NGC 7027 presents an amorphous appearance, and therefore has often been classified as " irregular " (Perek and Kohoutek 1967, Greig 1971). However, at radio wavelengths the nebula exhibits a striking degree of symmetry about two orthogonal axes (Harris and Scott 1976, Scott 1973).

Radio free-free, forbidden line and recombination line emissivities are all proportional to the square of the electron density. Therefore, the reason for the irregular optical appearance must be due to differential extinction by material lying along the line of sight.

To investigate this absorption effect a digitised Hα electronograph (shown as a contour map in figure 6.1) was divided point by point by a digitised version of the 5 GHz radio map of Scott (also shown as a contour map in figure 6.2) on a one arcsecond grid. The result is shown in figure 6.3, where contours of equal extinction are spaced by 0.25 m. Due to the dissimilar instrumental profiles - the optical profile is Gaussian, whereas that of the radio has negative lobes - figure 6.3 gives only a rough indication of the distribution of extinction across the face of the nebula. However, the overall impression of a ring or belt of obscuring matter possibly surrounding the nebula is apparent. In this respect NGC 7027 resembles the Bipolar Nebulae, which are thought to be HII regions with circumnebular dust rings.

Figure 6.1

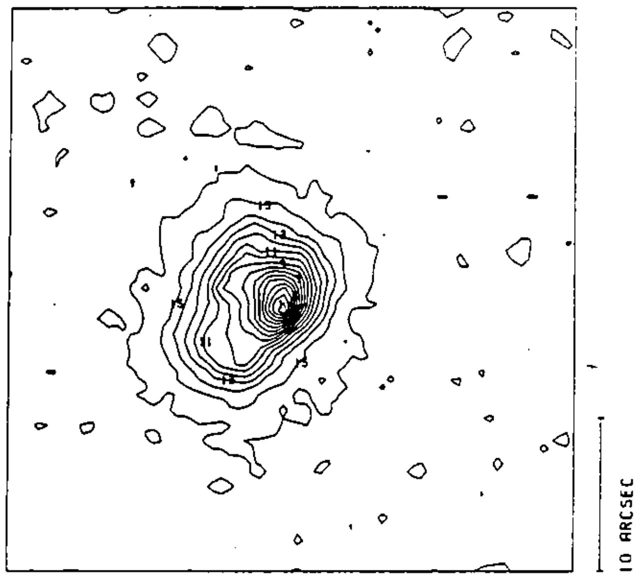

NGC 7027 - HI λ6563Å

Figure 6.2

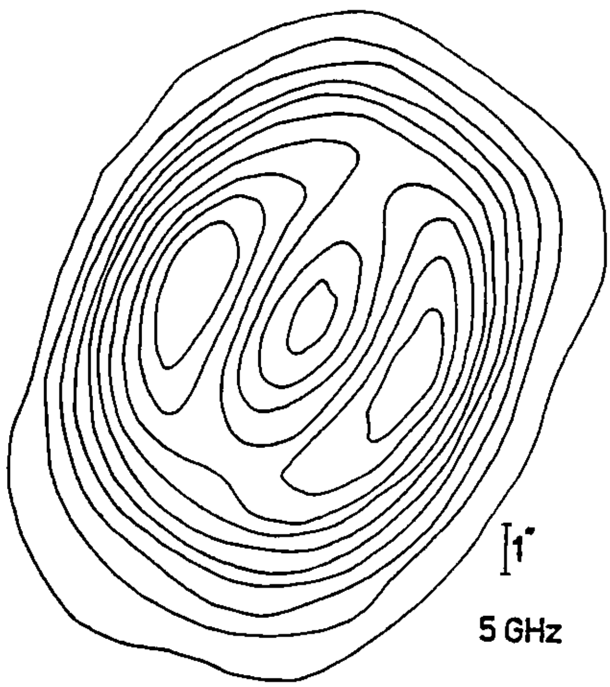

NGC 7027 - 5 GHz Continuum

Figure 6.3

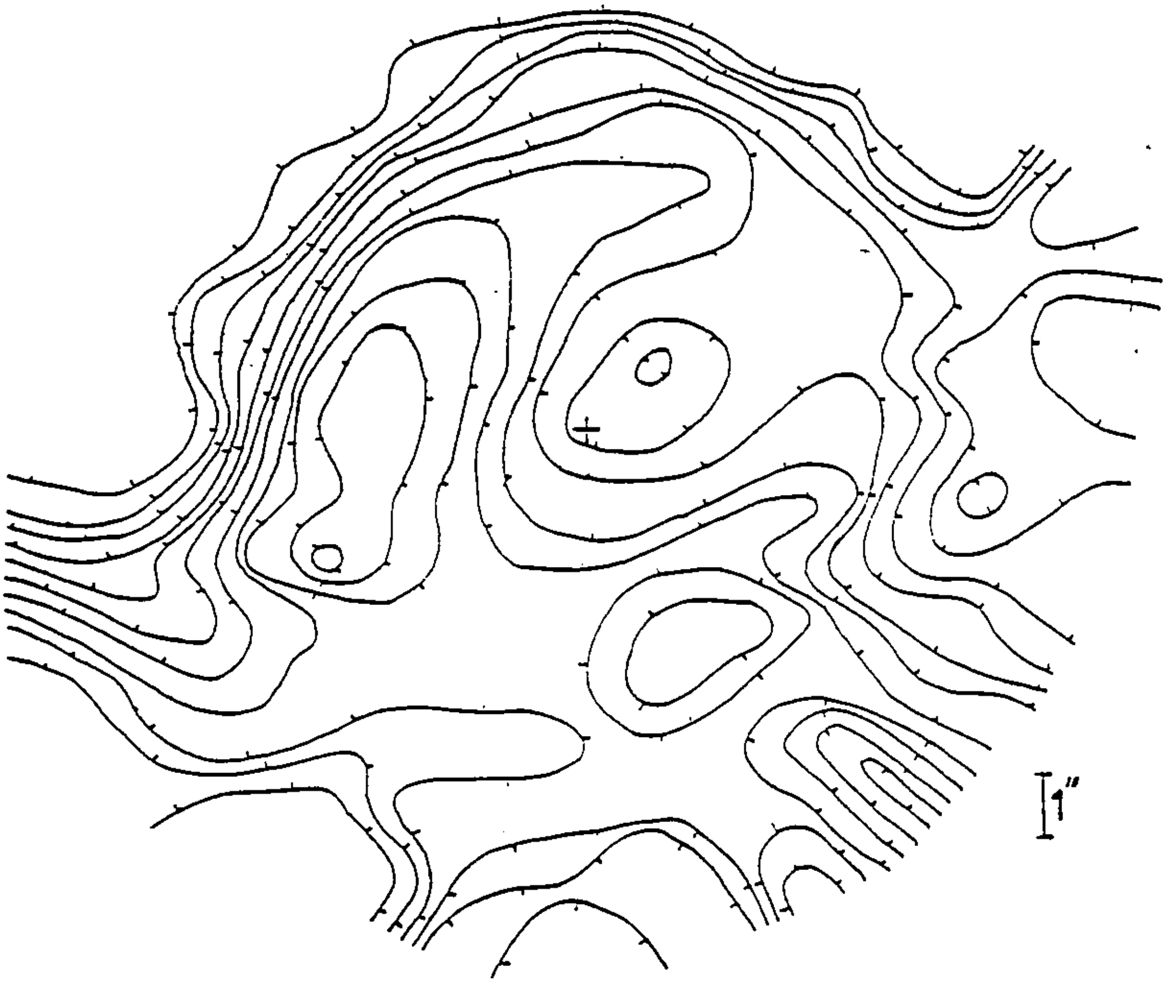

Contour interval = 0.25 m

NGC 7027 - Relative extinction at Hα

6.3 Possible Central Star

Wide-band optical photographs of NGC 7027 show little, if any, sign of the central star. However, it may be possible to locate it by using narrow-band interference filters situated well away from nebular emission lines to enhance the stellar continuum. Since the central star is very faint relative to the nebula continuum a differential technique is probably the best approach.

The method used was to photograph the nebula in the continuum at λ4788Å and λ6703Å, and in the light of a dominant nebular emission line, λ6563Å (Hα). Significant differences between the continuum and the emission line exposures were then looked for.

A distortion of the contours to the East of the bright knot in the λ4788Å exposure is clearly visible (figure 6.4) which is not present at Hα (figure 6.1). As a more quantitative check the λ4788Å and Hα electronographs were digitally ratioed to produce figure 6.5a. The distortion now appears as a fairly symmetric feature with a peak height approximately 20% above the surroundings, which are taken to be at unit height.

Confirmation that this feature is a stellar image was made by plotting the intensity variation along East-West slices taken through the feature in the λ4788Å and Hα contour maps (figure 6.5b). The difference between the two plots results in a Gaussian profile of full-width at half-maximum 1.1 arcseconds. This width is very nearly the same as that measured of a field star which was observed on the same evening.

Whether this star is really the central star or a fortuitously situated foreground star is uncertain, and so the following additional tests could be carried out :-

(i) do the star and nebula have the same proper motions ?
(ii) do the star and nebula have the same radial velocities ?
(iii) is the star hot enough to excite the nebula ?
(iv) is the star at the centre of the radio image ?

Figure 6.4

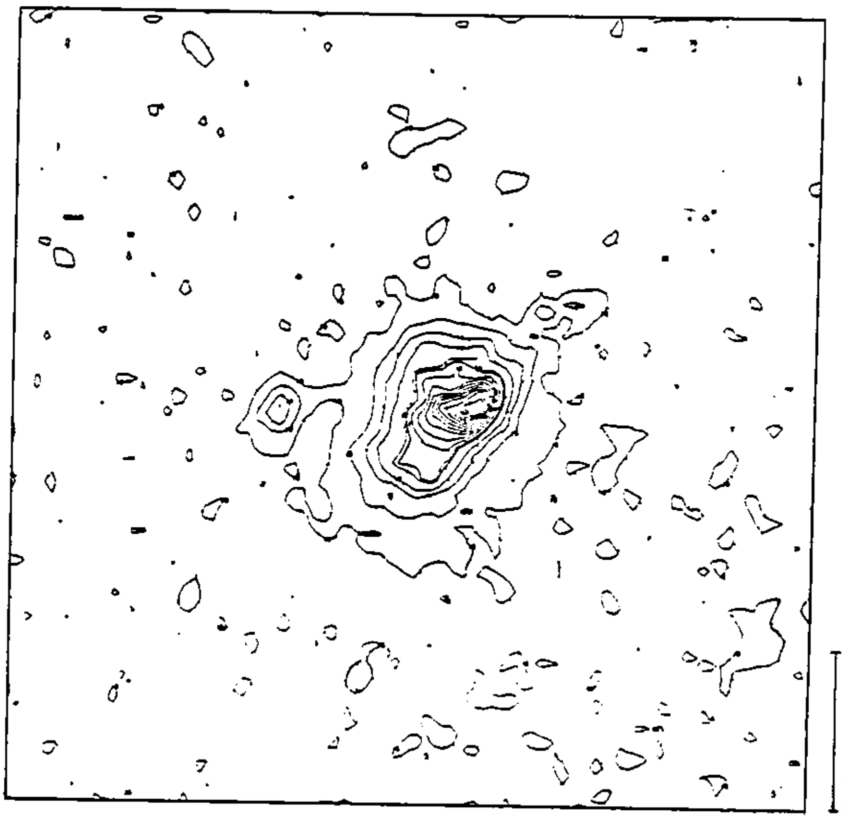

NGC 7027 - λ4788Å Continuum

Figure 6.5

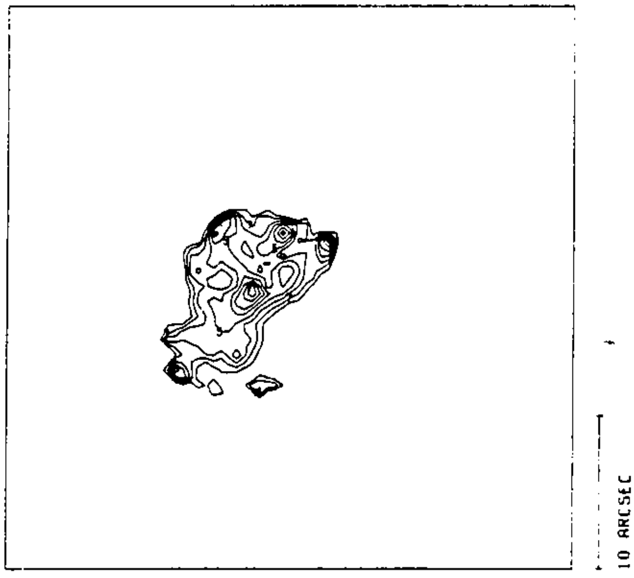

a) NGC 7027 - λ4788Å/λ6563Å ratio showing candidate central star

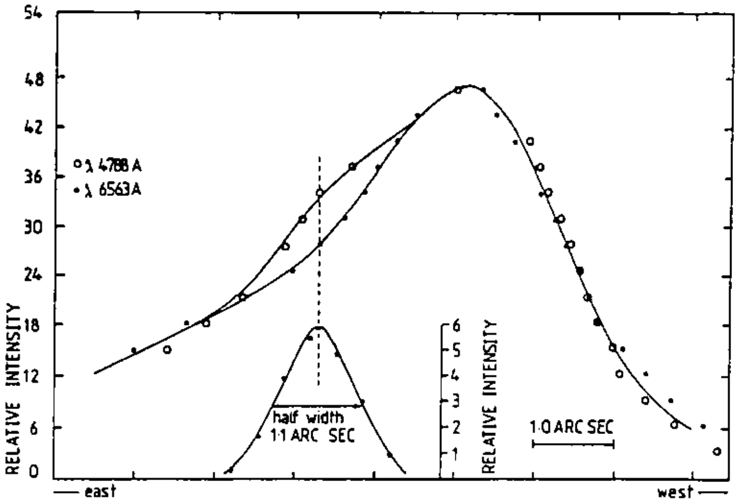

b) NGC 7027 - Comparison of RA scans through candidate central star

Test (i) is difficult owing to the lack of sufficiently sharp features in the nebula and the faintness of the star and time required.

To see if tests (ii) and (iii) are feasible trial observations of the spectrum of NGC 7027 were secured in May 1979 at the Royal Greenwich Observatory, using an image tube grating spectrograph. Unfortunately, bad weather rendered the results unusable. However, instruments aboard the International Ultra-violet Explorer (IUE) satellite may be capable of measuring the stellar spectrum.

Test (iv) was carried out in two stages. First, accurate coordinates of field stars common to the λ4788Å exposure and Palomar Sky Survey red plates were calculated using Smithsonian Astronomical Observatory reference stars. The coordinate measurements were made on the Coradograph X-Y measuring machine situated at the Royal Greenwich Observatory. The second stage involved using these field star coordinates (defined at the 1950 epoch) to match the λ4788Å contour map to the 5 GHz radio map, the coordinates of which are known very accurately. The final error in this process is approximately 0.5 arcseconds, and the candidate star is found to lie at the centre of the radio image to within this.

As test (iii) was not successful one could recourse to using electronographs taken at different continuum wavelengths to give a rough indication of the spectral type of the star. Unfortunately, the only other continuum exposure available, at λ6703Å, is too noisy to be of any use. In principle though it should be possible to record the stars' spectrum by carefully positioning the entrance slit of a spectrograph through the stars' known coordinates and subtracting the nebular spectrum which would be interpolated from the spectrum on either side of the star.

Zanstras' method combined with the λ4788Å observation can be used to calculate what the effective central star temperature should be to yield the observed nebular Hβ flux.

Assuming that the nebula is optically thick to Lyman series radiation (Seatons' case B) we have (Osterbrock 1974) :-

$$\frac{L^{*}_{H\beta}}{Q} = h\nu_{H\beta} \frac{\alpha^{eff}_{H\beta}(H^{o},T_{e})}{\alpha_{B}(H^{o},T_{e})} \frac{\pi F^{*}_{H\beta}}{\pi F^{neb}_{H\beta}}$$

where : $L^*_{H\beta}$ is the stellar luminosity at Hβ

Q is the number of photons per second emitted by the star which are capable of photo-ionizing H^o

$\alpha^{eff}_{H\beta}$ is the effective recombination coefficient for Hβ emission

and α_B is the total recombination coefficient to excited levels of H^o

The ratio of stellar to nebular flux at Hβ may be expressed as :-

$$\frac{F^*_{H\beta}}{F^{neb}_{H\beta}} = \frac{F^{neb}_{4788}}{F^{neb}_{H\beta}} \frac{F^*_{H\beta}}{F^*_{4788}} \frac{F^*_{4788}}{F^{neb}_{4788}}$$

Miller and Mathews (1972) give a value of 8.0 10^{-15} Hz^{-1} for the ratio F^{neb}_{4788} : $F^{neb}_{H\beta}$. Model atmosphere calculations by Hummer and Mihalas (1970) indicate that the stellar Hβ and λ4788Å fluxes are the same, and so we require only the ratio of stellar to nebular λ4788Å fluxes. The observed value of this quantity is given by the ratio of the respective " volumes " of the star and nebula as measured from the λ4788Å data :-

$$\frac{I^*_{4788}}{I^{neb}_{4788}} = 1.98\ 10^{-3}$$

This ratio has to be corrected for the extinction of the star by the nebula. In section 6.4 it will be shown that the nearside portion of the nebular shell attenuates the emission from the far side by 0.34 m at λ5007Å. The flux at the same wavelength from the star will also be reduced by this amount. From Osterbrock (1974) we note that for typical interstellar reddening curves the extinction at λ5007Å is approximately the same as that at λ4788Å. The intrinsic stellar to nebular flux ratio at λ4788Å is thus increased by $10^{0.4\times0.34}$ to 2.71 10^{-3}.

The ratio α^{eff}_{H} : α_B is approximately 1.0 : 8.7 (Miller and Mathews 1972) and so :-

$$\frac{L^*_{H\beta}}{Q} = 8.8\ 10^{-29}\ \text{ergs Hz}^{-1}$$

Comparison with the model stellar atmospheres of Hummer and Mihalas suggests an effective stellar temperature in excess of 200,000 K - which is entirely adequate to account for the very high degree of nebular excitation seen in NGC 7027.

6.4 Internal Extinction

Following the discovery by Gillett et al (1967) of a large Infra-red excess from NGC 7027 in the 2 to 14 micron region, Becklin et al (1973) mapped the nebula at 10 microns (figure 6.6). The similarity of the 10 micron and 5 GHz radio maps led them to conclude that the spatial distribution of the Infra-red and free-free emission regions are similar. This they say indicates that the hot dust giving rise to the Infra-red excess is not responsible for the patchy extinction seen at visible wavelengths. The dissimilarity of their 2.2 and 10 micron right-ascension scans through the centre of the nebula also implies an external source of obscuration, and so one may deduce that the sizes of the particles causing this extinction are less than about 10 microns. The absence of any observable Infra-red emission from this external dust component would indicate that it has a very low temperature.

What extinction the hot dust particles do cause is demonstrated by the work of Hicks et al (1976). Using a capacitance-sensed servo-controlled Fabry-Perot interferometer they have observed the [OIII] $\lambda 5007Å$ emission line profile at several positions on NGC 7027. Their results show a general weakening of the red side of the line profiles - indicative of internal extinction by dust. At a point corresponding to the centre of the 5 GHz radio image they calculate that the dust in the near portion of the nebular shell attenuates the emission from the rear of the shell by 0.34 m. Two possible interpretations may account for this result : either the obscuring matter is distributed throughout the nebula or it is located internal to the shell. The second alternative may be discounted by the fact that the line profiles observed well away from the centre of the nebula also exhibit a weakening of the red side. Also, as mentioned before, the close similarity of the 10 micron and 5 GHz radio maps indicates a co-spatial dust and gas distribution. In fact it is difficult to envisage a mechanism whereby dust could exist in the harsh environment close to a very hot star without the additional presence of ionized gas to shield it.

Figure 6.6

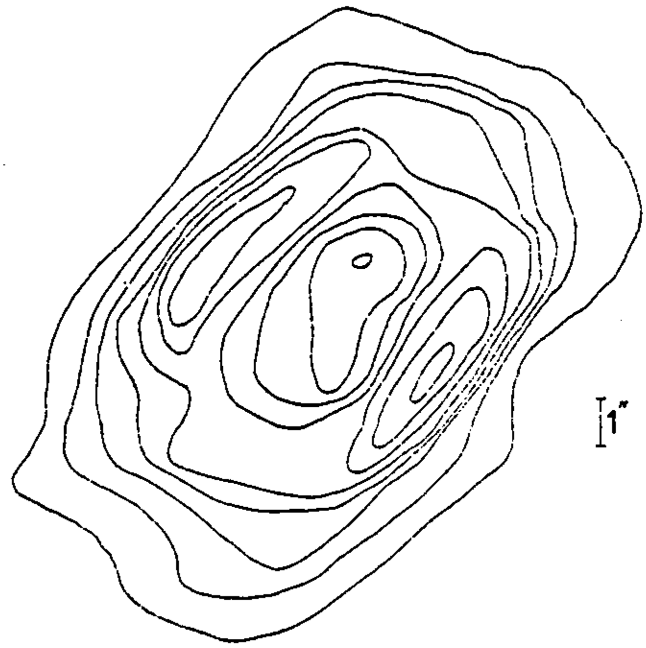

NGC 7027 - 10 micron Continuum

Figure 6.7

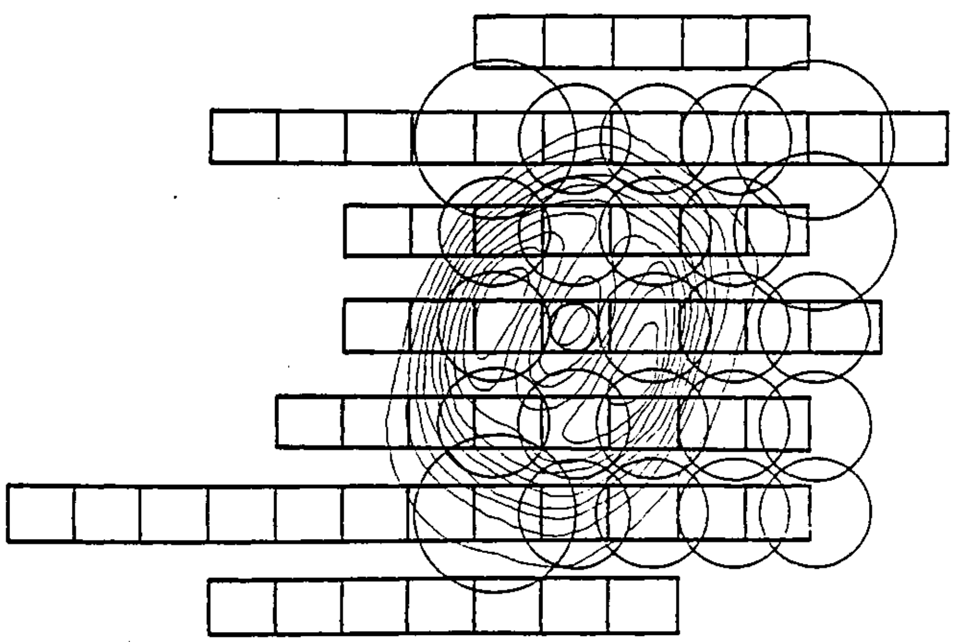

Apertures of Fabry-Perot interferometer and grating spectrograph superimposed upon 5 GHz radio contour map

6.5 [OIII] λ5007Å Line Profiles

A more detailed investigation than that of Hicks et al (1976), made by Atherton et al (1979) also shows the effect of internal absorption by dust mixed with ionized gas. This work was undertaken with two instruments : a Fabry-Perot interferometer and an image tube grating spectrograph.

The Fabry-Perot observations were made at the Coude focus of the 88" Mauna Kea Telescope, Hawaii using entrance apertures of 1.6, 3.3 and 5.0 arcsecond diameter at a resolution of 67,000. The sizes and positions of these apertures are shown in figure 6.7 superimposed upon the 5 GHz radio map of Scott (1973), whilst the line profiles are reproduced in figure 6.8.

Spectrographic observations were made with the Unit Spectrograph at the Cassegraine focus of the 36" Yapp Equatorial reflector situated at the Royal Greenwich Observatory, Herstmonceux. Spectra taken at intervals of 3 arcseconds in declination were recorded with an East-West oriented 100 micron wide slit at a reciprocal dispersion of 10 Å mm^{-1} on G5 nuclear track emulsion via a Spectracon image tube. Details of the Spectracon image tube and nuclear track emulsion may be found in McGee et al (1972). Reduction of the data in the format shown in figure 6.9 required the relative alignment of the spectra in the East-West direction. This was accomplished by using the known declination of each spectral slice relative to the bright optical knot to match each one to a direct λ5007Å electronographic contour map (figure 6.10). The line profiles were then produced on a Joyce-Loebl microdensitometer operated in the direct recording mode by scanning the aligned spectra along the dispersion axis at intervals of 2.25 arcseconds in right ascension with a 10 micron square aperture. The effective aperture of the scans presented in figure 6.9 is a square of side 1.5 arcseconds.

Figure 6.8

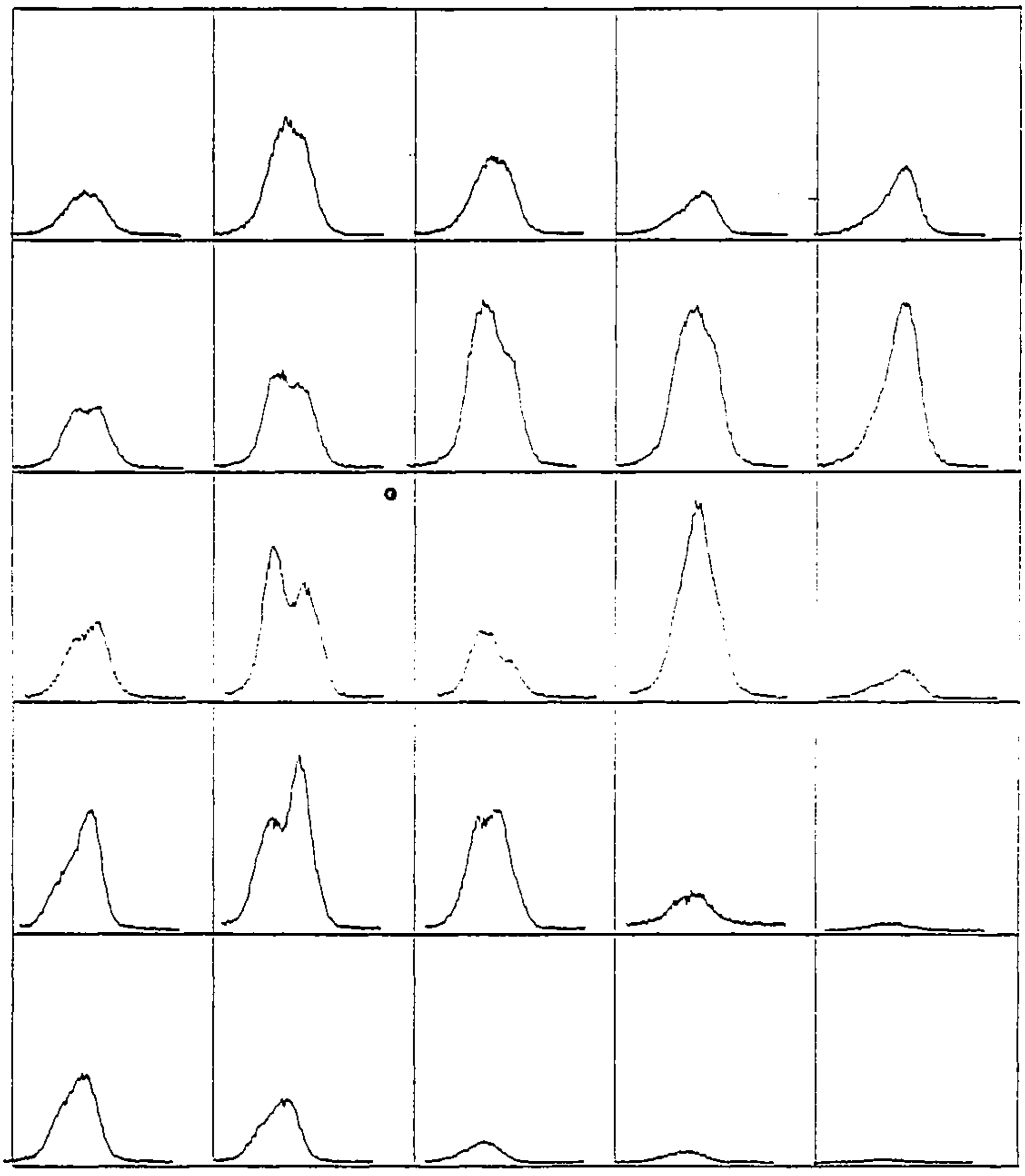

NGC 7027 - Fabry-Perot [OIII] λ5007Å line profiles

o - approximate centre of radio image.

Figure 6.9

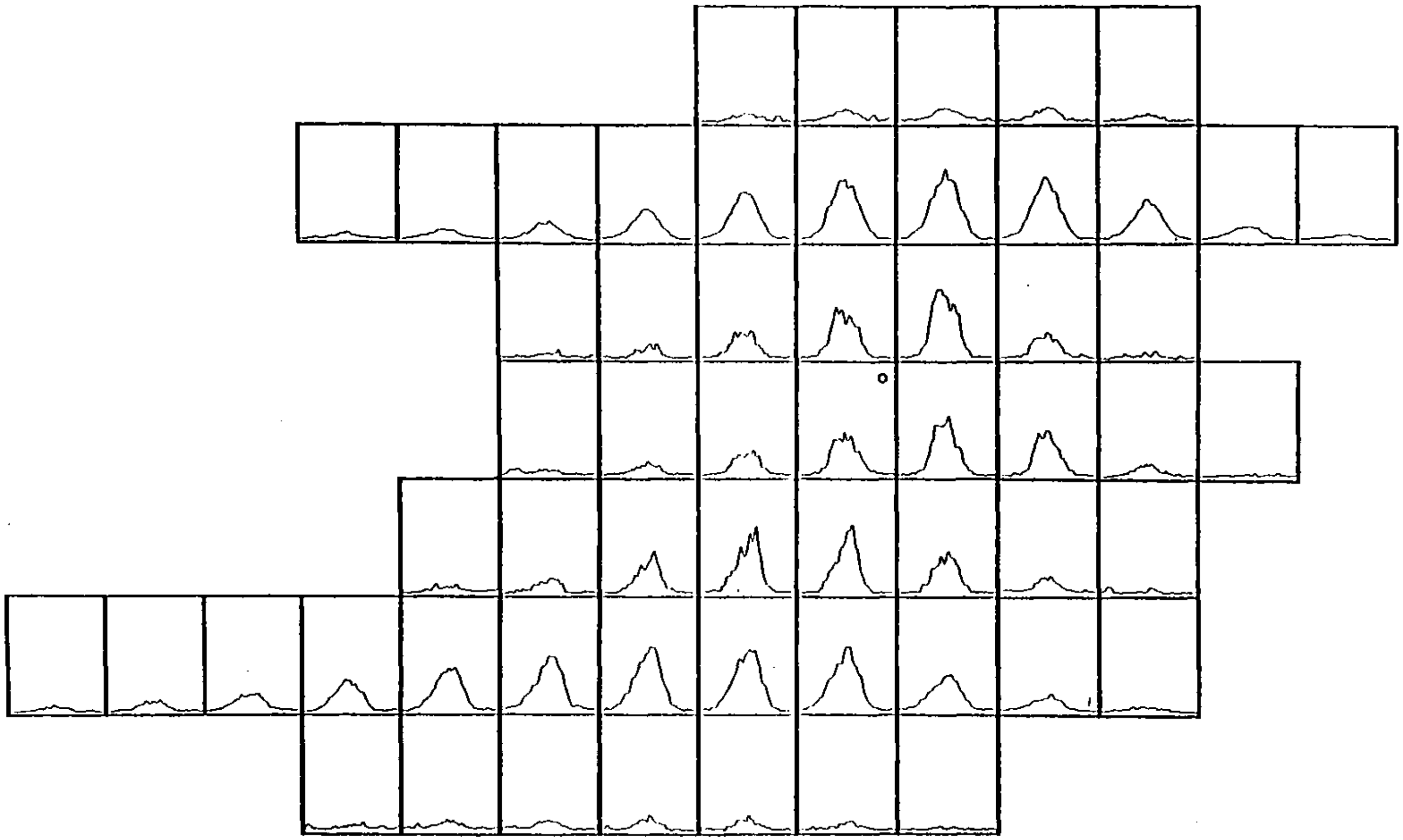

NGC 7027 - Grating spectrograph [OIII] λ5007Å line profiles

o - approximate centre of radio image.

Figure 6.10

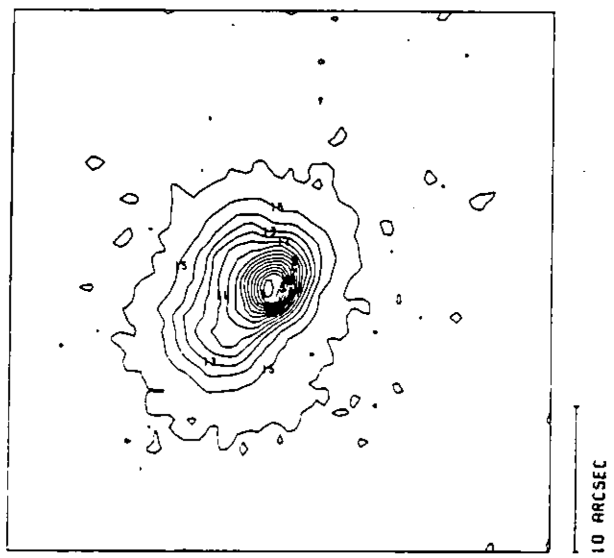

NGC 7027 - [OIII] λ5007Å

6.6 Interpretation of the Line Profiles

The similarity of the Hα and λ5007Å contour maps (figures 6.1 and 6.10) indicates that the spatial distributions of H^{+} and O^{++} are identical. Wilson (1950) has found that the spectral line splitting observed at the centres of many Planetaries is very nearly the same for HI, [OIII], and [NeIII]. Therefore, one can consider the O^{++} ions to be " tracers " of the velocity fields in the HII regions of these nebulae. The two useful features of the [OIII] λ5007Å line are that it is often the brightest line in the spectrum of gaseous nebulae and since oxygen has an atomic weight of 16 it has one quarter of the thermal width of hydrogen lines.

Weedman (1968) assumes that the oval nature of many Planetaries is due to the projection onto the sky of a prolate spheroidal shell, whereas Curtis (1918) interprets their forms as being due to intrinsically oblate shells. Slit spectra of Planetaries often show a tilt of their emission lines. This observation can sometimes provide a method of deciding between the two alternatives because for a prolate shape the line tilt will be maximum when the spectrograph slit is aligned along the apparent major axis, and zero when it is aligned along the minor axis. The converse holds for oblate shapes. These conclusions are only valid if the velocity field is symmetric about the axis of cylindrical symmetry. Unfortunately, if the tilt is found to be zero along both both axes then either the nebula is static or the axis of cylindrical symmetry lies in the plane of the sky. In the latter case it is virtually impossible to determine whether the nebula is prolate or oblate. However, if it can be assumed that there really is an axis of symmetry one may find the distribution of emitting material, in cylindrical coordinates, by the matrix-inversion technique used by Gulak (1958), or by an integro-differential solution of Abels' equation (chapter two). Since the axis of symmetry can in principle be along either the major or minor axis, two solutions will be possible. The comparison of these may help to resolve the prolate/oblate ambiguity.

Figures 7a and 7b of Atherton et al (1979), which show the variation in radial velocity of the [OIII] λ5007Å line profile components along the major and minor axes of NGC 7027, are cast into a different format in figures 6.11a and 6.11b in which only the mean line radial velocities are plotted. These plots show that the mean radial velocity along the major axis changes at a rate of 1.05 Km $s^{-1}arcsec^{-1}$ in going from South-East to North-West. The corresponding change along the minor axis is much smaller : 0.17 Km $s^{-1}arcsec^{-1}$, going from North-East to South-West.

From the foregoing discussion we may interpret these results as suggesting that NGC 7027 may be represented by a prolate spheroidal shell, with the North-Western end of its' major axis tilted away from the Earth.

Figure 6.12 is a section along the axis of symmetry of a thin shelled prolate spheroidal model nebula, tilted at an angle θ to the plane of the sky. The dotted line at an angle θ' is the locus of the centre of gravity of the line profile which would be observed if one assumes that the velocity at any point in the shell is proportional to that points' distance from the centre of the model, and that the volume emissivity is constant throughout the shell.

We can derive a relation between θ and θ' in terms of the lengths of the semi-major axis P and the semi-minor axis E :-

$$\tan\theta' = \frac{(P^2-E^2)\tan\theta}{P^2+E^2\tan^2\theta} \tag{6.1}$$

The Fabry-Perot data provides a value for the maximum line splitting $2V_o$ = 33.0 Km s^{-1} which is observed at the centre of the radio image, and the rate of change of radial velocity along the major axis g = 1.05 Km $s^{-1}arcsec^{-1}$. The projected length p of the major axis is measured from the unpublished 15 GHz map of Scott (figure 6.13) and is 3.81 arcseconds, and E is measured to be 2.8 arcseconds.

The expression for p in terms of θ, P and E is :-

$$p = (E^2\sin^2\theta + P^2\cos^2\theta)^{\frac{1}{2}} \tag{6.2}$$

e, which is shown in figure 6.12 is defined as :-

Figure 6.11

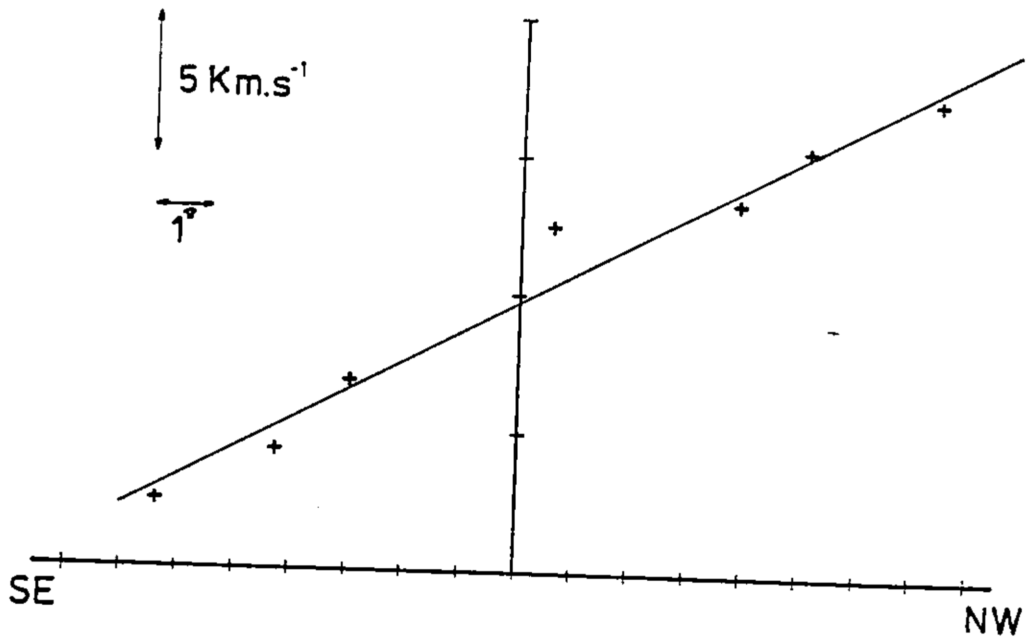

a) NGC 7027 - Radial velocity along major axis

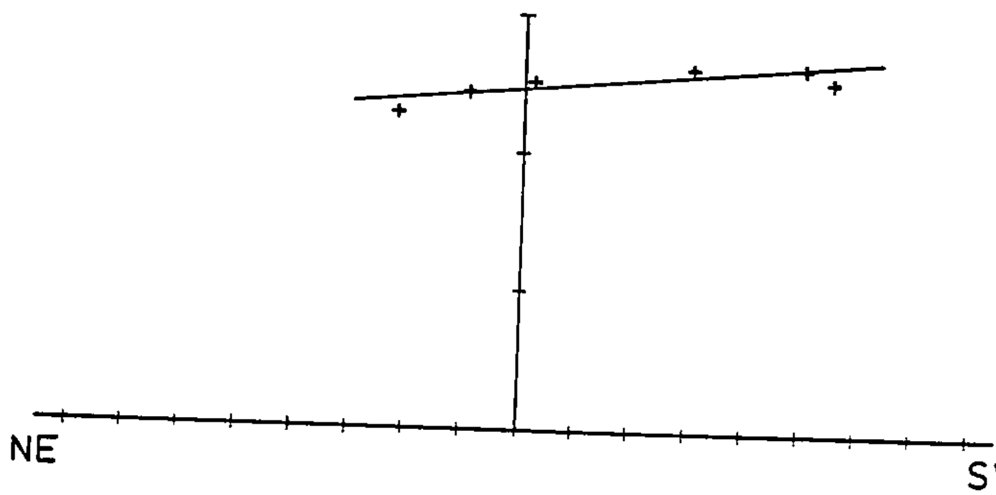

b) NGC 7027 - Radial velocity along minor axis

Figure 6.12

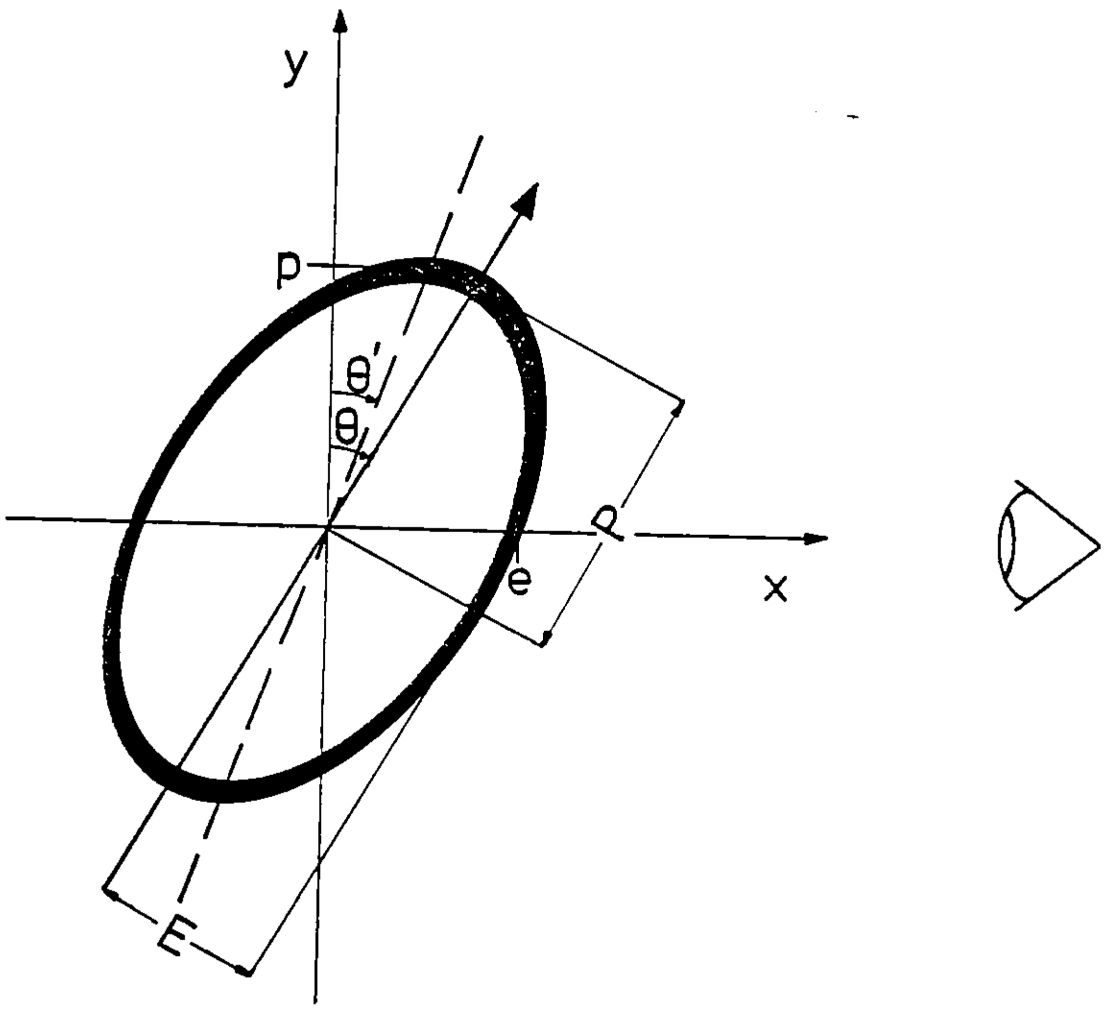

Cross-section through thin-shelled prolate spheroidal model

Figure 6.13

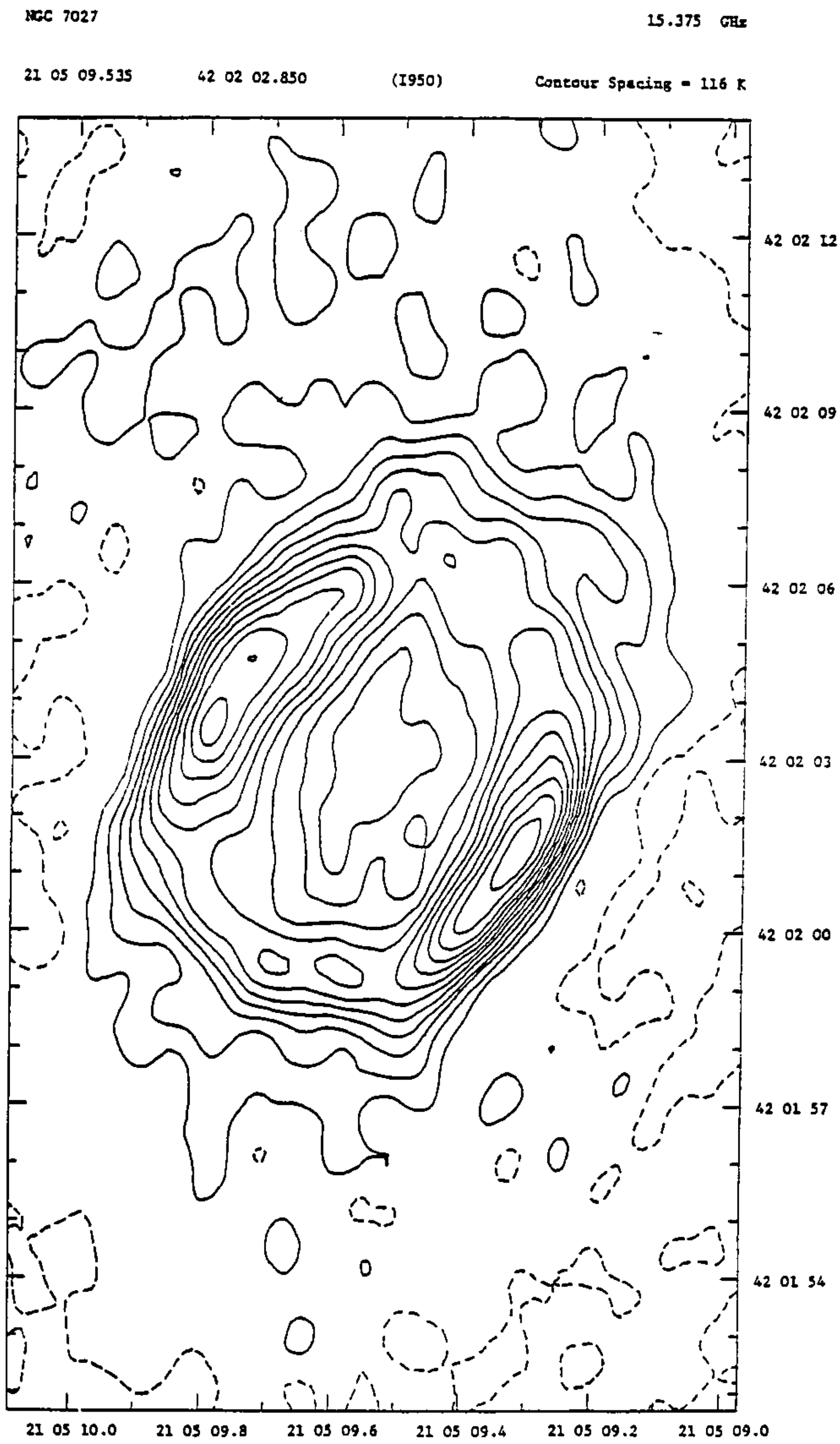

NGC 7027 - 15 GHz Continuum

$$e = \left(\frac{\sin^2\theta}{P^2} + \frac{\cos^2\theta}{E^2}\right)^{-\frac{1}{2}} = \frac{E\times P}{p} \qquad (6.3)$$

k is defined as the proportionality constant in the relation between velocity V and distance from the centre of the model r :-

$$V = k\times r \qquad (6.4)$$

Upon solving equations 6.2 to 6.4 and substituting numerical values for the variables we find that :-

$$P = p\left(1 - \frac{p^2E^2g^2}{(p^2-E^2)V_o^2}\right)^{-\frac{1}{2}} = 4.48 \text{ arcseconds}$$

$$\theta = \cos^{-1}\left(\frac{p^2-E^2}{P^2-E^2}\right)^{\frac{1}{2}} = 42^{\circ}.4$$

and $k = \dfrac{p\times V_o}{P\times E} = 5.01 \text{ Km s}^{-1}\text{arcsec}^{-1}$.

If we now relax the assumption that the emissivity is constant throughout the shell but instead falls as $r^{-2\alpha}$, where $\alpha>0$, then from figure 6.12 it is apparent that θ' will decrease as α increases. Equivalently, for a fixed θ' we see that θ will increase as α increases, and so for a more realistic model the value of $42^{\circ}.4$ for θ should perhaps be taken as a lower limit.

It is interesting to note that the axial ratio P : E = 1.6 : 1.0 is very similar to the ratio 1.5 : 1.0 used by Weedman (1968) in his interpretation of the structure of other Planetaries.

This particular interpretation of the Fabry-Perot data should be compared with that of Atherton (1979), who finds that $\theta = 15^{\circ}.0$ and $k = 7.3 \text{ Km s}^{-1}\text{arcsec}^{-1}$.

The data also shows that the cylindrical model of NGC 7027 proposed by Scott (1973) is incorrect because it is tilted the wrong way and would imply a constant line splitting along the major axis.

6.7 Thermal Bremsstrahlung Theory

The equation of radiative transfer for the radio continuum is :-

$$\frac{dI_\nu}{dx} = -k'(\nu,x)\times I_\nu + j(\nu,x) \tag{6.5}$$

where : I_ν is the radiation intensity in W $m^{-2}Ster^{-1}Hz^{-1}$
$k'(\nu,x)$ is the absorption coefficient per unit volume in m^{-1}
and $j(\nu,x)$ is the corresponding emissivity coefficient

Since, by Kirchhoffs' Law, $k'(\nu,x)$ and $j(\nu,x)$ are related in terms of the Planck black-body function $B_\nu(T_e)$ equation 6.5 can be expressed as :-

$$\frac{dI_\nu}{d\tau_\nu} = -I_\nu + B_\nu(T_e) \quad ; \quad \text{with } d\tau_\nu = k'(\nu,x)\, dx$$

The solution of this equation, assuming that there is no background radiation source present, is :-

$$I_\nu = \int_0^{\tau_\nu(max)} B_\nu(T_e)\exp(-\tau_\nu)\, d\tau_\nu \quad ; \quad \text{with } \tau_\nu = \int_0^x k'(\nu,x')\, dx'$$

The antenna brightness temperature T_b is defined by the Rayleigh-Jeans Law :-

$$I_\nu = \frac{2k_B\nu^2}{c^2}\, T_b$$

In terms of brightness temperature the solution of equation 6.5 becomes :-

$$T_b = \int_0^{\tau_\nu(max)} T_e(\tau_\nu)\exp(-\tau_\nu)\, d\tau_\nu \tag{6.6}$$

When the electron temperature T_e is constant equation 6.6 simplifies :-

$$T_b = T_e\{1 - \exp(-\tau_\nu(max))\} \tag{6.7}$$

The expression for $k'(\nu,x)$ is (Lang 1974) :-

$$k'(\nu,x) = \frac{0.98N_e(x)}{T_e^{3/2}(x)\nu^2} \sum_i Z_i^2 N_i(x) \log_e(4.954\ 10^7 T_e^{3/2}(x)\nu^{-1})\ m^{-1} \quad (6.8)$$

which is valid for $N_e \sim 10^4 cm^{-3}$ and $T_e \sim 10^4$ K.

From equation 6.8 and the definition of τ_ν , it is clear that :-

$$\lim_{\nu \to 0}(T_b) = T_e \quad ; \quad \lim_{\nu \to \infty}(T_b) = T_e \tau_\nu(max)$$

These are the optically thick and optically thin limits, respectively.

6.8 Temperature and Density Variations in NGC 7027

Figures 6.14a and 6.14b show the variation with Ionization Potential IP of the electron density N_e and electron temperature T_e in NGC 7027, plotted from the data of Kaler et al (1976). The solid lines in the graphs are fits to the data :-

$$N_e = 64.0\ IP^2\ cm^{-3} \quad ; \quad T_e = 11,500 + 0.0014\ IP^{7/2}\ K$$

We assume at this point that these variations are physically real, and are not artifacts of the incorrect application of atomic theory. By eliminating IP from these equations we arrive at a simple relation between T_e and N_e :-

$$T_e = 11,500 + 9.6\ (N_e/10^4)^{7/4} \qquad (6.9)$$

In section 6.6 it was shown that NGC 7027 may be interpreted as a tilted prolate spheroid, and so we model the nebula accordingly, although in more detail.

Figure 6.14

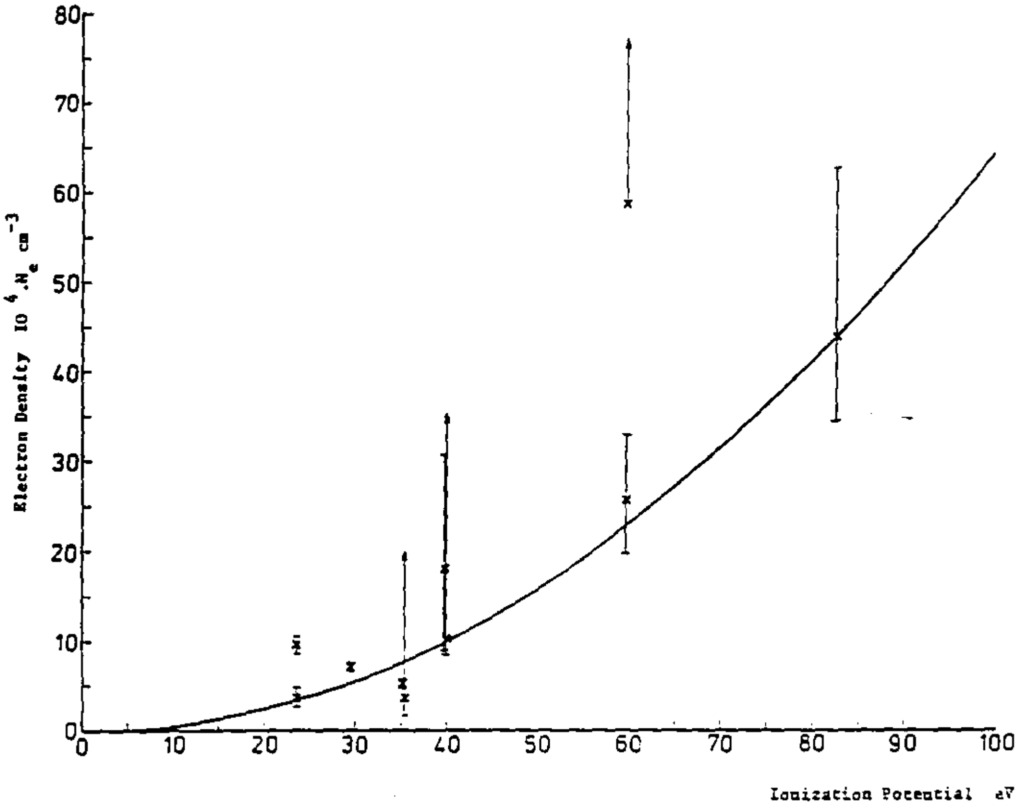

a) NGC 7027 - Electron density versus Ionization Potential

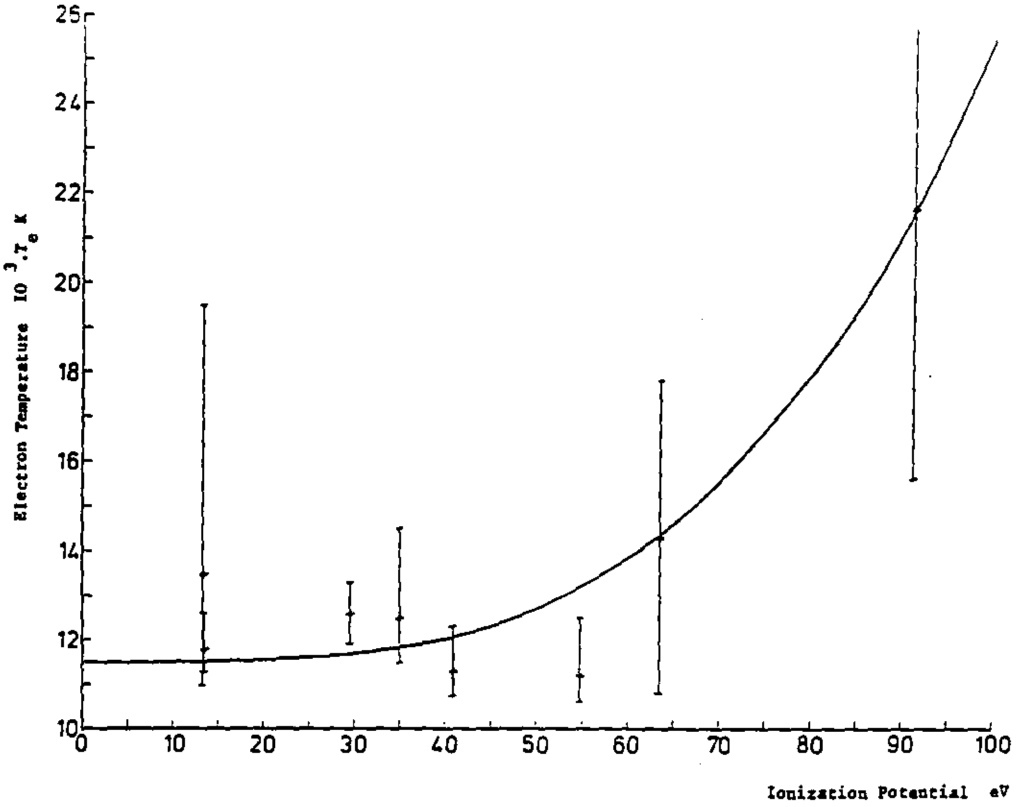

b) NGC 7027 - Electron temperature versus Ionization Potential

6.9 The HII Model

The model we have adopted for the HII region of NGC 7027 has an electron density variation :-

$$N_e(r) = N_e(e_i)\ (e_i/r)^{\alpha}\ \ cm^{-3} \tag{6.10}$$

and is bounded by two co-axial prolate spheroidal surfaces tilted at an angle θ to the plane of the sky. The axes are in the ratio $e_i : e_i : p_i$ for the inner surface, and $e_o : e_o : p_o$ for the outer surface where : $p_i \geq e_i$, $p_o \geq e_o$, $p_o \geq p_i$ and $e_o \geq e_i$. $N_e = 0$ at points inside the inner surface and outside the outer surface, and therefore for $\alpha > 0$ the electron density is a maximum at radius e_i.

Due to their low abundances we will ignore the contribution of elements heavier than helium to the free-free absorption coefficient (equation 6.8). We also assume that : $N(He^{++}) \propto N(He^{+}) \propto N(H^{+}) \propto N_e$ at all points throughout the shell. The proportionality of $N(He^{++})$ and $N(He^{+})$ is clearly absurd. However, from Miller and Mathews (1972) we note that the number densities of He^{++} and He^{+} relative to H^{+} are 0.042 and 0.085 respectively, and so this error will be minor.

Model fitting using the 15 GHz map of Harris and Scott (1976) was accomplished in two stages by running an inter-active least-squares fitting program on the CDC 6500 computer at Imperial College.

The first stage involved finding the geometrical parameters of the surfaces for a range of α . This was done by neglecting the variation of T_e given by equation 6.9 and using the optically thin form of equation 6.7. For half-integral and integral values of α this results in a straightforward algebraic expression for the brightness temperature as a function of the geometrical parameters. Initial values of the geometrical parameters were chosen and values proportional to T_b were computed over a ¼ arcsecond square grid. This array was then convolved with another two-dimensional array to account for the instrumental profile, and the final array was used to calculate the least-squares residual χ^2, relative to the digitised 15 GHz data. The procedure was then iterated, after the geometrical parameters had been simultaneously varied, until the change in χ^2 between successive runs was less than 0.1% . The least value of χ^2 was achieved for $\alpha = 1$.

The second stage involved taking the best fit model, replacing the explicit variation of T_e and relaxing the assumtion of optical thinness. The geometrical parameters were then " tweaked up " to produce a better fit. The final parameters appear in table 6.1.

By integrating over the model we can find the predicted total flux density in terms of $N_e^2(e_i).d_{Kpc}$, where d_{Kpc} is the distance to the nebula in Kiloparsecs. The flux density at 5 GHz is 6.05 Jy , and so :-

$$1.072\ N_e^2(e_i).d_{Kpc} = 172.0\ 10^8\ \mathrm{cm}^{-6}\mathrm{Kpc} \qquad (6.11)$$

where the numerical factor on the left hand side arises from the contribution to the free-free absorption coefficient by He^{++} and He^{+}.

At a distance of 1.34 Kpc (Cahn and Kaler 1971) we find :-

$$N_e(e_i) = 1.1\ 10^5\ \mathrm{cm}^{-3} \quad ; \quad \overline{N_e} = 7.9\ 10^4\ \mathrm{cm}^{-3}$$

$$(N_e)_{rms} = 8.1\ 10^4\ \mathrm{cm}^{-3} \quad ; \quad \mathrm{Mass}_{HII} = 0.06\ M_o$$

The figure of 0.06 M_o for the total mass of ionized gas agrees well with the value of 0.064 M_o calculated for the cylindrical model of Scott (1973).

Using the parameters listed in table 6.1 a 5 GHz model map has been produced, and is shown along with the 15 GHz model map in comparison with the 5 and 15 GHz observed maps in figure 6.15.

Table 6.1

Geometric Parameters of the 7027 Model

Parameter	Value	Explanation
α	1	Density exponent
θ	56°	Tilt of major axis relative to plane of sky
e_i	2.8"	Inner surface semi-minor axis
e_o	3.4"	Outer surface semi-minor axis
p_i	5.6"	Inner surface semi-major axis
p_o	6.2"	Outer surface semi-major axis

Figure 6.15

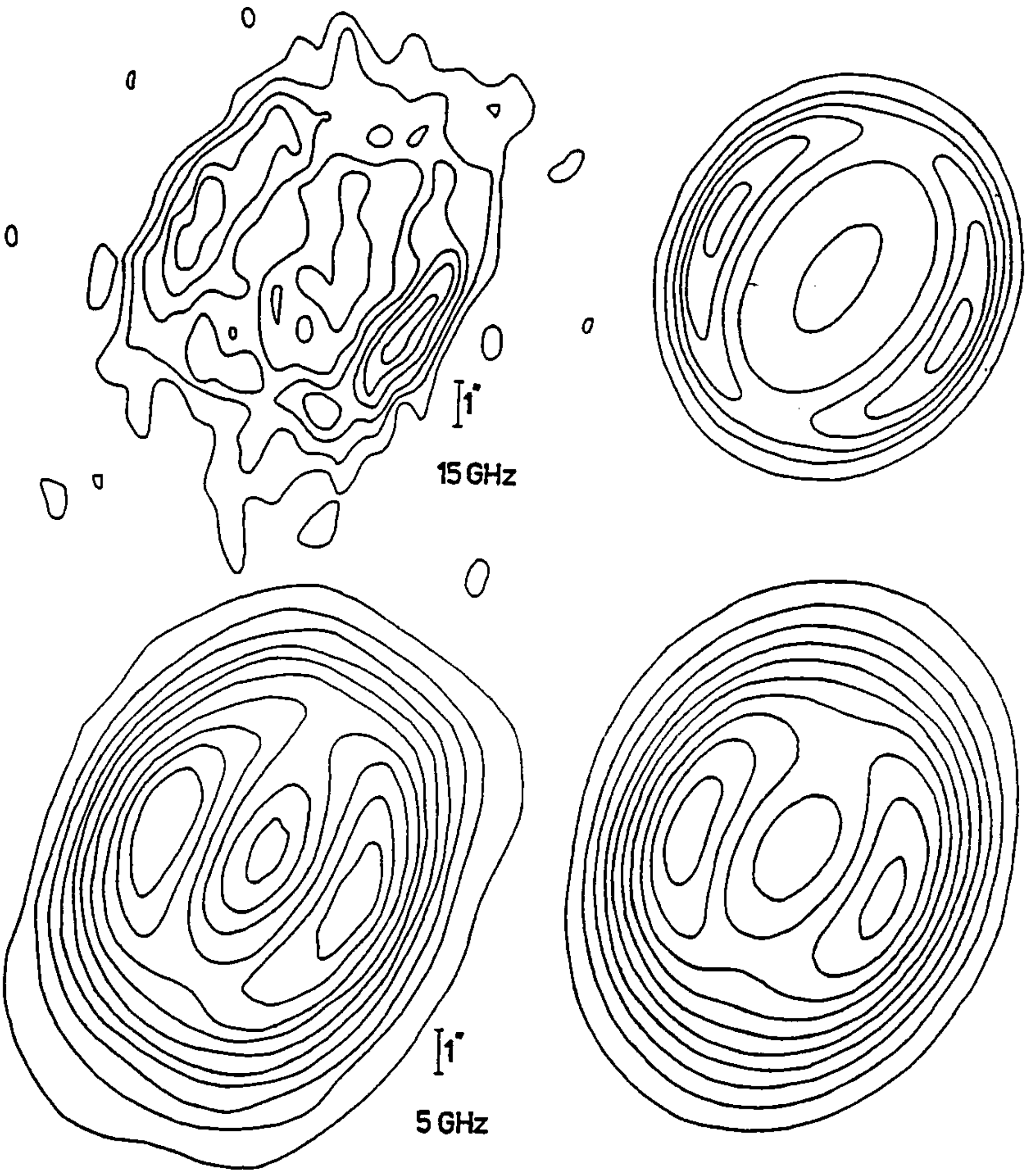

NGC 7027 - Comparison of model and observed 5 and 15 GHz radio maps

6.10 Radio Continuum Spectrum of NGC 7027

The HII model derived in the last section may be used to predict the radio continuum spectrum, which can then be compared with observation. Figure 6.16 shows the measured flux densities, which have been mainly taken from the compilation of Higgs (1971), but which also include results by Harris and Scott (1976) and Scott (1973). The optical data is included also, and is taken from Kaler et al (1976). The solid line in figure 6.16 represents the predicted spectrum, after a reddening correction of c = 1.2 has been applied (Osterbrock 1974). The agreement between the observations and the predicted spectrum is seen to be excellent.

An effect of temperature gradients through the nebula appears as an asymmetry about the minor axis of both the observed and model 5 GHz maps (figure 6.15). That such an effect can occur in a symmetric model can be expained by means of a simple model. Figure 6.17 represents a cross-section through a "Battenburg cake " HII region, which is basically a uniformly dense right cubic cylinder having two pairs of different temperature regions, where T(1) > T(2) (see figure 6.17, in which the axis of symmetry is also shown).

We wish to derive expressions for the brightness temperatures, $T_b(1)$ and $T_b(2)$, which would be observed along the upper and lower lines of sight respectively. For this purpose we use equation 6.6 :-

$$T_b(1) = \int_0^{\tau_\nu(\max)} T_e(\tau_\nu)\exp(-\tau_\nu)\, d\tau_\nu$$

$$T_b(1) = T(2)\{1 - \exp(-\tau_\nu(2))\}\exp(-\tau_\nu(1)) + T(1)\{1 - \exp(-\tau_\nu(1))\}$$

where $\tau_\nu(1)$ and $\tau_\nu(2)$ are the respective optical depths in the regions of electron temperature T(1) and T(2). Similarly,for the lower line of sight :-

$$T_b(2) = T(1)\{1 - \exp(-\tau_\nu(1))\}\exp(-\tau_\nu(2)) + T(2)\{1 - \exp(-\tau_\nu(2))\}$$

The difference between these two equation is a measure of the degree of asymmetry :-

Figure 6.16

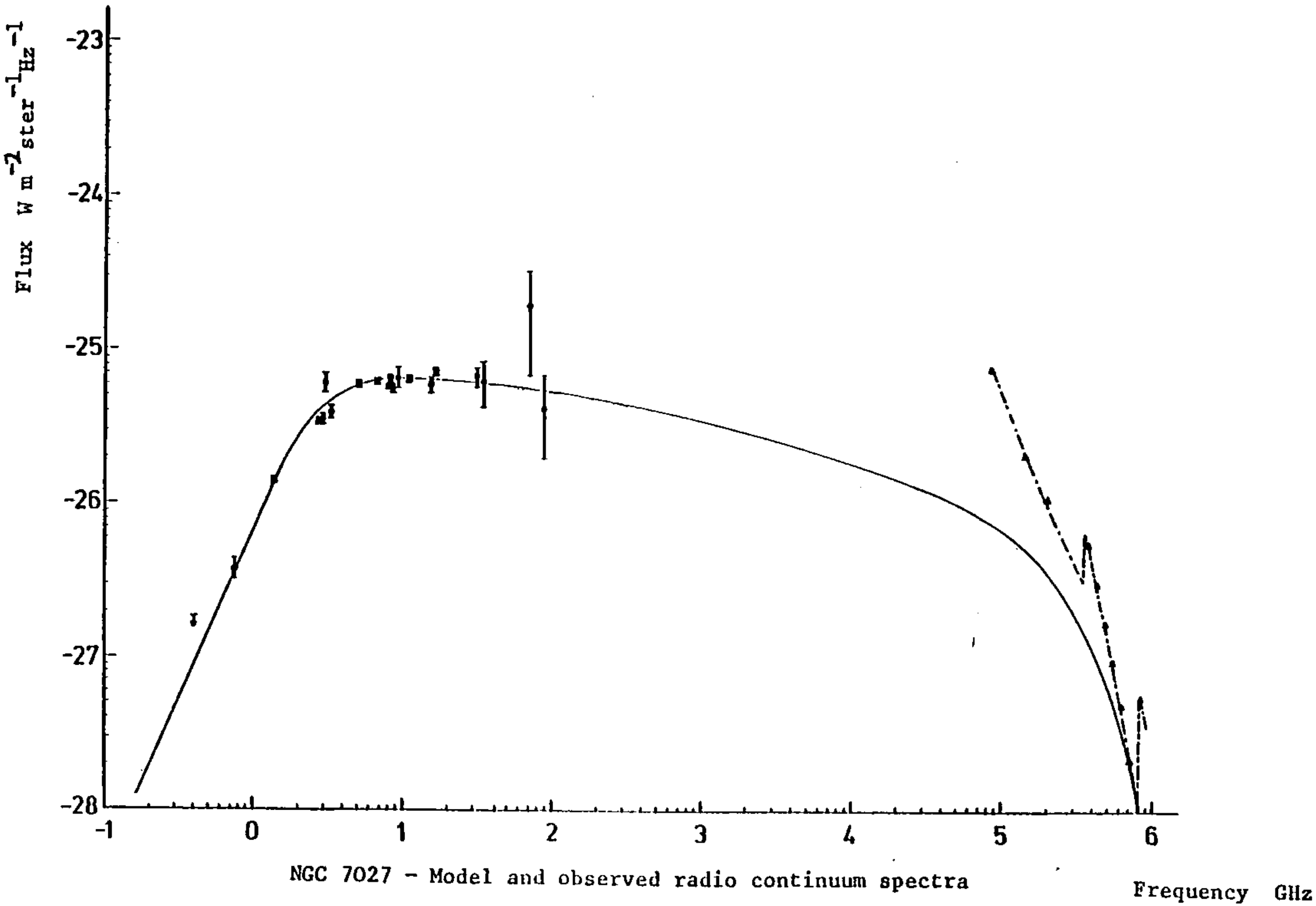

NGC 7027 - Model and observed radio continuum spectra

Figure 6.17

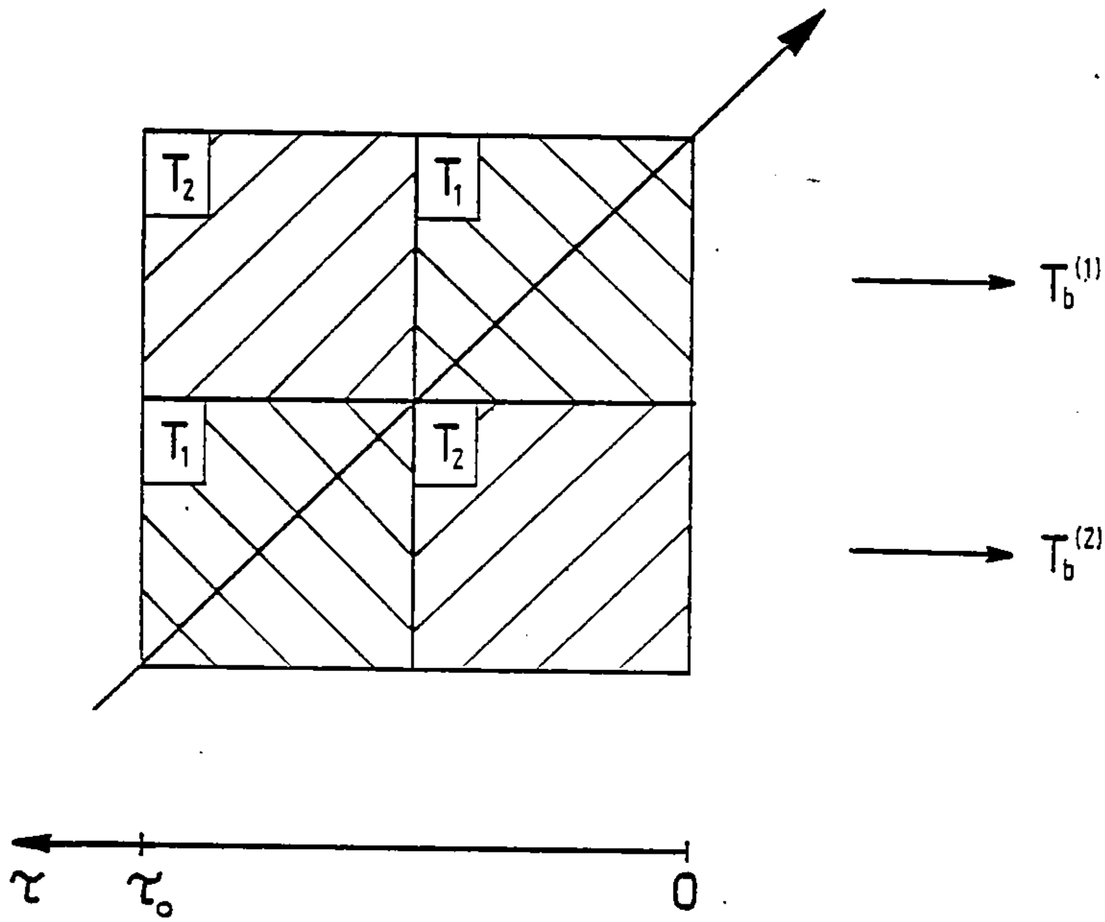

Cross-section through " Battenburg cake " HII model

$$T_b(2) - T_b(1) = \{T(2)-T(1)\}\{1 - \exp(-\tau_\nu(2))\}\{1 - \exp(-\tau_\nu(1))\} \quad (6.12)$$

Clearly, if the model is isothermal then the asymmetry vanishes, as it also does at sufficiently high frequencies.

The maximum asymmetry observed in NGC 7027 at 5 GHz is about 650 K and this occurs along the major axis at positions where the mean brightness temperature is about 4500 K. If the electron temperature at these points is approximately 11500 K then the corresponding optical depths are roughly 0.5 at 5 GHz. If we make the assumption that a relation similar to equation 6.12 can be applied to the case of NGC 7027 in the form :-

$$\Delta T_b = \Delta T_e(1 - \exp(-\tau_\nu))$$

then $\Delta T_e \sim 1660$ K is a rough indication of the range of temperature present in NGC 7027. This is consistent with the variation of temperature in figure 6.14b.

At 8 GHz the expected asymmetry is 290 K according to this scheme, whilst at 15 GHz it should be 90 K. From the 8 GHz map of Terzian (1978) we see that the asymmetry is about 200 K, which is consistent with what we expect. At 15 GHz the predicted value is just about equal to the noise level of the map of Harris and Scott (1976). This latter result partly justifies the neglection of the explicit form of the electron temperature variation (equation 6.9) when deriving the parameters of the HII model.

6.11 Radio Recombination Lines

6.11.1 Theory

The frequency of the transition from level n_2 to level n_1 in hydrogen is given by the Rydberg equation :-

$$\nu = Rc(n_1^{-2} - n_2^{-2}) \quad \text{Hz}$$

where $R = 1.097\ 10^7\ m^{-1}$ is the Rydberg constant.

Transitions between levels with $n_1 \sim n_2 \sim 100$ occur in the radio region and since $\Delta n = n_2 - n_1 << n_2$ we can write the Rydberg equation in the approximate form :-

$$\nu = Rc\frac{2\Delta n}{n^3} \quad \text{Hz} \qquad (6.13)$$

Such transitions are denoted : nα, nβ, nγ etc., where n is the upper level and α, β, γ etc. refer to $\Delta n = 1, 2, 3$ etc.

Under conditions of Local Thermodynamic Equilibrium (LTE), we can express the population distribution of levels by means of Sahas' equation :-

$$N_n^* = \frac{n^2 h^3 \exp(\chi_n/k_B T_e)}{(2\pi m_p k_B T_e)^{3/2}} N_p N_e \qquad (6.14)$$

where the symbols have their usual meanings.

In practice, collisional excitations and de-excitations by free electrons result in a departure of the population distribution N_n from the LTE value N_n^* . Conventionally, this departure is expressed in terms of the departure coefficient b_n which is a function of N_e and T_e :-

$$N_n = b_n N_n^*$$

Brocklehurst (1970) has tabulated values of b_n for a wide range of N_e and T_e using a cascade matrix technique. He also gives values for C_n , which is defined as : $C_n = -\log_{10}(d\log_e b_n/dn)$. As n tends to infinity,

b_n tends to unity, which simply means that as the bound electrons in an atom near the continuum level they approach an LTE distribution, where by definition $b_n = 1$.

The volume emissivity coefficient for a n to n-Δn transition is given by :-

$$j_1(\nu) = b_n N_n \frac{A_{n,n-\Delta n}}{4\pi} h\nu \ \phi_\nu$$

where : $A_{n-\Delta n,n}$ is the Einstein spontaneous emission coefficient
and ϕ_ν is the line profile function, normalised to unity.

From the Einstein relations and Kirchhoffs' law we may derive an expression for the line absorption coefficient :-

$$k_1(\nu) = \frac{c^2}{2\nu^2}\left(\frac{N_{n-\Delta n}}{\omega_{n-\Delta n}} - \frac{N_n}{\omega_n}\right)\omega_n \frac{A_{n,n\Delta n}}{4\pi}$$

where ω_n is the statistical weight of the n'th level. Using Sahas' equation this can be re-written :-

$$k_1(\nu) = b_n \beta N_e N_p \frac{e^2}{m_e c} \frac{h^3 n^2 \exp(\chi_n/k_B T_e)}{(2\pi m_e k_B T_e)^{3/2}} \{1 - \exp(-h\nu/k_B T_e)\}$$

$$\times f_{n,n-\Delta n}\phi_\nu$$

where $f_{n,n-\Delta n}$ is the oscillator strength of the transition and β is :-

$$\beta = \{1 - \frac{b_n}{b_{n-\Delta n}} \exp(-h\nu/k_B T_e)\}\{1 - \exp(-h\nu/k_B T_e)\}$$

or : $$\beta = 1 - \frac{k_B T_e}{h\nu} . \frac{d\log_e b_n}{dn} . \Delta n$$

Equation 6.5 is the equation of radiative transport for purely continuous radiation. When account is taken of radio transition lines it becomes (Goldberg 1966) :-

$$\frac{dI_\nu}{d\tau_\nu} = -I_\nu + \frac{k_1^*(\nu) b_n + k'(\nu)}{k_1^*(\nu) b_n \beta + k'(\nu)} B_\nu(T_e) \qquad (6.15)$$

where : $d\tau_\nu = (k_l^*(\nu) + k'(\nu))\, dx$

In terms of brightness temperature the solution of equation 6.15 is :-

$$T_c + T_l = \int_0^{\tau_\nu(\max)} T_e \, (k_l^*(\nu) b_n + k'(\nu)) \exp(-\tau_\nu') \, d\tau_\nu' \qquad (6.16)$$

where T_c and T_l are the continuum and line brightness temperatures respectively.

6.11.2 Line Profiles

Several factors determine the line profile factor ϕ_ν namely : thermal broadening, bulk velocity broadening, pressure broadening and the Stark effect. Greim (1967) has shown that the Stark effect is negligible to the pressure broadening by free electrons.

The classical theory of pressure, or impact, broadening is as follows : Assume that a continuously radiating hydrogen atom is being perturbed by passing free electrons so that the wavetrain suffers an abrupt change in phase during each encounter. If the sections of the wavetrain are uncorrelated in phase then the spectrum of the i'th one, of duration T_i seconds, will be a Sinc function centred at the frequency of the unperturbed wavetrain of full-width at zero-crossing points $2/T_i$ Hz. If the collisions are occuring randomly in time then the probability $P(T_i)$ of an interval T_i elapsing between successive collisions will follow a random walk pattern :-

$$P(T_i) = \exp(-T_i/\tau)\ d(T/\tau)$$

where τ is the mean interval between collisions. The combined spectrum of an ensemble of similar atoms will be the average of the individual Sinc functions, weighted by $P(T_i)$, and is a Lorentzian profile of half-width at half-maximum $\delta = (2\pi\tau)^{-1}$ Hz.

Brocklehurst and Leeman (1971) have computed δ over a range of electron densities by averaging over a Maxwellian electron velocity distribution :-

$$\delta = \frac{1}{2\pi}\,\overline{\sigma v}\,N_e \quad \text{Hz}$$

where σ is the inelastic collision cross-section. For Hnα lines they derive an empirical expression for δ :-

$$\delta = 4.7\ (n/100)^{4.4}(T_e/10^4)^{-0.1}\ N_e \quad \text{Hz} \tag{6.17}$$

The line profile from a Maxwellian velocity distribution is a Gaussian :-

$$\phi_\nu = \frac{1}{\delta\nu\pi^{\frac{1}{2}}}\exp\{((\nu-\nu_o)/\delta\nu)^2\} \quad ; \quad \frac{\delta\nu}{\nu_o} = \left(\frac{2k_BT_e}{m_pc^2}\right)^{\frac{1}{2}} \tag{6.18}$$

where ν_o is the rest frequency.

Broadening by the bulk velocity fields within nebulae is the most difficult mechanism to quantify. However, for our purposes it will be adequate to represent it with a Gaussian profile.

The resultant line profile factor is a Voigt function, which is obtained by the convolution of all of the above effects, including the broadening by the instrument. Allen (1964) gives a formula for the full-width at half-maximum ΔV of a Voigt profile, in terms of Gaussian and Lorentzian components :-

$$\Delta V = (\Delta V_I^2 + \Delta V_D^2 + \Delta V_E^2 + 0.25\ \Delta V_P^2)^{\frac{1}{2}} + 0.5\ \Delta V_P \tag{6.19}$$

where I, D, E and P refer to the instrumental, thermal, expansion and pressure broadening processes respectively. These widths are often expressed as equivalent Doppler velocities, in Km s^{-1}.

6.12 Radio Recombination Line Observations and Their Interpretation

Table 6.2 is an up to date list of all of the Hnα data on NGC 7027. Values of the line to continuum brightness temperature ratios are mainly taken from source. However, Brocklehurst and Seaton (1972) point out that radio astronomers often use empirical methods in the removal of rapidly fluctuating baselines from their data. For example, T_l/T_c and ΔV have been produced by Churchwell et al (1976) after the subtraction of a quadratic background, which was fitted to the data on either side of the line. They then fitted a Gaussian profile to the residual data to yield the line parameters quoted. This procedure is extremely suspect because at the electron densities observed in NGC 7027 (10^4 to 10^5 cm^{-3}) one would expect to see significant departures from Gaussian profiles for lines with $n > 100$ due to pressure broadening. For instance, when $N_e = 10^4$ cm^{-3} and $T_e = 10^4$ K the ratio of pressure to thermal broadening widths is 0.38 for the H109α line. Such baseline correction techniques can therefore lead to the removal of the broad wings of a Voigt profile and consequently result in the under-estimation of T_l/T_c and ΔV. In contrast, Chaisson and Malkan (1976) have used a strictly linear baseline correction and so obtain higher values of the line parameters for the H110α transition than Churchwell et al do for the H109α transition.

In order to place all of the data on an equal footing, the results of Churchwell et al have been re-interpreted using a linear baseline correction and these values appear in brackets in the table.

The corrected line parameters in table 6.2 are plotted in figures 6.18a, 6.18b and 6.18c. The optical line width, represented by a diamond, is taken from Wilson (1950).

Table 6.2

Observed Hnα Line Ratios and Widths of NGC 7027

Line	T_l/T_c		ΔV Km s^{-1}		Reference
76α	0.0370	±0.002	47.5	± 3	(1)
76α	0.0300	±0.004	41.0	± 7	(2)
85α	0.0310	±0.009	46.0	±12	(3)
85α	0.0230	±0.003	45.0	± 2	(4)
85α	0.0210	±0.002	52.8	± 5	(5)
90α	0.0170	±0.001	49.0	± 5	(6)
94α	0.0104	±0.002	44.0	±12	(7)
109α	0.0035(55)	±0.001	65(76).0	±12	(6)
110α	0.0096	±0.001	71.2	±13	(1)

Reference Key :	Symbol used in figure 6.18 :
(1) Chaisson and Malkan (1976)	□
(2) Bignell (1974)	▼
(3) Rubin and Palmer (1971)	×
(4) Terzian and Balick (1972)	Δ
(5) Higgs (1972)	o
(6) Churchwell et al (1976)	●
(7) Goad and Chaisson (1973)	+

Figure 6.18

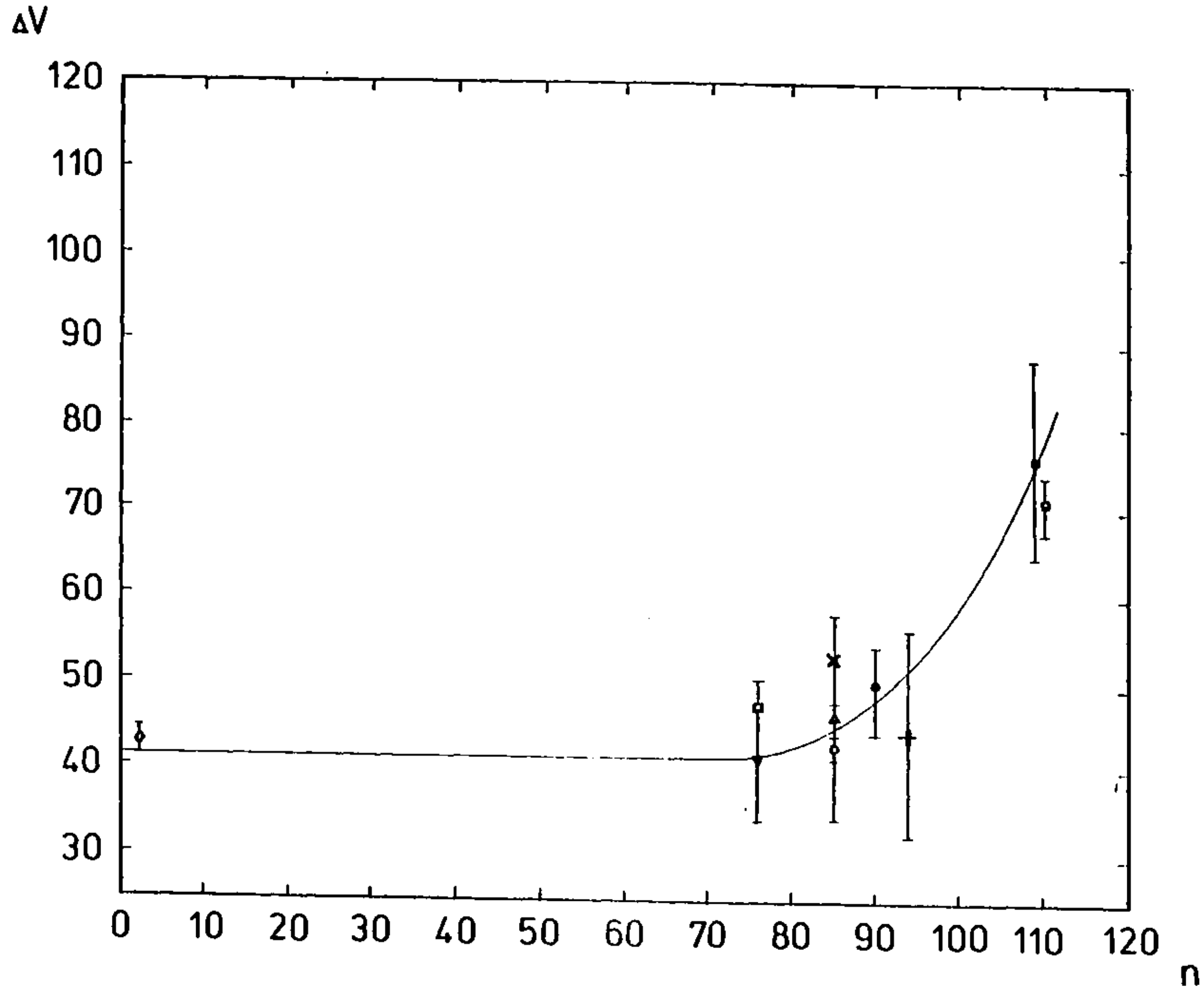

a) NGC 7027 - Hnα radio recombination line widths

Figure 6.18

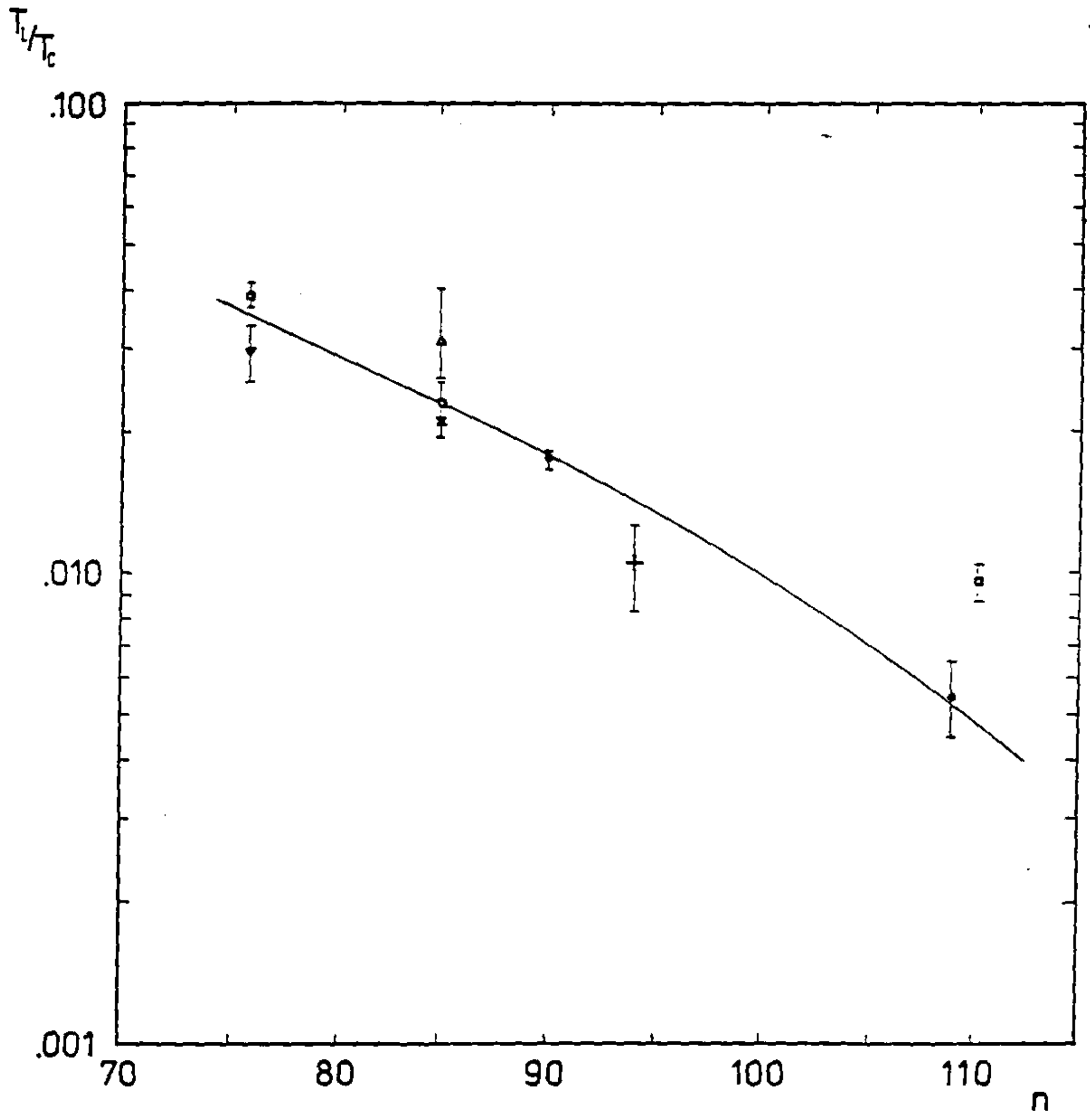

b) NGC 7027 - Hnα radio recombination line to continuum ratios

Figure 6.18

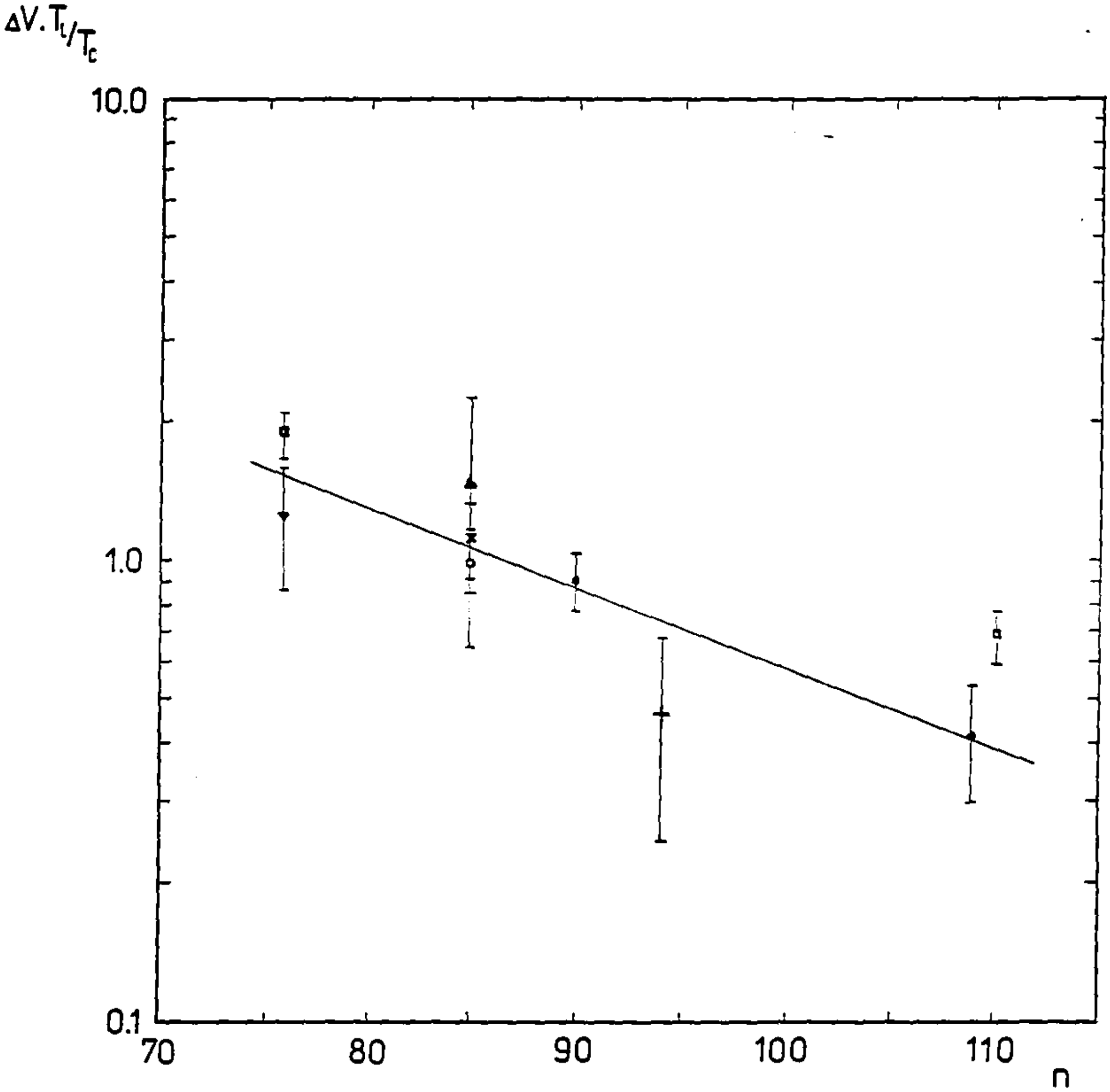

c) NGC 7027 - Product of line to continuum ratios and line widths

6.13 Predicted Radio Recombination Lines From the HII Model

The model which has been developed for explaining the radio structure of NGC 7027 may be used to predict radio recombination line parameters. Because N_e and T_e depend upon the radial distance in the model it is necessary to express b_n and β as functions of N_e. For this purpose the results of Brocklehurst (1971) were used to express b_n and β as power series in $N_e/10^4$. The expansion velocity line width $\Delta V_E = 25$ Km s^{-1} was taken from Wilson (1950).

When pressure broadening is negligible the line profile is Gaussian with a peak height $\phi_o = (\sqrt{\pi}\Delta V)^{-1}$, where ΔV is given by equation 6.19. To account for the effect of a finite amount of pressure broadening we can amend this expression in terms of the ratio x of Lorentzian to Gaussian component widths :-

$$\phi_o = \{\sqrt{\pi}\Delta V(1.0 + 0.39\,x - 0.10\,x^2)\}^{-1} \qquad (6.20)$$

This correction factor is a fit to the tabulated values of profile peak heights and widths in Allen (1964).

Equation 6.16 may be integrated over the volume of the model to obtain the predicted line profiles. In practice four values of T_1+T_c were computed for each of the lines listed in table 6.2 at the following positions :-

(i) At the line centre
(ii) 5 Km s^{-1} from the line centre
(iii) 30 Km s^{-1} from the line centre
and (iv) At effectively infinite distance from the line centre

Values (i) and (iv) were used to calculate T_1/T_c, whilst all four values were used to calculate the line width ΔV. Table 6.3 summarises the results of these calculations, for various values of the peak density $N_e(e_i)$.

The parameter generally used in the comparison of the theory and observation of radio recombination lines is the product of the line

Table 6.3

Predicted Hnα Line Ratios and Widths for the 7027 Model

$N_e(e_i)$ $10^4 cm^{-3}$		76	85	90	94	109	110
8.0	T_1/T_c	1.630	1.188	0.990	0.855	0.501	0.460
	ΔV km s^{-1}	41.8	43.8	45.5	48.0	66.0	68.0
9.0		1.586	1.136	0.935	0.808	0.464	0.436
		42.0	44.3	47.0	49.1	69.8	73.0
10.0		1.548	1.090	0.892	0.769	0.433	0.413
		42.2	44.7	47.3	50.1	73.6	76.0
11.0		1.516	1.052	0.876	0.744	0.408	0.392
		42.4	45.0	48.5	52.0	76.5	79.0
12.0		1.486	1.018	0.860	0.706	0.391	0.361
		42.6	45.7	50.0	54.0	81.5	84.0

to continuum brightness temperature ratio and the line full-width at half-maximum, expressed in Km s^{-1}. For a line which is unaffected by pressure broadening this parameter is proportional to the area, and hence energy, under the line.

A least-squares process was applied to the predicted line parameters in table 6.3 to find the best value of $N_e(e_i)$ which is $1.1 \pm 0.05\ 10^5\ cm^{-3}$. The solid lines in figures 6.18a, 6.18b and 6.18c represent this vale of $N_e(e_i)$.

Knowing independently the values of $N_e^2(e_i) \cdot d_{Kpc}$ and $N_e(e_i)$ we can calculate the distance to NGC 7027 :-

$$d_{Kpc} = \frac{172.0\ 10^8}{(1.1\ 10^5)^2\ 1.072} = 1.33 \pm 0.05$$

Cahn and Kaler (1971) find that the distance is 1.34 Kpc, although when account is taken of their incorrect assumption of hydrogen temperatures this is increased to 1.47. In contrast, Acker (1978), using data from several sources, finds that the distance is 1.09 Kpc.

Appendix

A1 Computer Program "SIMCONT"

```
      PROGRAM SIMCONT(INPUT=131B,OUTPUT=131B,TAPE5=INPUT,TAPE6,
+               DATA=131B,TAPE2=131B,TAPE1=DATA,TAPE64,TAPE66,TAPE61)
C
      DIMENSION CONT(30), NORD(14), NTICK(30,50), NNTICK(30)
C
      COMMON /BLK1/ AA(2,1024)
      COMMON /BLK2/ TL, TR, BL, BR, AAC
      COMMON /BLK3/ M, N, DX, DY
      COMMON /BLK4/ X(8), Y(8), NORDER(14,8)
      COMMON /BLK5/ ASDT(8), SCDT(8), DENS(9), DENM(9)
C
      DATA NORD /126,145,237,348,1358,1367,2456,
+      2478,12578,14678,23568,34567,123457,123468/
      DATA ((NORDER(I,J),J=1,8),I=1,14) /
+      3,0,1,6,2,0,0,0,   3,0,4,5,1,0,0,0,   3,0,2,7,3,0,0,0,
+      3,0,3,8,4,0,0,0,   4,0,3,8,5,1,0,0,   4,0,1,6,7,3,0,0,
+      4,0,4,5,6,2,0,0,   4,0,2,7,8,4,0,0,   5,0,2,7,8,5,1,0,
+      5,0,1,6,7,8,4,0,   5,0,3,8,5,6,2,0,   5,0,4,5,6,7,3,0,
+      3,3,4,5,1,2,7,3,   3,3,1,6,2,3,8,4/
C
C "SIMCONT" CONTOURS DATA FROM STANDARD FORMAT FILES. IF THE FILE HAS
C BEEN PRE-PROCESSED BY "PREVIEW" THEN INFORMATION SUCH AS BACKGROUND
C LEVEL/SLOPE AND NOISE LEVEL ARE PICKED UP AUTOMATICALLY. THE DATA
C IS INITIALLY ON TAPE #1 AND SELECTED PORTIONS OF IT ARE WRITTEN ON
C TAPE #2 BY THE SUB-ROUTINE "WINDOW". CONTOUR LEVELS ARE GENERATED
C SUBROUTINE "CONTOUR" ARE MAY BE LINEARALLY OR LOGARITHMICALLY SPACED.
C
C SINCE "SIMCONT" WORKS ON ONLY TWO LINES AT A TIME VERY LARGE ARRAYS
C MAY BE PROCESSED. N-S INVERSION, E-W REVERSAL AND TICK MARKS ON THE
C CONTOURS ARE OPTIONAL.
C
C THE PLOTTING OF THE CONTOURS IS ACCOMPLISHED BY MEANS OF "LOOK-UP"
C TABLES TO DETERMINE THE PATH OF A CONTOUR THROUGH A "PIXEL" BOX.
C
C INITIALISE ICCC PLOT PACKAGE.
C
      CALL START (2)
      CALL SWITCH (9HHARDCPYON)
C
   10 REWIND 1, 2
C
C READ HEADER FROM DATA TAPE #1.
C
      READ (1) IUR,ISC,NL,NPX,ASDT,SCDT,NDM,(DENS(J),DENM(J),J=1,NDM)
C
C REPORT NUMBER OF LINES, POINTS/LINE, BACKGROUND, RMS NOISE.
C
      WRITE (6,9010) NL,NPX,DENS(5),DENM(5)
C
C PROMPT FOR BLOCKING-UP FACTOR, SMOOTH SWITCH (TRUE=1), PLOT AREA.
C
      WRITE (6,9020)
      CALL BUFFEM (-6)
      READ (5,*) IBLK,ISMTH,MFST,MLST,NFST,NLST
```

```
C
C CHECK LIMITS, TRUNCATE SPECIFIED AREA IF NECESSARY.
C
      MFST = MAXO (1,MFST)
      MLST = MINO (NL,MLST)
      NFST = MAXO (1,NFST)
      NLST = MINO (NPX,NLST)
C
C COMPUTE M = NUMBER OF LINES, N = COLUMNS.
C
      M = ( MLST - MFST + 1 ) / IBLK
      N = ( NLST - NFST + 1 ) / IBLK
C
C AMEND HEADER PRIOR TO WRITING SELECTED REGION TO TAPE #2.
C
      DENS(1) = MFST           $  DENM(1) = NFST
      DENS(2) = MLST           $  DENM(2) = NLST
      DENS(3) = FLOAT (IBLK)   $  DENM(3) = FLOAT (ISMTH)
      NDM = MAXO (3,NDM)
C
      WRITE (2) IUR,ISC,M,N,ASDT,SCDT,NDM,(DENS(J),DENM(J),J=1,NDM)
C
      IF ( NDM .GE. 5 ) ISMTH = 2 * ISMTH
C
C FORM PLOT TAPE #2.
C
      CALL WINDOW (IBLK,ISMTH,NL,NPX,M,N,MFST,MLST,NFST,NLST,AAMAX)
C
C REPORT MAXIMUM HEIGHT OF SELECTED REGION.
C
      WRITE (6,9030) AAMAX
      CALL BUFFEM (-6)
C
C CONTOUR DATA.
C
   20 REWIND 2
C
      NCONT = 0
C
C PROMPT FOR CONTOUR PARAMETERS.
C
      WRITE (6,9040)
      CALL BUFFEM (-6)
C
      READ (END=20,ERR=20,5,*) MODE,A1,A2,NCONT,ALEAST
C
      IF ( MODE .NE. 1 .OR. MODE .NE. 2 ) GO TO 20
      IF ( NCONT .LE. 0 ) GO TO 20
C
C CALCULATE CONTOUR HEIGHTS.
C
      CALL CONTOUR (MODE,A1,A2,NCONT,ALEAST,CONT)
C
      INS = 0  $  IEW = 0  $  ITIC = 1
C
C IEW=1 FOR E-W REVERSAL, INS=1 FOR N-S INVERSION.
C ITIC =-1,0,+1 FOR ASCENDING, NONE, DESCENDING TICK MARKS ON CONTOURS.
C
C ENSURE THAT CONTOUR HEIGHTS ARE MULTIPLES OF 0.00001.
C INITIALISE TICK MARK ARRAY.
```

```
C
      DO 30 L = 1, NCONT
            NNTICK(L) = 0
            CONT(L) = 1.E-5 * AINT (1.E5 * CONT(L) + 0.5 ) + 1.E-5
         30 CONTINUE
C
      CALL NEWPAGE
      CALL HEADER
C
C INTICK IS THE INTERVAL BETWEEN TICK MARKS, SET AT ABOUT ONE/INCH.
C
      INTICK = 1 + N / 12
C
C IPLT=0 FOR BOX PLOT MODE, =1 FOR ST. ANDREWS CROSS PLOT MODE. SET TO
C 1 FOR SELECTED REGIONS CONTAINING LESS THAN 2500 PIXELS.
C
      IPLT = 0
      IF ( M * N .LE. 2500 ) IPLT = 1
C
C COMPUTE INVERSION COEFFICIENTS.
C
      C1 = IEW * ( N - 1 )  $  C2 = 1 - 2 * IEW
      C3 = INS * ( M - 1 )  $  C4 = 1 - 2 * INS
C
C WRITE INVERSION INFORMATION (IF PRESENT) ON TOP RIGHT OF PLOT.
C
      IF ( ( INS + IEW ) .EQ. 0 ) GO TO 40
      CALL SYMBOL (16.0,12.0,0.15,13HINVERSION   :,0.0,13)
      IF ( IEW .EQ. 1 ) CALL SYMBOL (18.1,12.0,0.15,3HE/W,0.0,3)
      IF ( INS .EQ. 1 ) CALL SYMBOL (18.1+IEW*0.6,12.0,0.15,3HN/S,0.0,3)
C
C WRITE CONTOUR LEVELS TO RIGHT OF PLOT.
C
   40 CALL SYMBOL (16.0,11.5,0.15,18HCONTOUR HEIGHT(S):,0.0,18)
C
      DO 50 L = 1, NCONT
            CALL NUMBER (16.0,(11.5-L*0.35),0.15,ABS(CONT(L)),0.0,4)
         50 CONTINUE
C
C DRAW BOX AROUND CONTOURS.
C
      CALL PLOT (0.0,0.0,-3)
      CALL PLOT (0.0,DY*(M-1),-2)
      CALL PLOT (DX*(N-1),0.0,-2)
      CALL PLOT (0.0,-DY*(M-1),-2)
      CALL PLOT (-DX*(N-1),0.0,-2)
C
C READ FIRST LINE OF DATA FROM TAPE #2 INTO UPPER ARRAY AA(1, ).
C NB. DATA IS BLOCKED UP INTO 512 WORDS/RECORD.
C
      LINE = 1
      NCBLK = N / 512  $  KE = N - NCBLK * 512
      KS = 0           $  KF = 0
C
      IF ( NCBLK .EQ. 0 ) GO TO 70
C
      DO 60 NB = 1, NCBLK
            KF = NB * 512  $  KS = KF - 511
C
            READ (2) (AA(1,K),K=KS,KF)
```

```
C
          60 CONTINUE
C
        IF ( KE .EQ. 0 ) GO TO 80
     70 KS = KF + 1
        KF = KF + KE
C
        READ (2) (AA(1,K),K=KS,KF)
C
     80 IF ( ITIC .EQ. 0 ) GO TO 120
C
C NTICK HOLDS THE LINE AND COLUMN NUMBERS OF EACH TICK MARK WHICH IS
C <= INTICK AWAY FROM THE CURRENT LINE. POINTS IN NTICK > INTICK FROM
C THE CURRENT LINE ARE REMOVED BY SHIFTING THE ARRAY LEFTWARDS.
C
        DO 110 L = 1, NCONT
               IF ( NNTICK(L) .EQ. 0 ) GO TO 110
               NN1 = 0
C
               DO 90 L1 = 2, NNTICK(L), 2
                     IF ( ABS (LINE-NTICK(L,L1-1)) .LE. INTICK ) GO TO 90
                     NN1 = NN1 + 2
                  90 CONTINUE
C
               IF ( NN1 .LE. 0 ) GO TO 110
               NNTICK(L) = NNTICK(L) - NN1
C
               DO 100 L1 = 1, NNTICK (L)
                      NTICK(L,L1) = NTICK(L,L1+NN1)
                  110 CONTINUE
C
          110 CONTINUE
C
C READ NEXT LINE OF DATA ON TAPE #2 INTO LOWER ARRAY AA(2, ).
C
    120 KS = 0   $  KF = 0
        IF ( NCBLK .EQ. 0 ) GO TO 140
C
        DO 130 NB = 1, NCBLK
               KF = NB * 512   $  KS = KF - 511
C
               READ (2) (AA(2,K),K=KS,KF)
C
           130 CONTINUE
C
        IF ( KE .EQ. 0 ) GO TO 150
    140 KS = KF + 1
        KF = KF + KE
C
        READ (2) (AA(2,K),K=KS,KF)

C
C LOOP ALONG UPPER AND LOWER DATA POINTS IN AA(   ) CONVERTING CORNERS
C OF EACH BOX TO WHOLE NUMBERS. AVERAGE CORNERS TO YIELD CENTRE VALUE.
C
C                      AA(1,K)=TL       (1)       AA(1,K+1)=TR
C                                   (5)      (6)
C                           (4)         AAC            (2)
C                                   (8)      (7)
C                      AA(2,K)=BL       (3)       AA(2,K+1)=BR
C
```

```
C ROUND TL, TR, BL, BR AND AAC TO NEAREST 0.001 SO THAT CONTOURS ONLY
C INTERSECT SIDES AND/OR DIAGONALS - NOT THE CORNERS OR CENTRE.
C
   43 DO 210 K = 1, N-1
           TL = 1.E-3 * AINT (1.E3 * AA(1,K) + 0.5)
           TR = 1.E-3 * AINT (1.E3 * AA(1,K+1) + 0.5)
           BL = 1.E-3 * AINT (1.E3 * AA(2,K) + 0.5)
           BR = 1.E-3 * AINT (1.E3 * AA(2,K+1) + 0.5)
           AAC = 0.25 * ( TL + TR + BL + BR )
C
           AAMAX = AMAX1 (TL,TR,BR,BL,AAC)
           AAMIN = AMIN1 (TL,TR,BR,BL,AAC)
C
C LOOP THROUGH CONTOUR LEVELS AT EACH PIXEL, TESTING FOR INTERSECTIONS.
C
           DO 200 NC = 1, NCONT
                C = CONT(NC)
C
C GO TO NEXT CONTOUR IF CONTOUR DOESN'T CROSS BOX SIDES.
C
                IF ( C .GE. AAMAX ) GO TO 210
                IF ( C .LE. AAMIN ) GO TO 210
C
C FIND INTERCEPTION POINTS OF CONTOUR WITH BOX SIDES AND DIAGONALS.
C NORDER(NTYPE) DEFINES THE ORDER IN WHICH THESE POINTS ARE TO BE
C LINKED.
C
                CALL INTERP (NT,C,LINE,K,C1,C2,C3,C4)
C
C FIND WHICH PATH CONTOUR TAKES IN BOX.
C
                DO 160 L = 1, 14
                     NTYPE = L
                     IF ( NORD(L) .EQ. NT ) GO TO 170
                 160 CONTINUE
C
C IF ARRIVE HERE THEN ALGORITHM IS FAULTY !
C
                STOP 123456
C
             170 IITIC = 0
                IF ( IITIC .EQ. 0 ) GO TO 190
C
                NN1 = NNTICK(NC)
C
                DO 180 L = 2, NN1, 2
                     ITEST = IABS (K-NTICK(NC,L))
                     ITEST = ITEST + IABS (LINE-NTICK(NC,L-1))
                     IF ( ITEST .LT. INTICK ) GO TO 190
                 180 CONTINUE
C
                     IF ( NN1 .GE. 50 ) GO TO 190
C
C IF OTHER TICK MARKS ARE > INTICK PIXELS AWAY ENABLE IITIC AND STORE
C LOCATION IN ARRAY INTICK.
C
                NN1 = NN1 + 2
                NTICK(NC,NN1-1) = LINE
                NTICK(NC,NN1) = K
                NNTICK(NC) = NN1
```

```
                     IITIC = ITIC
C
C SIGN OF (C-AAC) DEFINES THE DIRECTION OF TICK MARKS ON EACH CONTOUR,
C WHERE THE CONTOUR PATH IS TAKEN TO BE CLOCKWISE ABOUT THE CENTRE OF
C THE PIXEL.
C
                     IF ( C .LT. AAC ) IITIC = -IITIC
                 190 CALL PLOTXY (IPLT,NTYPE,IITIC)
                 200 CONTINUE
C
          210 CONTINUE
C
      LINE = LINE + 1
C
C END IF NEXT LINE IS LAST LINE, ELSE TRANSFER AA(2, ) INTO AA(1, )
C AND GO BACK TO READ IN ANOTHER LINE.
C
      IF ( LINE .GE. M ) GO TO 240
C
      DO 220 K = 1, N
             AA(1,K) = AA(2,K)
          220 CONTINUE
C
      GO TO 80
C
C PROMPT FOR PLOT OPTIONS.
C
  230 CALL PROMPT(49H HARDCOPY(H),NEW CONTOURS(C),NEW WINDOW(W),END(E),49)
C
      READ (END=230,ERR=230,5,9050) IOPTION
C
      IF ( IOPTION .EQ. 1HH ) CALL HARDCPY
      CALL NEWPAGE
      IF ( IOPTION .EQ. 1HW ) GO TO 10
      IF ( IOPTION .EQ. 1HC ) GO TO 250
      GO TO 240
C
C PROCESS PLOT TAPE AND END.
C
  240 CALL ENPLOT
C
      STOP
C
 9010 FORMAT (X,I4,7H LINES,,2X,I4,8H COLUMNS/X,12HBACKGROUND: ,
+               F10.5,2X,7HNOISE: ,F10.5)
 9020 FORMAT (X,43HBLOCKING FACTOR,SMOOTH(=1),FIRST+LAST LINES,
+               19H,FIRST+LAST COLUMNS)
 9030 FORMAT (X,13HMAXIMUM WAS: ,F10.5)
 9040 FORMAT (X,47HCONTOUR TYPE(1=LIN,2=LOG),MIN,MAX,NUMBER,LOWEST)
 9050 FORMAT (A1)
C
      END
C
C-------------------------------------------------------------------
C
      SUBROUTINE INTERP (NT1,CONT,LINE1,K1,C1,C2,C3,C4)
C
      COMMON /BLK2/ TL, TR, BL, BR, AAC
      COMMON /BLK3/ M, N, DX, DY
      COMMON /BLK4/ X(8), Y(8), NORDER(14,8)
```

```
C
C NORDER DEFINES THE 14 POSSIBLE ALTERNATIVE PATHS A CONTOUR MAY TAKE
C THROUGH A PIXEL IN TERMS OF THE ORDER OF CROSSING POINTS NT.
C X AND Y ARE MEASURED FROM THE LEFT HAND SIDE AND BOTTOM OF THE PLOT
C AREA RESPECTIVELY.
C
       C = CONT
       LINE = LINE1  $  K = K1
       CEW1 = C1     $  CEW2 = C2
       CNS1 = C3     $  CNS2 = C4
       NT = 0
C
       IF ( (C-TL)*(C-TR) .GE. 0.0 ) GO TO 2
       NT = NT * 10 + 1
       X(1) = ( CEW1 + CEW2 * ( K - 1 + (C - TL) / (TR - TL) ) ) * DX
       Y(1) = ( CNS1 + CNS2 * ( M - LINE ) ) * DY
C
     2 IF ( (C-TR)*(C-BR) .GE. 0.0 ) GO TO 3
       NT = NT * 10 + 2
       X(2) = ( CEW1 + CEW2 * K ) * DX
       Y(2) = ( CNS1 + CNS2 * ( M - LINE - (C - TR) / (BR - TR) ) ) * DY
C
     3 IF ( (C-BL)*(C-BR) .GE. 0.0 ) GO TO 4
       NT = NT * 10 + 3
       X(3) = ( CEW1 + CEW2 * ( K - 1 + (C - BL) / (BR - BL) ) ) * DX
       Y(3) = ( CNS1 + CNS2 * ( M - LINE - 1 ) ) * DY
C
     4 IF ( (C-BL)*(C-TL) .GE. 0.0 ) GO TO 5
       NT = NT * 10 + 4
       X(4) = ( CEW1 + CEW2 * ( K - 1 ) ) * DX
       Y(4) = ( CNS1 + CNS2 * ( M - LINE - (C - TL) / (BL - TL) ) ) * DY
C
     5 IF ( (C-TL)*(C-AAC) .GE. 0.0 ) GO TO 6
       NT = NT * 10 + 5
       DEL = 0.5 * (C - TL) / (AAC - TL)
       X(5) = ( CEW1 + CEW2 * ( K - 1 + DEL ) ) * DX
       Y(5) = ( CNS1 + CNS2 * ( M - LINE - DEL ) ) * DY
C
     6 IF ( (C-TR)*(C-AAC) .GE. 0.0 ) GO TO 7
       NT = NT * 10 + 6
       DEL = 0.5 * (C - TR) / (AAC - TR)
       X(6) = ( CEW1 + CEW2 * ( K - DEL ) ) * DX
       Y(6) = ( CNS1 + CNS2 + ( M - LINE - DEL ) ) * DY
C
     7 IF ( (C-BR)*(C-AAC) .GE. 0.0 ) GO TO 8
       NT = NT * 10 + 7
       DEL = 0.5 * (C - BR) / (AAC - BR)
       X(7) = ( CEW1 + CEW2 * ( K - DEL ) ) * DX
       Y(7) = ( CNS1 + CNS2 * ( M - LINE -1 + DEL ) ) * DY
C
     8 IF ( (C-BL)*(C-AAC) .GE. 0.0 ) GO TO 9
       NT = NT * 10 + 8
       DEL = 0.5 * (C - BL) / (AAC - BL)
       X(8) = ( CEW1 + CEW2 * ( K - 1 + DEL ) ) * DX
       Y(8) = ( CNS1 + CNS2 * ( M - LINE - 1 + DEL ) ) * DY
C
     9 NT1 = NT
C
       RETURN
C
```

```
      END
C
C-------------------------------------------------------------------
C
      SUBROUTINE PLOTXY (IPLT,NTYPE,IITIC)
C
      COMMON /BLK4/ X(8), Y(8), NORDER(14,8)
C
      N1 = NORDER(NTYPE,1)  $  N2 = NORDER(NTYPE,2)
      IF ( IPLT .EQ. 0 ) GO TO 30
C
C "ST. ANDREWS CROSS" MODE USES ALL CROSSING POINTS ON LINES 1-8.
C
      NS = 3  $  NF = N1 + 1
C
   10 DO 20 N = NS, NF
            L1 = NORDER(NTYPE,N)
            L2 = NORDER(NTYPE,N+1)
C
            CALL PLOT (X(L1),Y(L1),3)
            CALL PLOT (X(L2),Y(L2),2)
C
         20 CONTINUE
C
      IF ( IITIC .NE. 0 .AND. N2 .EQ. 0 ) CALL TICK (2+N1/2,N1-N1/2+3,
+                                                   NTYPE,IITIC)
C
      IF ( N2 .LE. 0 ) RETURN
C
      NS = 6  $  NF = 7  $  N2 = 0
      GO TO 10
C
C "BOX" MODE USES LINES 1-4.
C
   30 NS = 3  $  NF = N1 + 2
C
   40 L1 = NORDER(NTYPE,NS)
      L2 = NORDER(NTYPE,NF)
C
      CALL PLOT (X(L1),Y(L1),3)
      CALL PLOT (X(L2),Y(L2),2)
C
      IF ( IITIC .NE. 0 .AND. N2 .EQ. 0 ) CALL TICK (NS,NF,NTYPE,IITIC)
C
      IF ( N2 .EQ. 0 ) RETURN
C
      NS = 6  $  NF = 8  $  N2 = 0
      GO TO 40
C
      END
C
C-------------------------------------------------------------------
C
      SUBROUTINE HEADER
C
      DIMENSION PLDT1(4), PLDT2(4), PLDT3(4)
C
      COMMON /BLK3/ M, N, DX, DY
C
      DATA PLDT1 /10HLINE:     ,10H TO:      ,10HCOLUMN:   ,6H   TO:/
```

```
      DATA PLDT2 /10HBLOCKING F,6HACTOR:/
      DATA PLDT3 /10HDATA IS SM,6HOOTHED/
C
C READ HEADER FROM PLOT TAPE #2.
C
      READ (2) IUR,ISC,M,N,ASDT,SCDT,NDM,(DENS(J),DENM(J),J=1,NDM)
C
C DX=DY IS THE PLOT SCALE SUCH THAT MAX(M-1,N-1) IS EQUIVALENT TO 12".
C
      DX = 12.0 / ( AMAX0 (M,N) - 1 )  $  DY = DX
C
      CALL SYMBOL (0.0,15.0,0.15,ASDT,0.0,80)
      CALL SYMBOL (0.0,14.0,0.15,SCDT,0.0,80)
C
C RETURN IF DATA TAPE IS A COPY OF ORIGINAL ARCHIVE TAPE.
C
      IF ( NDM .LE. 1 ) RETURN
C
C     DENS(1) = MFST   DENS(2) = MLST
C     DENM(1) = NFST   DENM(2) = NLST
C     DENM(3) = SMOOTH SWITCH
C
      PLSC = DENS(4)  $  STEP = DENM(4)  $  BLK = DENS(3)
C
      CALL SYMBOL (0.0,13.0,0.15,PLDT1,0.0,36)
      CALL NUMBER (0.9,13.0,DENS(1),0.0,-1)
      CALL NUMBER (2.25,13.0,DENS(2),0.0,-1)
      CALL NUMBER (4.2,13.0,DENM(1),0.0,-1)
      CALL NUMBER (5.55,13.0,DENM(2),0.0,-1)
      CALL SYMBOL (6.45,13.0,0.15,PLDT21,0.0,16)
      CALL NUMBER (9.0,13.0,BLK,0.0,-1)
C
      IF ( DENM(3) .GE 1.0 ) CALL SYMBOL (9.6,13.0,0.15,PLDT3,0.0,16)
C
      IF ( NDM .LE. 3 ) RETURN
C
C DRAW 10 ARCSEC. LONG SCALE BAR.
C
      CHT = 10000.0 * DX / ( PLSC * STEP * BLK )
C
      X0 = DX * ( N - 1 ) + 0.25
C
      CALL PLOT (X0,0.0,3)
      CALL PLOT (X0+0.1,0.0,2)
      CALL PLOT (X0+0.05,0.0,3)
      CALL PLOT (X0+0.05,CHT,2)
      CALL PLOT (X0,CHT,3)
      CALL PLOT (X0+0.1,CHT,2)
C
      X0 = X0 + 0.2  $  Y0 = 0.5 * CHT - 0.075
C
      CALL SYMBOL (X0,Y0,0.15,2H10,0.0,2)
      CALL SYMBOL (X0+0.35,Y0+0.15,0.05,71,90.0,-1)
      CALL SYMBOL (X0+0.32,Y0+0.18,0.05,82,0.0,-1)
C
      IF ( NDM .LE. 4 ) RETURN
C
C DENS(5) = BACKGROUND MEAN LEVEL    $  DENM(5) = RMS NOISE.
C DENS(6) = BACKGROUND LINE COEFF.   $  DENM(6) = BACKGROUND COLUMN COEFF.
C DENS(7) = BACKGROUND CONSTANT      $  DENM(7) = NO. OF AREAS FITTED TO.
```

```
C
      CALL SYMBOL (16.0,15.0,0.15,22HBACKGROUND CORRECTION:,0.0,22)
      CALL SYMBOL (16.0,14.5,0.15,13HCONSTANT    :,0.0,13)
      CALL SYMBOL (16.0,14.0,0.15,13HLINE COEFF  :,0.0,13)
      CALL SYMBOL (16.0,13.5,0.15,13HCOLUMN COEFF:,0.0,13)
      CALL SYMBOL (16.0,13.0,0.15,13HBACKGROUND  :,0.0,13)
      CALL SYMBOL (16.0,12.5,0.15,13HRMS NOISE   :,0.0,13)
C
      CALL NUMBER (18.1,14.5,0.15,DENS(7),0.0,4)
      CALL NUMBER (18.1,14.0,0.15,DENS(6),0.0,4)
      CALL NUMBER (18.1,13.5,0.15,DENM(6),0.0,4)
      CALL NUMBER (18.1,13.0,0.15,DENS(5),0.0,4)
      CALL NUMBER (18.1,12.5,0.15,DENM(5),0.0,4)
C
      RETURN
C
      END
C
C----------------------------------------------------------------------
C
      SUBROUTINE TICK (M1,M2,NTYPE,IITIC)
C
      COMMON /BLK3/ M, N, DX, DY
      COMMON /BLK4/ X(8), Y(8), NORDER(14,8)
C
C PLACE 0.05" LONG TICK MARKS FROM AVERAGE OF POINTS M3, M4
C AT RIGHT ANGLES TO MM1, MM2 IN THE DIRECTION GIVEN BY IITIC.
C NB. IITIC = +1 FOR DESCENDING CONTOUR LEVELS.
C
      MM1 = NORDER(NTYPE,M1)
      MM2 = NORDER(NTYPE,M2)
      MM3 = NORDER(NTYPE,M2-1)
      MM4 = NORDER(NTYPE,M1+1)
C
      DELX = X(MM2) - X(MM1)
      DELY = Y(MM2) - Y(MM1)
      G = SQRT (DELX**2 + DELY**2)
      IF ( G .LE. 0.0 ) RETURN
C
      DELX = -DELX / G
      DELY = DELY / G
      G = DELY
      DELY = DELX * 0.05 * IITIC
      DELX = G * 0.05 * IITIC
C
      X1 = 0.5 * ( X(MM3) + X(MM4) )
      Y1 = 0.5 * ( Y(MM3) + Y(MM4) )
      X2 = AMAX1 (0.0,X1+DELX)
      X2 = AMIN1 ( (N-1) * DX,X2)
      Y2 = AMAX1 (0.0,Y1+DELY)
      Y2 = AMIN1 ( (M-1) * DY,Y2)
C
      CALL PLOT (X1,Y1,3)
      CALL PLOT (X2,Y2,2)
C
      RETURN
C
      END
C
C----------------------------------------------------------------------
```

```
C
      SUBROUTINE WINDOW (IBLK,ISMTH,NL,NPX,M,N,MFST,MLST,NFST,NLST,AAMAX)
C
      COMMON /BLK1/ AA(2,1024)
      COMMON /BLK5/ ASDT(8), SCDT(8), DENS(9), DENM(9)
C
      AAMAX = 0.0      $  RBLK = 1.0 / FLOAT (IBLK**2)
      NB1 = NPX / 512  $  NNB1 = NPX - NB1 * 512
      NB2 = N / 512    $  NNB2 = N - NB2 * 512
C
C
C IF BACKGROUND AND NOISE ARE NOT KNOWN ( ISMTH>2 ) USE
C APPROXIMATION OF SHOT NOISE ( SQRT ).
C
      SMOO = 1.0
      IF ( ISMTH .GE. 2 ) SMOO = DENM(5) / SQRT (DENS(5))
      SMOO = 0.5 * SMOO * ISMTH
C
      IF ( MFST .LE. 1 ) GO TO 20
C
C READ IN UNUSED LINES.
C
      DO 10 L = 1, MFST - 1
           CALL INOUT (NPX,1,NB1,NNB1,0.0,1,1.0,0,NPX,NB1,NNB1)
         10 CONTINUE
C
C READ IN LINES, BLOCKING UP AND SMOOTHING.
C
   20 DO 40 L = 1, M
           CALL INOUT (NPX,NFST,NB1,NNB1,SMOO,IBLK,RBLK,1,N,NB2,NNB2)
C
C FIND MAXIMUM HEIGHT OF PROCESSED LINE.
C
           DO 30 KK = 1, N
                AAMAX = AMAX1 (AAMAX,AA(1,KK))
              30 CONTINUE
C
         40 CONTINUE
C
      RETURN
C
      END
C
C-----------------------------------------------------------------
C
      SUBROUTINE INOUT (NPX,NFST,NB1,NNB1,SMOO,IBLK,RBLK,IOUT,N,NB2,NNB2)
C
      COMMON /BLK1/ AA(2,1024)
C
C THIS ROUTINE READS IN IBLK LINES, SMOOTHS EACH ONE USING SMOOTH VALUE
C (IF ISMTH IS SET) AND BLOCKS UP BY THE FACTOR IBLK.
C IF IOUT IS SET THE BLOCKED DATA IS OUTPUT TO TAPE #2.
C NB. THE DATA IS BLOCKED UP ON INPUT AND OUTPUT IN 512 WORDS/RECORD.
C
      DO 10 K = 1, N
           AA(1,K) = 0.0
         10 CONTINUE
C
      DO 70 I = 1, IBLK
           KS = 0  $  KF = 0
```

```
           IF ( NB1 .EQ. 0 ) GO TO 30
C
           DO 30 II = 1, NB1
                KF = II * 512
                KS = KF - 511
C
                READ (1) (AA(2,KK),KK=KS,KF)
C
             20 CONTINUE
           IF ( NNB1 .EQ. 0 ) GO TO 40
C
        30 KS = KF + 1
           KF = KF + NNB1
C
           READ (1) (AA(2,KK),KK=KS,KF)
C
        40 IF ( SMOO .NE. 0.0 ) CALL SMOOTH (N,SMOO)
C
           IKI = NFST - 1
C
           DO 60 K = 1, N
                TOT = 0.0
C
                DO 50 IK = 1, IBLK
                     IKI = IKI + 1
                     TOT = TOT + AA(2,IKI)
                  50 CONTINUE
C
                AA(1,K) = AA(1,K) + TOT * RBLK
             60 CONTINUE
C
        70 CONTINUE
C
      IF ( IOUT .NE. 1 ) RETURN
C
      KS = 0  $  KF = 0
      IF ( NB2 .EQ. 0.0 ) GO TO 90
C
      DO 80 II = 1, NB2
           KF = II * NB2
           KS = KF - 511
C
           WRITE (2) (AA(1,KK),KK=KS,KF)
C
        80 CONTINUE
C
      IF ( NNB2 .EQ. 0 ) RETURN
C
   90 KS = KF + 1
      KF = KF + NNB2
C
      WRITE (2) (AA(1,KK),KK=KS,KF)
C
      RETURN
C
      END
C
C-----------------------------------------------------------------
C
      SUBROUTINE SMOOTH (N,SMOO)
```

```
C
      COMMON /BLK1/ AA(2,1024)
C
C THIS ROUTINE ALTERS POINTS > 6 SIGMAS DIFFERENT FROM NEARBY POINTS.
C TESTING OF GROUPS OF 1,2,3,4 ADJACENT POINTS IS REPEATED UNTIL
C NO DISCREPANT POINTS REMAIN.
C
      SIGBG = 2.0 * SMOO
C
      DO 50 II = 1, 4
            IL = 1  $  IR = N - II - 1]
C
         10 NCORR = 0
            IFLG = 1
C
            DO 40 I = IL, IR
                  DEL = ( AA(2,I+II+1) - AA(2,I) ) / ( 1.0 + II )
C
                  DO 20 J = 1, II
                        TEST = AA(2,I) + DEL * J
                        SIG2 = 3.0 * SIGBG * SQRT (TEST)
                        TOP = AMAX1 (AA(2,I),AA(2,I+II+1)) + SIG2
                        BOT = AMIN1 (AA(2,I),AA(2,I+II+1)) - SIG2
                        IF (AA(2,I+J)-TOP)*(AA(2,I+J)-BOT).LT.0.0) GO TO 40
C
                     20 CONTINUE
C
                  DO 30 J = 1, II
                        AA(2,I+J) = AA(2,I+J) + DEL * J
                     30 CONTINUE
C
                  NCORR = NCORR + 1
                  IR = I
                  IF ( IFLG .EQ. 1 ) IL = I
C
                  IFLG = 0
               40 CONTINUE
C
            IF ( NCORR .NE. 0 ) GO TO 10
C
         50 CONTINUE
C
      RETURN
C
      END
C
C---------------------------------------------------------------------
C
      SUBROUTINE CONTOUR (MODE,A1,A2,NCONT,ALEAST,CONT)
C
      DIMENSION CONT(30)
C
      IF ( MODE .EQ. 2 ) GO TO 20
C
C CALCULATE HEIGHTS OF NCONT CONTOURS EQUI-SPACED BETWEEM MIN AND MAX
C IF ALEAST IS NOT 0.0 THEN THE FIRST CONTOUR IS ALEAST PERCENT ABOVE
C THE MEAN LEVEL AND NCONT IS INCREASED BY ONE.
C
      DELC = ( A2 - A1 ) / NCONT  $  IPC = 0
      CONT(1) = A1 + ALEAST * ( A2 - A1 )
```

```
      IF ( ALEAST .LE. 0.0 ) IPC = 1
C
      DO 10 K = 1, NCONT
            CONT(K+IPC) = A1 + ( K - 0.5 ) * DELC
         10 CONTINUE
C
      NCONT = NCONT + IPC
C
      RETURN
C
C CALCULATE HEIGHTS OF NCONT CONTOURS, THE LAST AT MAX, FIRST AT ALEAST
C PERCENT ABOVE THE MEAN BACKGROUND.
C
   20 DELTA = ( 2.0 - ALOG10 (ALEAST) ) / ( NCONT - 1 )
C
      DO 30 K = 1, NCONT
            CONT(K) = A1 + ( A2 -A1 ) * 10**( -DELTA * ( NCONT - K ) )
         30 CONTINUE
C
      RETURN
C
      END
```

A2 Computer Program "DOALL"

```
      PROGRAM DOALL(INPUT=131B,OUTPUT=131B, TAPE5=INPUT,TAPE6=OUTPUT,
+             DATA=131B,TAPE9=DATA,TAPE61=131B,TAPE66=131B,TAPE64=131B)
C
      DIMENSION NSC(3,15), NSCS(3), NPTS(3), TIME(3), LSTPK(3), NST(3),
+     Y(3,250), VEL(250), COUNTT(700), TEXT(3), POS(3), APER(3)
C
      COMMON /BLK1/ XP(250), YP(250)
      COMMON /BLK2/ YTOT(700), MIN, MAX, INC(3), CHISQ(250), YMAX
C
C "DOALL" PROCESSES AND PLOTS FP DATA STORED IN ASCII FORMAT ON DISC
C FILES IN THE STYLE : HEADER ; SEQUENTIAL DATA.
C
C INITIALISE ICCC PLOT PACKAGE.
C
      CALL START (2)
      CALL PENBGN (2)
      CALL SCALEZ (2.0)
      CALL SWITCH (9HHARDCPYON)
C
C ZERO TOTAL INTEGRATION TIME AND COUNT ARRAYS.
C
   10 DO 20 K = 1, 700
           COUNTT(K) = 0.0
           YTOT(K) = 0.0
        20 CONTINUE
C
      NPLOT = 1
      TOTIME = 0.0
      N = 1
C
      CALL BUFFEM (0)
      CALL NEWPAGE
C
C PROMPT FOR NEW SCAN PARAMETERS.
C
   30 CALL PROMPT (38HENTER SCAN NO AND NO OF SCANS,PLOT=0,0,38)
      READ (5,*) IWANT,IWANTS
C
      IF ( IWANT .LE. 0 ) GO TO 80
C
C READ DATA FILE UNTIL SELECTED SCAN FOUND; ELSE SIGNAL ERROR.
C
      REWIND (9)
C
   40 READ (END=50,9,*) NAME,A,B,C,D,E,F,LSTPK(N),NSCS(N)
      READ (9,*) (NSC(N,J),J=1,NSCS(N))
      READ (9,*) NPTS(N),NST(N),INC(N),TIME(N)
      READ (9,*) (Y(N,K),K=1,NPTS(N))
C
      IF ( IWANT .NE. NSC(N,1) ) GO TO 40
      IF ( IWANTS .NE. NSCS(N) ) GO TO 40
      IF ( INC(N) .NE. INC(1) ) GO TO 70
C
      TOTIME = TOTIME + TIME (N)
      GO TO 60
C
C PROMPT FOR ADDITIONAL SCANS ( MAX. OF 3 ).
```

```
C
   50 CALL PROMPT (21HSCAN NOT ON THIS FILE,21)
C
   60 CALL PROMPT (21HANOITHER SCAN=Y,PLOT=P,21)
C
      READ (5,9010) ANSCAN
C
      IF ( ANSCAN .NE. 1HY ) GO TO 80
      NPLOT =NPLOT + 1
      N = N + 1
      GO TO 30
C
   70 CALL PROMPT (21HINCREMENT DISCREPANCY,21)
      GO TO 30
C
C FIND EXTREME START AND END POINTS OF SELECTED SCANS.
C
   80 MIN = NST(1) + INC(1)
      IF ( IWANT .LE. 0 ) NPLOT = NPLOT - 1
      MAX = NST(1) + ( NPTS(1) - 3 ) * INC(1)
C
      DO 90 I = 1, NPLOT
            NSTCH = INC(1) * ( NST(I) / INC(1) )
            IF ( ((NST(I) - NSTCH)*2) .GE. INC(1) ) NSTCH = NSTCH + INC(1)
            NST(I) = NSTCH
            MIN = MIN0 (MIN,NST(I))
            MAX = MAX0 (MAX,(NST(I) + (NPTS(I) - 1) * INC(1)))
         90 CONTINUE
C
      DO 100 I = MIN, MAX, INC(1)
             YTOT(I) = 0.0
             COUNTT(I) = 0.0
         100 CONTINUE
C
C
C ACCUMULATE SCANS.
C
      DO 120 NN = 1, NPLOT
C
             DO 110 J = 1, NPTS(NN)
                    JJ = NST(NN) + ( J - 1 ) * INC(1)
                    YTOT(JJ) = YTOT(JJ) + Y(NN,J)
                    COUNTT(JJ) = COUNTT(JJ) + TIME(NN)
                110 CONTINUE
C
         120 CONTINUE
C
C SCALE ACCUMULATED SCANS AND FORM PLOT ARRAYS.
C
C
      YTOT(MIN) = 1000.0 * YTOT(MIN) / COUNTT(MIN)
      YMAX = YTOT(MIN)
      YMIN = YMAX
C
      DO 130 I = ( MIN + INC(1) ), MAX, INC(1)
             YTOT(I) = 1000.0 * YTOT(I) / COUNTT(I)
             YMAX = AMAX1 (YMAX,YTOT(I))
             YMIN = AMIN1 (YMIN,YTOT(I))
             YP( ( ( I - MIN ) / INC(1) ) + 1 ) = YTOT(I)
             XP( ( ( I - MIN ) / INC(1) ) + 1 ) = FLOAT (I)
```

```
            130 CONTINUE
C
C PLOT RAW ACCUMULATED DATA.
C
        NPTOT = IFIX ( FLOAT ( MAX - MIN ) / FLOAT ( INC(1) ) ) ) + 1
C
        CALL NEWPAGE
        CALL SCALE (FLOAT(MAX),FLOAT(MIN),INTX,SVALX,VINCX)
        CALL SCALE (YMAX,YMIN,INTY,SVALY,VINCY)
        CALL DRAW (NPTOT,INTX,INTY+1,SVALX,SVALY,VINCX,VINCY,10,1)
        CALL SYMBOL (0.0,11.0,0.5,8HRAW DATA,0.0,8)
        CALL BUFFEM (0)
C
C PROMPT FOR INTER-ORDER SPACING ROUTINE.
C
        CALL PROMPT (19HCALC CHISQ=IOS,GO=G,19)
C
        READ (5,9020) CHECK
C
        IF ( CHECK .NE. 3HIOS ) GO TO 160
        CALL IOSCALC (NPTSC)
C
        DO 140 K = 1, NPTSC
               CHISQ(K) = CHISQ(K) + SVALY
           140 CONTINUE
C
C ICCC ROUTINES FOR FINDING IOS VALUE USING CROSS-WIRES.
C
        CALL POINTS (XP,CHISQ,NPTSC)
        CALL KXWIRES (XPAGE,YPAGE,NF)
        CALL BUFFEM (0)
C
        XCHI = FLOAT (INTX) * XPAGE * VINCX / 15.0 + SVALX - FLOAT (MIN)
C
        CALL NUMBER (XPAGE,YPAGE,0.5,XCHI,0.0,-1)
C
        IF ( NF .NE. IHG ) GO TO 150
C
    160 CALL PROMPT (36HIOS VALUE,WAVELENGTH,BLOCKING FACTOR,36)
C
        READ (5,*) IOS,WAVE,NBLK
C
        IOS = IOS * ( 5006.85 / WAVE )
        IF ( IOS .GT. ( NPTOT * INC(1) ) ) IOS = ( NPTOT - 1 ) * INC(1)
        IOST = INC(1) * ( IOS / INC(1) )
        IF ( ( 2 * ( IOS - IOST ) ) .GE. INC(1) ) IOST = IOST + INC(1)
        IOS = IOST
        NIOS = ( MAX - MIN ) / IOS
C
        DO 180 K = MIN, MAX, INC(1)
               TEMP = 0.0
C
               DO 170 I = 1, NIOS
                      TEMP = TEMP + YTOT(K+(I-1)*IOS)
                  170 CONTINUE
C
               YTOT(K) = TEMP
           180 CONTINUE
C
C FOLD OVER SCAN TO LEAVE APPROX. 1.2 ORDERS.
```

```
C
      DO 190 K = MIN, ( MAX - IOS ), INC(1)
            YTOT(K) = ( YTOT(K) + YTOT(K+IOS) ) / FLOAT (1+NIOS)
        190 CONTINUE
C
C PLOT FOLDED DATA.
C
      CALL SCALE (FLOAT (MIN+IOS),FLOAT(MIN),INTX,SVALX,VINCX)
C
      NPT = IOS / INC(1) + 1
C
      CALL NEWPAGE
      CALL DRAW (NPT,INTX,INTY+1,SVALX,SVALY,VINCX,VINCY,10,1)
      CALL SYMBOL (0.0,11.0,0.5,11HFOLDED DATA,0.0,11)
C
  200 CALL BUFFEM (0)
C
C PROMPT FOR VELOCITY AXIS SCALE FACTORS.
C
      CALL PROMPT (27HENTER CENTRE,VCOG,VEL SCALE,27)
C
      READ (END=190,ERR=180,5,*) CMID,CVCOG,CVBYDN
C
      MID = CMID
      VCOG = CVCOG
      DVBYDN = CDVBYDN
C
  210 VELMIN = VCOG
      VELMAX = VCOG
      NBGN = ( ( MID / INC(1) ) - ( IOS / ( 2 * INC(1) ) ) ) * INC(1)
C
      IF ( NBGN .LT. MIN ) MID = MID + IOS
      IF ( NBGN .LT. MIN ) NBGN = NBGN + IOS
C
      DO 220 I = 1, NPT
            KK = ( I - 1 ) * INC(1) + NBGN
            IF ( KK .GT. ( MIN + IOS ) ) KK = KK - IOS
            XP(I) = VCOG + DVBYDN * FLOAT (INC(1) * (I-1) + NBGN - MID)
            YP(I) = YTOT(KK)
            VELMIN = AMIN1 (VELMIN,XP(I))
            VELMAX = AMAX1 (VELMAX,XP(I))
        220 CONTINUE
C
      CALL SCALE (VELMAX,VELMIN,INTX,SVALX,VINCX)
C
C PROMPT FOR TITLES.
C
  230 CALL PROMPT (12HENTER OBJECT,12)
C
      READ (END=230,ERR=230,5,9030) TEXT
C
  240 CALL PROMPT (8HPOSITION,8)
C
      READ (END=240,ERR=240,5,9030) POS
C
  250 CALL PROMPT (8HAPERTURE,8)
C
      READ (END=250,ERR=250,5,9030) APER
C
  260 CALL NEWPAGE
```

```
      CALL PLOT (1.0,0.0,-3)
      CALL WORDS (2.9,10.3,0.3,
+      53H$1H$2ELIOCENTRIC $1R$2ADIAL $1V$2ELOCITY ($1K$2M/SEC),0.0,53)
      CALL WORDS (15.6,3.7,0.3,14H$1C$2OUNTS/SEC,90.0,14)
      CALL WORDS (0.5,9.0,0.5,TEXT,0.0,30)
      CALL WORDS (5.0,9.0,0.3,POS,0.0,30)
      CALL WORDS (9.5,9.0,0.3,APER,0.0,30)
      CALL DRAW (NPT,INTX,INTY,SVALX,SVALY,VINCX,VINCY,1,1)
      CALL SYMBOL (0.2,12.6,0.2,28TENERIFFE 60  FLUX COLLECTOR,0.0,28)
      CALL SYMBOL (2.6,12.8,0.05,71,90.0,-1)
      CALL SYMBOL (12.2,12.6,0.2,13HAUG/SEPT 1978,0.0,13)
      CALL SYMBOL (0.2,12.2,0.2,16HBLOCKING FACTOR:,0.0,16)
      CALL NUMBER (3.6,12.2,0.2,FLOAT (NBLK),0.0,-1)
      CALL SYMBOL (12.2-1.&*NPLOT,12.2,0.2,12HSUM OF SCANS,0.0,12)
C
      DO 270 N = 1, NPLOT
             XS = 1.6 * N
             CALL SYMBOL (14.8-1.6*N,12.2,0.2,8H - (  ),0.0,8)
             CALL NUMBER (15.0-1.6*N,12.2,0.2,FLOAT (NSC(N,1)),0.0,-1)
             IF ( NSCS(N) .LE. 9 ) XS =XS - 0.2
             CALL NUMBER (15.8-XS,12.2,0.2,FLOAT (NSCS(N)),0.0,-1)
         270 CONTINUE
C
      CALL PLOT (0.0,12.0,-3)
      CALL PLOT (15.0,0.0,-2)
      CALL PLOT (0.0,1.0,-2)
      CALL PLOT (-15.0,0.0,-2)
      CALL PLOT (0.0,-1.0,-2)
      CALL BUFFEM (0)
C
C PROMPT FOR CHANGE OF AXES SCALES AND TITLES.
C
  280 CALL PROMPT (18HALTER SCAN SCALING,18)
C
      READ (END=280,ERR=280,5,9010) SHIFT
C
      IF ( SHIFT .NE. 1HY ) GO TO 310
C
  290 CALL PROMPT (31HVELOCITY:START,STEP,NO OF STEPS,31)
C
      READ (END=290,ERR=290,5,*) CSVALX,CVINCX,CINTX
C
      SVALX = CSVALX
      VINCX = CVINCX
      INTX = CINTX
C
  300 CALL PROMPT (33HCOUNT RATE:START,STEP,NO OF STEPS,33)
C
      READ (END=300,ERR=300,5,*) CSVALY,CVINCY,CINTY
C
      SVALY =CSVALY
      VINCY = CVINCY
      INTY = CINTY
C
  310 CALL PROMPT (22HCHANGE TITLE (HCPY=CR),22)
C
      READ (END=320,ERR=310,5,9010) NEWTIT
C
      IF ( NEWTIT .EQ. 1HY )  GO TO 230
      GO TO 310
```

```
C
C PROMPT FOR PROCESS PLOT, NEW PLOT.
C
 320 CALL PROMPT (16HDO YOU WANT HCPY,16)
C
     READ (END=320,ERR=320,5,9010) HCPY
C
     IF ( HCPY .EQ. 1HY ) CALL HARDCPY
C
 330 CALL PROMPT (8HNEW PLOT,8)
C
     READ (END=330,ERR=330,5,9010) NEWP
C
     IF ( NEWP .EQ. 1HY ) GO TO 10
C
     STOP
C
9010 FORMAT (A1)
9020 FORMAT (A3)
9030 FORMAT (3A10)
C
C
     END
C
C-------------------------------------------------------------
C
     SUBROUTINE SCALE (VMAX,VMIN,IINTV,SVAL,VINCV)
C
C ROUTINE TO SCALE AXES TO ANY DATA RANGE - BETTER THAN ICCC'S VERSION !
C
     VRANGE = VMAX - VMIN
     VSCALE = 10 ** ( AINT ( ALOG10 (VRANGE) ) )
     INTV = IFIX ( VRANGE / VSCALE )
     IF ( VRANGE .LT. VSCALE ) INTV = 1
     IF ( INTV .GT. 2 ) GO TO 10
C
     VSCALE = VSCALE * 0.2
     INTV = INTV * 5
  10 IF ( INTV .GT. 4 ) GO TO 20
C
     VSCALE = VSCALE * 0.5
     INTV = INTV * 2
C
  20 SVAL = AINT ( VMIN / VSCALE ) * VSCALE
     FVAL = AINT ( VMAX / VSCALE ) * VSCALE
     IF ( SVAL .LT. VMIN ) GO TO 30
C
     SVAL = SVAL - VSCALE
     INTV = INTV + 1
C
  30 IF ( FVAL .GT. VMAX ) GO TO 40
C
     FVAL = FVAL * VSCALE
     INTV = INTV + 1
     GO TO 30
C
  40 VINCV = VSCALE
     IINTV = IFIX ( ( ( FVAL - SVAL ) / VSCALE ) + 0.5 )
C
     RETURN
```

```
C
      END
C
C-----------------------------------------------------------------
C
      SUBROUTINE DRAW (NPTP,INTX,INTY,SVALX,SVAL;Y,VINCX,VINCY,NSUBX,NSUBY)
C
      COMMON /BLK1/ XP(250), YP(250)
C
C ROUTINE TO PLOT DATA AND AXES USING ICCC SOFTWARE.
C
      AX = 15.0 / FLOAT (INTX)
      AY = 10.0 / FLOAT (INTY)
      MODEX = -1
      MODEY = -1
      IF ( VINCX .LT. 1.0 ) MODEX = INT (0.9 - ALOG10 (VINCX))
      IF ( VINCY .LT. 1.0 ) MODEY = INT (0.9 - ALOG10 (VINCY))
C
      CALL LINAXS (1,10.0,AX,INTX,SVALX,VINCX,NSUBX,MODEX)
      CALL LINAXS (2,15.0,AY,INTY,SVALY,VINCY,NSUBY,MODEY)
      CALL POINTS (XP,YP,NPTP)
C
      RETURN
C
      END
C
C-----------------------------------------------------------------
C
      SUBROUTINE IOSCALC (NNN)
C
      COMMON /BLK2/ YTOT(700), MIN, MAX, INC(3), CHISQ(250), YMAX
C ROUTINE TO CACULATE DEVIATION OF SHIFTED SCAN FROM ORIGINAL.
C USED TO CALCULATE INTER-ORDER SPACING.
C
      NNN = ( MAX - MIN ) / INC(1) + 1
      CHIMAX = 0.0
C
      DO 20 I = 1, NNN
          CHISQ(I) = 0.0
C
          DO 10 K = ( MIN + (I-1) * INC(1) ), MAX, INC(1)
              IF ( ( MIN + (I-1) + INC (1) ) .GT. MAX ) GO TO 10
              CHISQ(I) = CHISQ(I) + (YTOT(K) - YTOT(K-(I-1)*INC(1)))**2
   10     CONTINUE
C
          CHISQ(I) = CHISQ(I) / FLOAT (NNN - I + 1)
          CHIMAX = AMAX1 (CHIMAX,CHISQ(I))
   20 CONTINUE
C
      DO 30 K = 1, NNN
          CHISQ(K) = CHISQ(K) * YMAX / CHIMAX
   30 CONTINUE
C
      RETURN
C
      END
```

References

Abel G., 1955, Pub. Astron. Soc. Pacific, 67, 258

Abel G. & Goldreich P., 1966, Pub. Astron. Soc. Pacific, 78, 232

Acker A., 1975, Astron. & Astrophys., 40, 415

Acker A., 1978, Astron. & Astrophys. Supp., 33, 319

Allen C.W., 1964, Astrophysical Quantities (London:Athlone Press)

Allen D.A., 1975, Infrared - The New Astronomy (Reid)

Aller L.H., 1956, Gaseous Nebulae (New York:Chapman & Hall)

Atherton P.D., 1979, Ph.D. Thesis, University of London

Atherton P.D., Hicks T.R., Reay N.K., Worswick S.P. & Smith W.H., 1978, Astron. & Astrophys., 66, 297

Atherton P.D., Hicks T.R., Reay N.K., Robinson G.J. & Worswick S.P., 1979, Astrophy. J., 232, 786

Bappu K.V. & Menzel D.H., Astrophys. J., 119, 508

Baum W.A., 1968, Astron. Techs., Ed. Hiltner W.A. (Chicago:Univ. of Chicago Press)

Beals C.S., 1931, Mon. Not. R. Astron. Soc., 91, 966

Becklin E.E., Neugebauer G. & Wynn-Williams C.G., 1973, Astrophys. Letts., 15, 87

Beckwith S., Neugebauer G., Beckwith E.E., Matthews K. & Persson S.E., 1980, Astron. J., 85, No 7, 886

Bignell R.C., 1974, Astrophys. J., 193, 687

Bohuski T. & Smith M.G., 1974, Astrophys. J., 193, 197

Bohuski T., Rubin R.H. & Smith M.G., 1970, Pub. Astron. Soc. Pacific, 82, 913

Bohuski T., Smith M.G. & Weedman D.W., 1970, Astrophys. J., 162, 27

Bowen I.S., 1928, Astrophys. J., 67, 1

Brocklehurst M., 1971, Mon. Not. R. Astron. Soc., 148, 417

Brocklehurst M. & Leeman S., 1971, Astrophys. Letts., 9, 35

Brocklehurst M. & Seaton M.J., 1972, Mon. Not. R. Astron. Soc., 157, 179

Cahn J.H. & Kaler J.B., 1971, Astrophys. J. Supp., 189, 319

Camm G.L., 1938, Mon. Not. R. Astron. Soc., 99, 71

Campbell W.W. & Moore J.H., 1918, Pub. Lick Obs., No 13

Cannon A.J., 1916, Harvard Annals, 76

Capriotti E.R., 1978, Planetary Nebulae, IAU Symp. No 76 (Holland:Reidel)

Carranza G., Courtes G. & Louise R., 1968, Planetary Nebulae, IAU Symp. No 34 (Holland:Reidel)

Chaisson E.J. & Malkan M.A., 1976, Astrophys. J., 210, 108

Chopinet M. & Lortet-Zuckermann M.C., 1976, Astron. & Astrophys. Supp., 25, 179

Churchwell E., Terzian Y. & Walmsley M., 1976, Astron. & Astrophys., 48, 331

Cudworth K.M., 1974, Astron. J., 79, 1384

Curtis H.D., 1918, Pub. Lick Obs., No 13

Danks A.C., 1971, Astron. & Astrophys., 14, 480

Dopita M.A., 1978, Planetary Nebulae, IAU Symp. No 76 (Holland:Reidel)

Doroshenko V.T., 1971, Sov. Astron., 15, 358

Doroshenko V.T., 1973, Astron. Zhur., 50, 501

Doroshenko V.T. & Kolotilov E.A., 1973, Astron. Zhur., 50, 1186

Dreyer J.L.E., 1888, A New General Catalogue of Nebulae and Clusters of Stars, Mem. R. Astron. Soc., 49, Part 1

Elliot K.H. & Meaburn J., 1977, Mon. Not. R. Astron. Soc., 181, 499

Evans D.S. & Thackeray A.D., 1950, Mon. Not. R. Astron. Soc., 110, 429

Faulkner D.J., 1970, Astrophys. J., 162, 513

Feibelman W.A., 1970, J. R. Astron. Soc. Canada, 64, 305

Feibelman W.A., 1971a, J. R. Astron. Soc. Canada, 65, 25

Feibelman W.A., 1971b, J. R. Astron. Soc. Canada, 65, 251

Ferch B.L. & Salpeter E.E., 1975, Astrophys. J., 202, 195

Finzi A. & Woolf R.A., 1971, Astron. & Astrophys., 11, 418

Flannery B.P. & Herbig G.H., 1973, Astrophys. J., 183, 491

Geballe T.R. & Rank D.M., 1973, Astrophys. Letts., 182, L113

Gillett F.C., Low F.J., & Stein W.A., 1967, Astrophys. J., 149, L97

Gillett F.C., Merrill K.M. & Stein W.A., 1972, Astrophys. J., 172, 367

Goad L.E. & Chaisson E.J., 1973, Mem. Soc. R. des Sci. de Liege No 5

Goldberg L., 1966, Astrophys. J., 144, 1225

Goudis C., McMullan D., Meaburn J., Tebbut N.J. & Terrett D.L., 1978, Mon. Not. R. Astron. Soc., 182, 13

Greig W.E., 1971, Astron. & Astrophys., 10, 161

Greig W.E., 1972, Astron. & Astrophys., 18, 70

Greim H.R., 1967, Astrophys. J., 148, 547

Gulak I.U., 1958, Soviet Astron. AJ, No 1, 802

Gurzadyan G.A., 1969, Planetary Nebulae (New York:Gordon & Breach)

Harman R.J. & Seaton M.J., 1964, Astrophys. J., 140, 824

Harris S. & Scott P.F., 1976, Mon. Not. R. Astron. Soc., 175, 371

Heap S.R., 1975, Astrophys. J., 196, 195

Henize K.G., 1961, Pub. Astron. Soc. Pacific, 73, 159

Herbig G.H. & Boyarchuk A.A., 1968, Planetary Nebulae, IAU Symp. No 34 (Holland:Reidel)

Hicks T.R., Reay N.K. & Scaddan R.J., 1974, J. Phys. E (Sci. Ins.), 7, 27

Hicks T.R., Phillips J.P. & Reay N.K., 1976, Mon. Not. R. Astron. Soc., 147, 339

Higgs L.A., 1971, Catalogue of Radio Obs. of Planetary Nebulae and Related Optical Data, Pub. Astrophys. Board, NRCC, Vol 1, No 1

Higgs L.A., 1972, Mem. Soc. R. des Sci. de Liege, No 5

Holtz J.Z., Geballe T.R. & Rank D.M., 1971, Astrophys. J., 164, L29

Hromov L., 1962, Astron. Zhurn., 39, 468

Hromov L. & Kohoutek L., 1968a, Bull. Astron. Soc. Czech., 19, No 1, 1

Hromov L. & Kohoutek L., 1968b, Bull. Astron. Soc. Czech., 19, No 2, 81

Hromov L. & Kohoutek L., 1968c, Bull. Astron. Soc. Czech., 19, No 2, 90

Hua C.T. & Louise R., 1970, Astron. & Astrophys., 9, 448

Huggins W., 1864, Proc. R. Soc. London, 13, 492

Hummer D.G. & Mihalas D., 1970, JILA Rep., No 10

Hummer D.G. & Seaton M.J., 1973, Mem. Soc. R. Liege, No 6

Hunter J.H. & Sofia S., 1971, Mon. Not. R. Astron. Soc., 154, 393

Jacquinot P., 1954, J. Opt. Soc. Amer., 44, No 10, 761

Johnson H.M., 1976, Astrophys. J., 208, 127

Johnson H.M., 1977, Astrophys. J., 216, 776

Kaler J.B., 1970, Astron. J., 160, 887

Kaler J.B., 1974, Astron. J., 79, 594

Kaler J.B., 1976, Astrophys. J., 220, 887

Kaler J.B. & Aller L.H., 1974, Pub. Astron. Soc. Pacific, 86, 635

Kaler J.B., Aller L.H. & Czyzak S.J., 1976, Astrophys. J. Supp., 31, 163

Kirkpatrick R.C., 1976, Astrophys. Letts., 17, 7

Kohoutek L., 1978, Planetary Nebulae, IAU Symp. No 76 (Holland:Reidel)

Lang K.R., 1974, Astrophysical Formulae (Berlin:Springer Verlag)

Liller L.H., 1965, Pub. Astron. Soc. Pacific, 77, 25

Liller L.H., 1978, Planetary Nebulae, IAU Symp. No 76 (Holland:Reidel)

Liller L.H. & Liller M.H., 1968, Planetary Nebulae, IAU Symp. No 34 (Holland:Reidel)

Liller M.H., Welther B.L. & Liller L.H., 1966, Astrophys. J., 144, 280

Louise R., 1974, Astron. & Astrophys., 30, 189

Lozinskaya T.A., 1973, Sov. Astron., 16, 945

Lucy L.B., 1967, Astron. J., 72, 813

Lutz J.H., 1978, Planetary Nebulae, IAU Symp. No 76 (Holland:Reidel)

Mathews W.G., 1966, Astrophys. J., 143, 173

Meaburn J., 1971, Astron. & Astrophys., 13, 478

Meaburn J., 1976, Detection and Spectrophotometry of Faint Light (Holland:Reidel)

McGee J.D., Bacik H., Coleman C.I. & Morgan B.L., 1972, AEEP, 33A, 13

Millikan A.G., 1974, Astron. J., 79, 1259

Miller J.S. & Mathews W.G., 1972, Astrophys. J., 172, 593

Minkowski R., 1946, Pub. Astron. Soc. Pacific, 58, 305

Minkowski R., 1947, Pub. Astron. Soc. Pacific, 59, 257

Minkowski R., 1948, Pub. Astron. Soc. Pacific, 60, 386

Minkowski R. & Osterbrock D.E., 1960, Astrophys. J., 131, 537

Mufson S.L., Lyon J. & Marionni P.A., 1975, Astrophys. Letts., 201, L85

Munch G., 1968, Planetary Nebulae, IAU Symp. No 34 (Holland:Reidel)

O'Dell C.R., 1963, Astrophys. J., 138, 67

Osterbrock D.E., 1950, Astrophys. J., 131 541

Osterbrock D.E., 1970, Astrophys. J., 159, 823

Osterbrock D.E., 1974, Astrophysics of Gaseous Nebulae (San Fransisco: Freeman)

Osterbrock D.E., Miller J.S. & Weedman D.W., 1966, Astrophys. J., 145, 697

Paczynski B., 1971, Acta Astron., 21, 417

Page T.L., 1942, Astrophys. J., 96, 78

Payne C., 1928, Harvard Bull., 855

Perek L. & Kohoutek L., 1967, Catalogue of Galactic Planetary Nebulae (Prague:Academia)

Perrine C.D., 1929, Astron. Nach., 237, 89

Pengelly R.M., 1964, Mon. Not. R. Astron. Soc., 127, 145

Pengelly R.M. & Seaton M.J., 1964, Mon. Not. R. Astron. Soc., 127, 165

Phillips J.P. & Reay N.K., 1977, Astron. & Astrophys, 59, 91

Phillips J.P. & Reay N.K., 1980, Astrophys. Letts., 21, 47

Pottasch S.R., Wu C-C., Wessilius P.R. & Van Duinen R.J., 1977, Astron. & Astrophys., 54, 435

Pottasch S.R., 1980, Astron. & Astrophys., 94, L13

Proisy P.E., 1974, Astron. & Astrophys., 35, 71

Rank D.M., Holtz J.Z., Geballe T.R. & Townes C.H., 1970, Astrophys. J., 161, L185

Reay N.K., 1981, Private Communication

Reay N.K. & Worswick S.P., 1979, Astron. & Astrophys., , 31

Rose W.K., 1966, Astrophys. J., 146, 838

Rubin R.H. & Palmer P., 1971, Astrophys. Letts., 8, 79

Scheuer P.A.G., 1960, Mon. Not. R. Astron. Soc., 120, 231

Scott P.F., 1973, Mon. Not. R. Astron. Soc., 161, 35

Scott P.F., 1978, Private Communication

Seaton M.J., 1959, Mon. Not. R. Astron. Soc., 119, 90

Seaton M.J., 1966, Mon. Not. R. Astron. Soc., 132, 113

Seyfert C.K., 1947, Pub. Astron. Soc. Pacific, 59, 35

Shao C.Y. & Liller W.L., 1968, Planetary Nebulae, IAU Symp. No. 34 (Holland:Reidel)

Shlovskii I.S., 1956, Astron Zh., 33, 315

Smith H.C., 1971, Astron. J., 76, 193

Smith H.C., 1973, Mon. Not. R. Astron. Soc., 164, 321

Smith L.F. & Aller L.H., 1969, Astrophys. J., 157, 1245

Smith M.G. & Gull T.R., 1975, Astron. & Astrophys., 44, 223

Smith R.L. & Rose W.K., 1972, Astrophys. J., 176, 395

Sobolev V.V., 1958, Voprosy Kosmogonii, 6, 112

Sofia S. & Hunter J.H., 1968, Astrophys. J., 152, 405

Spitzer L. & Greenstein J.L., 1951, Astrophys. J., 114, 407

Stoy R.S., 1933, Mon. Not. R. Astron. Soc., 93, 588

Stoy R.S., 1939, Pub. Astron. Soc. Pacific, 51, 233

Stromgren B., 1939, Astrophys. J., 89, 529

Taylor K., 1974, Astron. & Astrophys., 30, 45

Taylor K., 1977, Mon. Not. R. Astron. Soc., 181, 475

Taylor K., 1979, Mon. Not. R. Astron. Soc., 189, 511

Terzian Y., 1978, Planetary Nebulae, IAU Symp. No 76 (Holland:Reidel)

Terzian Y. & Balick B., 1972, Astrophys. Letts., 10, 41

Tinsley B.M., 1978, Planetary Nebulae, IAU Symp. No 76 (Holland:Reidel)

Treffers R.R., Fink U., Larson H.P. & Gautier T.N. III, 1976, Astrophys. J., 209, 793

Van Maanen A., 1934, Astron. J., 44, 9

Vine N.L., 1978, Applications of CAMAC to Astronomy, ESO/SRC Conf. Procs. Eds. Cullum M.J. & Stephens C.L.

Vityasev V.V., 1969, Astrofizika, 5, 83

Von Zeipel H., 1924, Mon. Not. R. Astron. Soc., 84, 665

Vorontsov-Velyaminov B.A., 1948, Gasnebel und Neue Sterne (Berlin: Verlag Kultur und Fortschritt)

Walker M.F., 1972, Mon. Not. R. Astron. Soc., 159, 379

Walker M.F., 1974, Mon. Not. R. Astron. Soc., 169, 199

Webster B.L., 1978, Planetary Nebulae, IAU Symp. No 76 (Holland:Reidel)

Weedman D.W., 1968, Astrophys. J., 153, 49

Weidemann V., 1968, Ann. Rev. Astron. & Astrophys., 6, 351

Westerlund B.E. & Henize K.G., 1967, Astrophys. Supp., 14, 154

Wilson O.C., 1946, Pub. Astron. Soc. Pacific, 58, 210

Wilson O.C., 1948, Astrophys. J., 108, 201

Wilson O.C., 1950, Astrophys. J., 111, 279

Wilson O.C., 1958, Rev. Mod. Phys., 30, 1025

Wilson O.C. & Aller L.H., 1951, Astrophys. J., 114, 412

Wilson O.C. & O'Dell C.R., 1963, Astrophys. J., 139, 511

Wright H.H., 1918, Pub. Lick Obs., No 13

Ya Kipper A., 1950, Dev. of Sov. Sci. in the Estonian SSR, 1940-1950

Zanstra H., 1931, Pub. Dom. Astron. Obs. Victoria, 4, 209